frontiers | Research Topics

Physical oceanography processes at eastern boundary upwelling systems

Edited by
Francisco Machín and Jose Gomez-Valdes

Published in
Frontiers in Marine Science

ISSN 1664-8714
ISBN 978-2-8325-4191-3
DOI 10.3389/978-2-8325-4191-3

About Frontiers

Frontiers is more than just an open access publisher of scholarly articles: it is a pioneering approach to the world of academia, radically improving the way scholarly research is managed. The grand vision of Frontiers is a world where all people have an equal opportunity to seek, share and generate knowledge. Frontiers provides immediate and permanent online open access to all its publications, but this alone is not enough to realize our grand goals.

Frontiers journal series

The Frontiers journal series is a multi-tier and interdisciplinary set of open-access, online journals, promising a paradigm shift from the current review, selection and dissemination processes in academic publishing. All Frontiers journals are driven by researchers for researchers; therefore, they constitute a service to the scholarly community. At the same time, the *Frontiers journal series* operates on a revolutionary invention, the tiered publishing system, initially addressing specific communities of scholars, and gradually climbing up to broader public understanding, thus serving the interests of the lay society, too.

Dedication to quality

Each Frontiers article is a landmark of the highest quality, thanks to genuinely collaborative interactions between authors and review editors, who include some of the world's best academicians. Research must be certified by peers before entering a stream of knowledge that may eventually reach the public - and shape society; therefore, Frontiers only applies the most rigorous and unbiased reviews. Frontiers revolutionizes research publishing by freely delivering the most outstanding research, evaluated with no bias from both the academic and social point of view. By applying the most advanced information technologies, Frontiers is catapulting scholarly publishing into a new generation.

What are Frontiers Research Topics?

Frontiers Research Topics are very popular trademarks of the *Frontiers journals series*: they are collections of at least ten articles, all centered on a particular subject. With their unique mix of varied contributions from Original Research to Review Articles, Frontiers Research Topics unify the most influential researchers, the latest key findings and historical advances in a hot research area.

Find out more on how to host your own Frontiers Research Topic or contribute to one as an author by contacting the Frontiers editorial office: frontiersin.org/about/contact

Physical oceanography processes at eastern boundary upwelling systems

Topic editors

Francisco Machín — University of Las Palmas de Gran Canaria, Spain

Jose Gomez-Valdes — Center for Scientific Research and Higher Education in Ensenada (CICESE), Mexico

Citation

Machín, F., Gomez-Valdes, J., eds. (2024). *Physical oceanography processes at eastern boundary upwelling systems*. Lausanne: Frontiers Media SA.

doi: 10.3389/978-2-8325-4191-3

Table of contents

frontiers | Frontiers in Marine Science

TYPE Editorial
PUBLISHED 11 December 2023
DOI 10.3389/fmars.2023.1337334

OPEN ACCESS

EDITED AND REVIEWED BY
Ming Li,
University of Maryland, College Park,
United States

*CORRESPONDENCE
Francisco Machín
francisco.machin@ulpgc.es

RECEIVED 12 November 2023
ACCEPTED 04 December 2023
PUBLISHED 11 December 2023

CITATION
Machín F and Gomez-Valdes J (2023) Editorial: Physical oceanography processes at eastern boundary upwelling systems.
Front. Mar. Sci. 10:1337334.
doi: 10.3389/fmars.2023.1337334

Editorial: Physical oceanography processes at eastern boundary upwelling systems

Francisco Machín[1]* and José Gomez-Valdes[2]

[1]Instituto Universitario de Acuicultura Sostenible y Ecosistemas Marinos (IU-ECOAQUA), University of Las Palmas de Gran Canaria, Las Palmas, Spain, [2]Physical Oceanography Department, Center for Scientific Research and Higher Education at Ensenada (CICESE), Ensenada, Mexico

KEYWORDS

physical oceanography, upwelling systems, observations, modelling, remote sensing

Editorial on the Research Topic
Physical oceanography processes at eastern boundary upwelling systems

With immense pleasure and pride, we present this special Frontiers in Marine Science Research Topic titled "*Physical Oceanography Processes at Upwelling Systems*." This Research Topic comprises ten exceptional research papers sourced from diverse oceanic realms across the globe.

The Upwelling Systems are captivating domains characterized by complex oceanographic processes that profoundly influence marine ecosystems, climate dynamics, and regional weather patterns. Exploring the intricate mechanisms in these unique systems is crucial for deciphering the fundamental drivers of oceanic behavior and their global implications. The research presented within this Research Topic unravels critical insights into these processes, enhancing our comprehension of the vast and intricate world beneath the surface waves. Spanning ten diverse articles, we traverse various locations, from the East Australian Current region to the Baltic Sea's Gulf of Riga, through the North Humboldt Upwelling System, the Sea of Japan, the eastern Atlantic Ocean and the Southwest East Sea.

Liu et al. delved into the seasonal variability of the East Australian Current (EAC), a significant component of the South Pacific subtropical circulation, revealing notable fluctuations in mesoscale eddy kinetic energy (EKE). Their study, which analyzed satellite altimeter data and employed an eddy-resolving ocean model, identified peak EKE in the upper ocean along Australia's east coast during summer and a minimum in winter. The research emphasized the influence of mixed instabilities, governed by both barotropic and baroclinic processes, and shed light on the dynamic mechanisms shaping EKE in the EAC region.

Alves et al. explored the intra-seasonal variability of the Canary upwelling system, focusing on the impact of low-level jets, including the continental coastal jet, Madeira's tip jets, and the Canary Islands' tip jets. Through a high-resolution fully coupled ocean-atmosphere numerical simulation, the study unraveled the intricate interactions among these jets, driven by oscillations in the Azores subtropical anticyclone. The

research highlighted the role of coastal-trapped oscillations, offering insights into potential climate change implications for the region.

Yari et al. analyzed the role of surface wind in the Peruvian upwelling system, conducting a detailed examination spanning seven decades. Their research identified significant fluctuations in the surface wind field over various timescales, with a focus on interannual semi-periodic wind fluctuation linked to El Niño Southern Oscillation (ENSO) and a decadal semi-regular fluctuation attributed to the Interdecadal Pacific Oscillation. The study revealed asymmetric wind anomaly patterns during ENSO phases and their implications for sea surface temperature and wind stress co-variability in the Humboldt Upwelling System.

Estrada-Allís et al. investigated turbulent mixing within the Cape Ghir upwelling filament in the African Eastern Boundary Upwelling System. Unlike previous assessments, their study detected enhanced turbulent kinetic energy dissipation rates linked to increased vertical current shear at the mixed layer's base. Through a one-dimensional turbulent entrainment approach, the research highlighted the impact of vertical shear and the active mixing layer depth on filament characteristics, emphasizing the importance of vertical shear often overlooked in existing parameterizations.

García-Reyes et al. utilized high-resolution sea surface temperature data to examine the spatial dynamics of Eastern Boundary Upwelling Systems (EBUS) and their coastal footprints. Their study suggested that the Humboldt and Iberian/Canary EBUS exhibit no contraction in their footprints on annual or seasonal scales, with implications for marine life and regional refugia. The research underscored the potential consequences for marine life and highlighted variations across regions and seasons.

Kim et al. investigated the quantitative contributions of wind stress and ocean currents to coastal upwelling along the southwest coast of the East Sea (Japan Sea), shedding light on the mechanisms influencing coastal upwelling and its impact on ocean ecosystems.

Rivas et al. explored the impact of the ENSO on the Northeastern Pacific Ocean, particularly the Baja California Peninsula. Using a mesoscale-resolving numerical ocean model, the study highlighted the role of air temperature and wind stress anomalies in driving regional warm anomalies with potential implications for biogeochemistry.

Fearon et al. delved into the influence of super-diurnal winds associated with the land-sea breeze (LSB) on the southern Benguela upwelling system. The LSB's crucial role in productivity and Harmful Algal Bloom development in St Helena Bay was emphasized, providing insights into the physical and biological functioning of the system.

Topé et al. utilized two high-resolution simulations of the NEMO model to elucidate the warming influence of the Niger River on the eastern part of the northern Gulf of Guinea upwelling. Their study revealed the Niger River's role in inhibiting cold-water upwelling through reinforcing stratification and preventing vertical shear of horizontal currents.

Skudra et al. investigated upwelling events in the Gulf of Riga from 2010 to 2022, revealing distinct phases and varied characteristics influenced by coastline orientation. The study suggested that weaker gradients could explain fast upwelling relaxation in the basin compared to larger Baltic Sea gulfs.

We want to express our heartfelt gratitude to the authors who entrusted us with their valuable contributions to this Research Topic. Your dedication and commitment to advancing marine science have enriched this compilation, adding depth and breadth to our understanding of the upwelling systems. Furthermore, we appreciate the diligent reviewers who invested their time and expertise in meticulously evaluating and refining the submissions. Your constructive feedback has been instrumental in maintaining the published works' highest quality and academic rigor. Additionally, our gratitude goes to the esteemed researchers who served as guest editors, guiding, and shaping the research articles and ensuring comprehensive and extensive coverage of this Research Topic.

This diverse set of studies not only enhances our understanding of the complex physical processes in coastal upwelling systems but also underscores their geographic significance and role in our oceans' global connectivity.

As we embark on this oceanographic journey, delving into the intricacies of Upwelling Systems, we invite you to immerse yourselves in the following pages. May this Research Topic inspire further exploration, collaboration, and innovation in the ever-evolving field of marine science.

Author contributions

FM: Writing – original draft, Writing – review & editing. JG: Writing – review & editing.

Conflict of interest

The authors declare that the research was conducted in the absence of any commercial or financial relationships that could be construed as a potential conflict of interest.

The author(s) declared that they were an editorial board member of Frontiers, at the time of submission. This had no impact on the peer review process and the final decision.

Publisher's note

frontiers | Frontiers in Marine Science

TYPE Original Research
PUBLISHED 02 December 2022
DOI 10.3389/fmars.2022.1069184

OPEN ACCESS

EDITED BY
Francisco Machín,
University of Las Palmas de Gran Canaria, Spain

REVIEWED BY
Chuanyu Liu,
Institute of Oceanology, Chinese Academy of Sciences (CAS), China
Joseph Kojo Ansong,
University of Ghana, Ghana

*CORRESPONDENCE
Shaojun Zheng
zhengsj@gdou.edu.cn

†These authors have contributed equally to this work

SPECIALTY SECTION
This article was submitted to Physical Oceanography, a section of the journal Frontiers in Marine Science

RECEIVED 13 October 2022
ACCEPTED 08 November 2022
PUBLISHED 02 December 2022

CITATION
Liu J, Zheng S, Feng M, Xie L, Feng B, Liang P, Wang L, Yang L and Yan L (2022) Seasonal variability of eddy kinetic energy in the East Australian current region. *Front. Mar. Sci.* 9:1069184. doi: 10.3389/fmars.2022.1069184

Seasonal variability of eddy kinetic energy in the East Australian current region

Jia Liu[1†], Shaojun Zheng[1,2,3*†], Ming Feng[4], Lingling Xie[1,2,3], Baoxin Feng[1,2,3], Peng Liang[1,2,3], Lei Wang[1,2,3], Lina Yang[1,2,3] and Li Yan[1,2,3]

[1]Laboratory for Coastal Ocean Variation and Disaster Prediction, College of Ocean and Meteorology, Guangdong Ocean University, Zhanjiang, Guangdong, China, [2]Key Laboratory of Climate, Resources, and Environment in Continental Shelf Sea and Deep Sea of Department of Education of Guangdong Province, Guangdong Ocean University, Zhanjiang, Guangdong, China, [3]Key Laboratory of Space Ocean Remote Sensing and Application, Ministry of Natural Resources, Beijing, China, [4]CSIRO Oceans and Atmosphere, Indian Ocean Marine Research Centre, Crawley, WA, Australia

The East Australian Current (EAC) is an important western boundary current of the South Pacific subtropical Circulation with high mesoscale eddy kinetic energy (EKE). Based on satellite altimeter observations and outputs from the eddy-resolving ocean general circulation model (OGCM) for the Earth Simulator (OFES), the seasonal variability of EKE and its associated dynamic mechanism in the EAC region are studied. High EKE is mainly concentrated in the shear-region between the poleward EAC southern extension and the equatorward EAC recirculation along Australia's east coast, which is confined within the upper ocean (0-300 m). EKE in this area exhibits obvious seasonal variation, strong in austral summer with maximum (465 ± 89 cm^2 s^{-2}) in February and weak in winter with minimum (334 ± 48 cm^2 s^{-2}) in August. Energetics analysis from OFES suggests that the seasonal variability of EKE is modulated by the mixed instabilities composed of barotropic and baroclinic instabilities confined within the upper ocean, and barotropic instability (baroclinic instability) is the main energy source of EKE in austral summer (winter). The barotropic process is mainly controlled by the zonal shear of meridional velocities of the EAC southern extension and the EAC recirculation. The poleward EAC southern extension and the equatorward EAC recirculation are synchronously strengthened (weakened) due to the local positive (negative) sea level anomalies (SLA) under geostrophic equilibrium, and the barotropic instability dominated by zonal shear is enhanced (slackened), which results in a high (low) level of EKE in the EAC region.

KEYWORDS

eddy kinetic energy, seasonal variability, barotropic and baroclinic instabilities, the East Australian Current, zonal shear of meridional velocities

1 Introduction

The East Australian Current (EAC) (Figure 1) is the western boundary current (WBC) of the South Pacific subtropical Circulation with high eddy kinetic energy (Everett et al., 2012; Pilo et al., 2015; Li et al., 2021) and feeds Southern Hemisphere supergyre circulation of the global thermohaline circulation (Ridgway, 2007; Speich et al., 2007). Studies on the characteristics of ocean currents off Australia's east coast have been carried out extensively through observations and models. The EAC usually carries warm and salty water southward along the offshore edge of the continental shelf. At about 30°S-32°S, part of the EAC turns east to New Zealand and then forms the EAC eastern extension (also known as the Tasman Front). The other part continues to flow southward along continental shelf to Tasmania as the EAC southern extension (Oke et al., 2019), and generates a large number of eddies (Bowen et al., 2005). In the east of the EAC southern extension, there is an equatorward current known as the EAC recirculation (Figure 1) (Everett et al., 2012; Oke et al., 2019). Zilberman et al. (2014) proved the existence of the poleward and equatorward currents in the EAC region along 32°S (0-2000 m) using Argo float profile and trajectory data. Based on the Regional Ocean Modelling System (ROMS) simulation and mooring array, Wijeratne et al. (2018) showed that the equatorward EAC recirculation could be found along 27°S, 32°S, and 36°S. Zilberman et al. (2018) found that the mean transport estimates of the poleward EAC southern extension and the equatorward EAC recirculation along 26°S were 19.5±2Sv and 2.5±0.5Sv from HR-XBT, Argo and altimetry data. Meanwhile, the poleward absolute geostrophic transport of the EAC is stronger in the austral summer ("austral" is implicit hereinafter) compared with winter. Zilberman et al. (2014) indicates a simultaneous strengthening of the geostrophic transport in the EAC southern extension and the EAC recirculation along 32°S. Wood et al. (2016) studied the seasonal cycle of vertical temperature structure in the EAC using mooring data along 34°S and indicated that warm upper waters appeared during the summer (December to February) and autumn (March to May), and cool bottom waters developed during the late winter and spring (August to November) and were maintained throughout the summer.

The EAC has strong variability in the period of 90 to 150 days, accompanied by extensively active mesoscale eddy activities (Mata et al., 2006; Sloyan et al., 2016; Archer et al., 2017). Everett et al. (2012) showed that there was high eddy activities south of the EAC separation point at about 32°S off Australia's east coast detected from altimetry. Cetina-Heredia et al. (2019) drew the same conclusion using the particle trajectory data set from the eddy-resolving ocean general circulation model (OGCM) for the Earth Simulator (OFES) and the Connectivity Modeling System and pointed out that cyclonic eddies mainly prevailed in the north of 32°S, but anticyclonic eddies mainly prevailed in the EAC southern

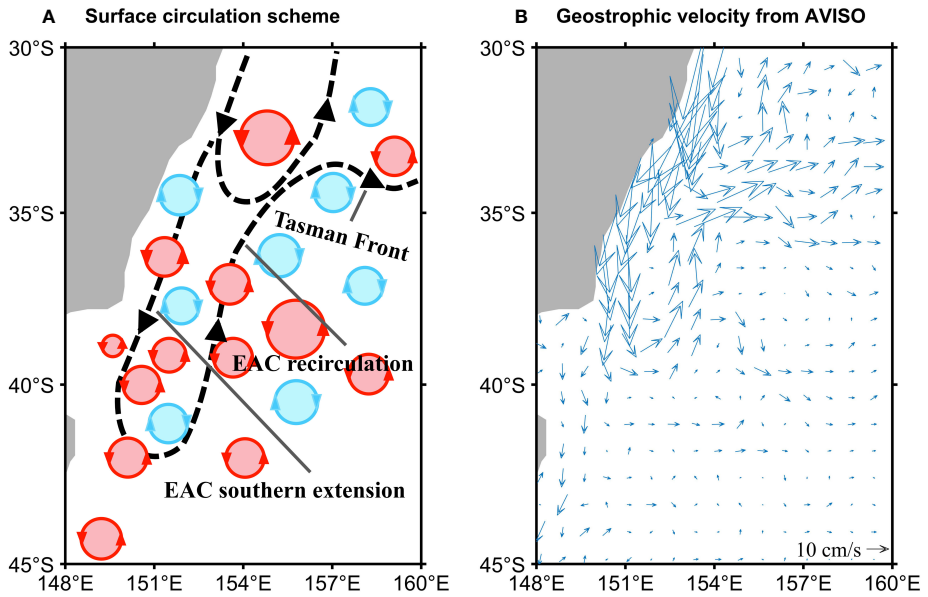

FIGURE 1
(A) A schematic diagram of identified current branches in the South Pacific subtropical Ocean modified from Oke et al. (2019). Schematic current branches (black dashed lines) are the EAC southern extension, the EAC recirculation, and the Tasman Front. The red and blue circles denote the mesoscale eddy field. **(B)** The distribution of climatological mean surface currents (arrow) in the EAC region (148°E-160°E, 30°S-45°S) from AVISO during January 1993-December 2019. The velocity vector represents the direction, and the length represents the magnitude of the velocity (10 cm s^{-1}).

extension. The anticyclonic eddies is larger than cyclonic eddies (Cetina-Heredia et al., 2019) and about 88% of the EAC system eddies propagate westward, turning south when they encounter Australia's east shelf slope (Pilo et al., 2015). The eddy amplitude and rotational speed in the EAC eddy core region (31°S-38°S) are significantly higher than that of global (Everett et al., 2012). Compared with Kuroshio current [1.5 m s^{-1}, (Tseng et al., 2011)], the velocity of the EAC is relatively weak [-0.4 m s^{-1}, (Zilberman et al., 2018)]. The magnitude of EKE in the EAC region (Pilo et al., 2015; Li et al., 2021) is about 1/2 of that in the Kuroshio region (Miyazawa et al., 2004; Wang and Pierini, 2020), and EKE in the EAC region is still relatively strong. Archer et al. (2017) showed that EKE exhibited seasonal variations in both magnitude and variance with a maximum in summer and a minimum in the EAC region in winter. Using the 1/3°×1/3° spatial resolution satellite altimetry data from 1992 to 2002, Qiu and Chen (2004) reported that EKE in the EAC was high in summer and low in winter, while the maximum appeared in March and the minimum appeared in August.

The impact of forcing on mesoscale variability in the EAC region is revealed in previous studies. Bowen et al. (2005) suggested that mesoscale energy and energy propagation of the EAC were consistent with the variability generated by the current itself in the separated region, and were not forced by mesoscale signals propagating westward from the South Pacific basin. Mata et al. (2006) further indicated that the growth of mesoscale eddies was modulated by the local instability of flow using a global ocean model and altimetric data. Bull et al. (2017) found the EAC itself had high variability and was rarely affected by remote ocean variability using Nucleus for European Modelling of the ocean (NEMO).

Previous studies have also done some energetics analysis to study the dynamic mechanism of mesoscale eddy generation and shedding in the EAC region. Bowen et al. (2005) indicated that barotropic instability played a leading role in the process of driving eddy shedding in the area where the EAC mainstream separates from the coast. However, Mata et al. (2006) and Bull et al. (2017) implied both barotropic and baroclinic instabilities were highly active in the process of eddy shedding in the EAC region. Oliver et al. (2015) suggested the barotropic and baroclinic instability processes in the EAC southern extension region could drive the continuous growth and increase the life cycle of anticyclonic eddies. The generation and shedding of eddies in the EAC region are accompanied by extensively high EKE (Macdonald et al., 2016). It is worth noting that the above studies mainly analyzed energy conversion between mean available potential energy (MPE) to eddy potential energy (EPE) caused by baroclinic instability.

As for the energy source of EKE in the EAC region, Li et al. (2021) implied that barotropic instability dominated the variation of EKE on the interannual scale by comparing the magnitude of barotropic instability and baroclinic instability (EPE to EKE) using the ROMS data, but did not analyze the roles of the two instability processes on the seasonal variability of EKE in detail. So far, the main factors controlling the seasonal variability of the EKE and the underlying mechanism in the EAC region are still unclear.

In this paper, based on satellite altimeter observations and OFES simulation, the seasonal variation of EKE in the EAC region is studied in detail, and its dynamic mechanism is clarified to reveal the relationship between EKE and large-scale ocean circulation in the western boundary current region. This study could deepen our understanding of the mesoscale process with the large-scale circulation. This paper is organized as follows: Sect. 2 describes the satellite altimeter observations, OFES simulation, and oceanic Lorenz energy cycle method. Sect. 3 presents the seasonal cycle and dynamic processes of EKE. Sect. 4 is the summary and discussions.

2 Data and methods

2.1 Satellite observation of sea level anomalies from AVISO

The daily satellite observation of sea level anomalies (SLA) is derived from the Copernicus Marine Environment Monitoring Service (CMEMS, https://marine.copernicus.eu/) authenticated by Archiving Validation and Interpretation of Satellite Data in Oceanography (AVISO). The SLA product combines different altimeter measurements from Jason-3, Sentinel-3A, HY-2A, Saral/AltiKa, Cryosat-2, Jason-2, Jason-1, T/P, ENVISAT, GFO, ERS1/2. The spatial resolution is 0.25°×0.25°, the temporal resolution is 1 day, and the data span is from January 1 1993 to December 31 2020. AVISO can capture eddy activities in the EAC region (Oliver et al., 2015). In this study, using SLA, observed surface EKE can be readily calculated by:

$$\mathrm{EKE} = \frac{g^2}{2f}\left[\left(\frac{\partial h'}{\partial x}\right)^2 + \left(\frac{\partial h'}{\partial y}\right)^2\right] \quad (1)$$

In Eq. (1), the Coriolis parameter $f = 2\Omega\sin(\varphi)$, which depends on latitude φ and angular rate Ω, and h' is sea level anomaly.

2.2 OGCM OFES

In this paper, OFES is used to study the vertical structure and dynamic mechanism of EKE. The flow field, temperature, and mesoscale eddy simulated by the OFES model are in good agreement with the observed results (e.g., transport (Wang et al., 2013; Cetina-Heredia et al., 2014), sea surface temperature (Wang et al., 2013), mesoscale eddy (Cetina-Heredia et al., 2019)). Thus, this model has the ability to reproduce the observed regional oceanographic features of the

circulation in the EAC region. The OFES-CLIM run is initialized from the World Ocean Atlas 1998 (Boyer and Levitus, 1997) and is spun-up with the climatological monthly forcing from the National Centers for Environmental Prediction/National Center for Atmospheric Research (NCEP/NCAR) reanalysis (Kalnay et al., 1996) from 1950 to 1999 (Masumoto, 2004). After the 50 year spin-up integration, the OFES-NCEP run is forced by the daily atmospheric forcing of the NCEP/NCAR reanalysis from 1950. The OFES-QSCAT run is forced by the QuikSCAT wind data, taking the National Centers for Environmental Prediction run (NCEP-run) simulation output on 20 July 1999 as its initial condition. The OFES-QSCAT with a spatial resolution of 10 km is used in this study, which fully characterize mesoscale variability (Maltrud and McClean, 2005; von Storch et al., 2012; Chassignet and Xu, 2017).The spatial resolution is 0.1°×0.1°, the number of vertical levels is 54, and the time interval for the model archive is 3 days from 22 July 1999 to 30 October 2009.

3 Methods

The oceanic Lorenz energy cycle (LEC) is an effective method to assess EKE variation (Lorenz, 1955; Böning and Budich, 1992; Beckmann et al., 1994; Zhuang et al., 2010; Zu et al., 2013; Brum et al., 2017; Yan et al., 2019), and has been successfully applied to areas with strong ocean currents [e.g., the Kuroshio Extension (Yang and Liang, 2018); the Gulf Stream Region (Kang and Curchitser, 2015); the North Equatorial Countercurrent (Chen et al., 2015); the East Madagascar Current (Halo et al., 2014); the California current (Marchesiello et al., 2003); the Agulhas Return Current (Zhu et al., 2018); the South Indian Countercurrent (Zhang et al., 2020); EAC (Li et al., 2021)]. The energetics analysis is utilized to determine the energy sources of EKE. The EKE governing equation is as follows (Oey, 2008; von Storch et al., 2012; Su and Ingersoll, 2016):

$$\frac{\partial \mathrm{EKE}}{\partial t} = -\vec{v} \cdot \nabla \mathrm{EKE} - \left[\overline{u'u'}\frac{\partial \bar{u}}{\partial x} + \overline{u'v'}\frac{\partial \bar{u}}{\partial x} + \overline{u'v'}\frac{\partial \bar{u}}{\partial y} + \overline{v'v'}\frac{\partial \bar{v}}{\partial y}\right] - \left(\overline{u'w'}\frac{\partial \bar{u}}{\partial z} + \overline{v'w'}\frac{\partial \bar{v}}{\partial z}\right) - \frac{g\overline{\rho'w'}}{\rho_0} + \frac{1}{\rho_0}\frac{\partial}{\partial z}\left(\overline{\tau_x{}' u'(z=0)} + \overline{\tau_y{}' v'(z=0)}\right) + \mathrm{res} \quad (2)$$

$$\mathrm{BTR} = -\left[\overline{u'u'}\frac{\partial \bar{u}}{\partial x} + \overline{u'v'}\frac{\partial \bar{u}}{\partial x} + \overline{v'v'}\frac{\partial \bar{u}}{\partial y} + \overline{v'v'}\frac{\partial \bar{v}}{\partial y}\right] \quad (3)$$

$$\mathrm{BCR} = -\frac{g\overline{\rho'w'}}{\rho_0} \quad (4)$$

$$\mathrm{BTR_v} = -\left(\overline{u'w'}\frac{\partial \bar{u}}{\partial z} + \overline{v'w'}\frac{\partial \bar{v}}{\partial z}\right) \quad (5)$$

$$\mathrm{BTR1} = -\overline{u'u'}\frac{\partial \bar{u}}{\partial x} \quad (6)$$

$$\mathrm{BTR2} = -\overline{u'v'}\frac{\partial \bar{v}}{\partial x} \quad (7)$$

$$\mathrm{BTR3} = -\overline{u'v'}\frac{\partial \bar{u}}{\partial y} \quad (8)$$

$$\mathrm{BTR4} = -\overline{v'v'}\frac{\partial \bar{v}}{\partial y} \quad (9)$$

$\bar{u}$ and $\bar{v}$ are zonal and meridional components of background currents with the time scale longer than 150 days, and u' and v' are high-frequency perturbations of zonal and meridional components with the time scale shorter than 150 days, consistent with previous studies in the EAC (Mata et al., 2006; Sloyan et al., 2016). Similarly, ρ' and w' are the perturbations of potential density and vertical velocity, respectively. Potential density ρ_0 = 1025kg m^{-3}. The gravitational constant g =9.8N kg^{-1}. The density ρ is calculated from the potential temperature (T) and salinity (S).

Eq. (2) is the EKE balance equation, which describes the EKE balances at steady state. $\frac{\partial \mathrm{EKE}}{\partial t}$ is the temporal change rate (time trend) of EKE; $-\vec{v}\cdot\nabla$ EKE means the redistribution rate of EKE through advection; the barotropic conversion rate (BTR) in Eq.(3) represents the EKE is produced by the shear and Reynolds stress of the flow. BTR serves as an indicator of energy transfer between mean kinetic energy (MKE) and EKE via barotropic instability and measures the strength of barotropic instability. Positive BTR indicates that energy is transferred from MKE to EKE (Orr, 1907) and the energy of the background circulation is transferred to eddies via barotropic instability (McWilliams, 2006), and negative BTR indicates that energy of background circulation is transferred to eddies. BCR in Eq.(4) serves as an indicator of energy transfer between EPE and EKE via baroclinic instability. The change in potential energy is performed by turbulent buoyancy forces on the vertical stratification. Positive BCR indicates that energy is transferred from EPE to EKE via baroclinic instability (Cushman-Roisin and Jean-Marie, 2011; Gula et al., 2015; Torres et al., 2018; Yu et al., 2019). the vertical barotropic conversion rate ($\mathrm{BTR_v}$) in Eq.(5) represents the energy is transferred due to small-scale shear instability. Since the vertical velocity w is much smaller than the horizontal velocity, it can be ignored. $\frac{1}{\rho_0}\frac{\partial}{\partial z}(\overline{\tau_x{}' u'(z=0)} + \overline{\tau_y{}' v'(z=0)})$ represents EKE is generated by the wind work and *res* is the energy dissipation, which can be ignored (Oey, 2008; von

Storch et al., 2012). For detailed derivation and further discussion of the LEC, please refer to (Böning and Budich, 1992; Rubio et al., 2009; Kang and Curchitser, 2015).

4 Results

4.1 Seasonal variability of EKE

The distribution of surface mean EKE from satellite altimeter observations in the EAC is shown in Figure 2A. High EKE (>500 $cm^2\ s^{-2}$) exists along Australia's east coast, and is mainly concentrated in the shear-region between the EAC southern extension and the EAC recirculation and extends to Tasmania, consistent with previous observations (Pilo et al., 2015; Li et al., 2021). There is a high EKE core at around 153°E, 35°S from observation data. The EKE averaged over the upper 300 m layer from OFES from July 1999 to October 2009 also shows a high core at around 153°E, 35°S (Figure 2B). Thus, the EKE averaged over the upper 300 m layer derived from the OFES simulation has similar spatial distribution and magnitude as the observed surface EKE from AVISO (Figures 2A, B). The EKE from OFES in south of 40°S is stronger than that from AVISO, which maybe come from overestimated modeled current (S1 in appendix) contrasting with that from AVISO (Figure 1B). In addition, the observed surface EKE averaged in 148°E-160°E, 30°S-45°S reaches the maximum (465±89 $cm^2\ s^{-2}$) in February, then gradually falls until it reaches the minimum (334±48 $cm^2\ s^{-2}$) in August, and then rises from September to January of the next year, with mean EKE value of 392 $cm^2\ s^{-2}$ (Figure 3, red solid line). The simulated seasonal variation of surface EKE (Figure 3, blue solid line) and averaged EKE over the upper 300 m layer (Figure 3, blue dash line) is strongest in February and weakest in July. EKE from satellite altimeter observations and OFES exhibits similar seasonal variations. Therefore, the OFES still provides a reasonable simulation of the spatial distribution and seasonal cycle of EKE in the EAC region.

The vertical structure of the EKE is studied using the OFES model output. The regional mean EKE at different depths is depicted as $E(t,z)$ following Chen et al. (2015). The $\frac{E(t,z)}{E(t,0)}$ indicates mean EKE normalized with the surface value is a function of depth. The black line shows that EKE drops rapidly with increasing depth and the mean EKE at 300 m is only approximately 35% of the surface value in the EAC region (Figure 4). The $C(z)$ indicates the coherence value of EKE time series at different depths relative to the surface EKE, defined by the following equation:

$$C(z) \equiv 1 - \frac{\langle\, [\, E(t,z) - r(z)\, E(t,0)\,]^2 \,\rangle}{\langle\, E^2(t,z)\,\rangle} \qquad (10)$$

where r(z) is a regression coefficient, $r(z) \equiv \langle E(t,z)E(t,0)/E^2(t,0)\rangle$. Physically, $C(z)$ indicates the ratio of $E(t,z)$ variance that is coherent in respect of $E(t,0)$. $C(z)$ exceeds 0.9 at all depths indicates that the temporal variability of EKE in the upper 300 m layer is similar to the surface (Figure 4). Considering the vertical distribution of EKE, the EKE, BTR, BCR, and current velocity are averaged over the upper 300 m layer to study the dynamic mechanism using the OFES simulation in the following.

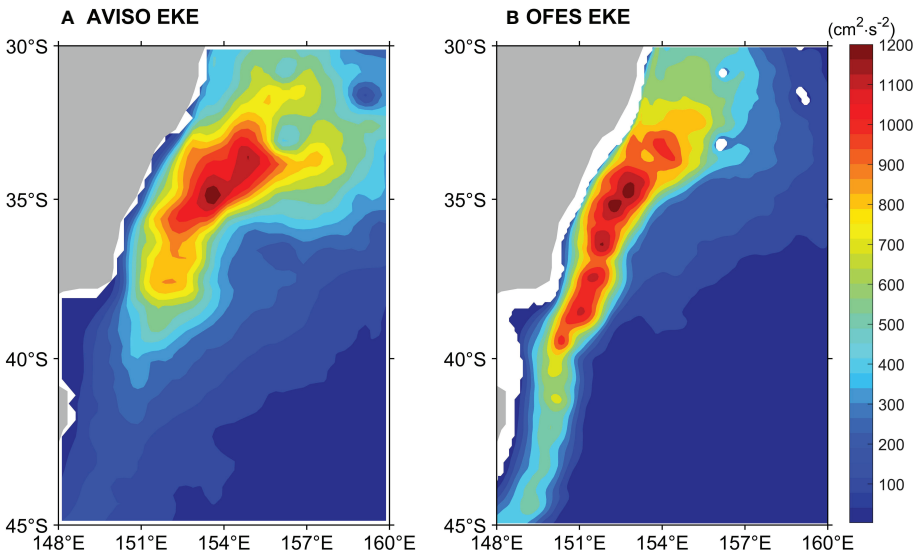

FIGURE 2
Climatological mean eddy kinetic energy (EKE, Unit: $cm^2\ s^{-2}$) calculated from the SLA data from **(A)** AVISO during January 1993-December 2019 and **(B)** OFES (0-300m) during July 1999-October 2009. EKE is calculated from Eq. (1).

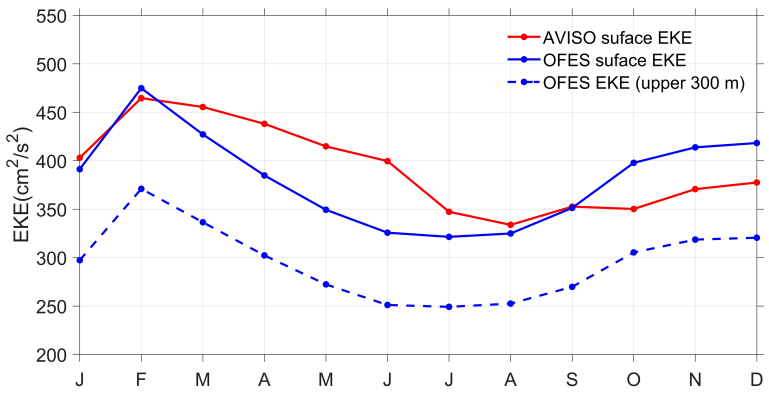

FIGURE 3
Monthly EKE time series in the EAC region (148°E-160°E, 30°S-45°S) calculated from AVISO during January 1993-December 2019 and from OFES during July 1999-October 2009. Red solid line and blue solid line represent surface EKE from AVISO and OFES, blue dash line represents averaged EKE over the upper 300 m layer from OFES.

4.2 Seasonal variability of BTR and BCR

Figure 5 shows the monthly spatial distribution of EKE averaged over the upper 300 m layer obtained by the OFES model from July 1999 to October 2009. High EKE always appears in the shear-region between the EAC southern extension and the EAC recirculation along Australia's east coast. The high EKE core near 151°E, 32°S in August (Figure 5H) is gradually strengthened and moves southward until it appears at 151°E, 38°S in February (Figure 5B). EKE is strongest in summer (Figures 5L, A, B) and weakest (Figures 5F–H) in winter in the shear region. Meanwhile, the

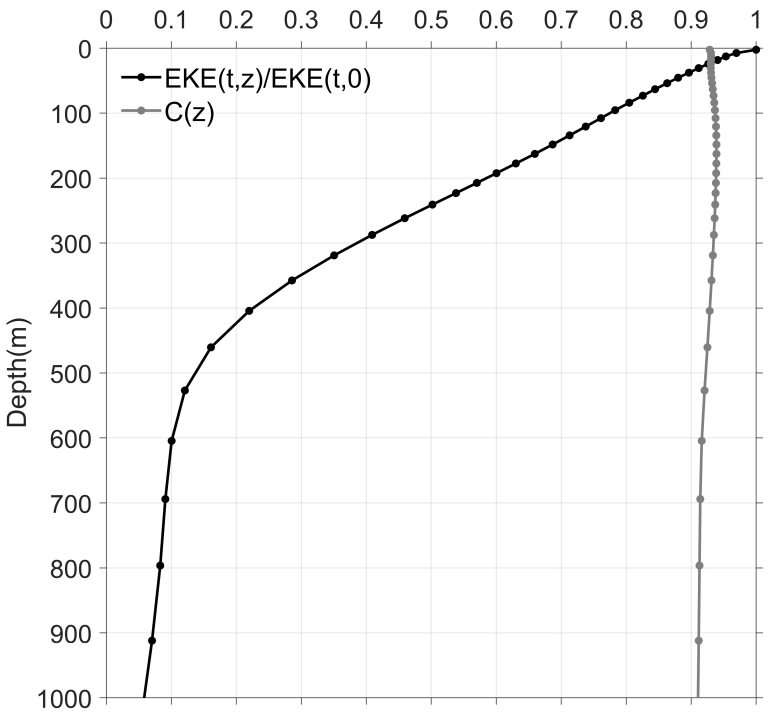

FIGURE 4
Black line: EKE averaged in 148°E-160°E, 30°S-45°S as a function of depth from OFES; the standardized EKE level as a function of depth: $\frac{E(t,z)}{E(t,0)}$. Gray line: the EKE coherence level as a function of depth relative to surface EKE: $C(z)$, and $C(z)$ is defined in Eq. (10).

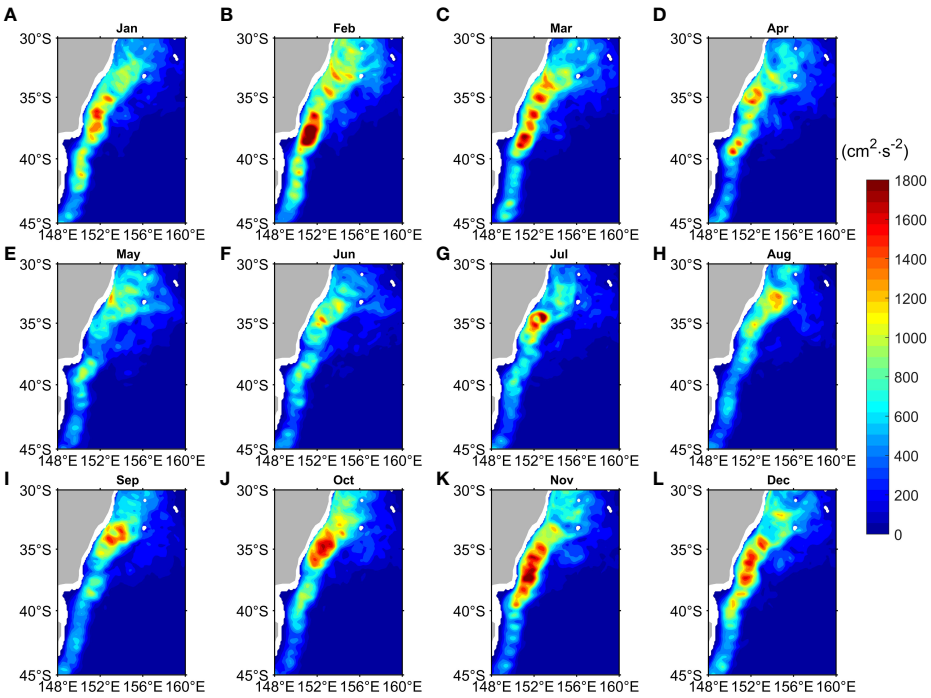

FIGURE 5
Monthly mean EKE distribution averaged over the upper 300 m layer from OFES during July 1999-October 2009 for **(A)** January, **(B)** February, **(C)** March, **(D)** April, **(E)** May, **(F)** June, **(G)** July, **(H)** August, **(I)** September, **(J)** October, **(K)** November and **(L)** December.

spatial distribution of EKE from AVISO is similar to that of OFES (S2 in Appendix).

MKE and EPE can be transferred to EKE via barotropic and baroclinic instabilities, respectively (Halo et al., 2014; Chen et al., 2015; Kang and Curchitser, 2015; Yang and Liang, 2018; Zhu et al., 2018; Zhang et al., 2020; Li et al., 2021). Next, we will ascertain the energy source of EKE on the seasonal scale in the region.

The BTR in the EAC region exhibits a mixed positive-negative pattern (Figure 6). The high positive and negative BTR is mainly concentrated in the shear-region corresponding to the high EKE (Figures 5, 6), consistent with previous studies (Bowen et al., 2005; Mata et al., 2006; Li et al., 2021). It implies that the energy conversion between the mean flow and the eddy field is active via barotropic instability. High negative BTR values indicate that inverse energy cascades frequently appear in the shear-region, and eddy energy transfer toward MKE may play an important role in influencing mean flow in the shear-region. The positive and negative values appear alternately along the EAC southern extension and EAC recirculation, and show significant along-stream variability (Figure 6), which is similar to the spatial pattern near the Charleston Bump in the Gulf Stream Region (Kang and Curchitser, 2015).

The transfers of MKE→EKE and EKE→MKE are highly energetic in each season. The positive BTR is strong in summer (Figures 6L, A, B) and weak in winter (Figures 6F–H), suggesting that energy transferred from MKE to EKE is an important energy source for eddies via barotropic instability in summer. BTR at the EAC main separation point (31°S-32°S) is not as high as BTR south of 32°S, indicating that the eastward Tasman Front is not the main factor for barotropic instability (Figure 6). In addition, the vertical profile of BTR averaged between 30°S and 45°S shows that conversion between MKE and EKE is mainly confined within the upper depths (0-300 m) and is consistent in the vertical direction (S3 in Appendix).

The spatial distribution of BCR is quite different from that of BTR in the EAC region. It is noteworthy that the magnitude of BCR is 1/8 of BTR (Figures 6, 7). In each season BCR is positive in most parts of the shear-region suggesting that energy transfer from EPE to EKE via baroclinic instability is active in this region. The negative BCR mainly exists along coast (32°S-38°S) and appears at 155°E, 33°S, and maybe results from the influence of the topography. Meanwhile, the positive BCR is strong in winter (Figures 7F, G, H), and in other seasons it is relatively weak. In addition, the vertical profile of BCR averaged between 30°S and 45°S demonstrates that the conversion of EPE between EKE is mainly confined within the upper depths (0-300 m). BCR is mainly positive, especially in winter suggesting that EPE tends to convert to EKE via baroclinic instability and more energy is converted to EKE in winter (S4 in Appendix).

To quantify the energy source of EKE in the EAC, Figure 8 depicts the monthly time series of the horizontal mean $\frac{\partial \mathrm{EKE}}{\partial t}$、

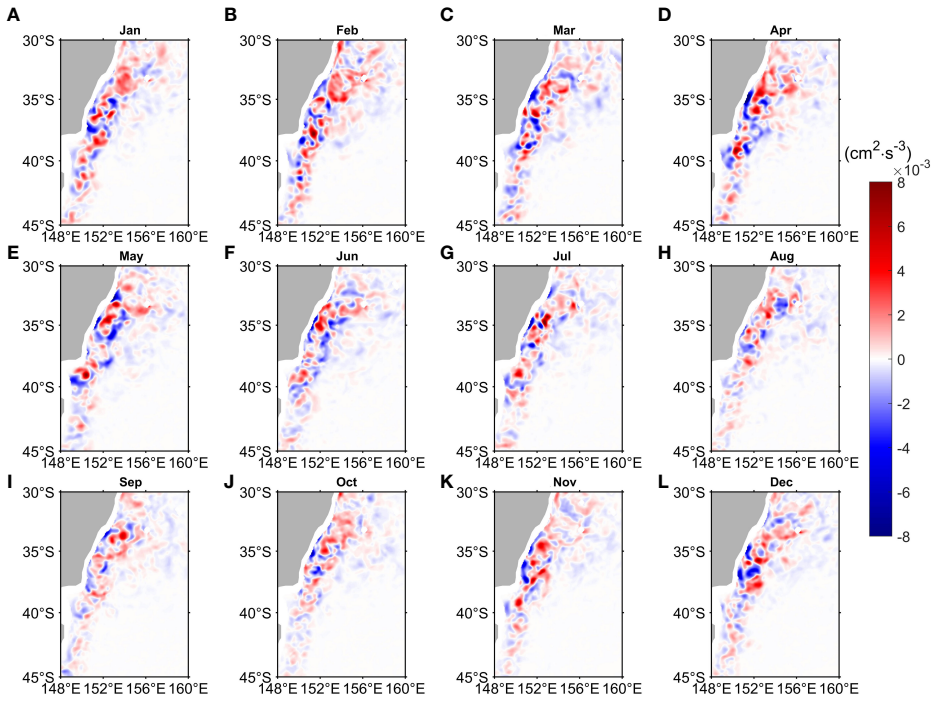

FIGURE 6
Monthly mean barotropic conversion rate (BTR, Unit: cm^2 s^{-3}) distribution averaged over the upper 300 m layer from OFES during July 1999-October 2009 for **(A)** January, **(B)** February, **(C)** March, **(D)** April, **(E)** May, **(F)** June, **(G)** July, **(H)** August, **(I)** September, **(J)** October, **(K)** November and **(L)** December. BTR is defined in Eq. (3).

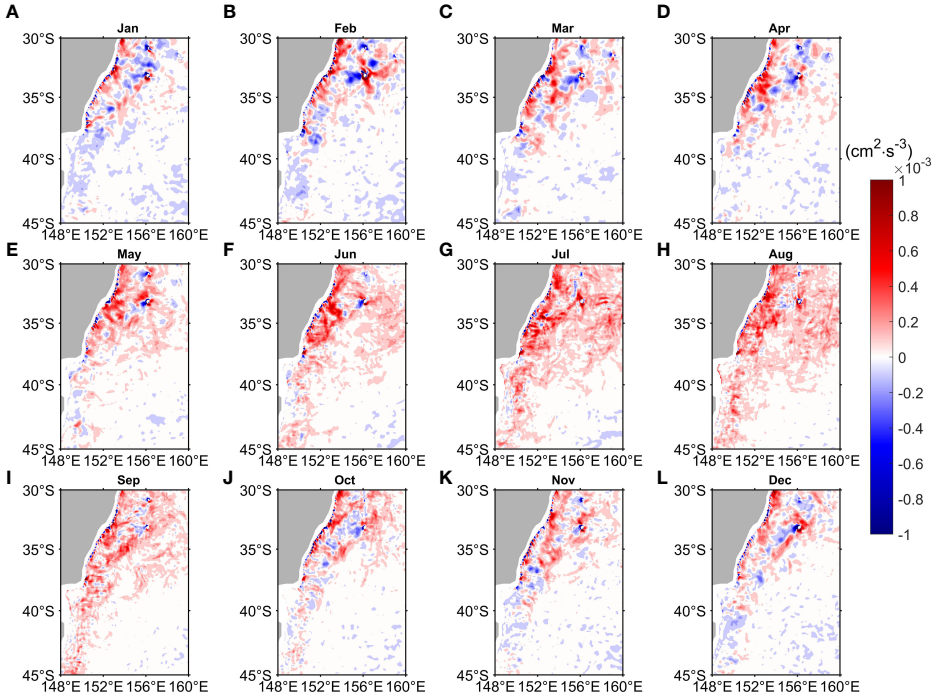

FIGURE 7
Monthly mean baroclinic conversion rate (BCR, Unit: cm^2 s^{-3}) distribution averaged over the upper 300 m layer from OFES during July 1999-October 2009 for **(A)** January, **(B)** February, **(C)** March, **(D)** April, **(E)** May, **(F)** June, **(G)** July, **(H)** August, **(I)** September, **(J)** October, **(K)** November and **(L)** December. BCR is defined in Eq. (4).

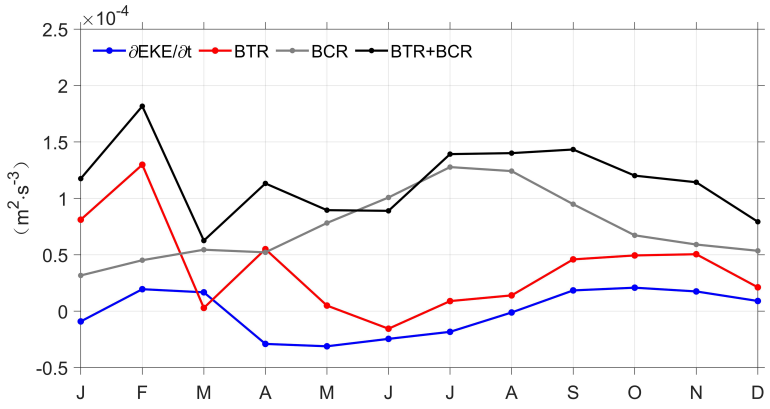

FIGURE 8
Seasonal variations of mean EKE trend (blue line), BTR (red line), BCR (gray line), and BTR+BCR (black line) averaged over the upper 300 m layer from OFES during July 1999-October 2009 in the EAC region (148°E-160°E, 30°S-45°S).

BCR、BTR, and the sum of BTR and BCR (BCR+BTR) in the EAC (148°E-160°E, 30°S-45°S). The $\frac{\partial \overline{EKE}}{\partial t}$ (blue line) is positive in February-March and September-December with an increase in EKE, while it is negative in other months with a decrease in EKE, presenting a double-peak structure in general. BCR+BTR (black line) are mainly positive confirming that both barotropic and baroclinic instabilities are the energy sources for EKE in the EAC region in climatological mean state, thus contributing to the intensive eddy activities in the EAC region. BTR (red line) reaches the maximum (1.30×10^{-4} cm^2 s^{-3}) in February and reaches the minimum (1.55×10^{-5} cm^2 s^{-3}) in June. The maximum (1.28×10^{-4} cm^2 s^{-3}) of BCR (gray line) appears in July and the minimum (3.17×10^{-5} cm^2 s^{-3}) appears in January. The main sources of EKE are the barotropic instability in summer and the baroclinic instability in winter, and the barotropic and baroclinic instabilities are equally important in other months. Because the order of magnitude of the spatial distribution of BCR is smaller than that of BTR, Li et al. (2021) believed that EKE in the EAC region on the interannual scale was mainly governed by barotropic instability. However, the spatial mean of BCR is comparable to that of BTR (Figure 8), because the positive and negative values of BTR are mostly offset (Figure 6). BCR+BTR is consistent with $\frac{\partial \overline{EKE}}{\partial t}$ on the seasonal scales (Figure 8), suggesting both barotropic and baroclinic instabilities play an important role in modulating the seasonal variability of EKE.

4.3 Mechanism of the seasonal variability of EKE

Since the enhancement of EKE in the EAC is mainly due to the strong barotropic instability in summer (Figure 8), we will study the main factors influencing BTR. Energetics analysis of Eq. (3) illustrates that BTR is closely related to the horizontal shear of flows. The seasonal variations of BTR1-BTR4 are quantitatively calculated to study the contribution of each term to BTR (Figure 9). BTR2 (green solid line) reaches its maximum (4.57×10^{-4} cm^2 s^{-3}) in February and its minimum (1.73×10^{-4} cm^2 s^{-3}) in August. Contrasting with mainly positive values of BTR (red solid line), both BTR1 (blue dash line) and BTR3 (black dash line) are negative each month, and out of phase with BTR. The amplitude of BTR4 is smaller than BTR2, and seasonal variability of BTR4 is not obvious and out of phase with BTR. Therefore, the influence of BTR4 can be ignored. Overall, the seasonal variation of BTR2 is consistent with that of BTR (Figure 8, 9), and the amplitude of BTR2 plays a dominant role in the four terms, suggesting that BTR2 makes the main contribution to BTR.

Because the BTR stands for energy transfer between MKE of background circulation and EKE via barotropic instability (McWilliams, 2006), and previous studies in the Celebes Sea (Yang et al., 2020) and in the North Equatorial Countercurrent of Western Pacific (Chen et al., 2015) show that variation of EKE is governed by barotropic instability of the background circulation. Next, we will analyze the role of background circulation in the variation of BTR. Considering that BTR2 partly represents the zonal gradient of low-pass filtered meridional velocity ($\frac{\partial \bar{v}}{\partial x}$) as shown in Eq. (7), and the location of high BTR corresponds to the shear-region between the poleward EAC southern extension and the equatorward EAC recirculation (Figures 1, 6), we should verify the role of the zonal gradient of meridional velocity in controlling the variation of BTR2 and BTR. The seasonal variability of $\frac{\partial \bar{v}}{\partial x}$ along 38°S is shown in Figure 10. The location of maximum southward velocity (the current axis of the EAC southern extension) is near 150.5°E, the location of maximum northward velocity (the current axis of the EAC recirculation) is near 152°E, and

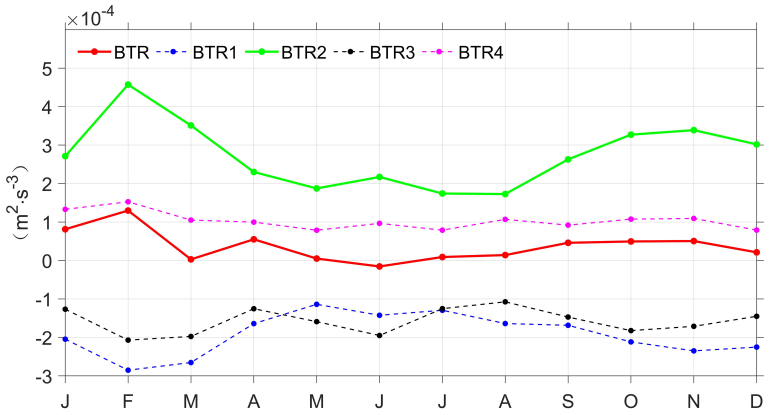

FIGURE 9
Seasonal variations of spatial mean BTR (red solid line), BTR1 (blue dash line), BTR2 (green solid line), BTR3 (black dash line), and BTR4 (magenta dash line) averaged over the upper 300 m layer from OFES during July 1999-October 2009 in the EAC region (148°E-160°E, 30°S-45°S).

maximum value of $\frac{\partial \bar{v}}{\partial x}$ is near 151.5°E. The $\frac{\partial \bar{v}}{\partial x}$ is strongest in February and weakest in July, consistent with the seasonal variation of BTR2 and BTR (Figures 8–10), confirming that zonal gradient of meridional velocity between the EAC southern extension and the EAC recirculation makes the main contribution to barotropic instability.

The minimum velocity between 150°E and 151.5°E and maximum velocity between 151.5°E and 152.5°E averaged over the upper 300 m along 38°S stand for the poleward EAC southern extension (Vmin) and the equatorward EAC recirculation (Vmax), respectively. And the difference between them (Vmin-Vmax) represents the zonal shear of meridional velocities of the EAC southern extension and the EAC recirculation. Both absolute values of Vmin and Vmax have the maximum in February and the minimum in July (Figure 11). The seasonal variation of the EAC southern extension (black line) and the EAC recirculation (blue line) is synchronous, consistent with previous studies indicating that the EAC southern extension is negatively correlated with the EAC recirculation (Zilberman et al., 2014; Sloyan and O'Kane, 2015). The Vmin-Vmax (red line) is strongest (-95.18 cm s^{-1}) in February and weakest (-19.11 cm s^{-1}) in July. The seasonal variation of zonal shear of meridional velocities is controlled by the synchronously seasonal varying

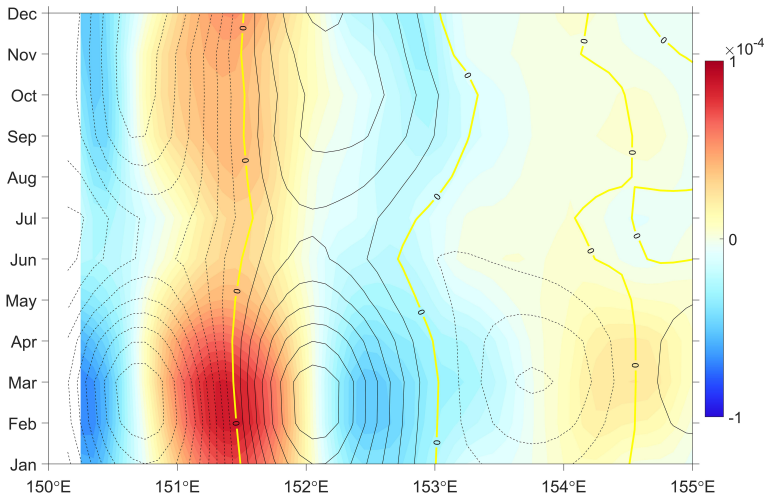

FIGURE 10
Seasonal variability of $\frac{\partial \bar{v}}{\partial x}$ (shaded color), and $\bar{v}$ (contour with 5 intervals, units: cm s^{-1}) along 38°S averaged over the upper 300 m layer from OFES during July 1999-October 2009. Solid (dash) lines represent positive (negative) meridional velocity.

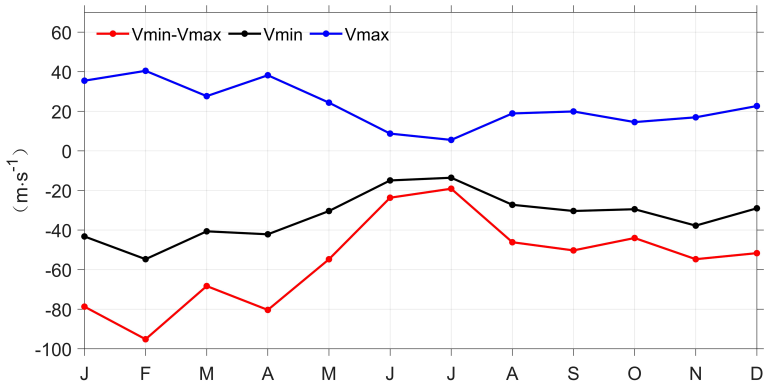

FIGURE 11
Seasonal variation of velocity of the EAC southern extension (Vmin, units: cm s^{-1}), the EAC recirculation (Vmax, units: cm s^{-1}), and the difference between the two currents (Vmin-Vmax, red line, units: cm s^{-1}) along 38°S. The black line is Vmin, the blue line is the Vmax, and the red line is Vmin-Vmax averaged over the upper 300 m layer from OFES during July 1999-October 2009.

poleward EAC southern extension and equatorward EAC recirculation (Figure 11).

The zonal shear of meridional currents matches well with the seasonal variation in EKE (Figures 3, 11), suggesting a synchronous phase relationship between the EKE and zonal shear of meridional currents. In other words, due to the dominant meridional circulation in this region, when the EAC southern extension and the EAC recirculation are strong, the zonal shear between the currents will be reinforced, and barotropic instability is enhanced, and it contributes to high EKE transferred from MKE. The result is consistent with other studies suggesting that horizontal shear of highly energetic flow tends to support EKE generation via barotropic instability (Chen et al., 2016; Zhan et al., 2016).

Furthermore, we examine the relationship between currents and SLA, the seasonal variation of SLA is obtained from AVISO from January 1999 to December 2009. In the EAC region, SLA is positive (negative) in summer (winter) (Figure 12), and the poleward EAC southern extension and the equatorward EAC recirculation are strengthened (weakened) due to geostrophic equilibrium (Figure 11). Then, the zonal shear of meridional currents is strengthened (weakened), and the EKE is strong (weak) *via* barotropic instability (Figures 3, 11). The SLA could influence the shear strength of upper ocean currents thus dynamically affecting the EKE. In addition, mesoscale eddies can be approximatively identified with SLA. Li et al. (2021) revealed there are more anticyclonic eddies than cyclonic eddies in the period of high EKE in the EAC on the interannual scale. Similarly, the anticyclonic circulation pattern of the poleward EAC southern extension and the equatorward EAC recirculation is more conducive to the formation of anticyclonic eddies in summer with high EKE (Figures 12L, A, B), and can explain the phenomenon found by Cetina-Heredia et al. (2019) that anticyclonic eddies are more common in EAC southern extension.

Figure 13 demonstrates the zonal distributions of temperature and velocity in the upper 300 m from the OFES model along 38°S. The zonal temperature gradient is positive on the west side of 152°E and negative on the east side, and the temperature trough reaches the deepest near 152°E in each season. The EAC southern extension (blue shaded color) and the EAC recirculation (red shaded color) are trapped above the west and east of the temperature trough, respectively (Figure 13). The velocity direction changes little with the increase of depth (S1 in appendix), which is consistent with the study of Mata et al. (2006) through satellite altimeter observations and current meter array. Here, the zonal mean depth of 15°C isotherm between 151°E-152°E along 38°S stands for the depth of temperature trough for quantitative analysis and is defined as D_{15}. The D_{15} reaches the deepest point (305.58 m) in February and reaches the shallowest point (221.81 m) in July (Figure 14). The D_{15} is high (low) in summer (winter), which is corresponding to more (less) anticyclonic eddies with positive (negative) SLA (Figure 12). Under geostrophic equilibrium, the poleward EAC southern extension and the equatorward EAC recirculation are strengthened (weakened), thus the variations of zonal shear and BTR have a good corresponding relationship with the D_{15} (Figures 8, 11, 14).

5 Summary and discussions

The seasonal cycle and dynamic mechanism of EKE in the EAC region are studied using satellite altimeter observations and high-resolution OFES-QSCAT model data. The high EKE is mainly concentrated in the shear-region of the poleward EAC southern extension and the equatorward EAC recirculation along Australia's east coast and is confined within the upper ocean (0-300 m). EKE displays a distinct seasonal cycle

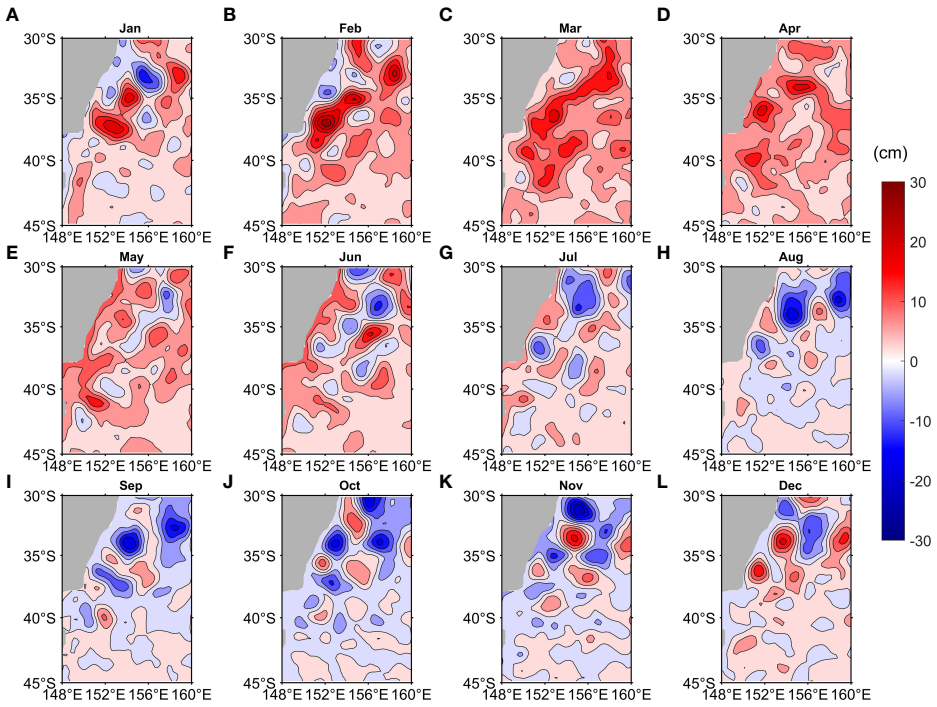

FIGURE 12
Monthly mean Sea Level Anomalies (SLA, Unit: cm) distribution from AVISO during January 1999-December 2009 for **(A)** January, **(B)** February, **(C)** March, **(D)** April, **(E)** May, **(F)** June, **(G)** July, **(H)** August, **(I)** September, **(J)** October, **(K)** November and **(L)** December.

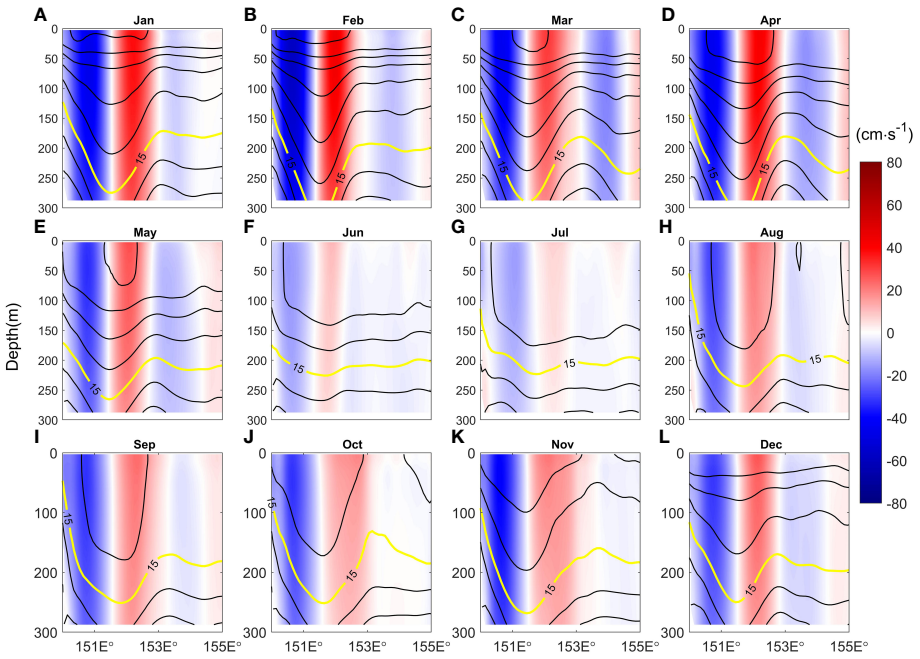

FIGURE 13
Zonal distributions of temperature (contour with 1 interval, units: °C) and velocity (shaded color, units: cm s^{-1}) in the upper 300 m along 38°S from OFES during July 1999-October 2009 for **(A)** January, **(B)** February, **(C)** March, **(D)** April, **(E)** May, **(E)** June, **(G)** July, **(H)** August, **(I)** September, **(J)** October, **(K)** November and **(L)** December.

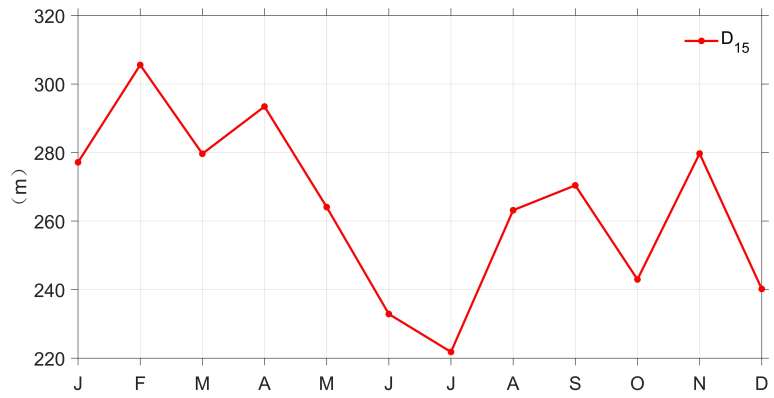

FIGURE 14
Seasonal variation of D_{15} along 38°S from OFES during July 1999-October 2009.

characteristic with a maximum value (465 cm^2 s^{-2}) in February and a minimum value (334 cm^2 s^{-2}) in August. The energy conversion terms are quantitatively analyzed, indicating that the seasonal variability of EKE is modulated by the mixed instabilities. Both barotropic and baroclinic instabilities are the energy sources of EKE in the EAC region, and barotropic instability dominates high EKE in summer and baroclinic instability influences EKE in winter. The variation of barotropic instability is dominated by zonal shear associated with synchronously-varying the poleward EAC southern extension and the equatorward EAC recirculation modulated by local SLA. In the EAC region, the local SLA is positive (negative) in summer (winter), then the poleward EAC southern extension and the equatorward EAC recirculation are synchronously strengthened (weakened) due to geostrophic equilibrium. And barotropic instability of the zonal shear between the poleward EAC southern extension and the equatorward EAC recirculation is enhanced (slackened), thus leading to high (low) EKE transferred from MKE.

Mata et al. (2006) have discovered the SLA propagates southward along the east Australian continental slope and it may account for the seasonal variation of local SLA in the shear-region. Besides, baroclinic instability which is the strongest in winter (Figure 8), Yang et al. (2022) presented that frictional forces played an important role in converting EPE to EKE in the global ocean as a result of active turbulent mixing induced by intense sea surface cooling and wind stirring in winter. In our study, this can be verified from the fact that mixed layer depth is the deepest in winter in the EAC region (Figures 13F–H). In addition, the seasonal variations of zonal shear and BTR are closely correlated to the seasonal variability of the depth of 15°C isotherm trough (Figures 8, 14). Therefore, the depth of 15°C isotherm trough can be used as an indicator of zonal shear or BTR in the EAC region. Moreover, transverse eddy heat transport and turbulent mixing are more intense in the WBC (Zhang et al., 2014). The effects of mesoscale eddies on the mass and heat transport in the EAC region need to be further studied.

Data availability statement

The original contributions presented in the study are included in the article/Supplementary Material. Further inquiries can be directed to the corresponding author.

Author contributions

SZ and JL contributed equally to this work. SZ initiated the idea, designed the study. JL and SZ analyzed the data and contributed to the writing of the manuscript. MF, LX, BF, PL, LW, LNY and LiY revised and edited the manuscript. All authors contributed to the article and approved the submitted version.

Funding

This study was supported by Guangdong Provincial College Innovation Team Project (2019KCXTF021), First-class Discipline Plan of Guangdong Province (080507032201, 080503032101 and 231420003), the Natural Science Foundation of China (42130605, 41706033 and 42006023), program for scientific research start-up funds of Guangdong Ocean University (R18023 and R19061). Guangdong Postgraduate Education Innovation Project (2022SFKC_057). The sea level anomaly (SLA) data was provided by Archiving, Validation and Interpretation of Satellite Oceanographic (AVISO, http://www.aviso.altimetry.fr/en/home.html). The OFES data were provided by Asia-Pacific Data Research Center (APDRC, http://apdrc.soest.hawaii.edu/dods/public_ofes/OfES/qscat_0.1_global_3day).

Conflict of interest

The authors declare that the research was conducted in the absence of any commercial or financial relationships that could be construed as a potential conflict of interest.

Publisher's note

All claims expressed in this article are solely those of the authors and do not necessarily represent those of their affiliated organizations, or those of the publisher, the editors and the reviewers. Any product that may be evaluated in this article, or claim that may be made by its manufacturer, is not guaranteed or endorsed by the publisher.

Supplementary material

The Supplementary Material for this article can be found online at: https://www.frontiersin.org/articles/10.3389/fmars.2022.1069184/full#supplementary-material

References

Archer, M. R., Roughan, M., Keating, S. R., and Schaeffer, A. (2017). On the variability of the East Australian current: Jet structure, meandering, and influence on shelf circulation. *J. Geophys. Res.-Ocean.* 122 (11), 8464–8481. doi: 10.1002/2017jc013097

Beckmann, A., BöNing, C. W., Brügge, B., and Stammer, D. (1994). On the generation and role of eddy variability in the central north Atlantic ocean. *J. Geophy. Res. Oceans* 99 (C10), 20381–20391. doi: 10.1029/94JC01654

Böning, C. W., and Budich, R. G. (1992). Eddy dynamics in a primitive equation model: Sensitivity to horizontal resolution and friction. *J. Phys. Oceanogr.* 22 (4), 361–381. doi: 10.1175/1520-0485(1992)022<0361:EDIAPE>2.0.CO;2

Bowen, M. M., Wilkin, J. L., and Emery, W. J. (2005). Variability and forcing of the East Australian current. *J. Geophys. Res.:Ocean.* 110 (C3), 1–10. doi: 10.1029/2004jc002533

Boyer, T. P., and Levitus, S. (1997). *Objective analyses of temperature and salinity for the world ocean on a 1/4° grid* (Silver Spring, Md: NOAA Atlas NESDIS, Natl. Oceanic and Atmos. Admin), 11.

Brum, A. L., Lima de Azevedo, J. L., de Oliveira, L. R., and Rezende Calil, P. H. (2017). Energetics of the Brazil current in the Rio grande cone region. *Deep-Sea Res. Part I-Oceanogr. Res. Pap.* 128, 67–81. doi: 10.1016/j.dsr.2017.08.014

Bull, C. Y. S., Kiss, A. E., Jourdain, N. C., England, M. H., and van Sebille, E. (2017). Wind forced variability in eddy formation, eddy shedding, and the separation of the East Australian current. *J. Geophys. Res.:Ocean.* 122 (12), 9980–9998. doi: 10.1002/2017jc013311

Cetina-Heredia, P., Roughan, M., van Sebille, E., and Coleman, M. A. (2014). Long-term trends in the East Australian current separation latitude and eddy driven transport. *J. Geophys. Res.:Ocean.* 119 (7), 4351–4366. doi: 10.1002/2014jc010071

Cetina-Heredia, P., Roughan, M., van Sebille, E., Keating, S., and Brassington, G. B. (2019). Retention and leakage of water by mesoscale eddies in the East Australian current system. *J. Geophys. Res.:Ocean.* 124 (4), 2485–2500. doi: 10.1029/2018jc014482

Chassignet, E. P., and Xu, X. B. (2017). Impact of horizontal resolution (1/12 degrees to 1/50 degrees) on gulf stream separation, penetration, and variability. *J. Phys. Oceanogr.* 47 (8), 1999–2021. doi: 10.1175/jpo-d-17-0031.1

Chen, X., Qiu, B., Chen, S., Qi, Y., and Du, Y. (2015). Seasonal eddy kinetic energy modulations along the north equatorial countercurrent in the western pacific. *J. Geophys. Res.:Ocean.* 120 (9), 6351–6362. doi: 10.1002/2015jc011054

Chen, X., Qiu, B., Du, Y., Chen, S. M., and Qi, Y. Q. (2016). Interannual and interdecadal variability of the north equatorial countercurrent in the Western pacific. *J. Geophys. Res.:Ocean.* 121 (10), 7743–7758. doi: 10.1002/2016jc012190

Cushman-Roisin, B., and Jean-Marie, B. (2011). *Introduction to geophysical fluid dynamics: Physical and numerical aspects* (Amsterdam, Netherlands: Academic Press).

Everett, J. D., Baird, M. E., Oke, P. R., and Suthers, I. M. (2012). An avenue of eddies: Quantifying the biophysical properties of mesoscale eddies in the Tasman Sea. *Geophys. Res. Lett.* 39, L16608. doi: 10.1029/2012gl053091

Gula, J., Molemaker, M. J., and McWilliams, J. C. (2015). Gulf stream dynamics along the southeastern US seaboard. *J. Phys. Oceanogr.* 45 (3), 690–715. doi: 10.1175/jpo-d-14-0154.1

Halo, I., Penven, P., Backeberg, B., Ansorge, I., Shillington, F., and Roman, R. (2014). Mesoscale eddy variability in the southern extension of the East Madagascar current: Seasonal cycle, energy conversion terms, and eddy mean properties. *J. Geophys. Res.:Ocean.* 119 (10), 7324–7356. doi: 10.1002/2014jc009820

Kalnay, E., Kanamitsu, M., Kistler, R., Collins, W., Deaven, D., Gandin, L., et al. (1996). Bulletin of the American Meteorological Society. *NCEP/NCAR 40-Year Reanalysis Proj.* 77 (3), 437–472. doi: 10.1175/1520-0477(1996)077<0437:Tnyrp>2.0.Co;2

Kang, D., and Curchitser, E. N. (2015). Energetics of eddy-mean flow interactions in the gulf stream region. *J. Phys. Oceanogr.* 45 (4), 1103–1120. doi: 10.1175/jpo-d-14-0200.1

Li, J., Roughan, M., and Kerry, C. (2021). Dynamics of interannual eddy kinetic energy modulations in a Western boundary current. *Geophys. Res. Lett.* 48 (19): e2021GL094115. doi: 10.1029/2021gl094115

Lorenz, E. N. J. T. (1955). Available potential energy and the maintenance of the general circulation. *Tellus* 7 (2), 157–167. doi: 10.3402/tellusa.v7i2.8796

Macdonald, H. S., Roughan, M., Baird, M. E., and Wilkin, J. (2016). The formation of a cold-core eddy in the East Australian current. *Cont. Shelf Res.* 114, 72–84. doi: 10.1016/j.csr.2016.01.002

Maltrud, M. E., and McClean, J. L. (2005). An eddy resolving global 1/10 degrees ocean simulation. *Ocean Model.* 8 (1-2), 31–54. doi: 10.1016/j.ocemod.2003.12.001

Marchesiello, P., McWilliams, J. C., and Shchepetkin, A. (2003). Equilibrium structure and dynamics of the California current system. *J. Phys. Oceanogr.* 33 (4), 753–783. doi: 10.1175/1520-0485(2003)33<753:esadot>2.0.co;2

Masumoto, Y. (2004). A fifty-year eddy-resolving simulation of the world ocean - preliminary outcomes of OFES (OGCM for the earth simulator). *J. Earth Simulator* 1, 35–56. doi: 10.32131/jes.1.35

Mata, M. M., Wijffels, S. E., Church, J. A., and Tomczak, M. (2006). Eddy shedding and energy conversions in the East Australian current. *J. Geophys. Res.: Ocean.* 111 (C9), C09034. doi: 10.1029/2006jc003592

McWilliams, J. C. (2006). *Fundamentals of geophysical fluid dynamics* (Cambridge, U.K: Cambridge University Press).

Miyazawa, Y., Guo, X., and Yamagata, T. (2004). Roles of mesoscale eddies in the kuroshio paths. *J. Phys. Oceanogr.* 34 (10), 2203–2222. doi: 10.1175/1520-0485(2004)034<2203:ROMEIT>2.0.CO;2

Oey, L. Y. (2008). Loop current and deep eddies. *J. Phys. Oceanogr.* 38 (7), 1426–1449. doi: 10.1175/2007jpo3818.1

Oke, P. R., Roughan, M., Cetina-Heredia, P., Pilo, G. S., Ridgway, K. R., Rykova, T., et al. (2019). Revisiting the circulation of the East Australian current: Its path, separation, and eddy field. *Prog. Oceanogr.* 176, 102139. doi: 10.1016/j.pocean.2019.102139

Oliver, E. C. J., O'Kane, T. J., and Holbrook, N. J. (2015). Projected changes to Tasman Sea eddies in a future climate. *J. Geophys. Res.:Ocean.* 120 (11), 7150–7165. doi: 10.1002/2015jc010993

Orr, W. M. F. (1907). The stability or instability of the steady motions of a perfect liquid and of a viscous liquid. part II: A viscous liquid. *Proc. R. Irish Acad. Sect. A: Math. Phys. Sci.* 27, 69–138.

Pilo, G. S., Mata, M. M., and Azevedo, J. L. L. (2015). Eddy surface properties and propagation at southern hemisphere western boundary current systems. *Ocean Sci.* 11 (4), 629–641. doi: 10.5194/os-11-629-2015

Qiu, B., and Chen, S. M. (2004). Seasonal modulations in the eddy field of the south pacific ocean. *J. Phys. Oceanogr.* 34 (7), 1515–1527. doi: 10.1175/1520-0485(2004)034<1515:smitef>2.0.co;2

Ridgway, K. R. (2007). Long-term trend and decadal variability of the southward penetration of the East Australian current. *Geophys. Res. Lett.* 34 (13), L13613. doi: 10.1029/2007gl030393

Rubio, A., Barnier, B., Jorda, G., Espino, M., and Marsaleix, P. (2009). Origin and dynamics of mesoscale eddies in the Catalan Sea (NW mediterranean): Insight from a numerical model study. *J. Geophys. Res.:Ocean.* 114:C06009. doi: 10.1029/2007jc004245

Sloyan, B. M., and O'Kane, T. J. (2015). Drivers of decadal variability in the Tasman Sea. *J. Geophys. Res.:Ocean.* 120 (5), 3193–3210. doi: 10.1002/2014jc010550

Sloyan, B. M., Ridgway, K. R., and Cowley, R. (2016). The East Australian current and property transport at 27 degrees s from 2012 to 2013. *J. Phys. Oceanogr.* 46 (3), 993–1008. doi: 10.1175/jpo-d-15-0052.1

Speich, S., Blanke, B., and Cai, W. J. (2007). Atlantic Meridional overturning circulation and the southern hemisphere supergyre. *Geophys. Res. Lett.* 34 (23), L23614. doi: 10.1029/2007gl031583

Su, Z., and Ingersoll, A. P. (2016). On the minimum potential energy state and the eddy size-constrained APE density. *J. Phys. Oceanogr.* 46 (9), 2663–2674. doi: 10.1175/jpo-d-16-0074.1

Torres, H. S., Klein, P., Menemenlis, D., Qiu, B., Su, Z., Wang, J. B., et al. (2018). Partitioning ocean motions into balanced motions and internal gravity waves: A modeling study in anticipation of future space missions. *J. Geophys. Res.:Ocean.* 123 (11), 8084–8105. doi: 10.1029/2018jc014438

Tseng, C.-T., Sun, C.-L., Yeh, S.-Z., Chen, S.-C., Liu, D.-C., and Su, W.-C. (2011). The kuroshio variations from satellite-derived sea surface temperature and Argos satellite-tracking Lagrangian drifters. *Int. J. Remote Sens.* 32 (23), 8725–8746. doi: 10.1080/01431161.2010.549523

von Storch, J. S., Eden, C., Fast, I., Haak, H., Hernandez-Deckers, D., Maier-Reimer, E., et al. (2012). An estimate of the Lorenz energy cycle for the world ocean based on the 1/10 degrees STORM/NCEP simulation. *J. Phys. Oceanogr.* 42 (12), 2185–2205. doi: 10.1175/jpo-d-12-079.1

Wang, X. H., Bhatt, V., and Sun, Y. J. (2013). Study of seasonal variability and heat budget of the East Australian current using two eddy-resolving ocean circulation models. *Ocean Dyn.* 63 (5), 549–563. doi: 10.1007/s10236-013-0605-5

Wang, Q., and Pierini, S. (2020). On the role of the kuroshio extension bimodality in modulating the surface eddy kinetic energy seasonal variability. *Geophys. Res. Lett.* 47 (3):e2019GL086308. doi: 10.1029/2019gl086308

Wijeratne, S., Pattiaratchi, C., and Proctor, R. (2018). Estimates of surface and subsurface boundary current transport around Australia. *J. Geophys. Res.:Ocean.* 123 (5), 3444–3466. doi: 10.1029/2017jc013221

Wood, J. E., Schaeffer, A., Roughan, M., and Tate, P. M. (2016). Seasonal variability in the continental shelf waters off southeastern Australia: Fact or fiction? *Cont. Shelf Res.* 112, 92–103. doi: 10.1016/j.csr.2015.11.006

Yang, C., Chen, X., Cheng, X., and Qiu, B. (2020). Annual versus semi-annual eddy kinetic energy variability in the celebes Sea. *J. Oceanogr.* 76 (6), 401–418. doi: 10.1007/s10872-020-00553-7

Yang, P., Jing, Z., Wang, H., Wu, L., Chen, Y., and Zhou, S. (2022). Role of frictional processes in mesoscale eddy available potential energy budget in the global ocean. *Geophys. Res. Lett.* 49 (13):e2021GL097557. doi: 10.1029/2021gl097557

Yang, Y., and Liang, X. S. (2018). On the seasonal eddy variability in the kuroshio extension. *J. Phys. Oceanogr.* 48 (8), 1675–1689. doi: 10.1175/jpo-d-18-0058.1

Yan, X. M., Kang, D. J., Curchitser, E. N., and Pang, C. G. (2019). Energetics of eddy-mean flow interactions along the Western boundary currents in the north pacific. *J. Phys. Oceanogr.* 49 (3), 789–810. doi: 10.1175/jpo-d-18-0201.1

Yu, X. L., Garabato, A. C. N., Martin, A. P., Buckingham, C. E., Brannigan, L., and Su, Z. (2019). An annual cycle of submesoscale vertical flow and restratification in the upper ocean. *J. Phys. Oceanogr.* 49 (6), 1439–1461. doi: 10.1175/jpo-d-18-0253.1

Zhang, N., Liu, G., Liu, Q., Zheng, S., and Perrie, W. (2020). Spatiotemporal variations of mesoscale eddies in the southeast Indian ocean. *J. Geophys. Res.: Ocean.* 125 (8), 1–18. doi: 10.1029/2019jc015712

Zhang, Z., Zhong, Y., Tian, J., Yang, Q., and Zhao, W. (2014). Estimation of eddy heat transport in the global ocean from argo data. *Acta Oceanol. Sin.* 33 (1), 42–47. doi: 10.1007/s13131-014-0421-x

Zhan, P., Subramanian, A. C., Yao, F., Kartadikaria, A. R., Guo, D., and Hoteit, I. (2016). The eddy kinetic energy budget in the red Sea. *J. Geophys. Res.:Ocean.* 121 (7), 4732–4747. doi: 10.1002/2015jc011589

Zhuang, W., Xie, S. P., Wang, D. X., Taguchi, B., Aiki, H., and Sasaki, H. (2010). Intraseasonal variability in sea surface height over the south China Sea. *J. Geophys. Res.:Ocean.* 115 (1), C04010. doi: 10.1029/2009jc005647

Zhu, Y. N., Qiu, B., Lin, X. P., and Wang, F. (2018). Interannual eddy kinetic energy modulations in the agulhas return current. *J. Geophys. Res.:Ocean.* 123 (9), 6449–6462. doi: 10.1029/2018jc014333

Zilberman, N. V., Roemmich, D. H., and Gille, S. T. (2014). Meridional volume transport in the south pacific: Mean and SAM-related variability. *J. Geophys. Res.:Ocean.* 119 (4), 2658–2678. doi: 10.1002/2013jc009688

Zilberman, N. V., Roemmich, D. H., Gille, S. T., and Gilson, J. (2018). Estimating the velocity and transport of Western boundary current systems: A case study of the East Australian current near Brisbane. *J. Atmos. Ocean. Technol.* 35 (6), 1313–1329. doi: 10.1175/jtech-d-17-0153.1

Zu, T., Wang, D., Yan, C., Belkin, I., Zhuang, W., and Chen, J. (2013). Evolution of an anticyclonic eddy southwest of Taiwan. *Ocean Dyn.* 63 (5), 519–531. doi: 10.1007/s10236-013-0612-6

frontiers | Frontiers in Marine Science

TYPE Original Research
PUBLISHED 02 May 2023
DOI 10.3389/fmars.2023.1165366

OPEN ACCESS

EDITED BY
Francisco Machín,
University of Las Palmas de Gran Canaria, Spain

REVIEWED BY
Xianqing Lv,
Ocean University of China, China
Reginaldo Durazo,
Autonomous University of Baja California, Mexico

*CORRESPONDENCE
Young-Heon Jo
joyoung@pusan.ac.kr

†These authors have contributed equally to this work

RECEIVED 14 February 2023
ACCEPTED 14 April 2023
PUBLISHED 02 May 2023

CITATION
Kim D, Choi J-G, Park J, Kwon J-I, Kim M-H and Jo Y-H (2023) Upwelling processes driven by contributions from wind and current in the Southwest East Sea (Japan Sea).
Front. Mar. Sci. 10:1165366.
doi: 10.3389/fmars.2023.1165366

Upwelling processes driven by contributions from wind and current in the Southwest East Sea (Japan Sea)

Deoksu Kim[1,2†], Jang-Geun Choi[3†], Jinku Park[4], Jae-Il Kwon[1,2], Myeong-Hyeon Kim[5,6] and Young-Heon Jo[7,8*]

[1]Coastal Disaster and Safety Research Department, Korea Institute of Ocean Science and Technology, Busan, Republic of Korea, [2]Department of Ocean Science, University of Science and Technology (UST), Daejeon, Republic of Korea, [3]Center for Ocean Engineering, University of New Hampshire, Durham, NH, United States, [4]Center of Remote Sensing and GIS, Korea Polar Research Institute, Incheon, Republic of Korea, [5]Center for Climate Physics, Institute for Basic Science (IBS), Busan, Republic of Korea, [6]Department of Climate System, Pusan National University, Busan, Republic of Korea, [7]BK21 School of Earth Environmental Systems, Pusan National University, Busan, Republic of Korea, [8]Department of Oceanography and Marine Research Institute, Pusan National University, Busan, Republic of Korea

The occurrence of coastal upwelling is influenced by the intensity and duration of sea surface wind stress and geophysical components such as vertical stratification, bottom topography, and the entrainment of water masses. In addition, strong alongshore currents can drive upwelling. Accordingly, this study analyzes how wind stress and ocean currents contribute to changing coastal upwelling along the southwest coast of the East Sea (Japan Sea), which has not yet been reported quantitatively. This study aims to estimate each geophysical factor affecting upwelling processes using the Upwelling Age index. The index assesses the major contributors to the upwelling process using the relationship between physical forcing and upwelling water fraction estimated from shipboard hydrographic data from January 1993 to October 2018. These findings reveal that wind-driven upwelling was dominant off the northern coast. In contrast, current-driven upwelling prevailed off the southern coast. These results suggest that persistent alongshore currents through the Korea Strait make the southern region a prolific upwelling area. Accordingly, it can shed light on the mechanisms of coastal upwelling in the study area, which is crucial for understanding the influence of physical forces on ocean ecosystems.

KEYWORDS

coastal upwelling, upwelling age (UA), Burger number, wind driven upwelling, current driven upwelling

1 Introduction

Coastal upwelling resulting from alongshore wind stress causes the offshore Ekman transport of surface waters (Huyer, 1983; Lentz and Chapman, 2004; Estrade et al., 2008; Jacox and Edwards, 2011). The occurrence of this phenomenon is primarily related to the strength and duration of the alongshore wind stress. Moreover, such upward onshore flow transports nutrient-rich water from the subsurface layer into the euphotic layer and stimulates the growth of phytoplankton and zooplankton (Lentz and Chapman, 2004; Chen et al., 2013; Shin et al., 2017). Coastal upwelling promotes the growth of certain species in unfavorable environments because of the sudden drop in water temperature (Alvarez et al., 2010). In the southwestern East Sea (Japan Sea; ES hereafter), coastal upwelling occurs with southerly winds during the summer (Seung, 1974; Lee, 1983; Lee and Na, 1985; Lee et al., 1998). From July to August, the East Asian Summer Monsoon system maintains a southerly or southwesterly wind flow that is responsible for coastal upwelling along the east coast of Korea, whereas northerly and northwesterly winds prevail in the winter (Lee, 1983; Lee and Na, 1985; Yoo and Park, 2009). Suh et al. (2001) reported that when southerly winds blow at speeds of approximately 3–5 m s^{-1}, the water temperature is generally reduced by 1–3°C and 2–7°C, respectively. Strong southerly winds of more than 6 m s^{-1} cause an extreme drop in water temperature along the east coast of Korea, leading to upwelling in just one day (Lee et al., 1998).

However, numerous factors are related to coastal upwelling intensity. Kim and Kim (2008) suggested that wind stress, adjacent bathymetry structure, and coastline orientation are the dominant factors contributing to the occurrence of coastal upwelling based on numerical model experiments. Furthermore, Ji et al. (2019) suggested the importance of cross-shore transport caused by the alongshore current using a scale analysis of the Gampo-Ulgi (GU) (Figure 1). Even if the upwelling-favorable wind is no longer present, the persistent alongshore current maintains the surface cold water for a couple of weeks along the southern coast of Korea (Jung and Cho, 2020). Lentz and Chapman (2004) described that the vertical velocity structure of upwelling and forces governing the compensational flow of offshore surface currents could be altered by the stratification intensity represented by the Burger number.

As shown in Figure 1, the east coast of Korea is influenced by a branch of the Kuroshio Current, the East Korea Warm Current (EKWC). The EKWC is transported through the Korea Strait and is analogous to the Western Boundary Current (WBC). The volume transport of the EKWC is approximately 1.5 Sv, which accounts for approximately 60% of the entire transport through the strait and gradually augments during the upwelling-favorable wind-blowing season (Chang et al., 2002; Kim et al., 2004). The EKWC causes current-driven upwelling; however, how the alongshore current influences the development of coastal upwelling in the southwest ES is not addressed. Therefore, this study aims to (1) estimate the impact of each geophysical factor by investigating the effect of upwelling index usage and (2) explain the results obtained by the analysis of the index in terms of dynamics.

Many indices have been used to predict upwelling events, such as the index using wind stress (Bakun, 1975). The index incorporates wind and ocean properties, such as sea surface temperature (García-Reyes et al., 2014), that relate the dynamics and structure of the cross-shelf circulation to stratification, bathymetry, and wind stress (Lentz and Chapman, 2004; Jacox and Edwards, 2011), or that characterize upwelling more completely from theory (Rossi et al., 2013) and model output (Jacox and Edwards, 2011; Jacox et al., 2018). In this study, we used an index named "Upwelling Age (UA)" (Jiang et al., 2012), which was improved by Chen et al. (2013), to understand upwelling occurrences and quantify the contribution of factors to coastal upwelling. The index is a non-dimensional number defined as the ratio of two different time scales: the wind event and the advection time scale (Jiang et al., 2012). The wind event time scale (i.e., wind duration) is a concept of how long the upwelling-favorable wind persists. In contrast, the advection time scale represents the time at which the water column is advected from the bottom layer to the surface layer. Thus, this index may be the most appropriate for analyzing different geophysical forcings for upwelling events.

To examine the upwelling processes, driven either by winds or currents, we first examined UA at 23 stations at regular latitudinal distances (approximately 16 km) along the east coast of the Korean Peninsula (Figure 1). Subsequently, the most determinant components at each station were quantitatively evaluated and compared with long-term *in situ* observations. The rest of this article is organized as follows: the data sources and analytical methods are described in *Section 2*. For the specific results, a temporal consistency comparison between UA and the water temperature measurements and geophysical contributors to UA is evaluated in *Sections 3.1* and *3.2*. In *Section 3.3*, the fraction of

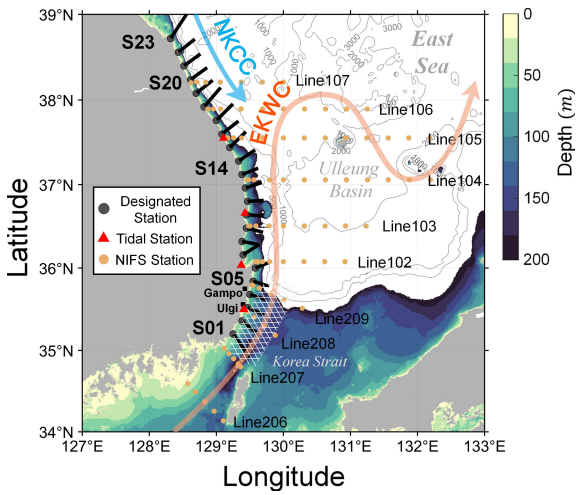

FIGURE 1
Study area based on topography derived from GEBCO and shown with contours. Black dots indicate designated stations, and red triangles represent observation stations (Ulsan [S03], Pohang [S07], Hupo [S10], and Mukho [S16]). Black lines show the cross-shore direction at each station. Orange dots are bimonthly repeated shipboard observation stations by the National Institute of Fisheries Science. Red and blue arrows indicate the mean flow defined as the East Korea Warm Current (EKWC) and North Korea Cold Current (NKCC), respectively. The S03 and S04 are known as Gampo-Ulgi (GU). The regions with white hash patterns off the coast of S01 through S05 are defined as the southern regions of the study area, whereas other stations are defined as the northern regions.

upwelled water masses estimated by water mass analysis is directly compared to the intensity of upwelling-favorable wind and alongshore currents. The dynamics of wind- and current-driven upwelling are discussed in *Section 4*, and the results discussed in *Section 3* are explained in terms of physical oceanography. To examine geostrophic current-induced upwelling processes, barotropic and baroclinic conditions were considered in *Sections 4.1* and *4.2*. The wind- and current-induced upwelling processes are further discussed based on the Burger number (S) in *Section 4.2*. The overall findings are summarized in *Section 5*.

2 Materials and methods

2.1 Data sources

To investigate coastal upwelling processes along the east coast of Korea, datasets (alongshore wind stress, bottom topography, and vertical density structure) were obtained to estimate UA from January 1993 to October 2018. Wind stress was estimated from the ERA-Interim 10-m wind data provided by the European Center for Medium-Range Weather Forecasts (ECMWF) with a spatial resolution of 0.75° (https://www.ecmwf.int). The shelf slope was estimated using the General Bathymetric Chart of the Oceans (GEBCO) bathymetry data, which is a 15-arcsecond global terrain model of the Earth's surface that integrates land topography and ocean bathymetry (https://www.gebco.net). In addition, the mixed layer depth (MLD) was calculated according to Kara et al. (2000), and the thermocline depth (TCD) was defined as the depth at which the temperature gradient was the largest below the MLD, using three-dimensional temperature structures obtained from daily Hybrid Coordinate Ocean Model (HYCOM) data with a spatial resolution of 1/12° (https://www.hycom.org).

In addition, we validated the temperature drop caused by coastal upwelling using *in situ* datasets. Sea surface temperature measurements were obtained at four observation stations (Mukho, Hupo, Pohang, and Ulsan) along the coastline. The datasets obtained from the Korea Hydrographic and Oceanographic Agency are available at http://www.khoa.go.kr/koofs/kor/observation/obs_real.do. Long-term bimonthly shipboard hydrographic data, observed and provided by the National Institute of Fisheries Science (available at https://www.nifs.go.kr/kodc/index.kodc), were used to estimate the upwelled water fraction. We performed additional quality control on the water temperature measurements and estimated the daily water temperature to match the time resolution of the UA. A 5-day running average was performed to eliminate high-frequency variability (Kämpf and Chapman, 2016). Observations from the Korea Hydrographic and Oceanographic Agency and the National Institute of Fisheries Science were from January 1993 to October 2018.

2.2 Estimation of UA

Jiang et al. (2012) and Chen et al. (2013) used a numerical model to validate UA. Based on Chen et al. (2013), we calculated the UA for regions along the east coast of Korea using satellite and reanalysis datasets. Figure 2 shows a conceptual schematic of the UA. UA (Γ) is defined as:

$$\Gamma = \frac{t_{wind}}{t_{ad}} \tag{1}$$

where t_{wind} is the time scale for the duration of an upwelling-favorable wind, and t_{ad} represents advection time. According to Chen et al. (2013), the advection time scale t_{ad} can be scaled as

$$t_{ad} = \frac{\rho f d(H_0 - H_1)}{\alpha\tau} + \frac{H_1 - H_2}{W}, \tag{2}$$

where the first term is the climbing time scale and the second term is the upwelling time scale. The former refers to the time it takes for cold water to ascend the slope from the thermocline to the transient depth, and the latter refers to the time it takes for cold water to move up from the transient depth to the surface. The factors that make up these two time scales determine the advection time and are the main factors that determine the occurrence of upwelling along with the duration of the wind. In Eq. 2, the climbing time scale is a function of water density (ρ), Coriolis parameter (f), bottom layer thickness (d), alongshore wind stress (τ), bottom slope (α), depth of the thermocline (H_0), and the switch-over depth between the climbing and upwelling processes (transition depth, H_1). The upwelling time scale consists of the transition depth, sea surface (H_2), and average vertical velocity over the upwelling region (W). $d = \pi\sqrt{2A_z/f}$ and $W = \tau/(\rho f L)$, where $A_z = 0.01\tau/(\rho f)$ is the vertical eddy viscosity and $L = 0.75\pi(\sqrt{2A_z/f})/\alpha$ is the cross-shore length scale of upwelling, which are empirical formula proposed by Chen et al. (2013).

Ultimately, the UA is expressed as a non-dimensional index. Whereas $\Gamma \gg 1$ results in an adequate accumulation of upwelled water at the coast and thus a large offshore transport forms a surface front, $\Gamma \leq 1$ results in no front forms owing to a lack of overturning (Jiang et al., 2012; Chen et al., 2013). To calculate the alongshore wind stress (τ), the wind data at each station were decomposed into alongshore and cross-shore components. In addition, the shelf slope, α, was calculated as the ratio of the depth of 200 m to the

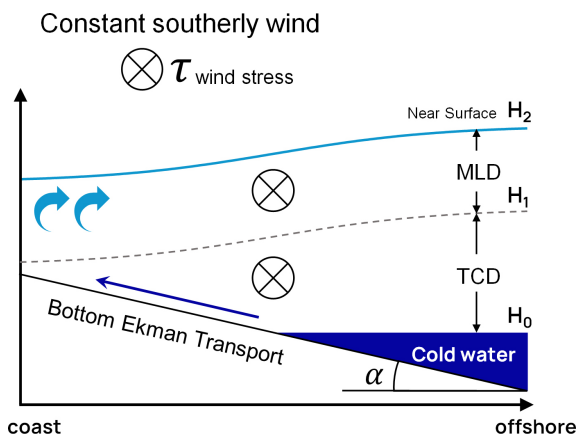

FIGURE 2
Schematic diagram of the wind-driven upwelling process and advection time (τ_{ad}) in the Northern Hemisphere.

distance between the coastline (0 m depth) and 200 m depth along the cross-shore line (black lines in Figure 1).

2.3 Multiple linear regression

Although UA is ideally defined using analytical equations, determining the contribution of each geophysical factor (input or predictor of UA) is challenging because the form of the analytical equations (Eqs. 1 and 2) is quite complex, especially when estimating the "independent" contribution of each input. By contrast, in a simple linear equation, the contribution and sensitivity of each factor do not depend on other factors. Thus, the independent contributions can be easily determined.

A complex analysis using machine learning (Jebri et al., 2022) requires big data to train the model, and the complexity of the model is high. Therefore, we projected the UA calculated using the original equations (Eqs. 1 and 2) into linear equations via multiple linear regression (MLR). To quantify the contribution of four geophysical factors (t_{wind}, τ, MLD, and TCD) to the upwelling occurrence, a multivariable linear regression model was applied according to the following formula:

$$\Gamma = \beta_0 + \beta_1 t_{wind} + \beta_2 \tau + \beta_3 MLD + \beta_4 TCD + \varepsilon, \quad (3)$$

where Γ is the dependent variable calculated from the equations in the previous section, $MLD = H_1 - H_2$, and $TCD = H_0 - H_1$. The parameter β_0 is a constant, $\beta_1 \cdots \beta_4$ are the regression coefficients for the independent variables, and ε is the error term.

Predictors in the MLR model must be independent of each other to yield correct results. We tested this for each predictor by calculating the variance inflation factor (VIF), which is an indicator of strong correlations between predictors; a VIF<10 indicates no strong relationship between the independent variables (Robinson and Schumacker, 2009). All input variables used in the MLR model did not have multicollinearity (VIF<10) and thus no significant dependency each other. The predictors used in MLR are not independent of one another regarding physics. In particular, MLD and TCD depend on the wind (t_{wind} and τ); vertical mixing that determines MLD is predominantly forced by wind at the surface layer, and TCD is controlled by the wind as a consequence of upwelling. Nevertheless, in our study area, we observed no statistical dependency issues between the predictors used in MLR, implying that the predictors can be considered independent parameters in terms of statistics. We suspect that the independence between the predictors implies a predominance of unresolved forcing by the UA (Eq. 2), such as atmospheric forcing (heating and cooling) or a current-driven effect that may significantly influence determining the vertical density structure than mixing caused by wind.

The proportional reduction of error (PRE) was used to evaluate the relative contribution of a predictor to the model using the following equation (Judd et al., 2011; Park et al., 2019):

$$PRE_i = (\varepsilon_{total} - \varepsilon_i)/\varepsilon_{total} * 100, \quad (4)$$

where ε_{total} is the error in the model computed over all independent variables, ε_i is the error in the calculated model after excluding a particular independent variable, and the subscript i represents the index for each predictor (i can be t_{wind}, τ, MLD, or TCD). The PRE allows the relative contribution of each independent variable to the total proportional reduction of the error to be calculated.

2.4 Water mass analysis to estimate the fraction of upwelled water mass

The fraction of upwelled water mass was estimated using the Expanded Optimal Multi-Parameter (EOMP) method and compared to physical environments such as upwelling-favorable wind stress and alongshore current intensity. The EOMP method calculates the fractions of specified source water masses in an observation using mixing equations. We defined four water masses in the study area: Surface Saline warm Water (SSW), Surface Fresh warm Water (SFW), Deep cold Eutrophic Water (DEW), and Deep cold Oligotrophic Water (DOW). The governing equations are as follows:

$$\begin{pmatrix} T_{SSW} & T_{SFW} & T_{DEW} & 0 \\ S_{SSW} & S_{SFW} & S_{DEW} & 0 \\ [NO_3]_{SSW} & [NO_3]_{SFW} & [NO_3]_{DEW} & 16 \\ [PO_4]_{SSW} & [PO_4]_{SFW} & [PO_4]_{DEW} & 1 \\ [SiO_4]_{SSW} & [SiO_4]_{SFW} & [SiO_4]_{DEW} & 16 \\ 1 & 1 & 1 & 0 \end{pmatrix} \begin{pmatrix} w_1 \\ w_2 \\ w_3 \\ w_4 \\ \Delta P \end{pmatrix} = \begin{pmatrix} T_{obs} \\ S_{obs} \\ [NO_3]_{obs} \\ [PO_4]_{obs} \\ [SiO_4]_{obs} \\ 1 \end{pmatrix} \quad (5)$$

where T_n, S_n, $[NO_3]_n$, $[PO_4]_n$, $[SiO_4]_n$, and w_n are the water temperature, salinity, nitrate, phosphate, silicate concentrations, and the fraction of source water, respectively. The subscript n indicates the index of observations (obs) and each source water mass. Eq. 5 is the mixing equation that defines the tracer concentrations of observations as a weighted summation (mixture) of four different source water masses and the non-conservative behavior of nutrient species (photosynthesis and respiration). The system of governing equations is overdetermined and thus solved by a linear least-squares problem solver with a non-negative constraint. However, the non-negative constraint was not applied to the biogeochemical change (ΔP) to resolve photosynthesis and respiration. The governing equations for tracer concentrations are normalized by the standard deviation of the source water characteristics (Glover et al., 2011). However, weighting factors were not induced, followed by all the tracers contributing evenly. Details of the definition of source water characteristics are described in the Supplementary Material (Appendix 1). The temperature and salinity of the surface source

water varied monthly in this study, eliminating the influence of surface heat and salinity fluxes. Using the defined upwelled water mass indicator, the relationship with force (e.g., wind stress and geostrophic current intensity) is discussed in *Section 3.3*.

3 Results

3.1 Evaluation of geophysical factors that determine UA

To evaluate upwelling occurrence in response to geophysical factor variations, the UA was adopted as its indicator. Most indices (e.g., upwelling index; Bakun, 1975) that evaluate upwelling occurrence consider only wind forcing as a decisive factor. A few indices (e.g., CUI; Jacox et al., 2018) that reflect the cross-shore current are unsuitable for the east coast of Korea because strong alongshore currents (e.g., EKWC) are entrained along the coastline throughout the year. However, UA makes it possible to deduce the impact of various geophysical factors because it is calculated using multiple variables such as MLD, TCD, bathymetry slope, wind duration, and wind stress. Additionally, this index has been adopted to analyze coastal upwelling in the study area (Kim et al., 2016; Shin et al., 2017). Thus, to accomplish our purpose, the multivariate index is a reliable proxy to evaluate upwelling occurrence.

Nevertheless, additional temporal comparisons were performed to evaluate whether the estimated UA was adequate. Even though the index was compared with the temperature reduction in this area (Kim et al., 2016; Shin et al., 2017), a temporal comparison between the observed water temperature from the observation station and the UA was additionally performed. The comparison determines whether UA reflects a decrease in sea surface temperature by Ekman transport in the study area because the specific conditions for the calculation of UA were slightly improved (Figure 3). Figure 3 shows the time series of UA and water temperature at four stations [Mukho (Figure 3A), Hupo (Figure 3B), Pohang (Figure 3C), and Ulsan (Figure 3D) marked as red triangles in Figure 1 and their corresponding observation stations S16, S10, S07, and S03, respectively] from 2012 to 2018. Gray lines indicate the water temperature anomaly at the observation station (seasonality is removed by subtracting the 60-day moving averaged component), and the black and red lines indicate $\Gamma \leq 1$ and $\Gamma > 1$ (i.e., upwelling occurrence), respectively. The water temperature reduction corresponds to the red line of the UA. Even though the magnitude of the reduction is not quantitatively proportional to the increase in the index, the sea surface temperature largely falls in

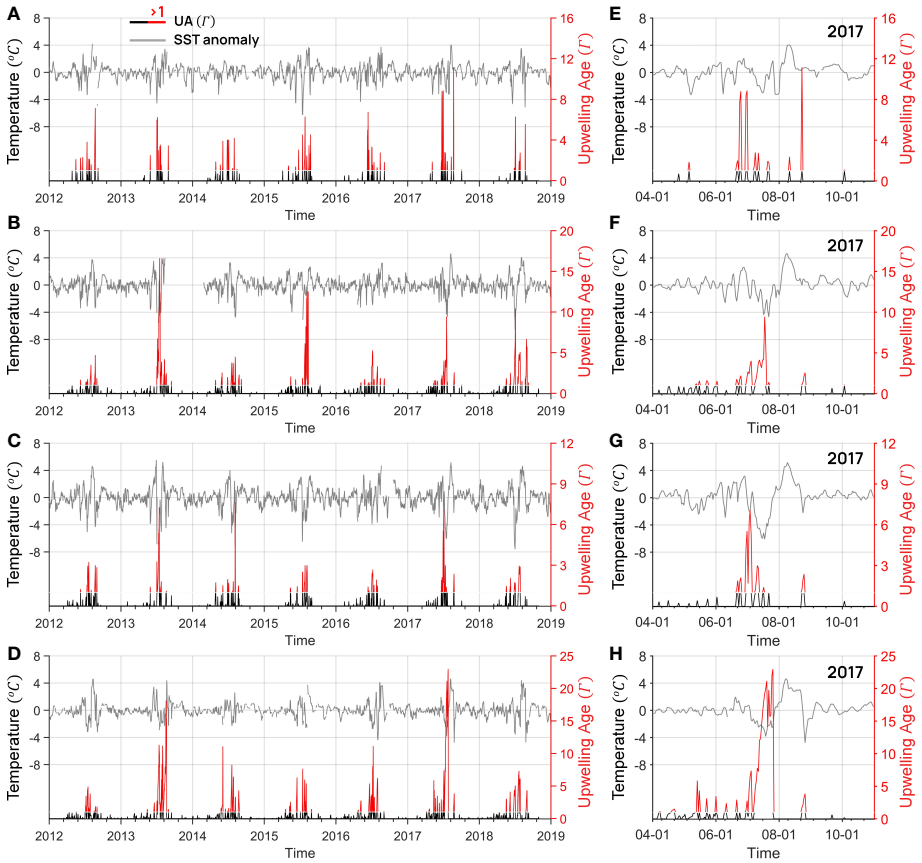

FIGURE 3
Time series of upwelling age (UA) and sea surface temperature anomaly of **(A, E)** Mukho [S16], **(B, F)** Hupo [S10], **(C, G)** Pohang [S07], and **(D, H)** Ulsan [S03] **(A–D)** from 2012 to 2018 and **(E–H)** from April to October 2017 (refer to Figure 1 for the specific locations). Gray lines indicate the water temperature anomaly derived from stations, and black and red lines indicate UA below and above 1, respectively.

response to the variation in the index when UA is >1. In addition, coastal upwelling mainly occurred during the boreal summer season at all stations, showing a distinct seasonality frequently reported in this area (Seung, 1974; Suh et al., 2001; Shin, 2019). A summer case in 2017 (Figures 3E–H) clearly shows that the water temperature in response to upwelling based on UA reflects the upwelled cold water on the sea surface.

The bathymetry slope plays a critical role in the development of upwelling in favorable environments (Jiang et al., 2012; Chen et al., 2013). Accordingly, the bathymetry slope should influence the upwelling under similar conditions. Eq. 2 shows that t_{ad} decreased as the bottom slope α increased; as a result, Γ increased (Eq. 1) as α increased. Therefore, UA predicted that upwelling was proportional to the bottom slope. In terms of the entire east coast of Korea, including both the southern and northern regions, there was no significant relationship between shelf slopes and upwelling frequency (Figure 4). However, a strong positive correlation was observed once the stations were classified into southern (below S14; blue circles in Figure 4) and northern (above S15; reddish circles in Figure 4) regions. Thus, these two regions were under two different conditions for upwelling occurrence, except for the bathymetry slope. Furthermore, the upwelling occurrences in the southern region were larger than those in the northern region, implying that the different conditions result in the southern region having a more upwelling-favorable environment than the northern region.

3.2 MLR analysis and contribution of wind and isopycnic parameters to UA

In addition to the effect of bathymetry slopes on upwelling occurrence, other time-dependent geophysical changes must be considered. As mentioned above, the geophysical elements (t_{wind}, τ, MLD, and TCD) used to calculate UA were evaluated using MLR, and the relative contribution of each element to upwelling events was estimated using PRE (Figure 5). It is worth noting that the wind stress ranges are in the order of 0.01 to 0.1 N/m^2 to develop wind-driven upwelling when UA is larger than one for several days. Although alongshore wind duration is a significant element for UA, the impact of alongshore wind stress, MLD, and TCD was mainly analyzed because our analysis focused on the contribution to advection time t_{ad}, which represents the time scale for the bottom water to reach the surface layer. The contribution of wind stress in the southern region (especially from S01 to S03, which corresponds to GU) is significantly smaller than that in the northern region (Figure 5). As a result, the contribution of the subsurface vertical density structure (including both MLD and TCD) is dominant in the southern regions. The contribution from wind stress gradually increased as the latitude increased. The contribution of wind stress from S01 to S03 of the GU was<20% and those of the vertical density structure of the region accounted for >80%. Correspondingly, the contribution of wind stress was negligible in the southern region and gradually increased in the northern region.

The analysis of the UA shows that the southern region (especially the GU) showed differences with the northern region regarding upwelling occurrence, bathymetry slope (Figure 4), and contribution of the other input variables (Figure 5). The southern region of the GU is adjacent to the Korea Strait and has a gentle slope and a shallow depth (<200 m). In addition, the EKWC, a branch of the Tsushima Warm Current, is consistently entrained through the strait, despite slight seasonal variations. Thus, the vertical density structure in this area can be controlled mainly by the presence of a background current rather than wind variations. In other words, the background alongshore current may play a crucial role in the development of coastal upwelling along the southwestern ES.

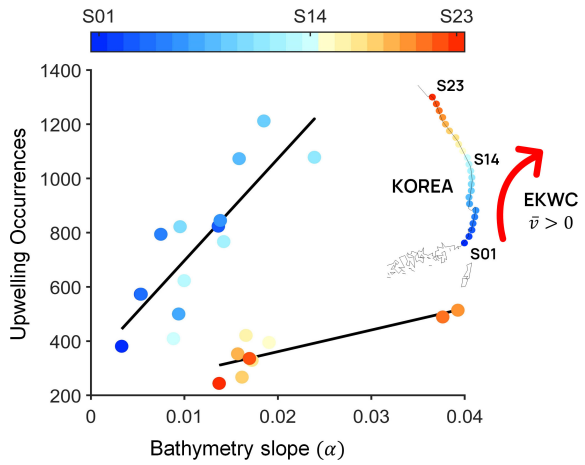

FIGURE 4
Relationships between upwelling occurrences and bathymetry slopes. Southern and northern regions are represented by a bluish and reddish color, respectively. Data are based on observations from KHOA (1993 to 2018).

3.3 Upwelled water mass fraction and its correlation with alongshore current and wind

Analysis using UA consistently shows that the southern and northern regions were different (Figures 4, 5), and it is hypothesized that the difference was caused by the presence of a persistent current (e.g., EKWC). In this section, the correlation between the fraction of upwelled water mass estimated by the EOMP and alongshore current intensity is discussed. In the case of the correlation between the alongshore geostrophic current and the upwelled water fraction in the northern region, the fraction of upwelled water decreased as the alongshore current increased and was not significantly correlated with the current. However, in another correlation, the stronger the current flows, the higher the upwelled water that accounted for the surface layer in the southernmost region, including observation lines 208 and 207 (Figures 6A, B). These results are evidence for current-driven upwelling in the southern region and support the hypothesis about current-driven upwelling elucidated by UA analysis. Furthermore, the moored observation data in the Korea Strait for 1 year show that onshore flow occurs at the bottom (Teague et al., 2002).

The Burger number $S = \alpha N/f$ [where h is water depth, $N = (-(g/\rho_0)\partial\rho'/\partial z)^{1/2}$ is the buoyancy frequency, and f is the

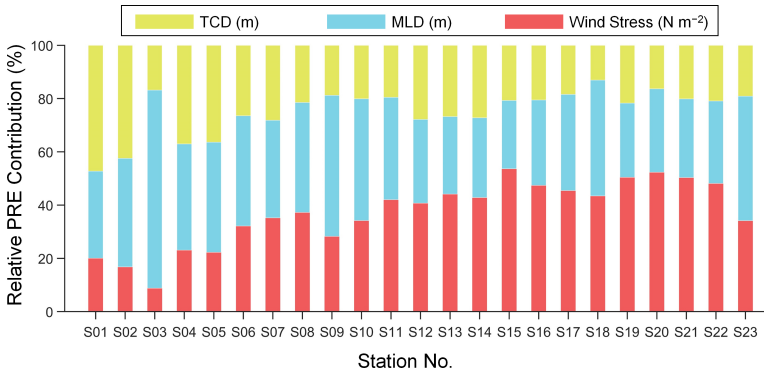

FIGURE 5
Bar charts of relative contribution rates among factors. The proportional reduction of error (PRE) indicates the contributions of each factor to the upwelling occurrence. Data are based on observations from KHOA (1993 to 2018).

Coriolis frequency] is a key non-dimensional number controlling many geophysical coastal phenomena, including wind-driven upwelling (Lentz and Chapman, 2004) and persistent alongshore currents over the shelf (Chapman, 2002). Although the alongshore wind stress showed a positive correlation with the fraction of upwelled water mass at all stations along the coast (Figure 7A), the correlation pattern between the upwelled water mass fraction and the alongshore geostrophic current (Figure 7B) matched the Burger number (Figure 7C). The northern region, with a high Burger number, had a relatively weak negative correlation, and the southern region, with a low Burger number, had a significant positive correlation. This implies that the Burger number plays an important role in controlling current-driven upwelling. In the following section, we discuss the theoretical background of wind- and current-driven upwelling and the role of stratification and the Burger number in current-driven upwelling.

4 Discussion

We describe the dynamics of the coastal upwelling process, and the details of the compensational flow are analyzed based on momentum equations and not volume compensation by surface Ekman transport. As reviewed by Brink (2016), although the basic concept of upwelling concerning volume conservation (vertical flow compensating offshore surface Ekman current) was realized and verified in the early 20th century, understanding the dynamic mechanism that triggers the compensational flow in terms of momentum balance is still ongoing. Various theoretical studies discussing the dynamic aspect of upwelling have used different assumptions based on research interests and study area characteristics (e.g., spatiotemporal scales). For example, Cushman-Roisin and Beckers (2011) adopted a reduced gravity model that assumes an infinitely deep (relative to the thickness of the surface layer) and motionless subsurface layer. Therefore, their theory systematically excludes the role of bottom friction, and compensational flow is attributed to adjustment flow, which is a consequence of the balance between the Coriolis force and the inertial term (Csanady, 1982). These are reasonable assumptions for stratified large-scale oceans; however, they are inadequate in this study, which focuses on small, shallow marginal oceans influenced by the branches of the WBC. The western boundary region is intrinsically dissipative (Pedlosky, 1987). Furthermore, the time

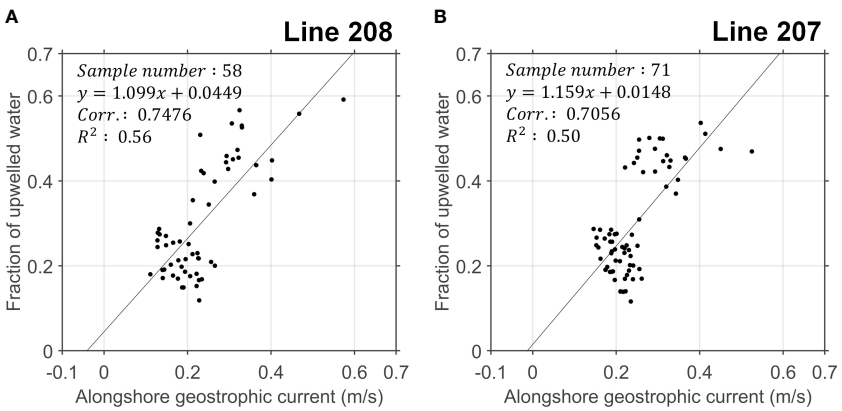

FIGURE 6
Scatter plot of upwelled water fraction and monthly geostrophic current at **(A)** Line 208 and **(B)** Line 207. For observation locations along the lines, refer to Figure 1. Data are based on observations from NIFS (1993 to 2018).

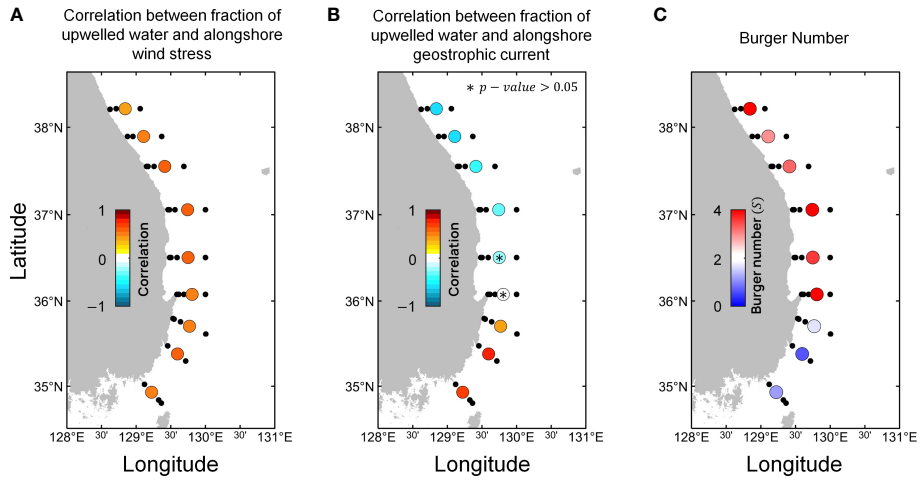

FIGURE 7
Scatter plot of **(A)** correlation between upwelling water fraction and alongshore wind stress, **(B)** correlation between upwelling water fraction and alongshore geostrophic current, and **(C)** Burger number, $S = \frac{\alpha N}{f}$. Data are based on observations from NIFS (1993 to 2018).

scale for upwelling events in our study area (months) is frequently longer than the frictional adjustment time scale (approximately 5 days), which indicates the importance of bottom friction (Chapman, 2002).

The shallow water equations have been adopted to study upwelling processes (Pringle, 2002; Roughan et al., 2003). For simplicity, we considered a geophysical scale in which the Rossby number was much less than one; thus, the inertial and lateral eddy viscosity terms were not considered. In addition, an anisotropic ocean (Pedlosky, 1987) was assumed, where the alongshore spatial scale (y-direction) was larger than the cross-shore scale (x-direction), $L_x \ll L_y$. In addition, this means that v was much greater than u ($u \approx L_x/T, v \approx L_y/T$). Based on this assumption, the terms associated with vertical eddy viscosity in the x-direction momentum equation were neglected. First, the barotropic limit assuming homogeneous density was analyzed using traditional shallow water equations to explain the dynamics of current-driven upwelling (*Section 4.1*). The modified shallow water equations by Chapman and Lentz (1997) (*Section 4.2*) are discussed to understand baroclinic dynamics and the role of stratification. Therefore, the following theoretical analysis provides a general overview of the dynamics of wind-driven and current-driven coastal upwelling processes while explaining the difference between the southern and northern regions caused by background currents and stratification.

4.1 Barotropic current-driven upwelling mechanism

The depth-averaged momentum and continuity equations of the shallow water system with the assumptions mentioned above are as follows:

$$-f\bar{v} = -g\frac{\partial \eta}{\partial x} \tag{6}$$

$$f\bar{u} = \frac{\tau_y^s}{h\rho_0} - \frac{\tau_y^b}{h\rho_0} \tag{7}$$

$$\frac{\partial \eta}{\partial t} + \frac{\partial (h\bar{u})}{\partial x} = 0, \tag{8}$$

where $\bar{u}$, $\bar{v}$, h, η, ρ_0, τ_y^s, and τ_y^b are the depth-averaged velocity components in the x- and y-directions, water depth, sea level, the constant density component, alongshore surface stress, and bottom stress, respectively. Cross-shore surface and bottom stresses were ignored by $L_x \ll L_y$ ($u \ll v$), which yields a predominantly geostrophic balance (relatively negligible in all the other terms in the cross-shore momentum equation). This is a common assumption in theoretical studies of upwelling in the long alongshore limit (Chapman, 2002; Lentz and Chapman, 2004; Choboter et al., 2005; Choboter et al., 2011) and reasonable assumptions in the study area where there is a predominant alongshore geostrophic current (Kim et al., 2016). If the sea level is assumed to be in a steady state ($\partial \eta / \partial t = 0$), hu, which indicates that cross-shore transport should be constant in x because $\partial (h\bar{u}) / \partial x = 0$, is induced from Eq. 8. Considering that the left boundary is bordered and closed by land ($u|_{x=0} = 0$), $\bar{u} = 0$ for all x. This indicates that cross-shore transport should be zero in the steady-state condition. Thus, Eq. 7 can be rewritten as follows:

$$\bar{u} = \frac{\tau_y^s}{fh\rho_0} - \frac{\tau_y^b}{fh\rho_0} = 0, \tag{9}$$

where $\tau_y^s / (fh\rho_0)$ represents the surface cross-shore Ekman current owing to wind stress and $\tau_y^b / (fh\rho_0)$ indicates the bottom Ekman current owing to bottom stress. As a result, Eq. 9 indicates that the divergence of the surface Ekman current was compensated by the convergence of the bottom Ekman current (Figure 2). Additionally, it demonstrates the equilibrium between the surface shear stress and the bottom shear stress in the steady state ($\tau_y^s = \tau_y^b$). Vertically averaged equations that cannot explicitly resolve vertical structures were used to simplify the mathematical development;

however, solutions that explicitly resolve vertical structures are known (Ekman, 1905; Welander, 1957; Estrade et al., 2008; Appendix 2). They are the surface and bottom Ekman currents, which are concentrated at the surface and bottom boundary layers, respectively, and exponentially decay as they get further away from the boundary layers. The bottom stress τ_y^b describes the bottom friction to be specific, as it can be defined as $\tau_y^b = \gamma\rho_0\bar{v}$ based on the linear frictional bottom boundary condition, where γ indicates the bottom friction coefficient in the velocity dimension. Eq. 6 and the bottom boundary condition show that the bottom Ekman current is attributed to geostrophic currents rendered by the pressure gradient formed by surface Ekman transport (Eq. 6). By substituting for the bottom boundary condition, Eq. 6 into Eq. 9 determines the cross-shore sea-level gradient, which is equated as

$$\frac{\partial \eta}{\partial x} = \frac{f}{g}\frac{\tau_y^s}{\gamma\rho_0}. \tag{10}$$

Eq. 10 represents the cross-shore sea-level gradient perturbed by the surface Ekman transport. The alongshore velocity component, which is the geostrophic current based on Eq. 6, during upwelling, a well-known upwelling jet (Kämpf and Chapman, 2016), is defined as $\bar{v} = (f/g)\,\partial\eta/\partial x = \tau_y^s/(\gamma\rho_0)$. The following descriptions describe how coastal wind-driven upwelling was driven: the divergence of the surface Ekman current decreased sea level at the coastal ocean based on the depth-integrated continuity equation (Eq. 8), and the alongshore geostrophic current was generated by the perturbed sea-level gradient and was responsible for the bottom frictional stress and rendering of the bottom Ekman current, which compensated for the divergence of the surface Ekman current (Figure 2).

The momentum balance of the shallow water equations shows that the compensating current was the bottom Ekman current, which responds to the friction of the alongshore currents. Therefore, this implies that coastal upwelling occurred due to the persistent alongshore current, even if the alongshore wind did not flow (Figure 8A). When τ_y^s is neglected, and $\bar{v} = \bar{v}_b$, which is a constant representing the presence of a persistent background current, Eq. 7 with the bottom boundary condition is induced as follows:

$$\bar{u} = -\frac{\gamma}{hf}\bar{v}_b, \tag{11}$$

This indicates that the bottom Ekman current was caused by the persistent alongshore current $\bar{v}_b$ (Figure 8A). Therefore, strong and persistent alongshore currents (e.g., WBC) result in transport by bottom friction (Oke and Middleton, 2000; Roughan et al., 2003) and thus develop current-driven upwelling. The EKWC was entrained along the coast of Korea and was enhanced during the prolific upwelling season. Thus, we expect current-driven upwelling to be dominant along a certain coast of Korea.

Eq. 11 implies that the basic concept of current-driven upwelling is imperfect because no flow compensates for the onshore bottom Ekman current. In terms of a steady-state and constant-density ocean, one of the forces ignored in the alongshore momentum equation is expected to generate a compensational flow. Even though the alongshore pressure gradient term was ignored in Eq. 11 for simplicity, it cannot be easily ignored because the scale of the term is intrinsically on the order of one. Therefore, the flow compensating the onshore Ekman current from the background alongshore current was attributed to the barotropic cross-shore geostrophic current, similar to Marchesiello and Estrade (2010).

4.2 Baroclinic current-driven upwelling and the role of stratification

To discuss the baroclinic dynamics of current-driven upwelling with stratification, a modified shallow water equation was adopted (Chapman and Lentz, 1997; Chapman, 2002). The alongshore and cross-shore momentum equations can be written as follows:

$$-fv = -\left(g\frac{\partial \eta}{\partial x} - \frac{g}{\rho_0}\frac{\partial \rho'}{\partial x}z\right) \tag{12}$$

$$f\bar{u} = -\frac{\gamma}{h}v|_{z=-h}, \tag{13}$$

where the cross-shore momentum equation (Eq. 12) was not vertically averaged, and the alongshore wind stress in Eq. 13 was ignored to focus on the current-driven upwelling. Substituting Eq. 12 into Eq. 13 yields

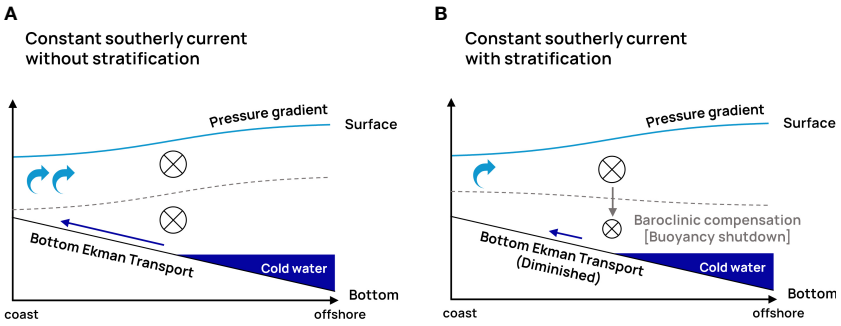

FIGURE 8
Schematic diagrams of **(A)** current-driven upwelling processes without stratification (barotropic) and **(B)** current-driven upwelling processes with stratification (baroclinic).

$$\bar{u} = -\frac{\gamma}{hf}\left(\bar{v}_b + \frac{gh}{f\rho_0}\frac{\partial \rho'}{\partial x}\right). \quad (14)$$

Note that $\bar{v}_b = (g/f)\ (\partial \eta/\partial x)$ is the background barotropic geostrophic current, which is a given constant, and the density gradient $\partial \rho\ /\partial x$ is negative in the environment of the study area (especially during upwelling events) and assumed to be constant, similar to Lentz and Chapman (2004). The cross-shore current component described by Eq. 14 is in the bottom Ekman current, based on Eq. 13. The additional terms related to the density gradient in Eq. 14, relative to Eq. 11, which does not consider stratification, indicate a baroclinic geostrophic current (thermal wind) component. As the stratification intensity increased (more negative density gradient), the alongshore current at the bottom $v|_{z=-h}$ became weaker than in the barotropic case without stratification because the barotropic velocity component $\bar{v}_b$ was canceled by the baroclinic component $gh/(f\rho_0)\partial \rho'/\partial x$ in Eq. 14 (Figure 8B). This alongshore current attenuation near the bottom is known as baroclinic compensation (Lee and Na, 1985; Jacobs et al., 2001) or buoyancy shutdown (Chapman, 2002). As a result, the cross-shore Ekman current caused by the alongshore current at the bottom (Eq. 13) was weakened and represented the bottom Ekman layer arrest process (MacCready and Rhines, 1993; Brink and Lentz, 2010). Consequently, Eq. 14 implies that the current-driven upwelling decreases as stratification increases. Appendix 2 provides the analytical solution for resolving the vertical structure of the stratified current-driven upwelling; however, the dynamics described by the solution are not different from those shown by the vertically averaged equations (Eqs. 13 and 14, respectively).

The thermal wind term is frequently scaled as the Burger number. Specifically, Lentz and Chapman (2004) showed an empirical relation between the lateral density gradient and buoyancy frequency, which is given as:

$$\frac{g}{\rho_0}\frac{\partial \rho'}{\partial x} \approx -afN, \quad (15)$$

where $a \approx 0.25$ is a proportional coefficient. The relative dominance of the thermal wind component on the barotropic geostrophic using Eq. 14 can be scaled as

$$O\left(\frac{gh}{f\rho_0}\frac{\partial \rho'}{\partial x}/\bar{v}_b\right) = \frac{aS}{\bar{v}_b/(fL_x)} = a\left(\frac{L_x}{L_y}\right)\frac{S}{Ro}, \quad (16)$$

where L_x/L_y is the aspect ratio and $R_o = 1/(fT)$ is the Rossby number. This can be considered a non-dimensional number representing the dominance of the current-driven current. If stratification is negligible and the slope is gentle ($S \approx 0$), the system becomes barotropic, and the alongshore current effectively generates a frictional bottom Ekman current. In contrast, for highly stratified environments over steep slopes ($S \approx 1$), the alongshore current is attenuated at the bottom because barotropic velocity is canceled by baroclinic velocity, and the cross-shore bottom Ekman current is not generated by the stratified alongshore current, and thus the non-dimensional number (Eq. 16) indicates the dominance of the current-driven upwelling. If the number is zero, the alongshore current generates a cross-shore bottom Ekman current, indicating dominant current-driven upwelling. In contrast, current-driven upwelling becomes negligible when the number is on the order of one because the bottom alongshore current is attenuated, and the bottom cross-shore Ekman current caused by the alongshore current weakens. A dimensionless number (Eq. 16) is consistent with the results of Chapman (2002), who showed that the governing equation for the alongshore current over a stratified shelf is controlled by two different non-dimensional numbers: the Rossby and Burger numbers. Consequently, the dimensionless number in Eq. 16 implies that the southern region had a dominant alongshore current and small Burger number, and thus current-driven upwelling may be considerable. However, the northern region, which had a relatively weak alongshore current and a high Burger number, may have been less affected by the current-driven upwelling. The correlation between the alongshore current and upwelled water mass fraction strongly agrees with the dynamics proposed in this study; a high correlation was observed in the southern region, where the Burger number was small, and vice versa in the northern region (Figure 7C). As a result, current-driven upwelling occurred in the southern region below 35° N.

5 Conclusions

We gained insights into the dominant upwelling processes under different local conditions in the southern and northern regions of the southwest ES by analyzing the contributions of major geophysical factors. The coastal upwelling off the study area was mainly evaluated using the wind-forcing impact. The southwesterly wind blowing in the boreal summer was mainly responsible for the compensation of bottom water to the surface, inducing cross-shore Ekman transport. However, the frequencies of upwelling showed regionally distinguishable relationships in response to bathymetry slopes (S01–S14 and S15–S23). Furthermore, according to the evaluation of the variable impact of upwelling, although wind forcing was the dominant factor in the northern region (>S14), upwelling in the southern region (<S14) was considerably smaller. These results imply that there are critical factors underlying the differences between the southern and northern regions.

In addition, a branch of the Tsushima Current (EKWC) gradually reinforced from the boreal summer to winter along the southwest ES (Teague et al., 2002; Kim et al., 2006). Accompanied by the robust boundary current, the current-driven upwelling resulted from the onshore bottom transport caused by bottom friction. Additionally, it should be noted whether the alongshore surface currents can be maintained at the bottom (barotropic). The theoretical analysis in *Section 4* shows that the current-driven upwelling decreased as the Burger number increased because the alongshore current at the bottom diminished due to buoyancy shutdown and bottom Ekman arrest. In conclusion, it is inferred that the southern region had a small Burger number and was governed by predominant current-driven upwelling, whereas the northern region, which had a high Burger number, was rarely

influenced by the currents and was thus governed by wind-driven upwelling.

Data availability statement

The original contributions presented in the study are included in the article/Supplementary Material. Further inquiries can be directed to the corresponding author.

Author contributions

Conceptualization: DK, J-GC, and JP. Data curation: DK and J-GC. Methodology: DK, J-GC, JP, and Y-HJ. Formal analyses: DK and J-GC. Writing the original draft: DK and J-GC. Writing, review, and editing: DK, J-GC, JP, J-IK, M-HK, and Y-HJ. Supervision: Y-HJ. All authors contributed to the article and approved the submitted version.

Funding

This research was supported by a National Research Foundation of Korea (NRF) grant funded by the Korean government (MSIP) (NRF-2018R1A2B2006555) for the project titled "Development of technology using analysis of ocean satellite images" (20210046). This study was partially supported by the Korea Institute of Marine Science & Technology Promotion (KIMST), funded by the Ministry of Oceans and Fisheries, Korea (20180447, Improvements in ocean prediction accuracy using numerical modeling and artificial intelligence technology).

Conflict of interest

The authors declare that the research was conducted in the absence of any commercial or financial relationships that could be construed as a potential conflict of interest.

Publisher's note

All claims expressed in this article are solely those of the authors and do not necessarily represent those of their affiliated organizations, or those of the publisher, the editors and the reviewers. Any product that may be evaluated in this article, or claim that may be made by its manufacturer, is not guaranteed or endorsed by the publisher.

Supplementary material

The Supplementary Material for this article can be found online at: https://www.frontiersin.org/articles/10.3389/fmars.2023.1165366/full#supplementary-material

References

Alvarez, I., Gomez-Gesteira, M., DeCastro, M., Gomez-Gesteira, J., and Dias, J. (2010). Summer upwelling frequency along the western cantabrian coast from 1967 to 2007. *J. Mar. Syst.* 79 (1-2), 218–226. doi: 10.1016/j.jmarsys.2009.09.004

Bakun, A. (1975). Daily and weekly upwelling indices, west coast of north america 1967-73. *U.S. NOAA technical report National Marine Fisheries Service SSRF*, Vol. 693 (Washington, DC: NOAA).

Brink, K. (2016). Cross-shelf exchange. *Annu. Rev. Mar. Sci.* 8, 59–78. doi: 10.1146/annurev-marine-010814-015717

Brink, K. H., and Lentz, S. J. (2010). Buoyancy arrest and bottom ekman transport. part I: steady flow. *J. Phys. Oceanography* 40 (4), 621–635. doi: 10.1175/2009JPO4266.1

Chang, K.-I., Hogg, N. G., Suk, M.-S., Byun, S.-K., Kim, Y.-G., and Kim, K. (2002). Mean flow and variability in the southwestern East Sea. *Deep Sea Res. Part I: Oceanographic Res. Papers* 49 (12), 2261–2279. doi: 10.1016/S0967-0637(02)00120-6

Chapman, D. C. (2002). Deceleration of a finite-width, stratified current over a sloping bottom: frictional spindown or buoyancy shutdown? *J. Phys. Oceanography* 32 (1), 336–352. doi: 10.1175/1520-0485(2002)032<0336:DOAFWS>2.0.CO;2

Chapman, D. C., and Lentz, S. J. (1997). Adjustment of stratified flow over a sloping bottom. *J. Phys. Oceanography* 27 (2), 340–356. doi: 10.1175/1520-0485(1997)027<0340:AOSFOA>2.0.CO;2

Chen, Z., Yan, X.-H., Jiang, Y., and Jiang, L. (2013). Roles of shelf slope and wind on upwelling: a case study off east and west coasts of the US. *Ocean Model.* 69, 136–145. doi: 10.1016/j.ocemod.2013.06.004

Choboter, P. F., Duke, D., Horton, J. P., and Sinz, P. (2011). Exact solutions of wind-driven coastal upwelling and downwelling over sloping topography. *J. Phys. Oceanography* 41 (7), 1277–1296. doi: 10.1175/2011JPO4527.1

Choboter, P. F., Samelson, R. M., and Allen, J. S. (2005). A new solution of a nonlinear model of upwelling. *J. Phys. oceanography* 35 (4), 532–544. doi: 10.1175/JPO2697.1

Csanady, G. T. (1981). "Circulation in the coastal ocean," in *Advances in geophysics*, vol. 23. (Dordrecht: Springer), 101–183. doi: 10.1007/978-94-017-1041-1

Cushman-Roisin, B., and Beckers, J.-M. (2011). *Introduction to geophysical fluid dynamics: physical and numerical aspects* (Cambridge, MA: Academic press).

Ekman, V. (1905). On the influence of the earth's rotation on ocean currents. *Arkiv Matematik Astronomi Fysik* 2:52.

Estrade, P., Marchesiello, P., De Verdière, A. C., and Roy, C. (2008). Cross-shelf structure of coastal upwelling: a two–dimensional extension of ekman's theory and a mechanism for inner shelf upwelling shut down. *J. Mar. Res.* 66 (5), 589–616. doi: 10.1357/002224008787536790

García-Reyes, M., Largier, J. L., and Sydeman, W. J. (2014). Synoptic-scale upwelling indices and predictions of phyto-and zooplankton populations. *Prog. Oceanography* 120, 177–188. doi: 10.1016/j.pocean.2013.08.004

Glover, D. M., Jenkins, W. J., and Doney, S. C. (2011). *Modeling methods for marine science* (Cambridge, UK: Cambridge University Press).

Huyer, A. (1983). Coastal upwelling in the California current system. *Prog. Oceanography* 12 (3), 259–284. doi: 10.1016/0079-6611(83)90010-1

Jacobs, G., Perkins, H., Teague, W., and Hogan, P. (2001). Summer transport through the tsushima-Korea strait. *J. Geophysical Research: Oceans* 106 (C4), 6917–6929. doi: 10.1029/2000JC000289

Jacox, M., and Edwards, C. (2011). Effects of stratification and shelf slope on nutrient supply in coastal upwelling regions. *J. Geophysical Research: Oceans* 116 (C3). doi: 10.1029/2010JC006547

Jacox, M. G., Edwards, C. A., Hazen, E. L., and Bograd, S. J. (2018). Coastal upwelling revisited: Ekman, Bakun, and improved upwelling indices for the US West coast. *J. Geophysical Research: Oceans* 123 (10), 7332–7350. doi: 10.1029/2018JC014187

Jebri, F., Srokosz, M., Jacobs, Z. L., Nencioli, F., and Popova, E. (2022). Earth observation and machine learning reveal the dynamics of productive upwelling regimes on the agulhas bank. *Front. Mar. Sci.* 9. doi: 10.3389/fmars.2022.872515

Ji, R., Jin, M., Li, Y., Kang, Y.-H., and Kang, C.-K. (2019). Variability of primary production among basins in the East/Japan Sea: role of water column stability in modulating nutrient and light availability. *Prog. Oceanography* 178, 102173. doi: 10.1016/j.pocean.2019.102173

Jiang, L., Breaker, L. C., and Yan, X.-H. (2012). Upwelling age: an indicator of local tendency for coastal upwelling. *J. Oceanography* 68 (2), 337–344. doi: 10.1007/s10872-011-0096-2

Judd, C. M., McClelland, G. H., and Ryan, C. S. (2009). *Data analysis: A model comparison approach* (New York: Routledge).

Jung, J., and Cho, Y.-K. (2020). Persistence of coastal upwelling after a plunge in upwelling-favourable wind. *Sci. Rep.* 10 (1), 1–9. doi: 10.1038/s41598-020-67785-x

Kämpf, J., and Chapman, P. (2016). *Upwelling systems of the world* (Cham: Springer).

Kara, A. B., Rochford, P. A., and Hurlburt, H. E. (2000). An optimal definition for ocean mixed layer depth. *J. Geophysical Research: Oceans* 105 (C7), 16803–16821. doi: 10.1029/2000JC900072

Kim, I. N. (2015). Estimating denitrification rates in the East/Japan Sea using extended optimum multi-parameter analysis. *Terrestrial Atmospheric Oceanic Sci.* 26, 145–152. doi: 10.3319/TAO.2014.09.24.01(Oc)

Kim, D.-W., Jo, Y.-H., Choi, J.-K., Choi, J.-G., and Bi, H. (2016). Physical processes leading to the development of an anomalously large cochlodinium polykrikoides bloom in the East sea/Japan sea. *Harmful Algae* 55, 250–258. doi: 10.1016/j.hal.2016.03.019

Kim, D.-S., and Kim, D.-H. (2008). Numerical simulation of upwelling appearance near the southeastern coast of Korea. *J. Korean Soc. Mar. Environ. Saf.* 14 (1), 1–7.

Kim, Y. H., Kim, Y. B., Kim, K., Chang, K. I., Lyu, S. J., Cho, Y. K., et al. (2006). Seasonal variation of the Korea strait bottom cold water and its relation to the bottom current. *Geophysical Res. Lett.* 33 (24). doi: 10.1029/2006GL027625

Kim, I. N., and Lee, T. S. (2004). Physicochemical properties and the origin of summer bottom cold waters in the Korea strait. *Ocean Polar Res.* 26 (4), 595–606. doi: 10.4217/OPR.2004.26.4.595

Kim, K., Lyu, S. J., Kim, Y.-G., Choi, B. H., Taira, K., Perkins, H. T., et al. (2004). Monitoring volume transport through measurement of cable voltage across the Korea strait. *J. Atmospheric Oceanic Technol.* 21 (4), 671–682. doi: 10.1175/1520-0426(2004)021<0671:MVTTMO>2.0.CO;2

Kim, I. N., Min, D. H., Kim, D. H., and Lee, T. (2010). Investigation of the physicochemical features and mixing of East/Japan Sea intermediate water: an isopycnic analysis approach. *J. Mar. Res.* 68 (6), 799–818. doi: 10.1357/002224010796673849

Lee, J.-C. (1983). Variations of sea level and sea surface temperature associated with and wind-induced upwelling in the southeast coast of Korea in summer. *J. Korean Ocean. Soc* 18, 149–160.

Lee, D.-K., Kwon, J.-I., and Hahn, S.-B. (1998). The wind effect on the cold water formation near gampo-ulgi coast. *Korean J. Fisheries Aquat. Sci.* 31 (3), 359–371.

Lee, J.-C., and Na, J.-Y. (1985). Structure of upwelling off the southease coast of Korea. *J. Korean Soc. Oceanography* 20 (3), 6–19.

Lentz, S. J., and Chapman, D. C. (2004). The importance of nonlinear cross-shelf momentum flux during wind-driven coastal upwelling. *J. Phys. Oceanography* 34 (11), 2444–2457. doi: 10.1175/JPO2644.1

MacCready, P., and Rhines, P. B. (1993). Slippery bottom boundary layers on a slope. *J. Phys. Oceanography* 23 (1), 5–22. doi: 10.1175/1520-0485(1993)023<0005:SBBLOA>2.0.CO;2

Marchesiello, P., and Estrade, P. (2010). Upwelling limitation by onshore geostrophic flow. *J. Mar. Res.* 68 (1), 37–62. doi: 10.1357/002224010793079004

Oke, P. R., and Middleton, J. H. (2000). Topographically induced upwelling off eastern Australia. *J. Phys. Oceanography* 30 (3), 512–531. doi: 10.1175/1520-0485(2000)030<0512:TIUOEA>2.0.CO;2

Park, J., Kim, J. H., Kim, H., Hwang, J., Jo, Y. H., and Lee, S. H. (2019). Environmental forcings on the remotely sensed phytoplankton bloom phenology in the central Ross Sea polynya. *J. Geophysical Research: Oceans* 124 (8), 5400–5417. doi: 10.1029/2019JC015222

Pedlosky, J. (1987). *Geophysical fluid dynamics* Vol. 710 (New York: Springer). doi: 10.1007/978-1-4612-4650-3

Pringle, J. M. (2002). Enhancement of wind-driven upwelling and downwelling by alongshore bathymetric variability. *J. Phys. Oceanography* 32 (11), 3101–3112. doi: 10.1175/1520-0485(2002)032<3101:EOWDUA>2.0.CO;2

Robinson, C., and Schumacker, R. E. (2009). Interaction effects: centering, variance inflation factor, and interpretation issues. *Multiple linear regression viewpoints* 35 (1), 6–11.

Rossi, V., Feng, M., Pattiaratchi, C., Roughan, M., and Waite, A. M. (2013). On the factors influencing the development of sporadic upwelling in the leeuwin current system. *J. Geophysical Research: Oceans* 118 (7), 3608–3621. doi: 10.1002/jgrc.20242

Roughan, M., Oke, P. R., and Middleton, J. H. (2003). A modeling study of the climatological current field and the trajectories of upwelled particles in the East Australian current. *J. Phys. Oceanography* 33 (12), 2551–2564. doi: 10.1175/1520-0485(2003)033<2551:AMSOTC>2.0.CO;2

Seung, Y. H. (1974). A dinamic consideration on the temperature distribution in the East coast of Korea in august. *J. Korean Soc. Oceanography* 9 (2), 52–58.

Shin, C.-W. (2019). Change of coastal upwelling index along the southeastern coast of Korea. *Sea* 24 (1), 79–91. doi: 10.7850/jkso.2019.24.1.079

Shin, J. W., Park, J., Choi, J. G., Jo, Y. H., Kang, J. J., Joo, H., et al. (2017). Variability of phytoplankton size structure in response to changes in coastal upwelling intensity in the southwestern East Sea. *J. Geophysical Research: Oceans* 122 (12), 10262–10274. doi: 10.1002/2017JC013467

Suh, Y. S., Jang, L.-H., and Hwang, J. D. (2001). Temporal and spatial variations of the cold waters occurring in the eastern coast of the Korean peninsula in summer season. *Korean J. Fisheries Aquat. Sci.* 34 (5), 435–444.

Teague, W. J., Jacobs, G., Perkins, H., Book, J., Chang, K., and Suk, M. (2002). Low-frequency current observations in the Korea/Tsushima strait. *J. Phys. Oceanography* 32 (6), 1621–1641. doi: 10.1175/1520-0485(2002)032<1621:LFCOIT>2.0.CO;2

Welander, P. (1957). Wind action on a shallow sea: some generalizations of Ekman's theory. *Tellus* 9 (1), 45–52.

Yoo, S., and Park, J. (2009). Why is the southwest the most productive region of the East Sea/Sea of Japan? *J. Mar. Syst.* 78 (2), 301–315. doi: 10.1016/j.jmarsys.2009.02.014

frontiers | Frontiers in Marine Science

TYPE Original Research
PUBLISHED 19 May 2023
DOI 10.3389/fmars.2023.1187202

OPEN ACCESS

EDITED BY
Francisco Machín,
University of Las Palmas de Gran Canaria, Spain

REVIEWED BY
Ebenezer Nyadjro,
Mississippi State University, United States
Peng Bai,
Zhejiang Ocean University, China

*CORRESPONDENCE
G. D. A. Topé
topeguy97@yahoo.com

RECEIVED 15 March 2023
ACCEPTED 03 May 2023
PUBLISHED 19 May 2023

CITATION
Topé GDA, Alory G, Djakouré S, Da-Allada CY, Jouanno J and Morvan G (2023) How does the Niger river warm coastal waters in the northern Gulf of Guinea? *Front. Mar. Sci.* 10:1187202. doi: 10.3389/fmars.2023.1187202

How does the Niger river warm coastal waters in the northern Gulf of Guinea?

G. D. A. Topé[1,2]*, G. Alory[3], S. Djakouré[1,2], C.Y. Da-Allada[1,4,5], J. Jouanno[3] and G. Morvan[3]

[1]International Chair in Mathematical Physics and Application (ICMPA)-UNESCO Chair/University of Abomey Calavi (UAC), Cotonou, Benin, [2]Laboratory of Matter, Environment and Solar Energy Sciences, Félix Houphouët Boigny University in Abidjan, Abidjan, Côte d'Ivoire, [3]Centre National d'Etudes Spatiales CNES, Centre National de la Recherche Scientifique (CNRS), Institut de Recherche pour le Développement (IRD), Université Paul Sabatier (UPS), Laboratoire d'Etudes en Géophysique et Océanographie Spatiales (LEGOS), University of Toulouse, Toulouse, France, [4]Laboratoire de Géosciences, de l'Environnement et Applications (LaGEA)/Ecole Nationale Supérieure des Travaux Publics (ENSTP)/Université Nationale des Sciences, Technologies, Ingénierie et Mathématiques (UNSTIM), Abomey, Benin, [5]Laboratoire d'Hydrologie Marine et Côtière (LHMC)/Institut de Recherche Halieutique et Océanologique du Benin (IRHOB), Cotonou, Benin

To highlight the processes by which the Niger River warms the coastal waters in the eastern part of the northern Gulf of Guinea upwelling, two simulations of the NEMO model at high resolution were used over the period 2010 - 2017. The first simulation is realistic while the second is a simulation in which the effects of the Niger River are not taken into account. The first step was to evaluate the outputs of the models, using satellite products and *in situ* observations. The average states of the Sea Surface Temperature, Salinity, Height, zonal current and vertical profiles of temperature and salinity showed the ability of the model to reproduce correctly the physical characteristics of the study area. The analysis of the heat balance terms of the two simulations showed that vertical diffusion and meridional advection processes are the causes of the warming induced by the Niger River. The stratification and vertical shear of the horizontal currents reveal that the river acts by inhibiting the upwelling of cold water induced by vertical diffusion. The river reinforces the stratification and prevents vertical shearing of horizontal currents at the bottom of the mixed layer.

KEYWORDS

coastal upwelling, Niger river plume, Gulf of Guinea, heat balance, tropical Atlantic

1 Introduction

The Northern Gulf of Guinea (NGG, 15°W-15°E, 10°S-8°N) is a region of the tropical Atlantic Ocean where coastal waters are subject to temperature changes caused mainly by a seasonal coastal upwelling, extending from Côte d'Ivoire to Nigeria and reaching its highest intensity in boreal summer from July to September (e.g., Djakouré et al., 2014; Djakouré et al., 2017; Sohou et al., 2020). This upwelling plays a key role on primary production, local fisheries and thus on the economy of the countries bordering the NGG (Koné et al., 2017;

Yago, 2021). It has also been shown that this coastal upwelling can influence the regional climate, in particularly rainfall along the coast, by interacting with the West-African Monsoon flux at seasonal and interannual timescale (Ali, 2009; Tanguy et al., 2021).

East of Cape Three-Points at 2°W, the coastal upwelling is wind-driven (Djakouré et al., 2017). East of 2°E, near the Niger River plume, the upwelling sharply weakens. Freshwater plumes have important effects on marine ecosystems. Indeed, they can significantly modify stratification, nutrient inputs, light penetration and ocean circulation (Hickey et al., 2005). Low salinity river plumes create lateral pressure gradients, inducing geostrophic surface currents oriented towards the coast, to the right of the estuary in the northern hemisphere (Fong and Geyer, 2002). These currents can then converge towards the coastal upwelling zone, in the Niger River case, potentially compensating the wind-driven upwelling (Marchesiello & Estrade, 2010). Therefore, quantifying the impact of the Niger River plume on the seasonal variability of the NGG coastal ocean dynamics is essential for a better understanding of the marine ecosystem evolution.

Previous investigations using ocean simulations have shown that the mixed layer would deepen in the absence of the Niger River in the NGG (Da-Allada et al., 2013). Recently, Alory et al. (2021) showed that the river has no direct effect on the vertical velocities associated with the upwelling, although it warms the upwelling area up to 1°C at the surface. Their study did not identify the mechanisms driving this river-induced coastal warming. These authors suggest that this warming could be explained by geostrophic currents that bring warmer offshore waters toward the coast. Also, stratification enhancement, associated with the plume, could contribute by trapping solar heat near the surface and reducing vertical mixing.

The main objective of this study is to determine the physical processes by which the Niger River warms the NGG coastal waters and to quantify their relative contribution. To achieve this, we will use simulations of a regional numerical model covering the NGG area, preliminary validated with observations.

The rest of the manuscript is organised as follows: the model description, the observation data and the methodology used are described in Section 2. The results including the evaluation of the model, simulated river-induced coastal warming, and the heat budget to identify physical processes that drive this warming are presented in section 3. Finally, discussion and conclusion are given in Section 4.

2 Data and methods

2.1 Observations

Different *in situ* and satellite datasets were used to evaluate the model.

Sea surface temperature (SST) *in situ* measurements are based on four coastal stations equipped with ONSET sensors installed along the NGG coast at Sassandra in Côte d'Ivoire (6.08°W; 4.95° N), Takoradi in Ghana (1.73°W; 4.88°N), Cotonou in Benin (2.67°E; 6.52°N) and Lagos in Nigeria (3.41°E; 6.42°N) in the framework of the Research Program in Physical Oceanography in West Africa (PROPAO). The *in situ* ONSET sensor hourly data series are available over the period 2008–2012 (Sohou et al., 2020). We also used the monthly version of the Moderate Resolution Imaging Spectroradiometer (MODIS-AQUA, L3, v2019, https://oceandata.sci.gsfc.nasa.gov) SST, with a spatial resolution of 4 km over the time period 2007-2017. We prefer to use this infrared SST product rather than blended satellite products that can underestimate SST cooling in coastal upwelling regions (Meneghesso et al., 2020). Sea surface salinity (SSS) satellite data were collected from the Soil Moisture Active Passive (SMAP) v5 product, with a 0.25° and 8-day resolution, which benefits from a correction of systematic biases near the coasts and adjustment of the long term mean in dynamical areas like river plumes (Dossa et al., 2021). We also used SSS measurements collected *in situ* from underway thermosalinographs (TSG) during eight cruises or crossings of French research and commercial ships in the Gulf of Guinea during the summer season between 2000 and 2018 (Gaillard et al., 2015; Bourlès et al., 2019; Alory et al., 2021).

As for the sea surface height (SSH), it was evaluated using the CMEMS (Copernicus Marine Environment Monitoring Service) product, combining data from several satellite missions interpolated daily on a quarter degree (1/4°) resolution grid (Le Traon et al., 1998; Ducet et al., 2000).

In addition, we used monthly averages of *in situ* National Oceanic and Atmospheric Administration (NOAA) surface drifters data for the assessment of the zonal surface current (Laurindo et al., 2017).

Finally, subsurface temperature and salinity were extracted from the World Ocean Atlas (WOA; Locarnini et al., 2018; Zweng et al., 2019). We used the seasonally averaged climatological product, with 0.25° horizontal resolution and a 5 m vertical resolution in the upper 100 m.

2.2 Numerical model

The numerical setup is based on the Nucleus for European Modeling of the Ocean (NEMO; Madec, 2016) model. The model solves in a Cartesian coordinate system the primitive equations discretised in an Arakawa C grid. The regional configuration covers the tropical Atlantic at 1/36° horizontal resolution (10°S - 6.5° N and 10.5° W - 13° E), with 50 vertical levels (12 levels within the first 20 m and 22 levels in the upper 100 m). At the surface, the model is forced with the DFS 5.2 product (Drakkar Forcing Set version 5.2, Dussin et al., 2016) and the nonsolar heat fluxes are provided by bulk formulae (Large and Yeager, 2009). A river flow based on data from Dai and Trenberth (2002) is prescribed near the river mouths as a surface freshwater flow, associated with vertical mixing over a characteristic 10 m depth, which decreases exponentially river waters has not been prescribed in the model. It is similar to that of the oceanic surface waters. A reference simulation ("REF") was carried out over the period 2005-2017, as well as a twin simulation ("noRIV") over the period 2008-2017, where river runoff is not taken into account. In the latter, vertical mixing near the river mouths is maintained to ensure that differences between the

simulations are only due to changes in freshwater flux. Both simulations follow a 2-year climatological spin up. Their monthly mean seasonal climatology will be compared over the common 2010-2017 period. The mixed layer depth (MLD) is defined as the depth at which the density has increased by 0.03 kg. m^{-3}, with reference to the density at 10 m. This criteria is recommended by De Boyer Montégut et al. (2004) and has been previously used in several studies in the region (e.g. Jouanno et al., 2011; Da-Allada et al., 2014; Jouanno et al., 2017; Alory et al., 2021; Da-Allada et al., 2021; Kanga et al., 2021). In particular, N'Guessan et al. (2019) show from visual inspection of more than 500 density profiles that it is the best suited criteria to determine the MLD in the Gulf of Guinea. The mixed layer is located between 9.5m and 12m in "REF" and between 10m and 13.5m in "noRIV" simulation, which means it extends over 9 or 10 model depth levels. These simulations were used for the first time in this work and have not been validated before.

2.3 Mixed layer heat budget

To examine the causes of the surface warming induced by the Niger River, a mixed-layer heat budget is used, in both the REF and noRIV simulations, which can be written as follows (Jouanno et al., 2011; Jouanno et al., 2017; Da-Allada et al, 2021):

$$\frac{\partial < T >}{\partial t} = \underbrace{\underbrace{-<u\,\partial_x T>}_{\text{XAD}} \underbrace{-<v\,\partial_y T>}_{\text{YAD}} + \underbrace{<D_l(T)>}_{\text{LDF}}}_{\text{HORIZ}}$$

$$\underbrace{\underbrace{-<w\,\partial_Z T>}_{\text{ZAD}} \underbrace{-\frac{1}{h}(k_z\,\partial_z T)_{z=-h}}_{\text{ZDF}} \underbrace{-\frac{1}{h}\frac{\partial h}{\partial t}(<T>-T_{z=-h})}_{\text{RES}}}_{\text{VERTIC}} \quad (1)$$

$$\underbrace{+\frac{Q^{*}+Q_s(1-f_{z=-h})}{\rho_0 C_p h}}_{\text{ATMOS}}$$

With

$$<\blacksquare>=\frac{1}{h}\int_{-h}^{0}\blacksquare\,dz \quad (2)$$

$$\Delta\langle -v\frac{dT}{dy}\rangle = -\Delta\langle v\rangle.\langle\frac{dT}{dy}\rangle - \langle v\rangle.\Delta\langle\frac{dT}{dy}\rangle - \Delta\langle v\rangle.\Delta\langle\frac{dT}{dy}\rangle \quad (3)$$

where, T is the model potential temperature, ρ_0 the surface reference density (set to 1,021 kg. m^{-3} as in Li et al., 2013), Cp the heat capacity (set to 3984 J kg^{-1} °C^{-1}as in Wade et al., 2011), h MLD, Q^{*} the nonsolar surface heat flux (sum of the net longwave radiation, the sensible and latent heat fluxes), $Q_s$the net shortwave radiation, $f_{z=-h}$ the fraction of the shortwave radiation that reaches the MLD, (u, v, w) the velocity components, k_z the vertical diffusion coefficient for tracers and $D_l(T)$ the lateral diffusion operator. The total temperature trend on the left-hand side of equation (1) is thus controlled from left to right by zonal and meridional advection (XAD and YAD respectively), lateral diffusion (LDF), vertical advection (ZAD), vertical diffusion (ZDF), entrainment (RES) at the base of the mixed layer, and finally the net air-sea heat flux (ATMOS). We group oceanic processes into two categories: horizontal processes as HORIZ (HORIZ=XAD+YAD+LDF) and vertical processes as VERTIC (VERTIC=ZAD+ZDF+RES). All terms in equation (1) are computed explicitly in the model, except for the entrainment term (RES) which is estimated as a residual. For the investigation of the causes of the variation in meridional advection, we used the following decomposition:

where Δ represents monthly seasonal variations and< > represents annual means.

The meridional current is decomposed into geostrophic and Ekman components. The geostrophic component is calculated as follows:

$$v_{geo} = \frac{g}{f}\frac{\partial SSH}{\partial x}, \quad (4)$$

Where SSH is sea level and f the Coriolis parameter. The Ekman velocity is obtained from the difference between the total velocity and the geostrophic velocity. The Brunt Vaïsala frequency N^2 (T, S) is decomposed into its components to describe the temperature stratification N^2(T) and the salinity stratification N^2(S). N^2 (T, S) is calculated as follows (e.g. Da-Allada et al., 2021):

$$N^2(T,\ S) = -\frac{g}{\rho}\frac{\partial \rho}{\partial z} \approx \underbrace{g\,\alpha\frac{\partial T}{\partial z}}_{N^2(T)} - \underbrace{g\,\beta\frac{\partial S}{\partial z}}_{N^2(S)} \quad (5)$$

where g is gravity, α is the coefficient of thermal expansion, β is the coefficient of haline contraction, $\frac{\partial T}{\partial z}$ and $\frac{\partial S}{\partial z}$, the vertical temperature and salinity gradients. The shear parameter Sh^2 is used to analyse the vertical shear of horizontal currents. Sh^2 is calculated as follows (e.g., Da-Allada et al., 2021):

$$Sh^2 = \left(\frac{\partial u}{\partial z}\right)^2 + \left(\frac{\partial v}{\partial z}\right)^2 \quad (6)$$

3 Results

3.1 Model validation

This section evaluates the ability of the model to reproduce the main characteristics of the NGG. Only a lower (1/12°) resolution regional NEMO version was previously validated (Alory et al., 2021).

a. Seasonal cycle of SST

The SST of the model was evaluated in comparison with the ONSET sensor data of the PROPAO program (Figure 1). The model reproduces well the average seasonal cycle of the SST of the ONSET sensors. However, we observe differences in SST between the model and the *in situ* observations, which are more pronounced in boreal summer (up to 2°C at the Sassandra station). These differences could be due to small-scale near-shore dynamics not simulated in the model. The model is slightly warmer than the *in situ*

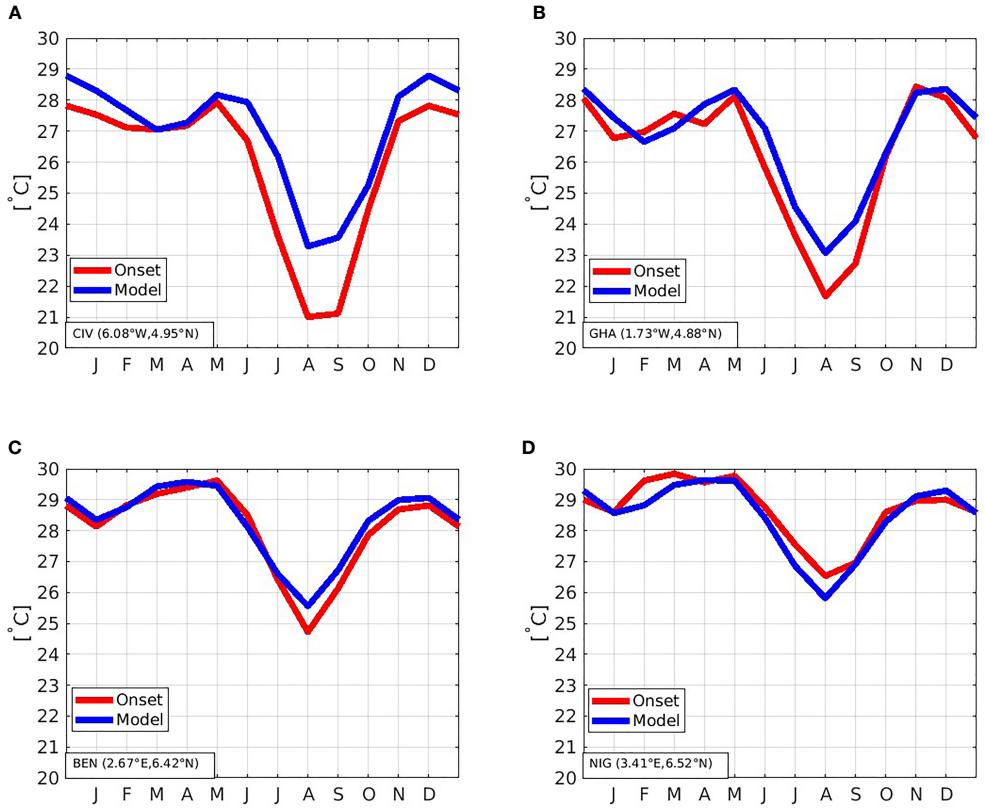

FIGURE 1
Seasonal cycle of the model SST (in blue) and the ONSET sensors SST (in red) over the period 2008-2012 at PROPAO stations: **(A)** Côte d'Ivoire; **(B)** Ghana; **(C)** Benin; **(D)** Nigeria.

measurements for all stations but the one in Nigeria where it is slightly colder, especially in summer. The later could be due to the fact that the temperature of the river waters, potentially warmer than the ocean, is not taken into account. These differences reach a maximum during the July-August-September (JAS) upwelling season, which timing is very consistent between the model and Onset sensors.

b. Summer climatology of SST, SSS, SSH and zonal surface current.

The climatological mean summer SST for both the model and the MODIS product for the 2007-2017 period are compared in Figures 2A, B. The model reproduces the main features of the NGG SST. The upwelling cells west and east of Cape Three Points are well represented. Both satellite and model show that the eastern cell is colder than the western cell downstream of Cape Palmas, as found by Djakouré et al. (2014). However, the model shows a cold bias in the coastal upwelling area relative to the satellite data, contrary to its warm bias relative to coastal stations. This suggests the satellite data may have deficiencies near the coast.

The model SSS is compared with the SMAP product in Figures 2C, D. The model reproduces roughly the SSS observed by the SMAP satellite, in particular the SSS minimum extending from 4°E to 6°E and associated with Niger River plume (Alory et al., 2021). However, salinity differences are observed, particularly in coastal upwelling area, East of capes where differences reach + 2 psu in SMAP product. Moreover, coastal freshening associated with rivers in western part of NGG are weaker in SMAP.

These differences are probably due to the difficulty of the satellite to observe salinity gradients near the coast (Dossa et al., 2021). Model SSS is also in good agreement with the TSG transects, with differences that may be due to interannual variability inherent to the sparse sampling (Alory et al., 2021).

The SSH of the model was also evaluated by comparison with the CMEMS altimetry data (Figures 2E, F). As expected, low SSH between longitudes 7°W and 2°E, is largely associated with cooling in the upwelling area. SSH increases eastward from 2°E with a maximum in the Niger River plume, due to steric variations associated with both temperature and salinity changes (Alory et al., 2021).

Finally, the zonal surface current is compared between the model and the drifters (Figures 2G, H). The model reproduces very well drifters' observations. The eastward Guinea Current intensifies between the Capes (7°W-2°W) then weakens until it disappears around 4°E.

c. Vertical sections of temperature and salinity

In addition to the surface data, south-north vertical temperature and salinity sections of the model are compared to the WOA climatological data along 0°E (Figures 3A, B). The model reproduces well the vertical temperature section. The warm

10.3389/fmars.2023.1187202

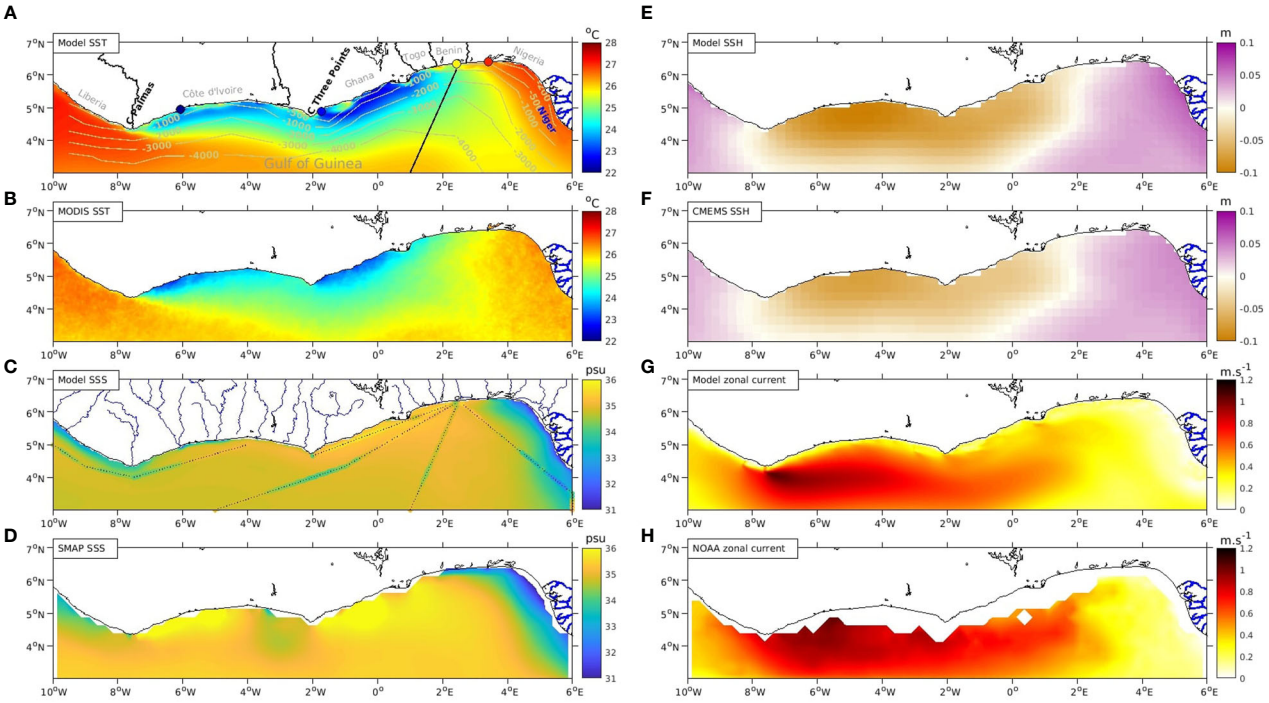

FIGURE 2
Summer mean (July-August-September) for the period from 2010 – 2017 (except for MODIS data): **(A)** Model SST, and location of coastal PROPAO stations (dots in blue, yellow and red colors near coast), cross-shore section used in Figure 3 (black line) and study area bathymetry (contours), **(B)** MODIS SST, **(C)** Model SSS and repeated 2000–2018 TSG transects (colored tracks), **(D)** SMAP SSS, **(E)** Model SSH, **(F)** CMEMS SSH, **(G)** Model zonal current, **(H)** NOAA drifter's zonal current.

surface waters are isolated from the cold bottom waters by the thermocline (approximated by the 20°C isotherm).

There is also an upward movement of the thermocline from the open ocean to the coast which is consistent with coastal upwelling. Also, the model reproduces well the vertical salinity section (Figures 3C, D), with a slope of the halocline (in this case the 35.5 psu isohaline) similar to the thermocline slope. However, the steepening of the thermocline and halocline seen in the model between 5°N and the coast, where upwelling is particularly strong, is not seen in WOA, probably due to a poor density of observations near the coast.

3.2 Observed warming induced by the Niger river

Figures 4A, B show the summer SST climatologies of the REF and noRIV simulations, respectively. Differences between these climatologies show a clear warming effect induced by the Niger River, with a maximum of around 0.5°C between 2°E and 4°E near the coast (Figure 4C). This warming confirms the results of Alory et al. (2021), although it was stronger and with a larger extension in their lower resolution simulation (1/12°).

In the following, we investigate the heat budget in the box bordered by 2°E - 4°E; 5.5°N – 7°N (Figure 4C), where the warming reaches its maximum.

3.3 Processes involved in warming

Processes influencing the temperature of the mixed layer can be classified into three categories: horizontal processes (zonal and meridional advection, lateral diffusion), vertical processes

(vertical advection, vertical diffusion and entrainment) and atmospheric processes (solar and nonsolar fluxes). Figure 5A shows their relative contribution to the total temperature tendency of the REF simulation mixed layer. Atmospheric and vertical processes are the main contributors to the mixed layer temperature trend.

Atmospheric processes warm the upper ocean all year long except in June, with a maximum contribution larger than 0.1°C.day^{-1} in August. Vertical processes have always a cooling effect, peaking below -0.1°C.day^{-1} in August too. Horizontal processes have a relatively small contribution, with absolute values always lower than 0.04°C.day^{-1}. The maximum cooling in June-July is mainly due to vertical processes as expected in a coastal upwelling region, but atmospheric processes contribute (in June) and also horizontal processes.

Figure 5B presents the REF-noRIV difference of the simulations with and without the Niger River. It shows that the river affects the 3 categories of processes. The river attenuates the cooling associated with horizontal and vertical processes, leading to warming. It also reduces the warming associated with atmospheric processes, which leads to cooling.

10.3389/fmars.2023.1187202

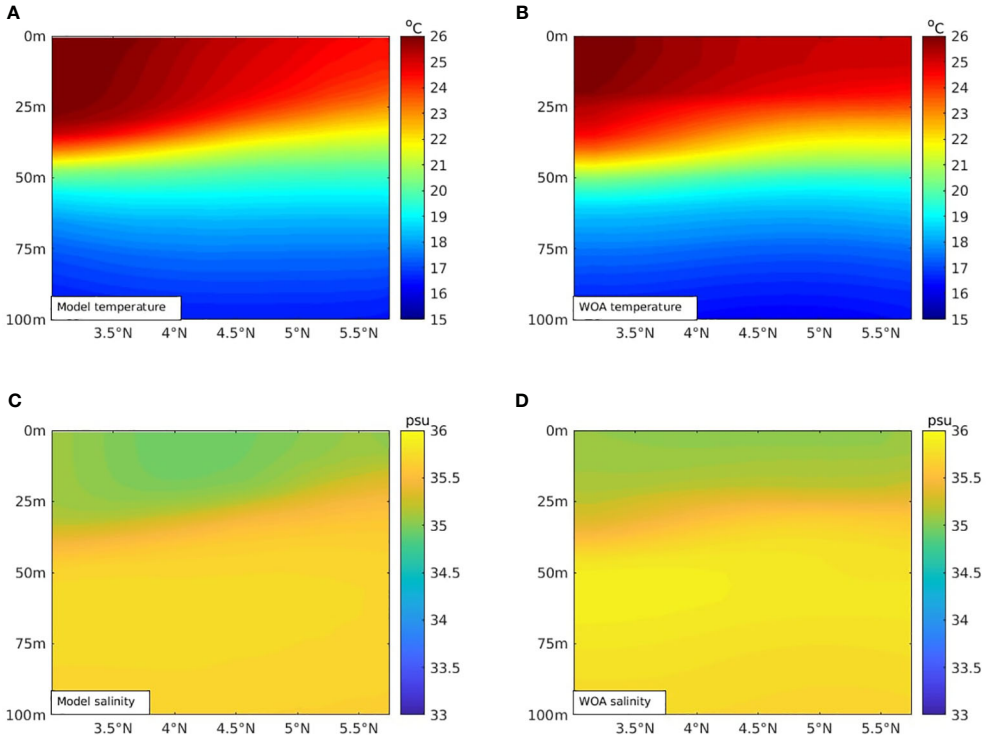

FIGURE 3
Mean summer cross-shore 0-100 m vertical sections: **(A)** Model temperature, **(B)** WOA temperature, **(C)** Model salinity, **(D)** WOA salinity. Temperature and salinity data from the model cover the period 2010-2017. The climatologies of vertical temperature and salinity sections of the WOA product are made for the periods 1955-2017 and 2005-2017 respectively.

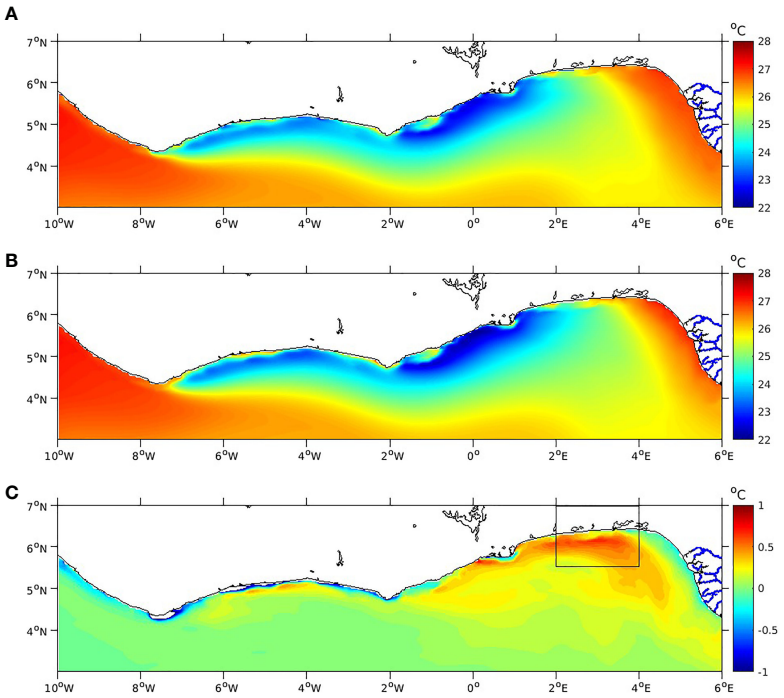

FIGURE 4
Mean summer (July-August-September) of SST over the period 2010-2017: **(A)** REF, **(B)** noRIV, **(C)** REF-noRIV.

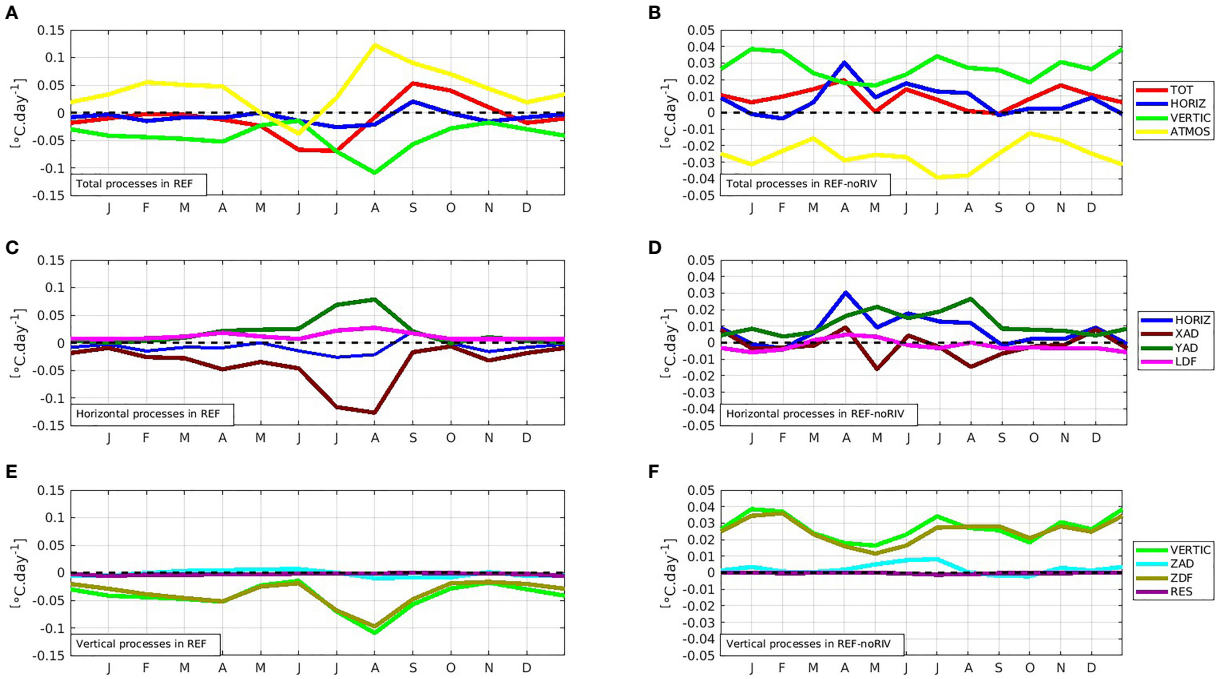

FIGURE 5
Mean seasonal cycles in REF and REF-noRIV for the period 2010-2017: **(A, B)** Total processes (TOT) with its components: horizontal processes (HORIZ), vertical processes (VERTIC), atmospheric processes (ATMOS), **(C, D)** horizontal processes with its components: zonal advection (XAD), meridional advection (YAD), lateral scattering (LDF), **(E, F)** vertical processes and its components: vertical advection (ZAD), vertical diffusion (ZDF), and entrainment (RES).

The warming prevails over the cooling most of the year. Thus, the net effect of the Niger River is to warm coastal waters, exclusively through oceanic processes (horizontal and vertical). The decomposition of each category of oceanic processes, into its different components, will allow to identify the terms of the heat balance through which the Niger River warms the coastal waters.

a. Horizontal processes

The contributions of zonal advection (XAD), meridional advection (YAD) and lateral diffusion (LDF) to horizontal processes (HORIZ) in the REF simulation are shown in Figure 5C. With minima below -0.1°C.day^{-1} reached in July-August, zonal advection is the main horizontal process influencing the temperature of the mixed layer, partly compensated by meridional advection, which reaches 0.075°C.day^{-1}. Lateral diffusion has a weak contribution throughout the year. The REF-noRIV difference in horizontal processes (Figure 5D) reveals that meridional advection is the only horizontal process through which the Niger River warms the coastal waters. The seasonal signal of meridional advection shows two peaks, with the highest peak during the upwelling season in August (~0. 027°C.day^{-1}).

b. vertical processes

Figure 5E shows the contributions of vertical advection (ZAD), vertical diffusion (ZDF) and entrainment (RES), to vertical processes (VERTIC) in the REF simulation. Vertical diffusion largely dominates the vertical processes, with vertical advection and entrainment relatively negligible. The REF-noRIV difference (Figure 5F), shows that river-induced changes in vertical processes are also almost entirely due to changes in vertical diffusion. The river thus contributes to mixed layer warming by limiting the cooling induced by vertical diffusion.

As vertical diffusion and meridional advection are the heat budget terms through which the Niger River warms the coastal waters, we proceed to examine in more details these warming terms.

3.4 Study of the processes associated with the warming induced by the Niger river

a. Vertical diffusion

Vertical diffusion is modulated by two mechanisms with opposite effects: stratification of the water column and vertical shear of horizontal currents.

Stratification isolates the surface waters, which are less salty and warmer, from the colder and saltier subsurface waters. On the contrary, vertical shear of the horizontal currents favours the upwelling of the subsurface water towards the mixed layer. To study the respective effects of these two mechanisms on vertical diffusion, we use the parameters N^2 (T), N^2 (S) and Sh^2 detailed in Section 2, calculated for each of the two simulations. The impact of the Niger River on vertical diffusion is evaluated from the REF-noRIV difference in the three parameters mentioned above. Figures 6A, B show the temperature stratification in the water column over the upper 100 m in the REF simulation and the REF-noRIV difference.

10.3389/fmars.2023.1187202

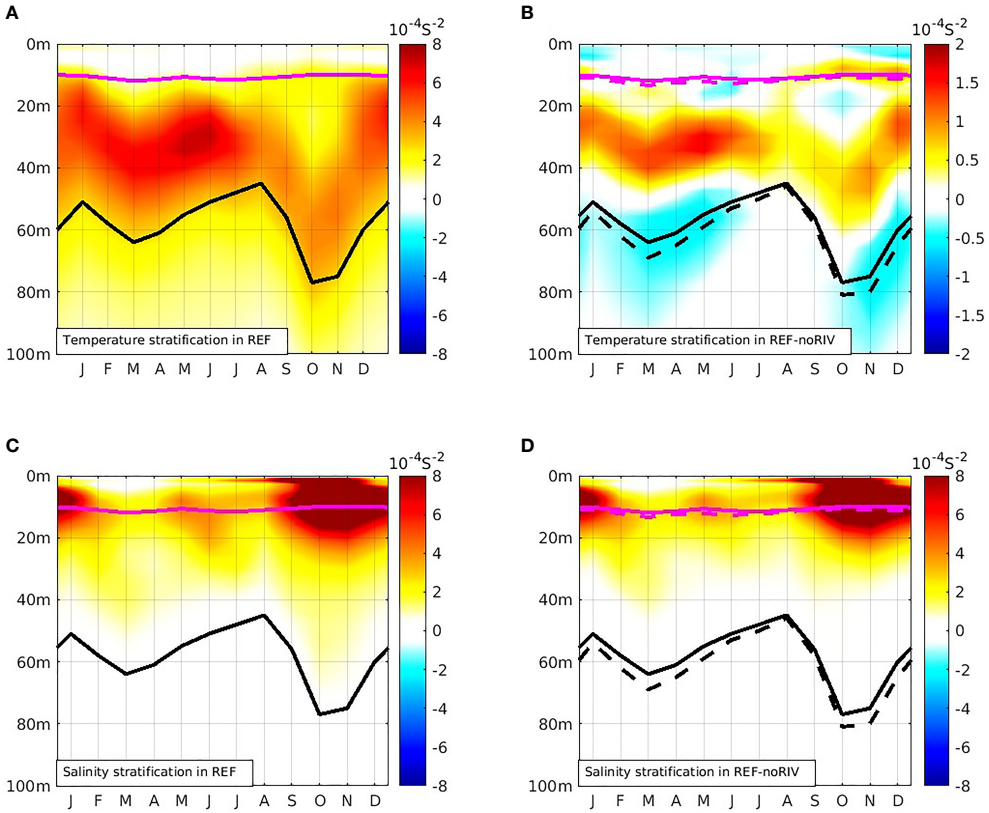

FIGURE 6
Seasonal cycle of vertical stratification in REF and noRIV for the period 2010-2017: **(A, B)** temperature stratification, **(C, D)** salinity stratification. The magenta lines (full line for REF and dashed line for noRIV) represent the depth of the mixed layer. The black lines represent the thermocline.

In REF, the strongest temperature stratification is observed between March and May, with values reaching $7*10^{-4}$ S^{-2} around a depth of 30 m. The positive stratification values in the REF-noRIV difference map show that stratification is stronger with the river at this depth. The river enhances by almost 60% the maximum temperature stratification between 20 m and 40 m depth.

Indeed, in the absence of a river, only solar radiation warms the waters of the mixed layer. In REF, in addition to the solar radiation, the stratification is reinforced by the freshwater input from the river plume. It also causes the mixed layer and thermocline to rise by a few metres as observed in Figure 6B.

The vertical stratification of salinity parameter $N^2(S)$, calculated in the two simulations, reveals that the salinity stratification is almost entirely due to the river's freshwater inputs. Indeed, the similarity of Figures 6C, D indicates that salinity stratification is very weak in the noRIV simulation. The salinity at the surface is almost the same at 100 m. But in the presence of the Niger River (REF), the water column becomes very stratified in the upper 20 m. The river contributes to the maximum salinity stratification about 91%. As the salinity stratification caused by the river is much higher than temperature stratification (Figures 6B, D), we conclude that the strong salinity gradient induced by the river's freshwater plume is the main cause of NGG sea water's stratification.

We have also diagnosed the influence of the Niger River on the vertical shear of the horizontal currents (Figures 7A, B). The shear remains almost the same in the mixed layer of both simulations, except between August and October, where it is reinforced by about 40% (Figure 7B). In the REF simulation (Figure 7A), no values are observed at the bottom of the mixed layer. On the other hand, negative values are observed at the bottom of the REF-noRIV mixed layer (Figure 7B). These values indicate the entrainment of subsurface water in the mixed layer of the noRIV simulation. The stratification induced by the fresh river water thus prevents the entrainment of the subsurface water into the mixed layer.

b. Meridional advection

The previous sections showed that meridional advection is one of the processes explaining the warming induced by the Niger River. In this section, we investigate the potential causes of its variation, namely meridional current and meridional temperature gradient (Figure 8).

The computation of the correlation coefficients shows that the changes in the meridional advection are strongly linked to the variation of the meridional current. Indeed, meridional current is the main driver of the variation in meridional advection (correlation r=0.61 between

the two-time series), with a weak contribution from the meridional temperature gradient (r=-0.10). Thus, the Niger River contributes to the advection of warm waters towards the coast by reinforcing the meridional current.

Regarding the changes in the meridional current, they are related to the variations of the two components (Figure 9).

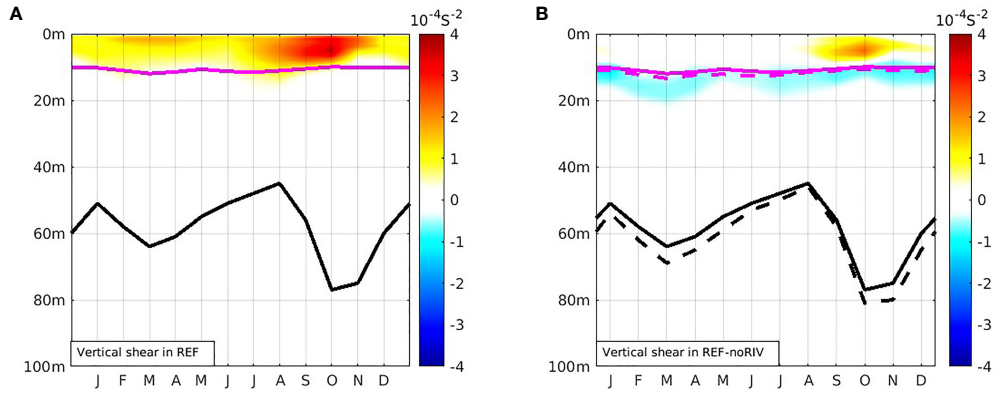

FIGURE 7
Mean cycle of vertical shear of horizontal currents for the period 2010-2017 in REF **(A)** and REF-noRIV **(B)**. The magenta lines (full line for REF and dashed line for noRIV) represent the depth of the mixed layer. The black lines represent the thermocline.

Between January and March and September to October, the geostrophic component dominates the changes in the meridian current while the Ekman component takes over from March to August and October to December.

4 Discussion and conclusion

We analysed the mechanisms explaining warming effect induced by Niger River in Northern Gulf of Guinea. As the temperature of the riverine waters is not taken into account in the model, only dynamical processes explaining this warming are considered. In terms of periodicity and spatial distribution, the model is in line with most of the products and observations used. The differences in salinity observed between the SMAP product and the model (Figures 2C, D) are due to the difficulty of the satellite to reproduce salinity gradients near the coast (Dossa et al., 2021). The data at the coast were calculated by extrapolating measurements made by the satellite further offshore; this explains the difficulty of the satellite in accounting for the desalination caused by coastal rivers near the coast.

A similar explanation applies to observations from NOAA's drifting buoys, which are located further offshore than at the coast (Figures 2G, H). The analysis of the heat balance terms showed that vertical diffusion is the main process explaining the warming effect induced by the Niger River. The Niger River freshwater plume creates a strong vertical stratification of the water column, which prevents vertical shearing of the horizontal currents at the bottom of the mixed layer. The stratification caused by the Niger River plume acts as a barrier, preventing the upwelling of cold and nutrient-rich waters. The reduction in upwelling intensity has a net warming effect on surface, which is more pronounced in the boreal summer.

Another unexpected result is the vertical diffusion as the main driver of the cooling of coastal waters in the northern Gulf of Guinea. Indeed, in the classical theory, the wind-induced divergence of the surface waters is balanced by the upward vertical velocities. That is the case for most of the main upwelling systems, especially on the eastern boundary. In the northern Gulf of Guinea, vertical

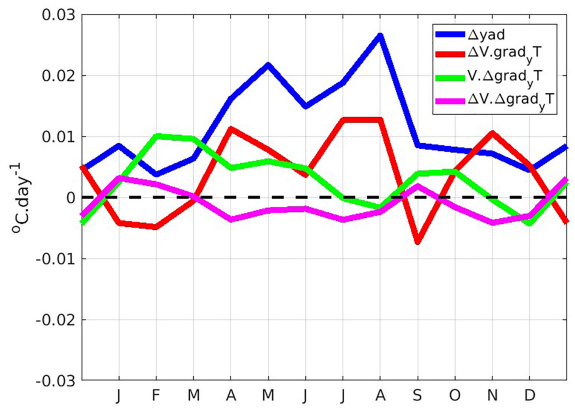

FIGURE 8
REF-noRIV seasonal variations of the meridional advection (blue), decomposed into components due to seasonal variations of the meridional current (red), of the meridional temperature gradient (green), or of both (pink), for the period 2010-2017.

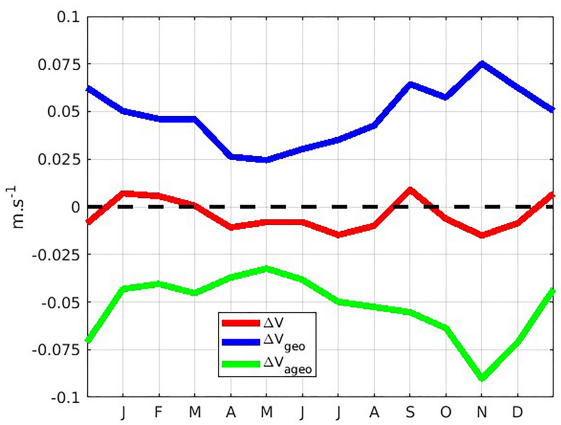

FIGURE 9
REF-noRIV seasonal variations of the meridional current (red), decomposed into its geostrophic (blue) and Ekman (green) components, for the period 2010-2017.

advection has a relatively small contribution compared to vertical diffusion in each simulation (Figures 5E, F). This confirms the importance of vertical diffusion for mixed layer temperature/salinity variations in the Gulf of Guinea (Jouanno et al., 2011; Da-Allada et al., 2014). In addition, the investigation of the causes of the changes in the meridional current showed a change in both components, especially the Ekman component. As the model is forced, the wind forcing is the same in both simulations. We expected the Ekman component to be identical in REF and noRIV, and thus to have a zero difference between them, which is not the observed case (Figure 9). This difference could be due to the effects of surface density fronts which modify the classical Ekman response to wind forcing. Indeed, In the classic Ekman theory, the fluid is homogenous and the wind stress induces an ageostrophic shear those accounts for the total surface shear. However, in frontal regions, the shear that balances the wind stress will have a geostrophic component and only a portion of the wind stress induces the ageostrophic surface shear and Ekman spiral. The wind stress should therefore be corrected by the stress associated with the pressure gradient-induced geostrophic shear. Cronin and Tomoki, (2006) have shown that these frontal effects cannot be neglected in tropical regions.

Data availability statement

The raw data supporting the conclusions of this article will be made available by the authors on demand, without undue reservation.

Author contributions

GA conceptualized the study, GDAT produced the figures, did analysis and wrote the manuscript under supervision of GA, SD and CD. JJ performed the model experiments and GM ran simulations. All authors contributed to the article and approved the submitted version.

Funding

This work was supported by the TRIATLAS project, which has received funding from the European Union's Horizon 2020 research and innovation program under grant agreement 817578.

Acknowledgments

It also contributes to the IRD JEAI IVOARE-UP and JEAI SAFUME projects. Supercomputing facilities were provided by the GENCI project GEN7298.

Conflict of interest

The authors declare that the research was conducted in the absence of any commercial or financial relationships that could be construed as a potential conflict of interest.

Publisher's note

References

Ali, K. (2009). *Relation entre les variations de la température de la surface de la mer et des précipitations le long de la bande côtière du nord du golfe de guinée* (Abidjan, Côte d'Ivoire: Université de Cocody (LAPA).

Alory, G., Da-Allada, C. Y., Djakouré, S., Dadou, I., Jouanno, J., and Loemba, D. P. (2021). Coastal upwelling limitation by onshore geostrophic flow in the gulf of Guinea around the Niger river plume. *Front. Mar. Sci.* 7. doi: 10.3389/fmars.2020.607216

Bourlès, B., Araujo, M., McPhaden, M. J., Brandt, P., Foltz, G. R., Lumpkin, R., et al. (2019). PIRATA: a sustained observing system for tropical Atlantic climate research and forecasting. *Earth Space Sci.* 6, 577–616. doi: 10.1029/2018EA000428

Cronin, M., and Tomoki, T. (2006). Steady staye ocean response to wind forcing in extratropical frontal regions. *Sci. Rep.* 6, 288842. doi: 10.1038/srep28842

Da-Allada, C. Y., Alory, G., du Penhoat, Y., Kestenare, E., Durand, F., and Hounkonnou, N. M. (2013). Seasonal mixed-layer salinity balance in the Tropical Atlantic Ocean: Mean sate and seasonal cycle. *J. Geophys. Res. Oceans* 118, 332–345. doi: 10.029/2012JC008357

Da-Allada, C. Y., Agada, J., Hounkonnou, M., Jouanno, J., and Alory, G. (2021). Causes of the northern gulf of Guinea cold event in 2012. *J. Geophysical Research: Oceans* 126, e2021JC017627. doi: 10.1029/2021JC017627

Da-Allada, C. Y., Du Penhoat, Y., Jouanno, J., Alory, G., and Hounkonnou, N. M. (2014). Modeled mixed-layer salinity balance in the gulf of Guinea: seasonal and interannual variability. *Ocean Dyn.* 64 (12), 1783–1802. doi: 10.1007/s10236-014-0775-9

Dai, A., and Trenberth, K. (2002). Estimates of freshwater discharge from continents: latitudinal and seasonal variations. *J. Hydrometeorol.* 3, 660–687. doi: 10.1175/1525-7541(2002)003,0660:EOFDFC.2.0.CO;2

De Boyer Montégut, C., Madec, G., Fischer, S., Lazar, A., and Iudicone, D. (2004). Mixed layer depth over the global ocean: an examination of profile data and a profile-based climatology. *J. Geophys. Res.* 109, C12003. doi: 10.1029/2004JC002378

Djakouré, S., Penven, P., Bourlès, B., Koné, V., and Veitch, J. (2017). Respective roles of the Guinea current and local winds on the coastal upwelling in the northern gulf of Guinea. *J. Phys. Oceanogr.* 47, 1367–1387. doi: 10.1175/JPO-D-16-0126.1

Djakouré, S., Penven, P., Bourlès, B., Veitch, J., and Koné, V. (2014). Coastally trapped eddies in the north of the gulf of Guinea. *J. Geophys. Res. Oceans* 119, 6805–6819. doi: 10.1002/2014JC010243

Dossa, A., Alory, Gaël., da Silva, A., Dahunsi, A., and Bertrand, A. (2021). Global analysis of coastal gradients of Sea surface salinity. *Remote Sensing.* 13, 2507. doi: 10.3390/rs13132507

Ducet, N., Le Traon, P., and Reverfdin, G. (2000). Global high-resolution mapping of ocean circulation from TOPEX/Poseidon and ERS-1 and-2. *J. Geophys. Res.* 105, 19,477–19,498. doi: 10.1029/2000JC900063

Dussin, R., Barnier, B., Brodeau, L., and Molines, J. M. (2016). *The making of the drakkar forcing set DFS5. DRAKKAR/MyOcean report.* Available at: https://www.drakkar-ocean.eu/publications/reports/report_DFS5v3_April2016.pdf.

Fong, A., and Geyer, W. R. (2002). The alongshore transport of freshwater in a surface-trapped river plume. *J. Phys. Oceanogr.* 32, 957–972. doi: 10.1175/1520-0485(2002)032<0957:TATOFI>2.0.CO;2

Gaillard, F., Diverres, D., Jacquin, S., Gouriou, Y., Grelet, J., Le Menn, M., et al. (2015). Sea surface temperature and salinity from French research vessels, 2001–2013. *Sci. Data* 2, 1–19. doi: 10.1038/sdata.2015.54

Hickey, B. M. S. L., Geier, S., Kachel, N., and et MacFadyen, A. (2005). A bi-directional river plume: the Columbia in summer. *Cont. Shelf Res.* 25, 1631–1656. doi: 10.1016/j.csr.2005.04.010

Jouanno, J., Hernandez, O., and Sanchez-Gomezet, E. (2017). Equatorial Atlantic inter-annual variability and its relation to dynamic processes. *Earth Syst. Dyn.* 8, 1061–1069. doi: 10.5194/esd-8-1061-2017

Jouanno, J., Marin, F., du Penhoat, Y., Sheinbaum, J., and Molines, J.-M. (2011). Seasonal heat balance in the upper 100 m of the equatorial Atlantic ocean. *J. Geophys. Res.* 116, C09003. doi: 10.1029/2010JC006912

Kanga, D. K., Kouassi, M. A., Trokourey, A., Toualy, E., N'Guessan, B. K., Brehmer, P., et al. (2021). Spatial and seasonal variability of mixed layer depth in the tropical Atlantic at 10°W using 40 years of observation data. *Eur. J. Sci. Res.* 158 (3), 207–217.

Koné, V., Lett, C., Penven, P., Bourlès, B., and Djakouré, S. (2017). A biophysical model of s. aurita early-life history in the northern gulf of Guinea. *Prog. Oceanogr.* 151, 83–96. doi: 10.1016/j.pocean.2016.10.00

Large, G., and Yeager, S. (2009). The global climatology of an interannually varying air–sea flux data set. *Clim. Dyn.* 33, 341–364. doi: 10.1007/s00382-008-0441-3

Laurindo, C., Mariano, J., and Lumpkin, R. (2017). An improved near-surface velocity climatology for the global ocean from drifter observations. *Deep Sea Res. Part I Oceanographic Res. Papers* 124, 73–92. doi: 10.1016/j.dsr.2017.04.009

Le Traon, P., Nadal, F., and Ducet, N. (1998). An improved mapping method of multisatellite altimeter data. *J. Atmos. Ocean. Technol.* 15, 522–534. doi: 10.1175/1520-0426(1998)015<0522:AIMMOM>2.0.CO;2

Li, Y., Wang, F., and Han, W. (2013). Interannual sea surface salinity variations observed in the tropical north pacific ocean. *Geophysical Res. Lett.* 40, 2194–2199. doi: 10.1002/grl.50429

Locarnini, M., Mishonov, V., Baranova, K., Boyer, P., Zweng, M., Garcia, E., et al. (2018). *World ocean atlas 2018*, (Silver Spring, Maryland: National Centers for Environmental Information), Vol. 81. 52.

Madec, G. (2016) *NEMO ocean engine*. Available at: https://www.nemo-ocean.eu/wp-content/uploads/NEMO_book.pdf.

Marchesiello, P., and Estrade, P. (2010). Upwelling limitation by onshore geostrophic flow. *J. Mar. Res.* 68, 37–62. doi: 10.1357/002224010793079004

Meneghesso, C., Seabra, R., Broitman, B., Wethey, D., Burrows, M., Chan, B., et al. (2020). Remotely-sensed L4 SST underestimates the thermal fingerprint of coastal upwelling. *Remore Sens. Environ.* 237, 111588. doi: 10.1016/j.rse.2019.111588

N'Guessan, B. K., Kouassi, A. M., Trokourey, A., Toualy, E., Kanga, D. K., and Brehmer, P. P. (2019). Eastern Tropical Atlantic mixed layer depth: assessment of methods from *In situ* profiles in the gulf of Guinea from coastal to high Sea. *Thalassas: Int. J. Mar. Sci.* 36, 20112. doi: 10.1007/s41208-019-00179-7

Sohou, Z., Koné, V., Da-Allada, C. Y., Djakouré, S., Bourlès, B., Racape, V., et al. (2020). Seasonal and inter-annual ONSET Sea surface temperature variability along the northern coast of the gulf of Guinea. *Regional Stud. Mar. Sci.* 35, 101129. doi: 10.1016/j.rsma.2020.101129

Tanguy, M., de Coëtlogon, G., and Eymard, L. (2021). Sea Surface temperature impact on diurnal cycle and seasonal evolution of the Guinea coast rainfall in boreal spring and summer. *Eur. J. Res.* 158 (3), 207–217. Available at: http://www.europeanjournalofscientificresearch.com.

Wade, M., Caniaux, G., and du Penhoat, Y. (2011). Variability of the mixed layer heat budget in the eastern equatorial Atlantic during 2005-2007 as inferred using argo floats. *J. Geophysical Res.* 116, C08006. doi: 10.1029/2010JC006683

Yago, A. (2021). *Modélisation biophysique de la dispersion et de la croissance des larves de sardinelles dans le golfe de guinée. ecosystèmes* (Français: Sorbonne Université ; Université Félix Houphouët Boigny (Abidjan, Côte d'Ivoire).

Zweng, M., Reagan, J., Seidov, D., Boyer, T., Locarnini, R., Garcia, H., et al. (2019). *WORLD OCEAN ATLAS 2018*, (Silver Spring, Maryland: National Centers for Environmental Information), Vol. 2.

frontiers | Frontiers in Marine Science

TYPE Original Research
PUBLISHED 04 July 2023
DOI 10.3389/fmars.2023.1186069

OPEN ACCESS

EDITED BY
Francisco Machín,
University of Las Palmas de Gran Canaria, Spain

REVIEWED BY
Johannes Röhrs,
Norwegian Meteorological Institute, Norway
Jesus Dubert,
University of Aveiro, Portugal

*CORRESPONDENCE
Giles Fearon
gfearon11@gmail.com
Marcello Vichi
marcello.vichi@uct.ac.za

RECEIVED 14 March 2023
ACCEPTED 22 May 2023
PUBLISHED 04 July 2023

CITATION
Fearon G, Herbette S, Cambon G, Veitch J, Meynecke J-O and Vichi M (2023) The land-sea breeze influences the oceanography of the southern Benguela upwelling system at multiple time-scales. *Front. Mar. Sci.* 10:1186069. doi: 10.3389/fmars.2023.1186069

The land-sea breeze influences the oceanography of the southern Benguela upwelling system at multiple time-scales

Giles Fearon[1,2,3]*, Steven Herbette[1,4], Gildas Cambon[4], Jennifer Veitch[3,5], Jan-Olaf Meynecke[6,7] and Marcello Vichi[1,2]*

[1]Department of Oceanography, University of Cape Town, Cape Town, South Africa, [2]Marine and Antarctic Research centre for Innovation and Sustainability (MARIS), University of Cape Town, Cape Town, South Africa, [3]Egagasini Node, South African Environmental Observation Network, Cape Town, South Africa, [4]Univ Brest, CNRS, Ifremer, IRD, Laboratoire d'Océanographie Physique et Spatiale (LOPS), IUEM, F29280, Plouzané, France, [5]Nansen-Tutu Center, Department of Oceanography, University of Cape Town, Cape Town, South Africa, [6]Griffith Climate Change Response Program, Griffith University, Southport, QLD, Australia, [7]Coastal and Marine Research Centre, Griffith University, Southport, QLD, Australia

The physical and biogeochemical functioning of eastern boundary upwelling systems is generally understood within the context of the upwelling - relaxation cycle, driven by sub-diurnal wind variability (i.e. with a time-scale of greater than a day). Here, we employ a realistically configured and validated 3D model of the southern Benguela upwelling system to quantify the impact of super-diurnal winds associated with the land-sea breeze (LSB). The ocean response to the LSB is found to be particularly enhanced within St Helena Bay (SHB), a hotspot for productivity which is also prone to Harmful Algal Bloom (HAB) development. We attribute the enhanced response to a combination of near-critical latitude for diurnal-inertial resonance (~32.5°S), the local enhancement of the LSB, and the local development of a shallow stratified surface layer through bay retention. Pronounced advection of the surface layer by diurnal-inertial oscillations contributes to large differences in day- and night-time sea surface temperatures (SST's) (more than 2°C on average in SHB). Event-scale diapycnal mixing is particularly enhanced within SHB, as highlighted by a numerical experiment initialised with a subsurface passive tracer. These super-diurnal processes are shown to influence sub-diurnal dynamics within SHB through their modulation of the vertical water column structure. A deeper thermocline retains the upwelling front closer to land during active upwelling, while geostrophically-driven alongshore flow is impacted through the modulation of cross-shore pressure gradients. The results suggest that the LSB is likely to play an important role in the productivity and therefore HAB development within SHB, and highlight potential challenges for observational systems and models aiming to improve our understanding of the physical and biological functioning of the system.

KEYWORDS

land-sea breeze, diurnal-inertial oscillations, vertical mixing, critical latitude, coastal upwelling, southern Benguela

1 Introduction

The physical and biogeochemical variability of the four major Eastern Boundary Upwelling Systems (EBUS) is largely understood to be driven by local wind forcing which varies at multiple time-scales. The seasonality in the wind forcing is governed by permanent but seasonally migrating subtropical high pressure systems over the Atlantic and Pacific oceans, as well as land-based thermal low pressure systems which develop to the east of the oceanic highs (García-Reyes et al., 2013). As such, summer months are characterised by intensified alongshore equatorward winds, increased upwelling and enhanced productivity, particularly at high latitudes (Chavez and Messie, 2009). Eastward traveling midlatitude cyclones result in periodic weakening or abatement of the equatorward winds, setting up the upwelling-relaxation cycle through wind variability with a time-scale of days to weeks. Intensified equatorward winds drive the upwelling of nutrient-rich subsurface waters while wind relaxation of equatorward winds is important for the retention of upwelled nutrients, thereby sustaining primary productivity (Roughan et al., 2006; Pitcher et al., 2014). The retention of primary productivity in upwelling systems may further play a role in the feeding behaviour of higher trophic levels, such as humpback whales (Dey et al., 2021). The land-sea breeze, set up by differential diurnal heating over the land and the ocean, drives wind variability at timescales of less than a day within all EBUS (Gille et al., 2003; 2005). Near latitudes of 30°N/S (which intersect all four major EBUS) the diurnal wind forcing is resonant with the inertial response of the ocean (Hyder et al., 2002; Simpson et al., 2002), driving high amplitude diurnal-inertial oscillations which are embedded within sub-diurnal upwelling/relaxation dynamics (Aguiar-Gonzalez et al., 2011; Lucas et al., 2014). In this paper we explore the impact of these super-diurnal processes at multiple time-scales through the lens of a 3D regional model of the southern Benguela upwelling system. We adopt the terminology of sub- and super-diurnal variability throughout to refer to variability with frequencies (as opposed to time-scales) below and above the diurnal frequency, respectively.

An important implication of the high amplitude diurnal-inertial oscillations driven by the land-sea breeze is their notable impact on enhanced diapycnal mixing. Diapycnal mixing is maximised at the critical latitude of 30°N/S (Zhang et al., 2010; Fearon et al., 2020), driven primarily by the locally forced diurnal-inertial oscillations (which are amplified by the resonance effect), while evanescent first baroclinic mode internal waves play a secondary role (Fearon et al., 2022). It has been suggested that these processes may play an important role in the biological functioning of these systems primarily through the entrainment of nutrient-rich subsurface waters into the surface, thereby enhancing primary productivity (Fawcett et al., 2008; Aguiar-Gonzalez et al., 2011; Lucas et al., 2014). It has further been suggested that enhanced vertical mixing driven by the land-sea breeze may impact lower frequency physical processes through its modulation of the vertical water column structure. A deepened thermocline may for instance steepen cross-shore pressure gradients and intensify alongshore flows, as indicated by observations in the Coastal Southern California Bight (Nam and Send, 2013). The 2D numerical experiments of Fearon et al. (2022) suggested that a deepened Ekman boundary layer driven by land-sea breeze forcing near the critical latitude would serve to maintain the upwelling front closer to the land boundary, with a net warming effect on nearshore surface waters.

A further implication of the land-sea breeze within the context of EBUS is the role it plays in pronounced horizontal advection of the upwelling front. High amplitude surface oscillations can drive the outcropping and subduction of the upwelling front over the diurnal cycle, a process which has been cited as playing a key role in diurnal temperature variability in a number of *in-situ* observations in EBUS (Kaplan et al., 2003; Woodson et al., 2007; Bonicelli et al., 2014; Walter et al., 2017). The relative contributions of solar irradiance and wind-driven advection to diurnal variability in sea surface temperatures can however be difficult to separate in site specific observations.

While the literature suggests that an accurate depiction of diurnal wind variability in the forcing of ocean models of EBUS may be important, previous modelling studies have either adopted surface wind forcing which excludes diurnal variability (e.g. daily averaged or climatological forcing), or if higher frequency winds have been used, their importance in the model solution has not as yet been explicitly quantified. Here, we present a realistically configured and validated model of the southern Benguela upwelling system, employing 3 km and 1 km horizontal resolution domains in a 2-way nested configuration, with the aim of elucidating the extent to which the land-sea breeze drives both the super- and sub-diurnal variability in coastal temperatures and circulation of the system.

Super-diurnal effects in sea surface temperatures (SST) are distilled by comparing day- and night-time climatologies for simulations which both include and exclude land-sea breeze forcing, and we compare the model results with day- and night-time SST data from a geostationary satellite. We then consider the effect of land-sea breeze forcing on diapycnal mixing over a selected upwelling event, allowing us to identify processes revealed by previous reduced physics models (Fearon et al., 2020; 2022). This experiment is aided by the inclusion of a subsurface tracer as a proxy for subsurface nutrients. Finally, we present the effects of land-sea breeze forcing on the seasonal mean vertical water column structure and circulation. We consider upwelling and relaxation wind regimes separately for this analysis, as different sub-inertial circulation patterns are at play during each.

St Helena Bay, located in the lee of Cape Columbine (Figure 1), is a particular focus of this study, given that energetic diurnal-inertial motions are routinely observed here (Fawcett et al., 2008; Lucas et al., 2014). This region is also well documented for its importance as a hotspot for primary productivity (e.g. Weeks et al., 2006; Demarcq et al., 2007). Fearon et al. (2020) argued that St Helena Bay possesses a combination of physical characteristics (proximity to the critical latitude, local amplification of diurnal anticyclonic winds, and the development of shallow stratified surface layers during relaxation of equatorward winds) which favour the local development of high amplitude forced surface oscillations and associated mixing. The presented experiments provide us with an opportunity to further consider this

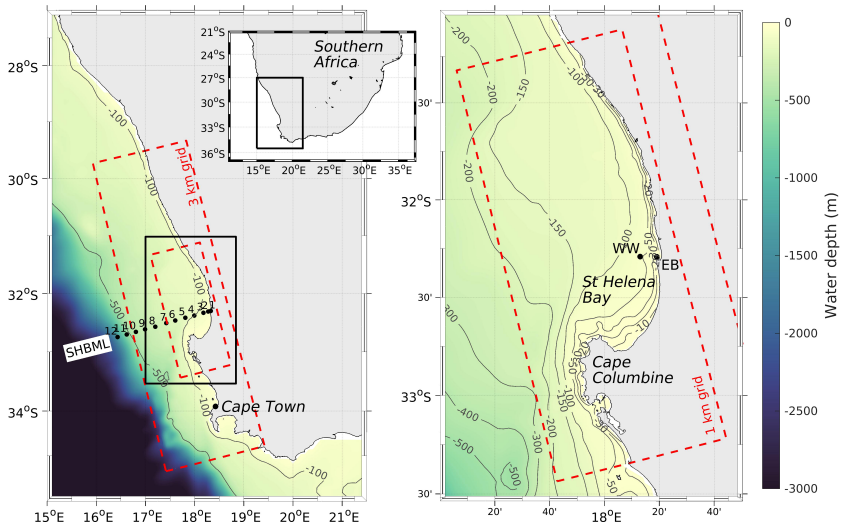

FIGURE 1
Locality map indicating the model grid extents, bathymetry and locations of previously published *in-situ* data. A 1 km resolution child domain, centred over St Helena Bay, is nested within a 3 km resolution parent domain. The shown bathymetry within the model domains is derived from digital navigation charts for the region provided by the Hydrographer of the SA Navy, while data outside the model is taken from the 30-arc second GEBCO dataset.

hypothesis, and the potential role which the land-sea breeze may play in driving the biology of the system.

2 Methods

2.1 *In situ* data for model validation

Various *in-situ* datasets are presented alongside model output, with the aim of assessing the model performance at multiple time-scales, starting from seasonal climatologies.

The seasonal variability of the water column structure across the continental shelf is taken from quasi monthly Conductivity-Temperature-Depth (CTD) casts along the St Helena Bay Monitoring Line (SHBML) from March 2000 to August 2017 (Oceans and Coastal Research, 2017). The transect is comprised of twelve stations orientated approximately perpendicular to the isobaths off St Helena Bay (Figure 1). A detailed description of the data is provided in Lamont et al. (2015). Measurements from all available cruises were used to calculate monthly climatologies of temperature and salinity at each station on a 1 m vertical grid.

The inter-annual and event-scale upwelling/relaxation dynamics in the nearshore region of St Helena Bay is taken from daily averaged temperature observations from a fixed mooring in Eland's Bay near the surface (~5 m water depth) and at the seabed (~20 m water depth) over the three year period from November 2008 to November 2011 ('EB' in Figure 1). These data are described in more detail in Pitcher et al. (2014).

The super-diurnal variability of the system is informed by concurrent deployments of Wirewalker wave-powered profilers (Rainville and Pinkel, 2001; Pinkel et al., 2011) and bottom-mounted Acoustic Doppler Current Profilers (ADCP) providing horizontal velocity components and temperature at a temporal resolution of 10 min and vertical resolutions of 1 m and 0.25 m, respectively ('WW' in Figure 1). The full dataset is described in detail in Lucas et al. (2014), although only data from the month of March 2011 are revisited in this study for model validation purposes. This period was specifically selected so that the model output could be compared with the reduced physics experiments of Fearon et al. (2020; 2022). The data were filtered in time to provide a two hour running mean at 30 min intervals, sufficient for analysing the super-diurnal processes of interest.

2.2 Satellite SST data

This study makes use of the Group for High Resolution Sea Surface Temperature (GHRSST) dataset for the Eastern Atlantic Region from the Spinning Enhanced Visible and InfraRed Imager (SEVIRI, https://podaac.jpl.nasa.gov/dataset/SEVIRI_SST-OSISAF-L3C-v1.0) (OSISAF, 2015). The geostationary orbit of the satellite allows data to be made available at hourly intervals from June 2004 to present, on a 0.05° regular grid. The high temporal resolution of the data is used to assess day vs night-time SST's over the area of interest. Only data with a quality flag of 3 and greater are used in the presented analysis, as recommended in the scientific validation report for the product (SAF, 2018).

2.3 Description of the model

The ocean model employed in this study is the V1.0 official release of the Coastal and Regional Ocean COmmunity model (CROCO, http://www.croco-ocean.org/), an ocean modelling

system built upon ROMS AGRIF (Shchepetkin and McWilliams, 2005). CROCO is a free-surface, terrain-following coordinate oceanic model which solves the Navier-Stokes primitive equations by following the Boussinesq and hydrostatic approximations. The model solves equations governing the conservation of horizontal momentum, hydrostatic balance, incompressibility and the conservation of tracers (temperature and salinity). A curvilinear Arakawa C-grid is used for the discretisation of the horizontal plane, while the vertical grid is discretised using a terrain-following (σ) coordinate reference system.

The choice of the vertical turbulent viscosity scheme is particularly important within the context of this study, as we attempt to highlight diapycnal mixing driven by super-diurnal wind variability. Initial simulations indicated that CROCO's default K-profile parameterization (LMD-KPP) scheme resulted in an over-estimation of vertical mixing within the nearshore regions of St Helena Bay when compared with the observations. The results presented in this study therefore adopt the k-ϵ turbulent closure scheme within the Generic Length-Scale (GLS) formulation (Umlauf and Burchard, 2003; 2005), which provided a better fit to the observations. Horizontal eddy viscosity and diffusivity are typically ignored in regional configurations using ROMS (e.g. Marchesiello et al., 2003; Veitch et al., 2010). Instead, horizontal dissipation at the grid scale is determined by dissipation associated with a split and rotated third-order upstream biased horizontal advection scheme (Marchesiello et al., 2009). Bottom friction is parametrised using a quadratic drag law, where the bottom roughness length parameter is taken as 0.001 m. A nonlinear equation of state is used for the computation of density (Jackett and Mcdougall, 1995). The model configuration, as described below, effectively constitutes a dynamical downscaling of a global reanalysis product to ~1 km resolution over St Helena Bay, so that the high-frequency bay-scale processes can be better assessed.

2.3.1 Discretisation

The model is comprised of a ~3 km horizontal resolution parent domain as well as a ~1 km horizontal resolution child domain, both centred around St Helena Bay and aligned according to the approximate orientation of the coastline (Figure 1). 2-way nesting is implemented between the parent and child domains, whereby at each time-step the parent domain provides boundary conditions for the child domain, which in turn provides feedback to the parent domain (Debreu et al., 2012). 50 levels are used to define the vertical grid of both domains. Baroclinic time-steps of 6 min and 2 min are adopted for the temporal integration of the parent and child domains, respectively, reflecting the factor 3 difference in the spatial resolution of the domains. 60 barotropic time-steps are computed within each baroclinic time-step.

2.3.2 Bathymetry

The bathymetry assigned to the model grids is interpolated from digital versions of the most detailed available navigation charts for the region, as provided by the Hydrographer of the South African Navy. The interpolated bathymetry is smoothed to maintain a slope parameter ($r = \frac{\nabla H}{H}$) of less than 0.25 everywhere in the domain in an attempt to circumvent the well-known horizontal pressure gradient errors associated with σ-coordinate models with steep slopes (e.g. Haney, 1991). Minimum depths of 20 m and 5 m are enforced for the parent and child domains, respectively, to avoid vertical advection errors associated with thin vertical layers in shallow water. A semi-implicit vertical advection scheme is adopted to further assist in this regard. A hyperbolic tangent function is used over the sponge layer of the parent domain (10 grid cells wide) to gradually ramp up the model bathymetry to the 30-arc second GEBCO dataset at the open boundaries of the model (Weatherall et al., 2015). This was done to match the internal bathymetry at the model boundaries with that of the global model providing lateral boundary forcing conditions (Section 2.3.4). The resulting model bathymetry is shown in Figure 1.

2.3.3 Atmospheric forcing

Atmospheric variables to force the model at the surface (10 m wind velocity components, short- and long-wave solar radiation, air temperature, relative humidity and precipitation) are taken from a Weather Research and Forecasting (WRF) model configuration developed by the Climate Systems Analysis Group (CSAG) at the University of Cape Town (UCT). The atmospheric simulation is a dynamical downscaling of the ERA-Interim global atmospheric reanalysis (https://www.ecmwf.int/en/forecasts/datasets/reanalysis-datasets/era-interim) to high resolution over southern Africa, as part of the Wind Atlas for South Africa (WASA) project (Lennard et al., 2015). The WASA model output is available on a 3 km horizontal resolution grid at hourly intervals for the period November 2005 to October 2013 (8 years). The offshore extent and orientation of our parent grid coincides with that of the 3 km resolution WRF model grid.

We use three different types of wind forcing with the aim of isolating the influence of the land-sea breeze on the dynamics of the system, as summarised in Table 1. τ^{real} uses bulk parameterisation

TABLE 1 Summary of wind forcing nomenclature adopted in this paper.

Wind forcing	Description
τ^{real}	Bulk parameterisation for hourly wind stress components from WASA 10 m wind velocity components
τ^{daily}	Forced daily averaged wind stress components output from the simulation using τ^{real}
$\tau^{daily+ac}$	Forced hourly averaged wind stress components corresponding to the diurnal anticyclonic rotary component of the WASA winds (τ^{ac}), added to the daily averaged wind stresses (τ^{daily})

(Fairall et al., 1996; 2003) for the online computation of hourly wind stress components from the WASA 10 m wind velocity components. τ^{daily} uses forced daily averaged wind stress components which are output from the simulation using τ^{real}. In so doing, simulations using τ^{daily} maintain the identical net Ekman dynamics as simulations using τ^{real}, while the influence of the super-diurnal winds is removed. We further perform simulations where the diurnal anticyclonic rotary component of the wind stress (τ^{ac}) is super-imposed onto τ^{daily}, and adopt the nomenclature $\tau^{daily+ac}$ for this wind forcing. τ^{ac} is computed from consecutive 7 day windows, as described in Fearon et al. (2020), and represents the component of the winds which rotates at a diurnal frequency and in the same direction as the locally forced inertial oscillations. With this forcing we aim to excite the diurnal-inertial oscillations in response to the land-sea breeze, while excluding any additional effects induced by the super-diurnal component of the winds which may be present in τ^{real}. All three simulations use bulk parameterisation (Fairall et al., 1996; 2003) for the online computation of hourly freshwater and heat fluxes from the WASA data.

2.3.4 Lateral boundary conditions

Lateral boundary conditions for the parent domain are interpolated from daily averaged data of the ocean state (temperature, salinity, horizontal current components and surface elevation) obtained from a 1/12° global ocean reanalysis product provided by the HYCOM consortium (https://www.hycom.org/data/glbu0pt08/expt-19pt1). Following Dey et al. (2021), monthly biases in the HYCOM temperature and salinity data, computed with respect to the CSIRO Atlas of Regional Seas climatology (CARS2009, https://www.cmar.csiro.au/cars), were removed to improve model performance in the coastal region of interest. The specified water levels exclude tidal variability, which has been shown to make an insignificant contribution to current observations within St Helena Bay (Fawcett et al., 2008).

Open boundary conditions (OBCs) are implemented at the lateral boundaries of the model as described in Marchesiello et al. (2001). The model solution is 'nudged' to the specified boundary values using relaxation times of 1 day and 1 year for inward and outward radiation, respectively. Nudging is applied within the sponge layer of the model (10 grid cells wide) using a gradual decrease (cosine profile) from the open boundary to the inner border of the sponge layer.

2.4 Computation of climatologies

Each of the three types of wind forcing (Table 1) are used to integrate the model over the period 01 November 2005 to 31 December 2012 (7 years), spanning the duration over which all forcing data are available. Three hourly 'snapshots' of temperature generated over the entire simulation period are used to assess day- vs night-time sea surface temperature differences in the model. We use model output times of 14:00 and 02:00 (local time, UTC+2) for this purpose, and limit the analysis to the nominally upwelling months of October to March, which also coincides with enhanced land-sea breeze forcing in the region of interest (Fearon et al., 2020).

Daily averaged output from the 7 year simulations are used to compute climatologies of temperature and horizontal currents, allowing for an assessment of the impact of the land-sea breeze on the mean state of the vertical water column structure and circulation over the area of interest. Again, this analysis is confined to the nominally upwelling months of October to March. Upwelling and relaxation wind regimes are considered separately, as different sub-diurnal processes are at play in each. To distinguish between these regimes we consider the time-series of the 3 day average alongshore wind stress for a location in the centre of St Helena Bay, as shown in Figure 2. We take active upwelling as times where the 75^{th} percentile 3 day average alongshore wind stress is exceeded (i.e. the black time-series above the red line), while relaxation periods are identified as times where the 3 day average alongshore wind stress falls below the 25^{th} percentile value (i.e. the black time-series below the blue line). Composite means are then presented based on these wind regimes.

2.5 Event-scale mixing experiment

Given that one of the main implications of the land-sea breeze in EBUS is its effect on vertical mixing, we present an experiment specifically designed to examine the event-scale mixing processes in the model over the weekly time-scale associated with upwelling

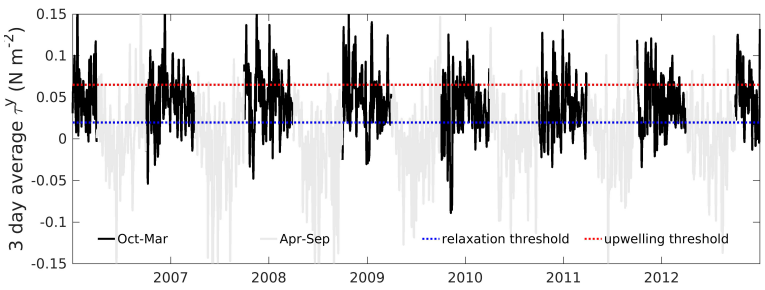

FIGURE 2
Time-series of 3 day average alongshore wind stress (τ^y) extracted from the model at a location in the centre of St Helena Bay ('P' in Figure 3). The shown relaxation and upwelling thresholds correspond to the 25^{th} and 75^{th} percentile τ^y for the nominally upwelling months of October-March.

events. To do this, we compare hourly output from two simulations, one forced by τ^{daily} and one forced by $\tau^{daily+ac}$, each initialised on 25 January 2007 from the simulation forced with τ^{daily} (this ensures that the influence of the land-sea breeze is absent from the initial condition in both simulations). The initialisation date was subjectively chosen to be at the end of a relaxation event during which a shallow stratified surface layer developed within St Helena Bay, as shown in Figures 3A, B. The vertical isotherms at the offshore extent of this shallow surface layer (60 to 80 km offshore) are associated with the upwelling cell off Cape Columbine, and associated equatorward flowing Columbine Jet, which represents a dynamic offshore boundary of the bay. The model is integrated over a 7 day period which is characterised by a local amplification of land-sea breeze, as indicated by the amplitude of the diurnal

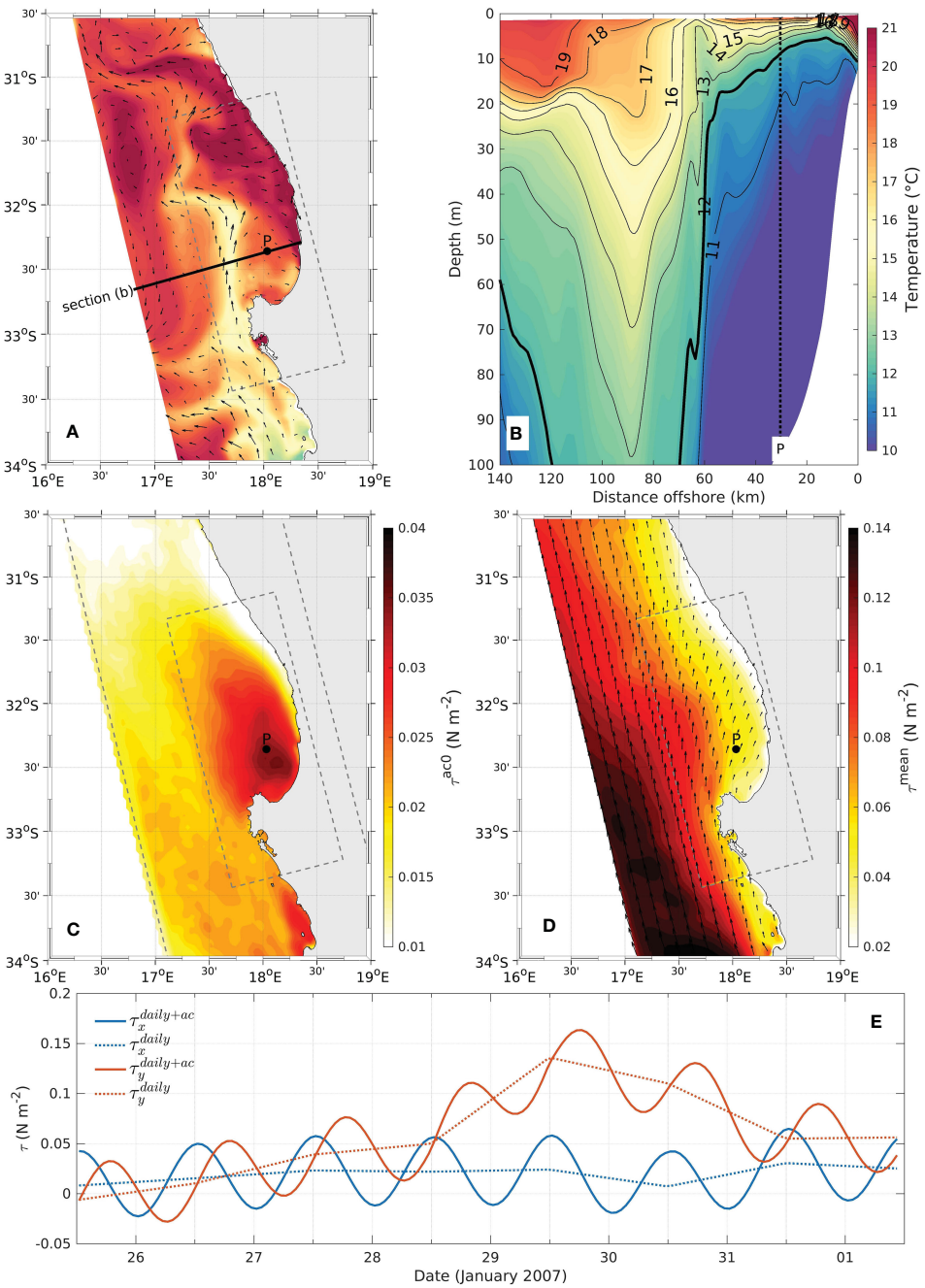

FIGURE 3
Initial temperature condition and wind stress forcing for 7 day experiments initialised on 25 January 2007 from the model forced with τ^{daily}. **(A)** Mean sea surface temperature. **(B)** Mean vertical section of temperature across the model domain over the upper 100 m of the water column. **(C)** Amplitude of the diurnal anticlockwise rotary component of the wind stress (τ^{ac0}) over the 7 day duration of the experiment. **(D)** Mean wind stress (τ^{mean}) over the 7 day duration of the experiment. **(E)** Time-series of wind stress components for τ^{daily} and $\tau^{daily+ac}$ at Station 'P', in the centre of St Helena Bay.

anticlockwise rotary component of the winds (τ^{ac0}) (Figure 3C). It is also a period of upwelling-favourable winds, as indicated by the mean wind stress (Figure 3D). Note that we use τ^{ac0} to refer to the amplitude of the rotating wind stress component, while τ^{ac} denotes the rotating wind stress vector. Figure 3E provides the time-series of wind stress components for τ^{daily} and $\tau^{daily+ac}$ for a location in the centre of St Helena Bay.

The analysis of diapycnal mixing in the model is aided by initialising the model with a subsurface passive tracer (C, in arbitrary tracer units per volume, ATU m^{-3}). C is initialised to a value of 1 for temperatures of 12°C and less, 0 for temperatures of 13°C and above, while linear interpolation is applied for temperatures between 12°C and 13°C. This approach is also adopted for specifying the passive tracer at the lateral boundaries of the model. The cumulative diapycnal mixing in the model is quantified by integrating the passive tracer from the depth of the 12°C isotherm to the surface:

$$C_s = \int_{z_{12°C}}^{0} C \quad dz\,. \tag{1}$$

It is informative to isolate the effect of the land-sea breeze forcing on C_s, which is done by computing the difference in C_s for simulations which both include and exclude the diurnal anticlockwise rotary component of the wind stress (τ^{ac}):

$$\Delta C_s = C_{s\_\tau^{daily+ac}} - C_{s\_\tau^{daily}}\,. \tag{2}$$

ΔC_s therefore represents a diagnostic aimed at highlighting the increase in cumulative diapycnal mixing due to the inclusion of land-sea breeze forcing.

We further use the vertical displacement of the 12°C isotherm to diagnose internal wave generation and propagation in the model due to the inclusion of land-sea breeze forcing. To this end, the depth of the 12C isotherm is presented as the displacement from the daily running average, allowing us to isolate the super-diurnal variability induced by the applied land-sea breeze forcing.

3 Results

3.1 Model validation

The purpose of the model validation is to assess the skill of the model at representing the variability of the system at multiple time-scales, including seasonal fluctuations (Figure 4), upwelling/relaxation events (Figure 5), and higher frequency process associated with the land-sea breeze (Figure 6). Preference is given to *in-situ* data over satellite observations for the model validation owing to the nearshore and high-frequency nature of the processes of interest.

Figure 4 presents a comparison of modelled and observed seasonal temperature climatologies along the St Helena Bay Monitoring Line ('SHBML' in Figure 1). The vertical water column characteristics for the offshore region (Station 7 and offshore) is shown to be distinct from those in the nearshore waters of St Helena Bay (Stations 1 to 4). During austral summer (December to February), Stations 3 and 4 (in the middle of St Helena Bay) are characterised by a highly stratified shallow surface layer overlaying cool subsurface waters. In contrast, winter months at these stations are characterised by a nearly fully mixed water column. Nearshore temperatures are on average cooler than those offshore, particularly during summer, in line with the seasonal variability in upwelling-favourable winds. The climatological

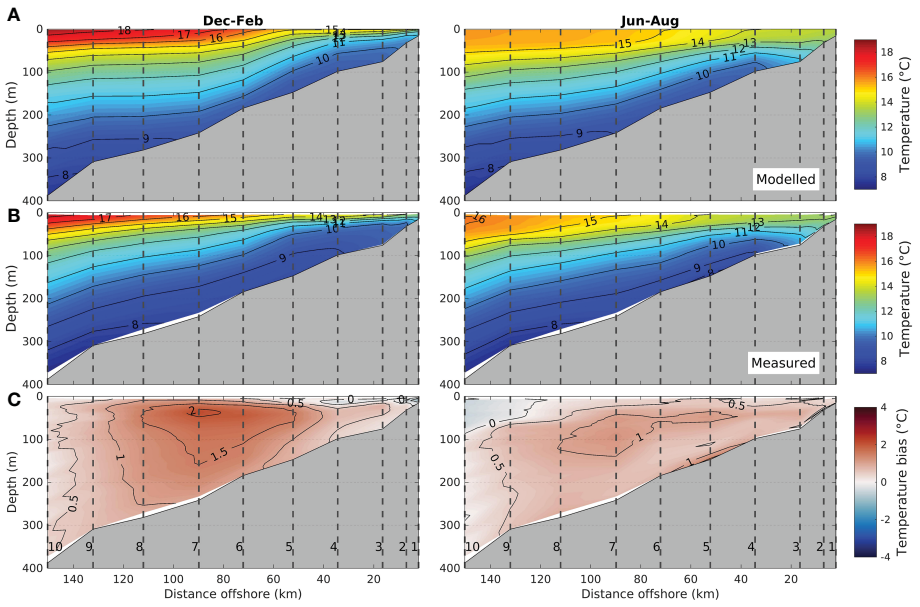

FIGURE 4
Seasonal temperature climatologies for the St Helena Bay Monitoring Line (SHBML) as computed from the model **(A)**, from the observations **(B)** and the resulting model bias **(C)**. The numbered vertical dashed lines denote the station locations shown in Figure 1.

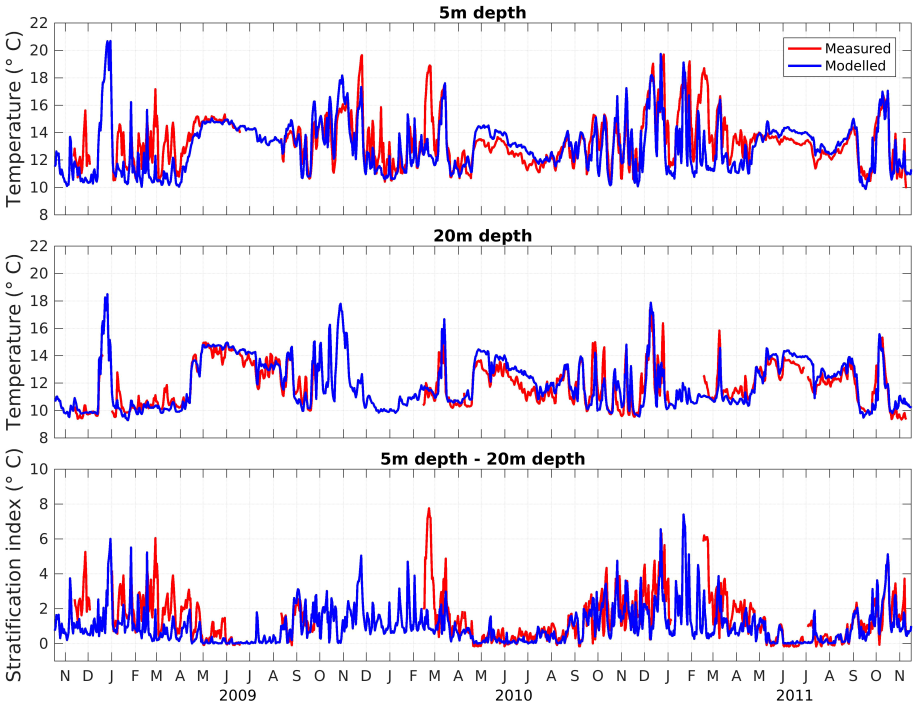

FIGURE 5
Time-series comparison of daily averaged measured and modelled temperature at 5 m and 20 m depths at the Elands Bay fixed mooring ('EB' in Figure 1), located in 20 m water depth). The stratification index is simply the difference between the temperature at 5 m and 20 m depths.

model bias within St Helena Bay (Stations 1 to 4) is below 1°C for both summer and winter seasons, indicating that the seasonal variability in the mean state of water column over the area of interest is well represented in the model.

Figure 5 presents a 3 year time-series of measured and modelled daily averaged temperature at the Elands Bay fixed mooring ('EB' in Figure 1), while summary statistics for the nominally winter (April-September) and summer (October-March) periods are provided in

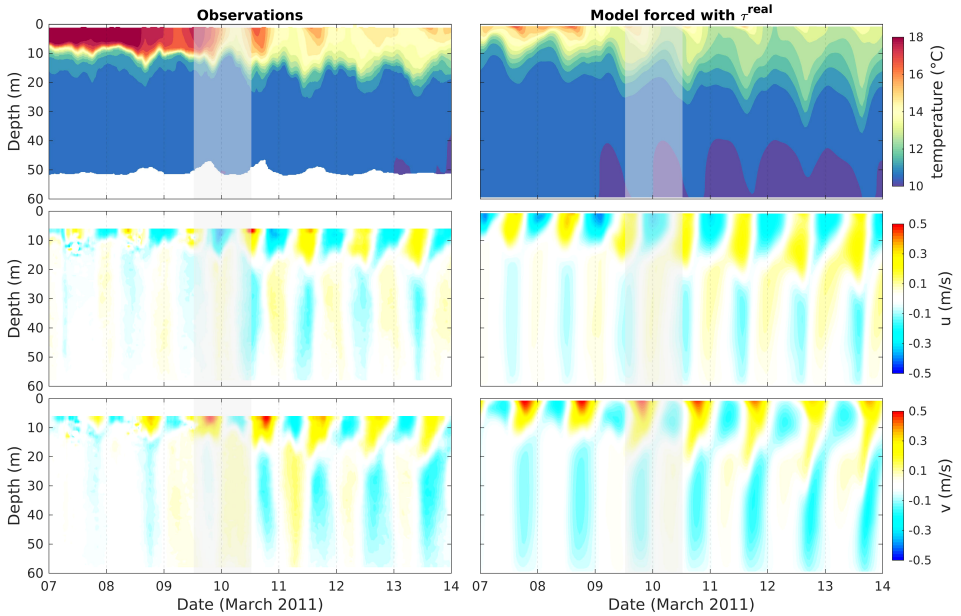

FIGURE 6
Observed (left) and modelled (right) temperature and horizontal velocity components over an upwelling event accompanied by diapycnal mixing at the Wirewalker fixed mooring in 60 m water depth ('WW' in Figure 1). The shaded time denotes the period considered in Figure 7.

the Supplementary Table S1. The data indicate a well-mixed water column during winter with relatively little variability, while summer reflects the variability associated with upwelling/relaxation events. Extended periods of upwelling result in a drop in temperature in both surface and subsurface waters, while relaxation of equatorward winds drive stratification events through the warming of surface waters which are advected inshore and poleward (Fawcett et al., 2007; Fawcett et al., 2008; Pitcher et al., 2014). Relaxation events can lead to the subduction of warm water to the bottom, as reflected in the time-series at 20 m depth. The model is shown to under-predict surface warming for some relaxation events (top panel of Figure 5), suggesting that the surface heat flux and/or the inshore and poleward advection of heat is not adequately captured for these events. This results in a cool bias of ~1.2C in the surface waters during summer. Surface model temperatures achieve correlation coefficients of 0.8 and 0.92 for the summer and winter periods, respectively. Subsurface bias is low throughout the year (<0.6C) with correlation coefficients of 0.88 and 0.89 for the summer and winter periods, respectively. Overall, these results indicate that the model shows acceptable skill at capturing the salient features of the upwelling/relaxation dynamics in the nearshore waters of St Helena Bay.

For reference, Supplementary Table S2 provides summary statistics at the Elands Bay mooring, but for the simulation forced with daily averaged wind stress (τ^{daily}). The statistics confirm that the model performance is significantly reduced when the super-diurnal winds are excluded in the model forcing. For example, the correlation coefficient for surface temperature reduces from 0.8 to 0.68 during summer, and from 0.92 to 0.83 during winter, highlighting the importance of super-diurnal winds in representing upwelling-relaxation dynamics in the model.

We now further analyse the extent to which the observed super-diurnal variability, embedded within the sub-diurnal upwelling dynamics, is captured by the model forced with τ^{real}. Figure 6 presents the temporal evolution of temperature and horizontal velocity components through the water column for a 7 day period at the Wirewalker mooring in 60 m water depth ('WW' in Figure 1), both in the observations and in hourly output from the model. For reference, this is the same 7 day period considered in the reduced physics experiments of Fearon et al. (2020; 2022). A time-series of wind stress components over this time period at the Wirewalker location can be found in Figure 2 of Fearon et al. (2022). The considered period begins with a relaxation event characterised by a highly stratified two layer system. The onset of an upwelling event is shown to be accompanied by strong variability at the diurnal-inertial frequency in both the temperature and horizontal velocity profiles, with a 180° phase shift between the surface and subsurface currents. The model performance over the full month of March 2011 is summarised in the Supplementary Figure S1. Modelled temperatures are shown to be under-estimated near the surface, although here temperature correlation is highest (~0.8 in the surface layer of the model), reflecting general agreement in the super-diurnal variability in surface temperature. Correlation coefficients of 0.4-0.6 and 0.6-0.7 are attained for near-bottom and near-surface current velocities, respectively. Overall, the comparison indicates agreement between the modelled and observed super-diurnal variability, and provides some confidence that the model can be used to gain further insight into the spatial and temporal variability of the processes of interest.

3.2 Super-diurnal effects of the land-sea breeze

The shaded time in Figure 6 denotes a 24 hour period characterised by the onset of strong diurnal variability in surface temperature, both in the observations and in the model. The evolution of the spatial variability in sea surface temperature (SST) and surface currents over St Helena Bay for this 24 hour period is further assessed in Figure 7. It is worth noting that the shown period displays some typical features of the region, as documented in the literature. For instance, upwelling along the coastline south of St Helena Bay sets up a shelf edge front and the associated Goodhope Jet, a strong equatorward current in geostrophic balance with the cross-shore pressure gradient (Strub et al., 1998; Veitch et al., 2018). North of Cape Columbine, the Goodhope Jet tends to bifurcate due to shelf widening, resulting in offshore and alongshore components (Shannon and Nelson, 1996; Veitch et al., 2018), the latter corresponding to the Columbine Jet which effectively defines a dynamic boundary between the nearshore waters of St Helena Bay and those offshore (Lamont et al., 2015). Also evident in the model is upwelling along a narrow belt on the eastern periphery of the bay and the formation of an inner shelf upwelling front (Jury, 1985; Taunton-Clark, 1985). Mean surface flow on the inner shelf during active upwelling is typically equatorward, in agreement with observations (Fawcett et al., 2008).

Figure 7 highlights the super-diurnal variability in surface currents and temperature embedded within these features, particularly within St Helena Bay. Here, the oscillatory nature of the surface currents is clearly evident, whereby the cross-shore component in the surface current is offshore at night, turning to onshore during the day. This phasing is tied to that of the land-sea breeze, indicating they are driven primarily by the diurnal-inertial resonance phenomenon. The surface currents drive the outcropping of the inner shelf upwelling front within St Helena Bay during the night (e.g. refer to the 08:30 time-step), however six hours later the newly upwelled waters are once again subducted by onshore surface currents. These processes contribute to temperature variability of greater than 5°C within the inner shelf regions of St Helena Bay over the considered 24 hour period.

Given this stark difference between day- and night-time surface temperature for this particular 24 hour period, it is prudent to assess the persistence of this effect. This is achieved by computing day- and night-time climatologies of SST, considering only the nominally upwelling months of October to March. Figure 8 presents this analysis for the GHRSST-SEVIRI satellite data over the 7 year duration of the model integration, while that of the realistically forced model is presented in Figure 9. The satellite data confirm that indeed the observed day-time SST's are on average warmer than those at night, and that the effect increases towards the coast, where the difference exceeds 1°C (Figure 8C). A similar

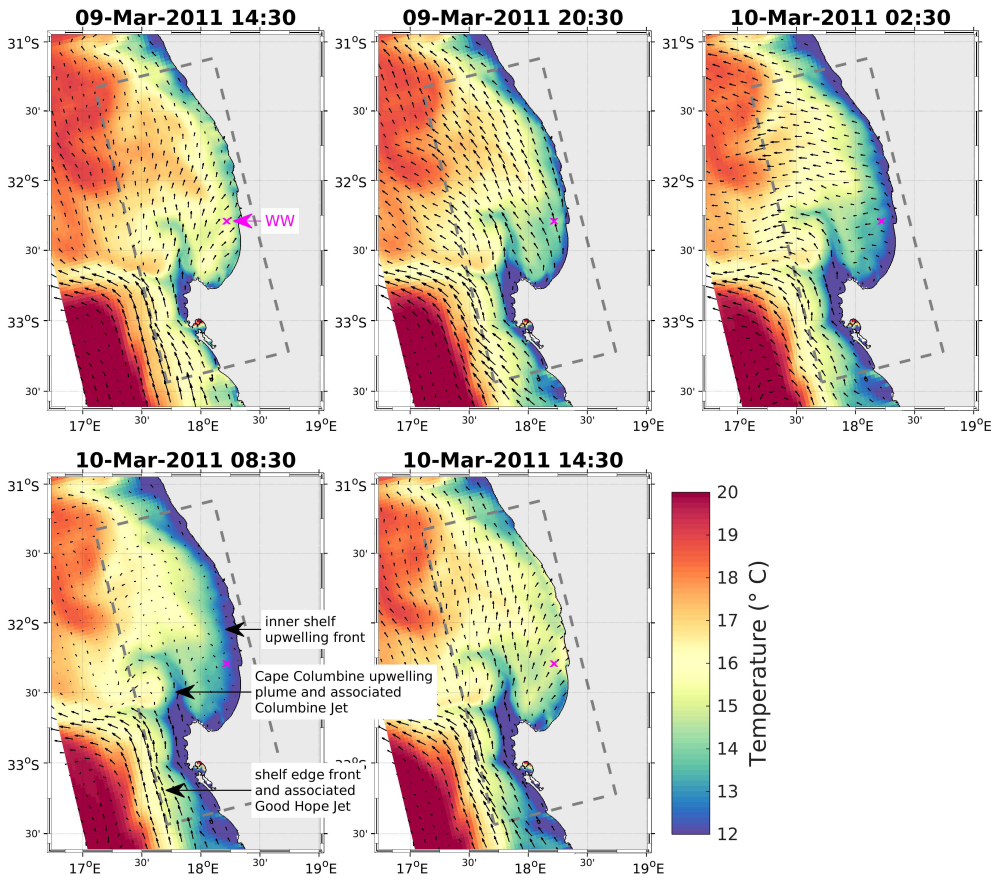

FIGURE 7
6 hourly snapshots of modelled SST and surface current vectors over an upwelling event, demonstrating the outcropping and subduction of the inner shelf upwelling front over a day in response to inertial motions. The Wirewalker observations (denoted by the magenta cross) capture the strong diurnal variability in SST, as shown in Figure 6. Times are local time, UTC+2.

pattern is seen in the model, although the effect is more exaggerated, particularly in the nearshore region of St Helena Bay where the mean day-night difference in SST exceeds 2°C over much of the bay (Figure 9C). SST's are also notably higher in the satellite data than in the model (Figures 8A, B vs Figures 9A, B). It should however be noted that flagging techniques used to 'de-cloud' thermal infrared satellite data are known to contribute to large warm biases in upwelling systems by attributing cold upwelled water as missing data (Dufois et al., 2012; Smit et al., 2013; Meneghesso et al., 2020; Carr et al., 2021). Our high frequency model output is therefore seen as a preferred reference for assessing diurnal variability in SST's over the area of interest.

Although a strong day-night signal is evident in Figure 9C, it isn't clear how much of this signal is due to the movement of the front by the diurnal-inertial oscillations versus surface heat fluxes driven by solar irradiance (the land-sea breeze is itself a product of diurnal heating/cooling over the land and ocean). To distil these two effects we make use of the 7 year simulation forced with τ^{daily} (Table 1), which maintains hourly heat fluxes but removes the diurnal-inertial oscillations. The mean day-night difference in SST for this simulation is shown in Figure 9D, while the effect of the diurnal-inertial oscillations is estimated by subtracting this from the overall signal (Figure 9E). The influence of the land-sea breeze on the diurnal fluctuations in SST is shown to be particularly enhanced in the nearshore region of St Helena Bay, where the mean difference exceeds 1°C. Diurnal warming due to solar irradiance is also enhanced in the southern extent of the bay, leading to a pronounced combined effect.

3.3 Event-scale diapycnal mixing

One of the main implications of the high amplitude diurnal-inertial oscillations is their impact on vertical mixing. We now present the results from an experiment specifically designed to examine these processes over an upwelling event accompanied by an enhanced land-sea breeze (refer to Section 2.5 for the experiment setup). Figure 10 shows the temporal evolution of the cross-shore component of velocity and the passive tracer at a location in the centre of St Helena Bay ('P' in Figure 3). The comparison of the simulations forced with both $\tau^{daily+ac}$ (left panels) and τ^{daily} (right panels) clearly demonstrates how the inclusion of τ^{ac} leads to shear-driven deepening of the thermocline primarily in response to the diurnal-inertial resonance phenomenon and the associated injection of subsurface waters into the surface layer, all of which are embedded in the sub-diurnal upwelling dynamics.

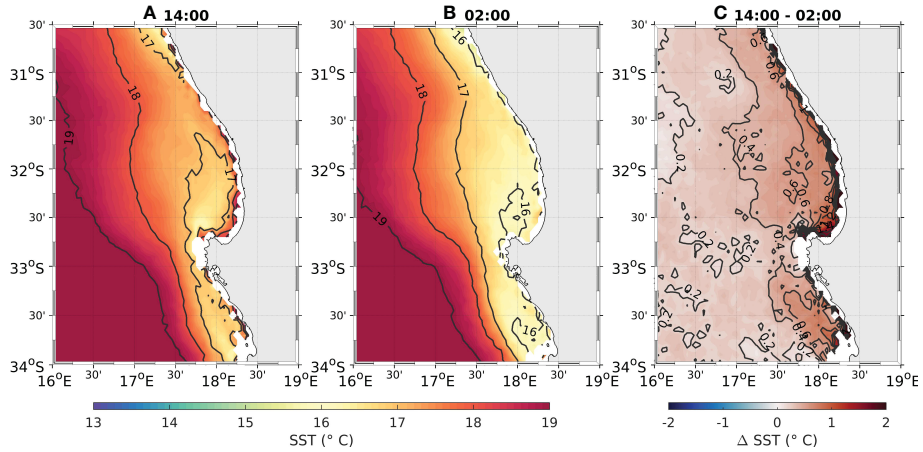

FIGURE 8
Day- and night-time climatologies of SST derived from GHRSST-SEVIRI satellite data for the 'upwelling' months of October-March. **(A)** Climatology computed from data at 14:00. **(B)** Climatology computed from data at 02:00. **(C)** The difference between climatologies computed at 14:00 and 02:00. Times are local time, UTC+2.

Figure 10 also indicates the depth of the 12°C isotherm, which reveals a complex pattern of thermocline displacements when land-sea breeze forcing is included in the model. These thermocline displacements can be interpreted from the Hovmöller diagram shown in Figure 11A. The model reveals how the super-diurnal onshore and offshore advection of the surface layer generates large thermocline displacements at both the landward and offshore extents of the bay. Offshore surface flow is associated with upward thermocline displacements at the land boundary and downward thermocline displacements at the offshore extent of the bay, and vice versa for onshore surface flow. These forced diurnal vertical motions trigger offshore and onshore propagating internal waves which are evanescent, given that the latitude is poleward of 30°S (Zhang et al., 2010). In addition to the expected thermocline pumping and internal wave generation at the land boundary (Millot and Crepon, 1981; Fearon et al., 2022), the results point to an additional offshore source of internal wave generation associated with the Cape Columbine upwelling plume, where thermocline pumping is in fact larger than at the land boundary. This is attributed largely to the spatial heterogeneity in the depth of the Ekman layer which changes abruptly at the upwelling plume (see Figure 3B) and introduces large spatial variability in the forced diurnal-inertial surface currents. Enhanced vorticity associated with the alongshore jet would further serve to introduce spatial variability in the diurnal-inertial motions in this region (Weller, 1982; Klein et al., 2004; Elipot et al., 2010). The spatial variability in the forced diurnal-inertial oscillations drive convergences and divergences in the surface flow which are responsible for the thermocline pumping and internal waves seen in the model.

Figure 11B illustrates the development of enhanced diapycnal mixing across St Helena Bay due to the inclusion of super-diurnal winds (refer to Equation 2 for how this diagnostic is computed). We note that the relative contribution of the locally forced oscillations and the evanescent internal waves on the cumulative diapycnal mixing can be difficult to separate, although we would expect mixing to be largely driven by the locally forced oscillations, while the internal waves are expected to play a secondary role (Fearon et al., 2022). The region of maximum enhanced diapycnal mixing is shown to be associated with the shallow stratified surface layer within St Helena Bay. Within this region, the cumulative diapycnal mixing varies considerably at time-scales of less than a day, in response to the onshore and offshore advection of the surface layer, and the large thermocline displacements. Regions of the largest enhancement of cumulative diapycnal mixing are typically associated with large downward thermocline displacements, given that C_s represents the integration of C from the 12°C isotherm to the surface. This super-diurnal variability is embedded within the sub-diurnal offshore advection of the region of maximum enhanced mixing associated with the surface layer. The spatial variability in enhanced diapycnal mixing is further explored in Figure 12, which presents the increase in C_s due to the inclusion of land-sea breeze forcing, averaged over the fifth day of the simulation (29-30 January 2007). The analysis clearly identifies a region of particularly enhanced diapycnal mixing relative to the surrounding areas, associated with the shallow surface layer which had formed within St Helena Bay (Figure 3).

3.4 Sub-diurnal effects of the land-sea breeze

We now consider how the presented super-diurnal processes may affect the mean state of the vertical water column structure and circulation over the area of interest. This is achieved by comparing 7 year climatologies for simulations forced with τ^{daily} and $\tau^{daily+ac}$, thereby isolating the effect of the diurnal anticlockwise rotary component of the wind stress (τ^{ac}) (Table 1). Climatological comparisons are provided in Figures 13, 14 for upwelling and relaxation wind regimes, respectively (refer to Section 2.4 for how upwelling and relaxation wind regimes are defined for this analysis).

The inclusion of τ^{ac} during upwelling conditions is shown to drive a notable deepening of the thermocline within St Helena Bay

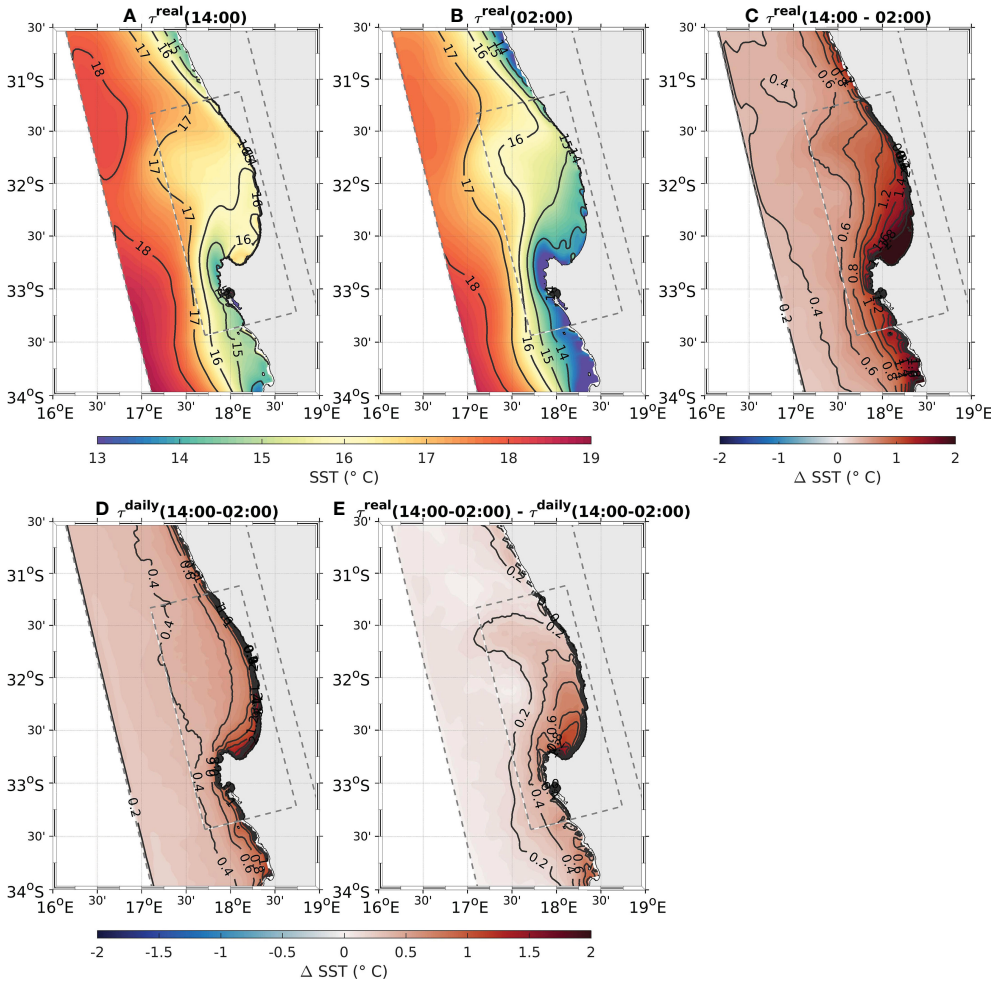

FIGURE 9
Day- and night-time climatologies of modelled SST for the 'upwelling' months of October-March. **(A)** SST climatology at 14:00 from the model forced by τ^{real}. **(B)** SST climatology at 02:00 from the model forced by τ^{real}. **(C)** Difference in day- and night-time SST climatologies from the model forced by τ^{real}. **(D)** Difference in day- and night-time SST climatologies from the model forced by τ^{daily}. **(E)** C - D, isolating the effect of the super-diurnal component of the winds on day- and night-time SST climatologies. Times are local time, UTC+2.

(Figure 13B), consistent with the effects of enhanced vertical mixing driven by the diurnal-inertial oscillations. For example, at an offshore distance of 30 km, the mean 12°C isotherm depth is ~14 m for the simulation forced with τ^{daily}, increasing to a depth of ~21 m for the simulation forced with $\tau^{daily+ac}$. The net warming of the entire water column in the inner shelf region (right panel of Figure 13B) however points to effects which can't be explained purely by the vertical exchange of surface and subsurface waters. Fearon et al. (2022) used a 2D model to show how a deepened thermocline leads to a reduction in the offshore advection of the surface layer, thereby maintaining the upwelling front closer to the coast and driving a net warming of nearshore waters. This is invoked as an explanation for the nearshore warming seen in the 3D model during upwelling conditions.

Figure 13C reveals mean alongshore currents which are largely geostrophically driven, considering the cross-shore structure of the isotherms (Figure 13B). The strong equatorward current offshore of St Helena Bay (mean surface current >0.4 m s^{-1} at an offshore distance of ~55 km) corresponds to the Columbine Jet, in geostrophic balance with the cross-shore pressure gradient set up by the Columbine upwelling plume. The model also indicates an equatorward mean flow associated with the inner shelf upwelling front (<~15 km offshore), in agreement with observations (Fawcett et al., 2008), while a poleward mean flow is associated with the offshore extent of the shallow surface layer inside St Helena Bay (refer to depths of ~10-30 m and offshore distances of ~20-35 km). Mean near-bottom currents within St Helena Bay are shown to be poleward, which may in part be linked to barotropic continental shelf waves (Holden, 1987), cyclonic barotropic flow in the lee of Cape Columbine (Penven et al., 2000), and negative wind stress curl through the Sverdrup relation (Veitch et al., 2010). The inclusion of land-sea breeze forcing (τ^{ac}) is shown to amplify the geostrophically driven alongshore currents associated with either end of the shallow surface layer within St Helena Bay. For example, the mean equatorward currents associated with the inner shelf upwelling front are roughly doubled in the area of maximum impact, increasing from 0.09 m s^{-1} to 0.17 m s^{-1} (right panel of Figure 13C). The mean poleward flow at the offshore end of the surface layer increases from 0.02 m s^{-1} to 0.05 m s^{-1} in the area of maximum impact. These impacts are consistent with a

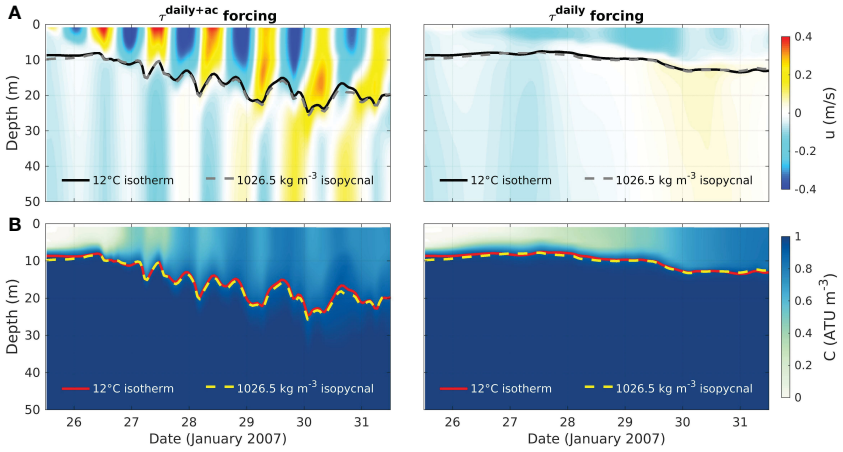

FIGURE 10
Temporal evolution of the model solution for the cross-shore component of velocity **(A)** and the passive tracer **(B)** over the upper 50 m of the water column at a location in the centre of St Helena Bay ('P' in Figures 3, 12). The model is initialised on 25 January 2007 (Figure 3) and forced with both $\tau^{daily+ac}$ (left panels) and τ^{daily} (right panels).

locally deepened thermocline, which serves to steepen cross-shore pressure gradients and therefore alongshore geostrophic flow.

During periods of wind relaxation, the inclusion of land-sea breeze forcing (τ^{ac}) is shown to drive cooler SST's over most of the model domain (right panel of Figure 14A). This effect is particularly evident within the nearshore regions of St Helena Bay, where the mean difference between the two simulations exceeds 2°C. Inspection of the vertical water column structure (Figure 14B) reveals that the lower SST's driven by τ^{ac} are compensated by warmer subsurface waters due to a deeper thermocline, consistent with the effects of enhanced diapycnal mixing by the diurnal-inertial oscillations. It is interesting to note that the net warming of the nearshore water column in response to τ^{ac} during upwelling periods (Figure 13B) is not at all present during periods of relaxation. This further supports the suggested mechanism for the net warming to be linked to reduced offshore advection of the surface layer, which would be largely absent during relaxation of equatorward winds.

Periods of wind relaxation are associated with a weakened Columbine Jet, and a poleward mean flow within St Helena Bay, again consistent with inner shelf observations (Fawcett et al., 2008). During these periods, the only notable impact of τ^{ac} on the mean flow is again on the inner shelf, where a geostrophically driven poleward flow is associated with the subduction of the thermocline. In this case, the deepened thermocline due to the inclusion of τ^{ac} serves to reduce the cross-shore pressure gradients and weakens this poleward flow.

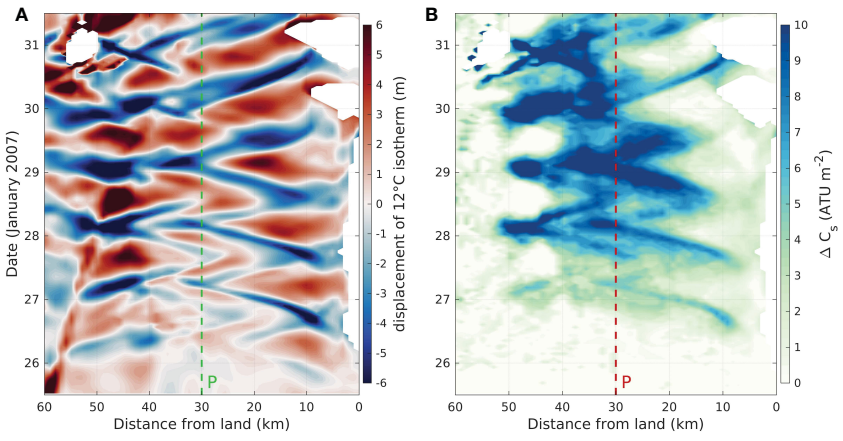

FIGURE 11
(A) Hovmöller diagram of the displacement of the 12°C isotherm from the daily running average isotherm for the model forced with $\tau^{daily+ac}$. Blue (red) denotes downward (upward) displacement of the thermocline. **(B)** Hovmöller diagram of the increase in the passive tracer integrated from the 12°C isotherm to the surface (C_s) due to the inclusion of τ^{ac} (refer to Equation 2). The initial condition for both simulations is shown in Figure 3. The section used to compute the Hovmöller diagrams is shown in Figure 12. The missing data in the model output corresponds to the outcropping of the 12C isotherm.

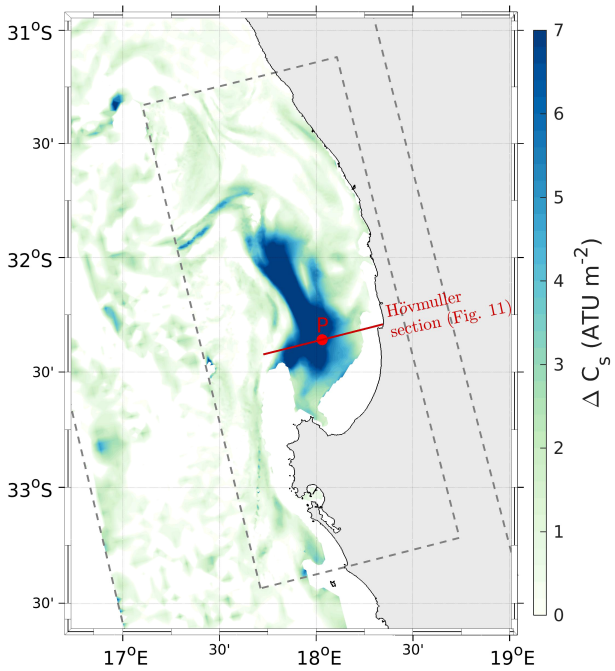

FIGURE 12
Increase in the passive tracer integrated from the 12°C isotherm to the surface (C_s) due to the inclusion of τ^{ac}, averaged over the fifth day of the simulation (refer to Equation 2). The missing data in the model output corresponds to the outcropping of the 12°C isotherm.

4 Discussion and conclusions

We have used a validated 3D model of the southern Benguela upwelling system to explore the influence of the land-sea breeze on temperature and current variability of the system across multiple time-scales. An over-arching finding, common to all of the presented analyses, is that the effects of land-sea breeze forcing are particularly enhanced within the inner shelf region of St Helena Bay, which is also the most productive region in the southern Benguela (Weeks et al., 2006; Demarcq et al., 2007). This is consistent with previous observational studies which have noted the ubiquitous presence of diurnal-inertial current variability in the nearshore regions of the bay (Fawcett et al., 2008; Lucas et al., 2014). Fearon et al. (2020) hypothesised that St Helena Bay possesses a combination of three physical characteristics which might promote a locally enhanced forced response to the land-sea breeze. Firstly, the bay is at a latitude of ~32.5°S (inertial period of ~22 hr), allowing for near-resonance between the diurnal periodicity of the land-sea breeze and the inertial response of the ocean. Secondly, the diurnal anticyclonic rotary component of the winds, which can be used as a first order estimate of the forced diurnal-inertial currents (Fearon et al., 2020), is locally enhanced over St Helena Bay. This is evident in the wind forcing over our event-scale mixing experiment (Figure 3) as well as from a seasonal climatology of this variable (Fearon et al., 2020). Thirdly, the well-known retentive circulation within the bay allows for the local development of a shallow stratified surface layer, which results in water masses which are distinct from those offshore (Lamont et al., 2015). This is an important consideration in the context of this study, as shallower surface layers are associated with larger amplitude diurnal-inertial oscillations and enhanced mixing. The confluence of these physical attributes are invoked as an explanation for the intensification of land-sea breeze-driven effects within St Helena Bay, as observed in the model.

An important finding from the model is the extent to which day- vs night-time sea surface temperatures (SST's) vary over the model domain. The effect is again particularly stark within St Helena Bay, where modelled mean day-time SST's are more than 2°C warmer than those at night over the nominally upwelling months of October to March. Diurnal solar irradiance does indeed contribute to this signal, particularly during conditions of low winds and high solar irradiance (Stuart-Menteth et al., 2003), however the model indicates that within St Helena Bay more than half of the signal can be attributed to the horizontal advection of strong SST gradients by diurnal-inertial surface oscillations forced by the land-sea breeze (Figure 9E). This reveals a picture of strong super-diurnal advection of water masses within the bay, which may pose challenges for observation systems in the region. *In-situ* observations aimed at understanding the physical and biological functioning of the system rarely capture this high-frequency variability; the observations of (Lucas et al., 2014) being a notable exception. For example, daily *in-situ* observations of coastal seawater temperature have provided a useful basis for computing monthly coastal temperature climatologies along the entire South African coastline (Smit et al., 2013). Our results however suggest that the time of day of these observations could play a large role in the outcome of the analysis and should be considered if the data are to be used as a ground truth for mean coastal SST's. There are also implications for the ecological monitoring of the region. The biogeochemical conditions observed with coarse seasonal monitoring and long transects may measure the response to physical features that occurred in a different location and have been advected to the sampling location by the movement of the front.

Our results have further revealed an indirect effect of land-sea breeze-driven vertical mixing, through its effect on cross-shore pressure gradients and their associated geostrophically-driven alongshore flows. The results during upwelling favourable conditions (Figure 13C) are in agreement with observations in the Coastal Southern California Bight which indicate that diurnal-inertial resonance can lead to steeper cross shore isotherms and intensified alongshore flows (Nam and Send, 2013). The near-coastal poleward current set up by the subduction of the thermocline during relaxation events is however shown to be weakened by a deeper thermocline induced by diurnal-inertial resonance (Figure 14C). These impacted alongshore flows may be important with respect to their role in setting up the retentive sub-inertial circulation of St Helena Bay, important both for primary productivity and their role in creating a nursery ground for several fish species (Shelton and Hutchings, 1982; Huggett et al., 2003; Ragoasha et al., 2019). Impacts on sub-diurnal flow are however shown to be limited to shallow surface layer within St Helena Bay, where vertical mixing effects are greatest. Neither the equatorward Columbine Jet nor the poleward near-bottom currents are notably impacted by the land-sea breeze forcing.

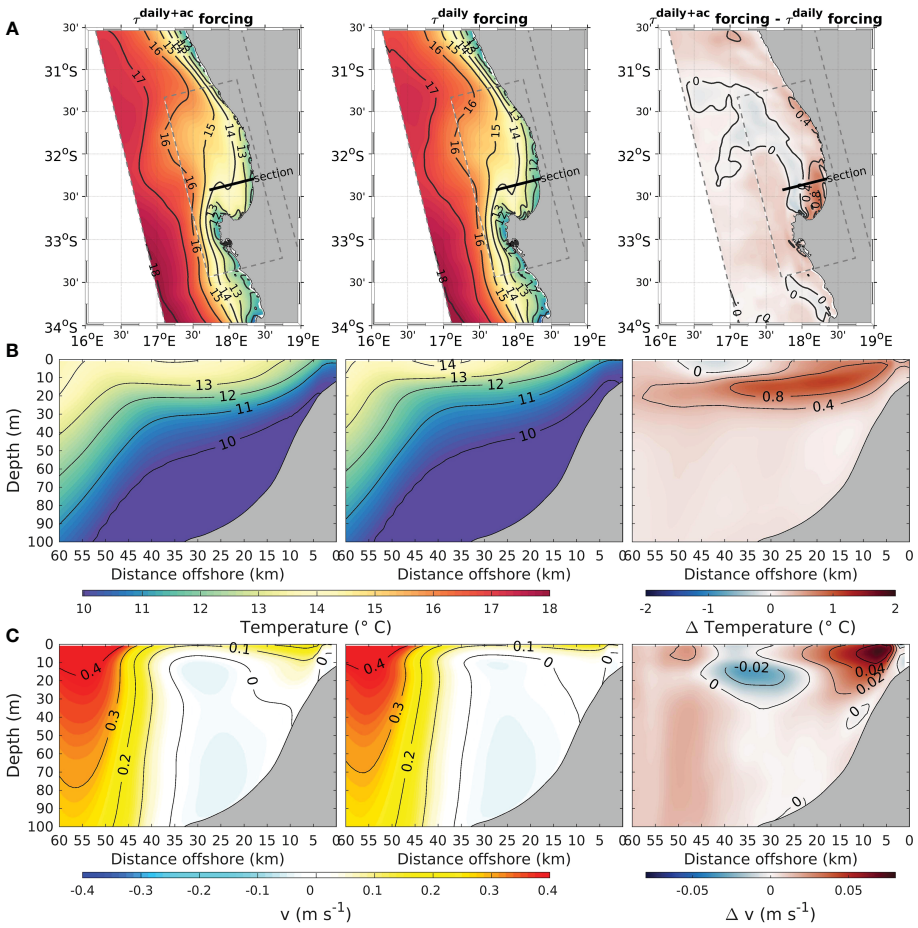

FIGURE 13
Impact of the diurnal anticlockwise rotary component of the wind stress (τ^{ac}) on the mean temperature and alongshore currents during upwelling conditions. The left panels show results for the simulation forced with $\tau^{daily+ac}$, the middle panels show results for the simulation forced with τ^{daily}, while the right panels show the difference between the two, highlighting the impact of τ^{ac}. **(A)** Climatology of SST. **(B)** Climatology of temperature for a vertical section through St Helena Bay (the location of the section is shown in a). **(C)** Climatology of the equatorward (i.e. alongshore) component of horizontal velocity (*v*) for a vertical section through St Helena Bay.

The fact that St Helena Bay is also a hotspot for productivity leads to speculation as to the role which the land-sea breeze may play in the overall productivity of the system. Based on nearshore observations, Lucas et al. (2014) argued that shear-driven nutrient flux to the surface layer, driven by diurnal-inertial oscillations forced by the land-sea breeze, was likely of first order importance in phytoplankton bloom phenomenology within St Helena Bay. Our event-scale mixing experiment used a subsurface tracer as a proxy for subsurface nutrients, revealing how these subsurface waters are mixed to the surface in response to land-sea breeze forcing (Figure 12), providing further support for this hypothesis. The persistence of shear-driven vertical mixing in this region is also evident in our 7 year experiment, which highlights how the land-sea breeze maintains a deepened thermocline, during periods of both active upwelling (Figure 13B) and wind relaxation (Figure 14B). A potential indirect impact on productivity may lie in the enhanced retention of the upwelling front, given that a deepened thermocline serves to reduce sub-inertial offshore advection of the surface layer (Fearon et al., 2022). As already emphasised, the retentive properties of the bay are commonly cited as a leading cause for enhanced productivity in this region. Our model indicates that the land-sea breeze drives a warming of nearshore waters during periods of active upwelling (Figure 13B), which we attribute to the retention of the upwelling front. The event-scale mixing experiment has further revealed how the land-sea breeze drives large thermocline displacements within St Helena Bay (Figure 11A), notably in the vicinity of the inner shelf upwelling front where productivity is highest. These super-diurnal vertical displacements, and their timing with respect to sunlight availability, are likely to play a role in the event-scale phytoplankton bloom dynamics.

A notable feature of the ocean response to land-sea breeze forcing in St Helena Bay is the introduction of strong subsurface oscillations (Figure 6), which would significantly elevate bed stresses in the nearshore regions of the bay. This is likely to play an important role in the re-suspension of bed sediments, which would introduce regenerated nutrients into subsurface waters. Indeed, observations within St Helena Bay confirm that on-shelf trapping of remineralised nutrients enhances the nutrient pool in the subsurface waters of the bay (Flynn et al., 2020). The elevated bed stresses in the nearshore waters of the bay would ultimately play a role in the fate of organic

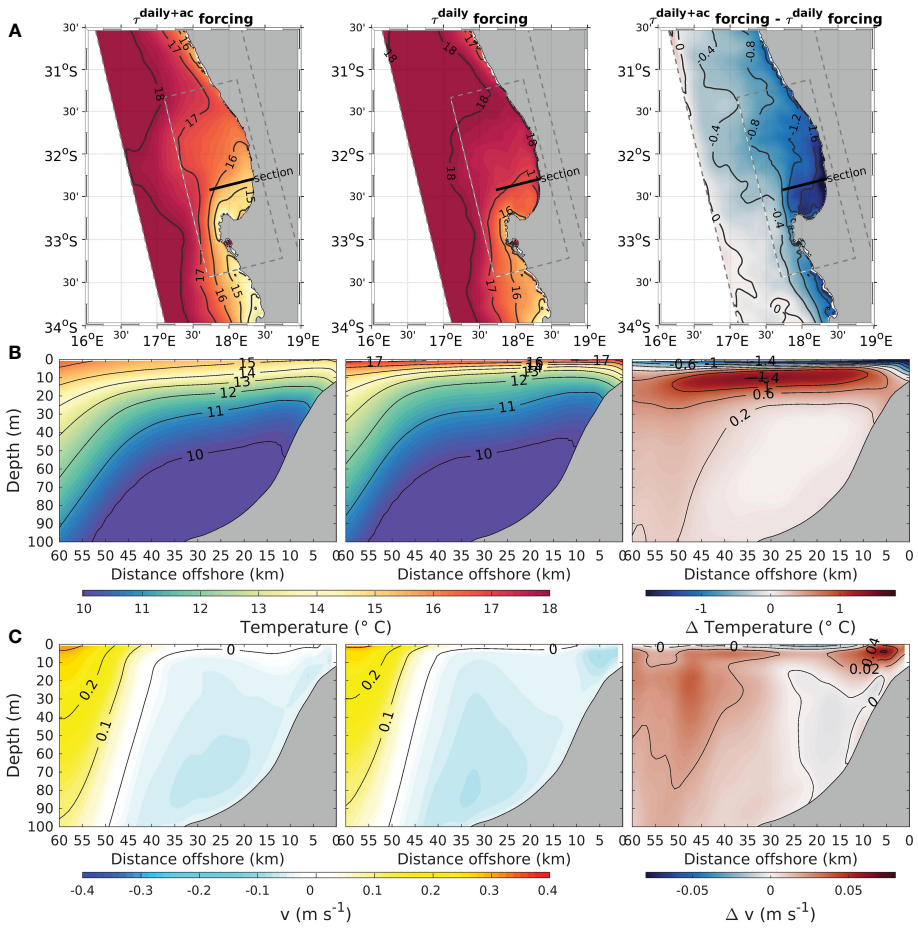

FIGURE 14
As per Figure 13 but for relaxation conditions.

matter from bloom events, which tends to settle out along a narrow terrigenous mud belt (Monteiro and Roychoudhury, 2005).

If the land-sea breeze is indeed implicated in enhanced productivity within St Helena Bay, its potential role in the development of Harmful Algal Blooms (HABs) cannot be overlooked. HABs in St Helena Bay are typically associated with the decay of high biomass non-toxic blooms within the shallow nearshore environment, leading to anoxia in bottom waters through microbial respiration (Pitcher and Probyn, 2011; Pitcher et al., 2014). Conditions favourable for the development of HABs are associated with periods of sustained relaxation of equatorward winds, where the retentive properties of the bay in conjunction with solar irradiance allow for the development of a warm shallow stratified surface layer which favours the development of high biomass dinoflagellate blooms (Pitcher et al., 1998; Pitcher and Nelson, 2006; Fawcett et al., 2007). Negative impacts of HABs in St Helena Bay can be severe, including mass mortality of fish, shellfish, marine mammals, seabirds and other animals, with significant commercial implications (e.g. Cockcroft et al., 2000). Our results indicate that even though relaxation events are generally associated with a lower amplitude land-sea breeze (Fearon et al., 2020), the land-sea breeze serves to modulate the formation of the shallow surface layer within St Helena Bay through the entrainment of subsurface waters (Figure 14B). This could provide an important contribution of nutrients to the surface waters, thereby promoting the accumulation of high-biomass blooms largely responsible for HAB development.

Finally, the results of this study suggest that physical and biogeochemical models of the study area may be improved through a more accurate representation of land-sea breeze effects. This is highlighted by the fact that our model configuration forced with hourly averaged winds significantly outperforms the configuration forced with daily averaged winds (Supplementary Tables S1, S2). Climate scale models typically exclude land-sea breeze effects, which suggests a limitation in their ability to predict long-term effects of climate change on the nearshore dynamics of the system. The spatial variability in the land-sea breeze can be considerable (e.g. Figure 3C), indicating that both the temporal and spatial resolution of the atmospheric forcing should be sufficiently high to properly represent the forcing mechanism. Similarly, ocean models are required to be of sufficient spatial resolution to capture the forced and internal wave response to the land-sea breeze. While the ocean model configuration presented here appears to resolve the high frequency ocean response reasonably well (Figure 6), it should be stressed that the model accuracy is dependent on the adopted vertical

turbulence closure scheme. We employed the GLS k-ϵ turbulent closure scheme in this study, as CROCO's default LMD-KPP scheme resulted in an over-estimation of vertical mixing. It is suggested that St Helena Bay represents a study area which could be used to test various vertical mixing parameterisations in the context of the development of shallow stratified surface layers in retention zones of upwelling systems. It furthermore remains an open question as to the importance of solving the non-hydrostatic processes induced by the land-sea breeze, which were not considered in this study.

Data availability statement

The CROCO configuration files used to generate the model output analysed in this study are available via the following DOI: https://doi.org/10.5281/zenodo.7947550. The raw data supporting the conclusions of this article will be made available by the authors, without undue reservation.

Author contributions

GF, SH, and MV contributed to conception and design of the study. GF set up the model experiments, ran the simulations, performed the analysis and wrote the first draft of the manuscript. GC assisted with technical aspects of the model setup. All authors contributed to the article and approved the submitted version.

Funding

This research benefited from funding from a private charitable trust as part of the Whales and Climate Research Program (https://www.whalesandclimate.org/) and from the European Union's Horizon 2020 research and innovation programme under grant agreement No 862923. GF further acknowledges financial assistance from the South African Environmental Observation Network (SAEON), as well mobility grants from LabexMER and the French Embassy in South Africa.

Acknowledgments

This study benefited from various previously published *in-situ* datasets which proved extremely useful for the validation of the model. To this end, we thank the South African Department of Forestry, Fisheries and the Environment (DFFE) for the provision of the SHBML data, Grant Pitcher (Fisheries Management, DFFE) for providing the Elands Bay mooring data, and Drew Lucas (Scripps Institution of Oceanography) for providing the Wirewalker and ADCP data. We thank the Climate Systems Analysis Group (CSAG) for the provision of their WRF atmospheric model output and the South African Navy Hydrographic Office (SANHO) for the provision of bathymetric data. The study benefited from computational facilities provided by the University of Cape Town's ICTS High Performance Computing team (hpc.uct.ac.za).

Conflict of interest

The authors declare that the research was conducted in the absence of any commercial or financial relationships that could be construed as a potential conflict of interest.

Publisher's note

Supplementary material

The Supplementary Material for this article can be found online at: https://www.frontiersin.org/articles/10.3389/fmars.2023.1186069/full#supplementary-material

References

Aguiar-Gonzalez, B., Rodrıguez-Santana, A., Cisneros-Aguirre, J., and Martınez-Marrero, A. (2011). Diurnal–inertial motions and diapycnal mixing on the Portuguese shelf. *Continental Shelf Res.* 31, 1193–1201. doi: 10.1016/j.csr.2011.04.015

Bonicelli, J., Moffat, C., Navarrete, S. A., Largier, J. L., and Tapia, F. J. (2014). Spatial differences in thermal structure and variability within a small bay: interplay of diurnal winds and tides. *Continental Shelf Res.* 88, 72–80. doi: 10.1016/j.csr.2014.07.009

Carr, M., Lamont, T., and Krug, M. (2021). Satellite Sea surface temperature product comparison for the southern African marine region. *Remote Sens.* 13 (7), 1244. doi: 10.3390/rs13071244

Chavez, F. P., and Messie, M. (2009). A comparison of Eastern boundary upwelling ecosystems. *Prog. Oceanogr.* 83, 80–96. doi: 10.1016/j.pocean.2009.07.032

Cockcroft, A. C., Schoeman, D. S., Pitcher, G. C., Bailey, G. W., and Van Zyl, D. L. (2000). "A mass stranding, orwalk out'of west coast rock lobster, jasus lalandii, in elands bay, south Africa: causes, results, and implications," in *Biodiversity crisis and Crustacea* (United Kingdom: Taylor & Francis), 673–688.

Debreu, L., Marchesiello, P., Penven, P., and Cambon, G. (2012). Two-way nesting in split-explicit ocean models: algorithms, implementation and validation. *Ocean Model.* 49–50, 1–21. doi: 10.1016/j.ocemod.2012.03.003

Demarcq, H., Barlow, R., and Hutchings, L. (2007). Application of a chlorophyll index derived from satellite data to investigate the variability of phytoplankton in the benguela ecosystem. *Afr. J. Mar. Sci.* 29, 271–282. doi: 10.2989/AJMS.2007.29.2.11.194

Dey, S. P., Vichi, M., Fearon, G., Seyboth, E., Findlay, K. P., Meynecke, J.-O., et al. (2021). Oceanographic anomalies coinciding with humpback whale super-group occurrences in the southern benguela. *Sci. Rep.* 11, 20896. doi: 10.1038/s41598-021-00253-2

Dufois, F., Penven, P., Peter Whittle, C., and Veitch, J. (2012). On the warm nearshore bias in pathfinder monthly SST products over Eastern boundary upwelling systems. *Ocean Model.* 47, 113–118. doi: 10.1016/j.ocemod.2012.01.007

Elipot, S., Lumpkin, R., and Prieto, G. (2010). Modification of inertial oscillations by the mesoscale eddy field. *J. Geophys. Res.: Oceans* 115 (C9). doi: 10.1029/2009JC005679

Fairall, C. W., Bradley, E. F., Hare, J. E., Grachev, A. A., and Edson, J. B. (2003). Bulk parameterization of air–Sea fluxes: updates and verification for the COARE algorithm. *J. Climate* 16, 571–591. doi: 10.1175/1520-0442(2003)016h0571:BPOASFi2.0.CO;2

Fairall, C. W., Bradley, E. F., Rogers, D. P., Edson, J. B., and Young, G. S. (1996). Bulk parameterization of air-sea fluxes for tropical ocean-global atmosphere coupled-ocean atmosphere response experiment. *J. Geophys. Res.: Oceans* 101, 3747–3764. doi: 10.1029/95JC03205

Fawcett, A., Pitcher, G., Bernard, S., Cembella, A., and Kudela, R. (2007). Contrasting wind patterns and toxigenic phytoplankton in the southern benguela upwelling system. *Mar. Ecol. Prog. Ser.* 348, 19–31. doi: 10.3354/meps07027

Fawcett, A., Pitcher, G., and Shillington, F. (2008). Nearshore currents on the southern namaqua shelf of the benguela upwelling system. *Continental Shelf Res.* 28, 1026–1039. doi: 10.1016/j.csr.2008.02.005

Fearon, G., Herbette, S., Veitch, J., Cambon, G., Lucas, A. J., Lemarie, F., et al. (2020). Enhanced vertical mixing in coastal upwelling systems driven by diurnal-inertial resonance: numerical experiments. *J. Geophys. Res.: Oceans* 125 (9). doi: 10.1029/2020JC016208

Fearon, G., Herbette, S., Veitch, J., Cambon, G., and Vichi, M. (2022). The influence of the land–sea breeze on coastal upwelling systems: locally forced vs internal wave vertical mixing and implications for thermal fronts. *Ocean Model.* 176, 102069. doi: 10.1016/j.ocemod.2022.102069

Flynn, R. F., Granger, J., Veitch, J. A., Siedlecki, S., Burger, J. M., Pillay, K., et al. (2020). On-shelf nutrient trapping enhances the fertility of the southern benguela upwelling system. *J. Geophys. Res.: Oceans* 125, e2019JC015948. doi: 10.1029/2019JC015948

García-Reyes, M., Sydeman, W. J., Black, B. A., Rykaczewski, R. R., Schoeman, D. S., Thompson, S. A., et al. (2013). Relative influence of oceanic and terrestrial pressure systems in driving upwelling-favorable winds. *Geophys. Res. Lett.* 40, 5311–5315. doi: 10.1002/2013GL057729

Gille, S. T., Lee, S. M., and Llewellyn Smith, S. G. (2003). Measuring the sea breeze from QuikSCAT scatterometry. *Geophys. Res. Lett.* 30 (3). doi: 10.1029/2002GL016230

Gille, S. T., Llewellyn Smith, S. G., and Statom, N. M. (2005). Global observations of the land breeze. *Geophys. Res. Lett.* 32 (5). doi: 10.1029/2004GL022139

Haney, R. L. (1991). On the pressure gradient force over steep topography in sigma coordinate ocean models. *J. Phys. Oceanogr.* 21, 610–619. doi: 10.1175/1520-0485(1991)021h0610:OTPGFOi2.0.CO;2

Holden, C. J. (1987). Observations of low-frequency currents and continental shelf waves along the west coast of south Africa. *South Afr. J. Mar. Sci.* 5, 197–208. doi: 10.2989/025776187784522360

Huggett, J., Freon, P., Mullon, C. , and Penven, P. (2003). Modelling the transport success of anchovy *Engraulis encrasicolus* eggs and larvae in the southern benguela:: the effect of spatio temporal spawning patterns. *Mar. Ecol. Prog. Ser.* 250, 247–262. doi: 10.3354/meps250247

Hyder, P., Simpson, J. H., and Christopoulos, S. (2002). Sea-Breeze forced diurnal surface currents in the thermaikos gulf, north-west Aegean. *Continental Shelf Res.* 22, 585–601. doi: 10.1016/S0278-4343(01)00080-2

Jackett, D. R., and Mcdougall, T. J. (1995). Minimal adjustment of hydrographic profiles to achieve static stability. *J. Atmos. Oceanic Technol.* 12, 381–389. doi: 10.1175/1520-0426(1995)674012h0381:MAOHPTi2.0.CO;2

Jury, M. R. (1985). Mesoscale variations in summer winds over the cape columbine [[/amp]]mdash; St Helena bay region, south Africa. *South Afr. J. Mar. Sci.* 3, 77–88. doi: 10.2989/025776185784461162

Kaplan, D. M., Largier, J. L., Navarrete, S., Guinez, R., and Castilla, J. C. (2003). Large Diurnal temperature fluctuations in the nearshore water column. *Estuar. Coast. Shelf Sci.* 57, 385–398. doi: 10.1016/S0272-7714(02)00363-3

Klein, P., Smith, S. L., and Lapeyre, G. (2004). Organization of near-inertial energy by an eddy field. *Q. J. R. Meteorol. Soc.* 130, 1153–1166. doi: 10.1256/qj.02.231

Lamont, T., Hutchings, L., van den Berg, M. A., Goschen, W. S., and Barlow, R. G. (2015). Hydrographic variability in the st. Helena bay region of the southern benguela ecosystem: hydrographic variability in the benguela. *J. Geophys. Res.: Oceans* 120, 2920–2944. doi: 10.1002/2014JC010619

Lennard, C., Hahmann, A. N., Badger, J., Mortensen, N. G., and Argent, B. (2015). Development of a numerical wind atlas for south Africa. *Energy Proc.* 76, 128–137. doi: 10.1016/j.egypro.2015.07.873

Lucas, A. J., Pitcher, G. C., Probyn, T. A., and Kudela, R. M. (2014). The influence of diurnal winds on phytoplankton dynamics in a coastal upwelling system off southwestern Africa. *Deep Sea Res. Part II: Topical Stud. Oceanogr.* 101, 50–62. doi: 10.1016/j.dsr2.2013.01.016

Marchesiello, P., Debreu, L., and Couvelard, X. (2009). Spurious diapycnal mixing in terrain-following coordinate models: the problem and a solution. *Ocean Model.* 26, 156–169. doi: 10.1016/j.ocemod.2008.09.004

Marchesiello, P., McWilliams, J. C., and Shchepetkin, A. (2001). Open boundary conditions for long-term integration of regional oceanic models. *Ocean Model.* 3, 1–20. doi: 10.1016/S1463-5003(00)00013-5

Marchesiello, P., McWilliams, J. C., and Shchepetkin, A. (2003). Equilibrium structure and dynamics of the California current system. *J. Phys. Oceanogr.* 33, 753–783. doi: 10.1175/1520-0485(2003)33h753:ESADOTi2.0.CO;2

Meneghesso, C., Seabra, R., Broitman, B. R., Wethey, D. S., Burrows, M. T., Chan, B. K. K., et al. (2020). Remotely-sensed L4 SST underestimates the thermal fingerprint of coastal upwelling. *Remote Sens. Environ.* 237, 111588. doi: 10.1016/j.rse.2019.111588

Millot, C., and Crepon, M. (1981). Inertial oscillations on the continentral shelf aof the gulf of lions - observations and theory. *J. Phys. Oceanogr.* 11, 639–657. doi: 10.1175/1520-0485(1981)011<0639:IOOTCS>2.0.CO;2

Monteiro, P. M. S., and Roychoudhury, A. N. (2005). Spatial characteristics of sediment trace metals in an eastern boundary upwelling retention area (St. Helena bay, south africa): a hydrodynamic–biological pump hypothesis. *Estuar. Coast. Shelf Sci.* 65, 123–134. doi: 10.1016/j.ecss.2005.05.013

Nam, S., and Send, U. (2013). Resonant diurnal oscillations and mean alongshore flows driven by Sea/Land breeze forcing in the coastal southern California bight. *J. Phys. Oceanogr.* 43, 616–630. doi: 10.1175/JPO-D-11-0148.1

Oceans and Coastal Research (2017). *Preliminary processed downcast CTD data from the St Helena bay monitoring line cruises from 2000 to 2017* (Cape Town, South Africa: Department of Forestry, Fisheries and the Environment).

OSISAF (2015). *GHRSST level 3C Atlantic subskin Sea surface temperature from the spinning enhanced visible and infrared imager (SEVIRI) on MSG-3 weather satellite (GDS2 version)* (CA, USA: NASA PO.DAAC). doi: 10.5067/GHSEV-3CO01

Penven, P., Roy, C., Colin de Verdiere, A., and Largier, J. (2000). Simulation of a coastal jet retention process using a barotropic model. *Oceanologica Acta* 21, 615–634. doi: 10.1016/S0399-1784(00)01106-3

Pinkel, R., Goldin, M. A., Smith, J. A., Sun, O. M., Aja, A. A., Bui, M. N., et al. (2011). The wirewalker: a vertically profiling instrument carrier powered by ocean waves. *J. Atmos. Oceanic Technol.* 28, 426–435. doi: 10.1175/2010JTECHO805.1

Pitcher, G., Boyd, A., Horstman, D., and Mitchell-Innes, B. (1998). Subsurface dinoflagellate populations, frontal blooms and the formation of red tide in the southern benguela upwelling system. *Mar. Ecol. Prog. Ser.* 172, 253–264. doi: 10.3354/meps172253

Pitcher, G. C., and Nelson, G. (2006). Characteristics of the surface boundary layer important to the development of red tide on the southern namaqua shelf of the benguela upwelling system. *Limnol. Oceanogr.* 51, 2660–2674. doi: 10.4319/lo.2006.51.6.2660

Pitcher, G. C., and Probyn, T. A. (2011). Anoxia in southern benguela during the autumn of 2009 and its linkage to a bloom of the dinoflagellate ceratium balechii. *Harmful Algae* 11, 23–32. doi: 10.1016/j.hal.2011.07.001

Pitcher, G. C., Probyn, T. A., du Randt, A., Lucas, A. J., Bernard, S., Evers-King, H., et al. (2014). Dynamics of oxygen depletion in the nearshore of a coastal embayment of the southern benguela upwelling system. *J. Geophys. Res.: Oceans* 119, 2183–2200. doi: 10.1002/7332013JC009443

Ragoasha, N., Herbette, S., Cambon, G., Veitch, J., Reason, C., and Roy, C. (2019). Lagrangian Pathways in the southern benguela upwelling system. *J. Mar. Syst.* 195, 50–66. doi: 10.1016/j.jmarsys.2019.03.008

Rainville, L., and Pinkel, R. (2001). Wirewalker: an autonomous wave-powered vertical profiler. *J. Atmos. Oceanic Technol.* 18, 1048–1051. doi: 10.1175/1520-0426(2001)018h1048:WAAWPVi2.0.CO;2

Roughan, M., Garfield, N., Largier, J., Dever, E., Dorman, C., Peterson, D., et al. (2006). Transport and retention in an upwelling region: the role of across-shelf structure. *Deep Sea Res. Part II: Topical Stud. Oceanogr.* 53, 2931–2955. doi: 10.1016/j.dsr2.2006.07.015

SAF, O. (2018). *OSI-250L3C hourly Sea surface temperature (GHRSST) data record release 1 - MSG* (EUMETSAT SAF on Ocean and Sea Ice). doi: 10.15770/EUMSAFOSI0004

Shannon, L. V., and Nelson, G. (1996). "The benguela: Large scale features and processes and system variability," in *The south Atlantic: present and past circulation*. Eds. G. Wefer, W. H. Berger, G. Siedler and D. J. Webb (Berlin, Heidelberg: Springer), 163–210. doi: 10.1007/978-3-642-80353-69

Shchepetkin, A. F., and McWilliams, J. C. (2005). The regional oceanic modeling system (ROMS): a split explicit, free-surface, topography-following-coordinate oceanic model. *Ocean Model.* 9, 347–404. doi: 10.1016/j.ocemod.2004.08.002

Shelton, P. A., and Hutchings, L. (1982). Transport of anchovy, engraulis capensis Gilchrist, eggs and early larvae by a frontal jet current. *ICES J. Mar. Sci.* 40, 185–198. doi: 10.1093/icesjms/40.2.185

Simpson, J. H., Hyder, P., Rippeth, T. P., and Lucas, I. M. (2002). Forced oscillations near the critical latitude for diurnal-inertial resonance. *J. Phys. Oceanogr.* 32, 177–187. doi: 10.1175/1520-0485(2002)032h0177:FONTCLi2.0.CO;2

Smit, A. J., Roberts, M., Anderson, R. J., Dufois, F., Dudley, S. F. J., Bornman, T. G., et al. (2013). A coastal seawater temperature dataset for biogeographical studies: Large biases between *In situ* and remotely-sensed data sets around the coast of south Africa. *PloS One* 8, e81944. doi: 10.1371/journal.pone.0081944

Strub, P. T., Shillington, F. A., James, C., and Weeks, S. J. (1998). Satellite comparison of the seasonal circulation in the benguela and California current systems. *South Afr. J. Mar. Sci.* 19, 99–112. doi: 10.2989/025776198784126836

Stuart-Menteth, A. C., Robinson, I. S., and Challenor, P. G. (2003). A global study of diurnal warming using satellite-derived sea surface temperature. *J. Geophys. Res.: Oceans* 108 (C5). doi: 10.1029/2002JC001534

Taunton-Clark, J. (1985). The formation, growth and decay of upwelling tongues in response to the mesoscale wind field during summer. *South Afr. ocean colour upwelling experiment*, 47–61.

Umlauf, L., and Burchard, H. (2003). A generic length-scale equation for geophysical turbulence models. *J. Mar. Res.* 61, 235–265. doi: 10.1357/002224003322005087

Umlauf, L., and Burchard, H. (2005). Second-order turbulence closure models for geophysical boundary layers. a review of recent work. *Continental Shelf Res.* 25, 795–827. doi: 10.1016/j.csr.2004.08.004

Veitch, J., Hermes, J., Lamont, T., Penven, P., and Dufois, F. (2018). Shelf-edge jet currents in the southern benguela: a modelling approach. *J. Mar. Syst.* 188, 27–38. doi: 10.1016/j.jmarsys.2017.09.003

Veitch, J., Penven, P., and Shillington, F. (2010). Modeling equilibrium dynamics of the benguela current system. *J. Phys. Oceanogr.* 40, 1942–1964. doi: 10.1175/2010JPO4382.1

Walter, R. K., Reid, E. C., Davis, K. A., Armenta, K. J., Merhoff, K., and Nidzieko, N. J. (2017). Local diurnal wind-driven variability and upwelling in a small coastal embayment: local wind-driven 783 variability. *J. Geophys. Res.: Oceans* 122, 955–972. doi: 10.1002/2016JC012466

Weatherall, P., Marks, K. M., Jakobsson, M., Schmitt, T., Tani, S., Arndt, J. E., et al. (2015). A new digital bathymetric model of the world's oceans. *Earth Space Sci.* 2, 331–345. doi: 10.1002/2015EA000107

Weeks, S., Barlow, R., Roy, C., and Shillington, F. (2006). Remotely sensed variability of temperature and chlorophyll in the southern benguela: upwelling frequency and phytoplankton response. *Afr. J. Mar. Sci.* 28, 493–509. doi: 10.2989/18142320609504201

Weller, R. A. (1982). The relation of near-inertial motions observed in the mixed layer during the JASIN, (1978) experiment to the local wind stress and to the quasi-geostrophic flow field. *J. Phys. Oceanogr.* 12, 1122–1136. doi: 10.1175/1520-0485(1982)012h1122:TRONIMi2.0.CO;2

Woodson, C. B., Eerkes-Medrano, D. I., Flores-Morales, A., Foley, M. M., Henkel, S. K., Hessing-Lewis, M., et al. (2007). Local diurnal upwelling driven by sea breezes in northern Monterey bay. *Continental Shelf Res.* 27, 2289–2302. doi: 10.1016/j.csr.2007.05.014

Zhang, X., Smith, D. C., DiMarco, S. F., and Hetland, R. D. (2010). A numerical study of Sea-breeze driven ocean poincare wave propagation and mixing near the critical latitude. *J. Phys. Oceanogr.* 40, 48–66. doi: 10.1175/2009JPO4216.1

frontiers | Frontiers in Marine Science

TYPE Original Research
PUBLISHED 12 July 2023
DOI 10.3389/fmars.2023.1179649

OPEN ACCESS

EDITED BY
Francisco Machín,
University of Las Palmas de Gran Canaria, Spain

REVIEWED BY
Mariona Claret,
Spanish National Research Council (CSIC), Spain
Tengfei Xu,
Ministry of Natural Resources, China

*CORRESPONDENCE
David Rivas
david.camargo@uib.no

RECEIVED 04 March 2023
ACCEPTED 19 June 2023
PUBLISHED 12 July 2023

CITATION
Rivas D, Counillon F and Keenlyside N (2023) On dynamical downscaling of ENSO-induced oceanic anomalies off Baja California Peninsula, Mexico: role of the air-sea heat flux.
Front. Mar. Sci. 10:1179649.
doi: 10.3389/fmars.2023.1179649

On dynamical downscaling of ENSO-induced oceanic anomalies off Baja California Peninsula, Mexico: role of the air-sea heat flux

David Rivas[1,2]*, François Counillon[1,3] and Noel Keenlyside[1,3]

[1]Geophysical Institute, University of Bergen and Bjerknes Centre for Climate Research, Bergen, Norway, [2]Departamento de Oceanografía Biológica, Centro de Investigación Científica y de Educación Superior de Ensenada (CICESE), Ensenada, Mexico, [3]Nansen Environmental and Remote Sensing Center and Bjerknes Centre for Climate Research, Bergen, Norway

The El Niño Southern Oscillation (ENSO) phenomenon is responsible for important physical and biogeochemical anomalies in the Northeastern Pacific Ocean. The event of 1997-98 has been one of the most intense in the last decades and it had large implications for the waters off Baja California (BC) Peninsula with a pronounced warm sea surface temperature (SST) anomaly adjacent to the coast. Downscaling of reanalysis products was carried out using a mesoscale-resolving numerical ocean model to reproduce the regional SST anomalies. The nested model has a 9 km horizontal resolution that extend from Cabo Corrientes to Point Conception. A downscaling experiment that computes surface fluxes online with bulk formulae achieves a better representation of the event than a version with prescribed surface fluxes. The nested system improves the representation of the large scale warming and the localized SST anomaly adjacent to BC Peninsula compared to the reanalysis product. A sensitivity analysis shows that air temperature and to a lesser extent wind stress anomalies are the primary drivers of the formation of BC temperature anomaly. The warm air-temperature anomalies advect from the near-equatorial regions and the central north Pacific and is associated with sea-level pressure anomalies in the synoptic-scale atmospheric circulation. This regional warm pool has a pronounced signature on sea level anomaly in agreement with observations, which may have implications for biogeochemistry.

KEYWORDS

regional numerical ocean model, reanalysis product, dynamical downscaling, Baja California Peninsula, El Niño 1997–98

1 Introduction

The interannual climatic anomalies attributed to the El Niño Southern Oscillation (ENSO) have important physical and biological consequences for the Northeastern Pacific Ocean. In the last decades, El Niño events like those that occurred in the years 1982-83, 1997-98, and 2015-16 were characterized by intense sea surface temperature (SST) anomalies (>2.5°C) in the southern and central California Current System (Jacox et al., 2016). Other effects of these events include biogeochemical and ecological changes including reductions in nutrients and biological production (Bograd and Lynn, 2001; Chavez et al., 2002; Deutsch et al., 2021), redistribution and disappearance of species from their typical habitat (Chavez, 2002), and changes in dissolved oxygen and pH at the surface levels (Turi et al., 2018). In particular, the 1997-98 El Niño event - the focus of this paper - was responsible for important effects on the pelagic ecosystem off Baja California (BC) peninsula (Kahru and Mitchell, 2000; Reyes Bonilla, 2001; Lavaniegos et al., 2003). Given its environmental importance at different spatial scales, the dynamics and predictability of El Niño phenomenon have been previously studied (*e.g.* Santoso et al., 2019) as well as their impact on the ocean (*e.g.* Dorantes-Gilardi and Rivas, 2019) and the atmosphere (*e.g.* Magaña and Ambrizzi, 2005). Herein, we focus on how the air-sea exchanges modulate the ENSO signals using an eddy-resolving numerical ocean model.

The El Niño phenomenon involves coupled ocean-atmosphere interactions, arising in the equatorial Pacific and affecting the rest of the Pacific and beyond. Nowadays, air-sea coupled reanalysis products are able to represent the ENSO dynamics variability and provide a realistic representation of ocean and atmospheric fields. However, the ocean resolution of the products (*e.g.* 1° of longitude/latitude) is usually inadequate to represent important shelf and near-coastal dynamics, causing large regional biases in the reanalysis. Downscaling techniques can overcome these issues.

Downscaling of global coarse-resolution datasets (*i.e.* reanalysis products and general circulation models) can be carried out either by statistical methods (*e.g.* Wilby and Dawson, 2013) or by dynamical downscaling methods like the implementation of a finer-resolution regional model (*e.g.* Xu et al., 2019). Herein we adopt the latter approach by nesting (in a one-way, offline fashion) a primitive equation model with a terrain-following vertical coordinate of higher spatial resolution (*e.g.* Rivas and Samelson, 2011; Cruz-Rico and Rivas, 2018; Arellano and Rivas, 2019; Dorantes-Gilardi and Rivas, 2019). The downscaling of the coarse-resolution solutions seeks an improvement of the variability patterns reproduced in the outer model, as the mesoscale dynamics is better resolved, and so is the coast line and bathymetry (*e.g.* continental shelf and break, bathymetric features, coastal-wind horizontal shear, etc.).

The purpose of this paper is: first, to test different approaches to implement the dynamical downscaling and best reproduce the spatial and temporal patterns of the sea surface temperature (SST) anomalies off the BC Peninsula in 1997-98, also corroborated for the 2015-16 period. Second, identify the key atmospheric-forcing fields responsible for the development of this anomaly. Third, relate the regional forcing with synoptic-scale atmospheric circulation associated to ENSO.

The rest of the paper is organized as follows. Section 2 provides a description of the model setup, the different experiments carried out for the downscaling of reanalysis datasets, and sensitivity analyses of the SST anomaly to individual forcing fields. Section 3 describes the results of this study, including the impact of the practical implementation of the forcing fields in the nested configuration; the contribution of each atmospheric variable to the representation of the regional warming, and the atmospheric pattern associated with this warming. Section 4 discusses some implications of this study. Finally, Section 5 summarizes the main results of this work.

2 Methods

2.1 Numerical ocean model

A regional three-dimensional numerical model, based on the Regional Ocean Modeling System (ROMS; *e.g.* Shchepetkin and McWilliams, 2005) version 3.8, was implemented for a region of the Northeastern Pacific Ocean that extends roughly from Cabo Corrientes to Point Conception, which includes Southern California Bight (SCB), Baja California (BC) Peninsula, and the Gulf of California (Figure 1). This domain is oriented 31-41° counterclockwise from the north in order to optimize grid points over the seawater. The horizontal resolution is 8-10 km (a horizontal grid of 352×162 grid points) and has 30 sigma-levels in the vertical with enhanced resolution near the bottom and near the surface (5 and 8 levels in the lower and upper tenth of the water column, respectively), specified by the stretching parameters θ_s = 4.0 and θ_b = 0.9 in the stretching function 4 and transform equation 2 described in the ROMS website: https://www.myroms.org/. The model's grid was prepared using Charles James' *G*ridBuilder v0.99.1 software, available in *A*ustides Consulting website (https://austides.com/), but replacing the bathymetry by that taken from the ETOPO1 global-topography product (Amante and Eakins, 2009). Along the coast, the minimum water depth was fixed at 10 m. Bottom slopes were smoothed to meet the r-factor criterion of 0.20 to prevent horizontal pressure gradient errors (Beckmann and Haidvogel, 1993).

This model includes a splined density Jacobian scheme for pressure gradient calculations (Shchepetkin and McWilliams, 2003), and a fourth-order-centered scheme together with a split third-order upstream ("SU3") scheme for advection of momentum and tracers (Marchesiello et al., 2009). Subgrid-scale mixing is parameterized by the Mellor-Yamada level 2.5 model (Mellor and Yamada, 1982) in the vertical direction, with background values of 5×10^{-6} m^2 s^{-1}, and by harmonic diffusivity and viscosity in the horizontal direction, with constant coefficients 1 m^2 s^{-1} in the grid interior. A sponge layer was included along the open boundaries (Figure 1), which extended throughout 10 grid points toward the interior, where the diffusivity/viscosity coefficients increase linearly from their interior value to 10 m^2 s^{-1} at the boundaries. Lateral diffusion of tracers (temperature and salinity) and momentum are restricted to geopotential (constant depth) and constant sigma-level surfaces, respectively.

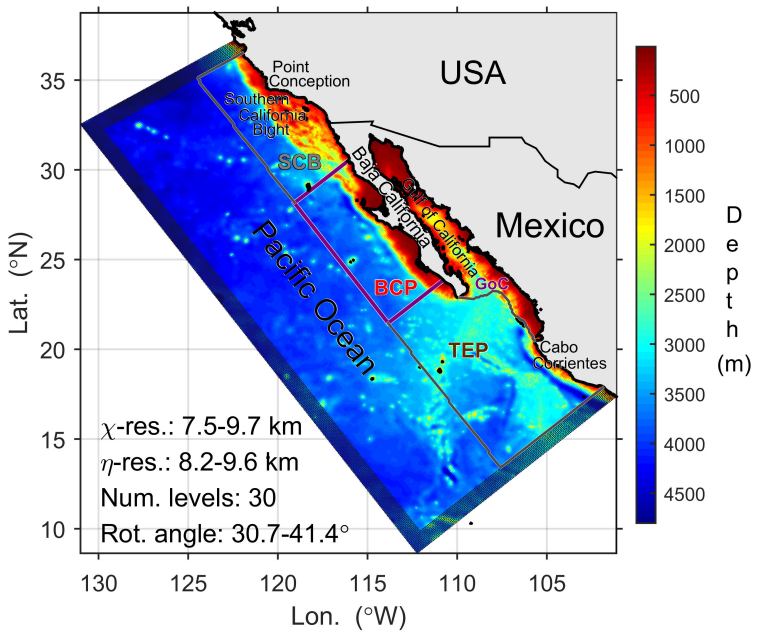

FIGURE 1
Model domain and bathymetry (in m). Relevant locations are shown. Purple along-shore box, BC Peninsula (BCP), corresponds to a coastal region where SST anomalies are analyzed for sensitivity experiments and model-data correlations. Gray lines delimit three additional regions for the SST model-data correlations: Southern California Bight (SCB), Tropical Eastern Pacific (TEP), and Gulf of California (GoC). The dashed region along the domain's open boundaries corresponds to a sponge layer.

At the model's open boundaries (west, south, and north), monthly values of temperature, salinity, water velocity, and sea level for the 1993-2002 period were imposed, taken from the Global Ocean Data Assimilation System (GODAS; e.g. Huang et al., 2008; Ravichandran et al., 2013) provided by the NOAA - ESRL PSD through its website: http://www.esrl.noaa.gov/psd/data/gridded/. This oceanic reanalysis product has a spatial resolution of 1° latitude/longitude and a temporal resolution of 1 month. Radiation plus nudging conditions are imposed for the free surface, depth-dependent horizontal momentum and tracers (temperature and salinity), and a Flather condition is used for depth-averaged momentum. Nudging (relaxation) time scales are 6 and 360 days for active (inflow) and passive (outflow) open boundary conditions (with no nudging toward the grid's interior), respectively. No-normal flow and no-slip conditions are imposed at the coast. At the bottom, no-normal flow and a quadratic stress are applied. The top corresponds to a material free surface.

At its free surface, the regional model was forced by surface meteorological fields from the North American Regional Reanalysis (NARR; Mesinger et al., 2006). This meteorological reanalysis product has a spatial resolution of ~ 30 km and a temporal resolution of 3 hours. We ran two different implementations of the forcing in the following experiments.

- *Experiment A*, with prescribed surface fluxes: Monthly net heat flux and freshwater flux (evaporation minus precipitation), together with daily wind stress (calculated from the 3-hourly wind vector applying drag-coefficient parameterizations proposed by Smith, 1988), are directly supplied to the model.
- *Experiment B*, with instantaneous (internally calculated) surface fluxes: Net heat flux, freshwater flux, and wind stress are instantaneously calculated by the model (using bulk formulae proposed by Fairall et al., 1996a; Fairall et al., 1996b) as it runs, using monthly air temperature, pressure, relative humidity, rain fall rate, downward longwave radiation, and daily wind vector as input variables.

Both experiments use a bias-correction term (Barnier et al., 1995) defined as

$$Q_{cr} = \left(\frac{dQ_{net}}{dT_s}\right)_{ref}(T_s - T_{ref}) \quad , \tag{1}$$

where the amount in the first parenthesis is the sensitivity of the net heat flux Q_{net} to the surface temperature T_s, and the whole term is a heat-flux compensation acting as T_s drifts from the reference temperature T_{ref} at which Q_{net} was calculated. The sensitivity factor is represented as a spatiotemporally-varying coefficient calculated the NARR data and the SST from the GODAS product as T_{ref}, using the software described by Penven et al. (2008). Thus, Eq. (1) helps to prevent the model's SST to drift away from the reference thermal state.

The model was initialized as a motionless and horizontally-uniform ocean, with a thermohaline vertical structure consistent with climatological profiles taken from the National Oceanographic Data Center (NODC) datasets available in its website (https://

www.nodc.noaa.gov/). The model was run for 20 years with forcing fields from an annual climatology (1993-2002) for spin-up processes and then it was run with interannual atmospheric forcing fields for the time period 1993-2002. This time period starts early enough to spin up for the event of interest, the 1997-1998 El Niño event (Jacox et al., 2016), and that extends afterwards to assess of the downstream consequences. The initial condition is the same for both Experiments A and B (obtained after the 20 years of spin-up).

Time series of monthly mean anomalies of the model's outputs and forcing fields were calculated by subtracting a monthly climatology for the 1993-2002 period to remove seasonal variability. An Empirical Orthogonal Function (EOF) analysis was then carried out using the method based on a singular-value decomposition (SVD) of the spatio-temporal anomalies used in Dorantes-Gilardi and Rivas (2019). The SST's first variation mode is a good indicator of the El Niño's signal off BC Peninsula (Dorantes-Gilardi and Rivas, 2019). This mode is compared to that of each atmospheric variable involved in the calculation of the surface fluxes, in order to identify its key driver.

2.1.1 Forcing-sensitivity experiments

Additional experiments were done in order to explore the sensitivity to individual forcing fields. To evaluate the importance of the atmospheric anomalies in the surface fluxes associated with the SST anomalies off BC Peninsula, shorter simulations (March 1997 through September 1998) were carried out (Section 2.1). For each atmospheric variable, interannual variability was removed by substituting the original values by its climatological seasonal cycle (1993-2002 mean monthly values). The model configuration that best reproduced the SST anomaly associated with the 1997-98 El Niño event was selected for these experiments. The results from seven experiments, one for each atmospheric variable involved in the surface fluxes calculations (air temperature, wind stress, relative humidity, downward longwave radiation, atmospheric pressure, rain rate, net shortwave radiation), were ranked according to their capability to reproduce the SST anomaly (within the along-shore box shown in purple in Figure 1) of the original simulation (with no modification of the atmospheric variables). This capability was assessed by a linear correlation coefficient between this original simulation and each forcing-sensitivity simulation. The lower the correlation, the more important is the analyzed atmospheric variable to the SST anomaly. The correlation coefficient was calculated between the monthly mean SST anomaly from Experiment B, within the along-shore box and in the period from March 1997 to September 1998, and that from each sensitive experiment in which the interannual variability of one atmospheric variable was removed. The root-mean-square error (RMSE) and the mean deviation (MD) were also calculated to complement the skill assessment of the model simulations.

2.1.2 Verification experiments

As established above, the El Niño 1997-98 event is the focus of this paper and our analyses are centered on the peak of its thermal anomaly off BC Peninsula. Subsequent numerical experiments were carried out in order to corroborate whether using internally-calculated surface fluxes helps to improve the SST anomalies in other warm oceanic events. Therefore, the ROMS-B experiment described in Section 2.1 was extended forward in time to include the El Niño 2015-16 event, which was characterized by mean SST anomalies > 2°C off BC Peninsula (*e.g.*, Dorantes-Gilardi and Rivas, 2019). Additionally, a contrasting simulation was carried, based on ROMS-A Experiment's configuration but starting on 1 January 2014, right before the warm anomaly off BC started (Dorantes-Gilardi and Rivas, 2019), with its initial condition taken from the extended ROMS-B experiment; this simulation was shorter due to technical limitations. As before, monthly anomalies were calculated from these new simulations, also with respect to the 1993-2002 climatology.

2.2 Ancillary data

SST satellite data were used for an evaluation of model performance. These data consisted of monthly composites of 4 km-resolution SST for the period 1993-2002, taken from the Advanced Very High Resolution Radiometer (AVHRR) product available in numerous websites including those held by the National Oceanic and Atmospheric Administration (NOAA), *e.g.* the CoastWatch website: https://coastwatch.noaa.gov/.

The Southern Oscillation Index (SOI; *e.g.* Trenberth, 1984) was used in order to identify the timing and intensity of the El Niño 1997-98 event. Monthly values of this index for the period are available in the NOAA - National Centers for Environmental Information (NCEI) site: https://www.ncdc.noaa.gov/.

2.3 Calculations of air-sea fluxes

2.3.1 Net heat-flux budget

The components of the net surface heat flux are herein analyzed, either by comparing prescribed vs. internally-calculated fluxes or by illustrative calculations for simplified cases, in order to elucidate the dominant processes involved in the model's air-sea heat exchanges. According to Fairall et al. (Fairall et al., 1996a; Fairall et al., 1996b), Rutgersson et al. (2007); Yu (2019), and others, the net surface heat flux is defined as

$$Q_{net} = Q_{sw} - Q_{sn} - Q_{lt} - Q_{lw} \quad , \tag{2}$$

where the components can be defined as follows.

* Net shortwave radiation flux: Q_{sw}, the difference between the downward and the upward (reflected) solar irradiance received at the surface, is an input variable taken from the atmospheric dataset.

* Sensible heat flux:

$$Q_{sn} = \rho_a \, C_{pa} \, C_h \, U \, (T_s - T_a) \, , \tag{3}$$

where ρ_a is the air density, C_{pa} = 1006 J kg^{-1}°C^{-1} is the specific heat capacity of air at constant pressure, $C_h = 10^{-3}$ is an exchange coefficient for sensible heat, U is the mean wind speed, T_s is the sea surface interface temperature (*i.e.*, SST), and T_a is the air temperature.

* Latent heat flux:

$$Q_{lt} = \rho_a L_e C_e U (0.98 q_s - q_a), \quad (4)$$

where $L_e = (2.501 - 0.00237 \quad T_s) \times 10^6$ is the latent heat of vaporization, $C_e = 10^{-3}$ is an exchange coefficient for latent heat, q_a is the specific humidity, q_s is saturation specific humidity at T_s (at the sea surface), and the factor of 0.98 compensates the contribution of salinity in this variable's calculation. In the evaluation of Eq. (4), for practical reasons, q_s is expressed as $0.622(e_s/P_a)$. (*e.g.*, Hess, 1959) where P_a is the sea level pressure, and e_s is the saturation vapor pressure at the sea surface which is herein estimated as a function of temperature only (Adem, 1967).

* Net longwave radiation flux:

$$Q_{lw} = 0.97(\sigma(T_s + 273.15)^4 - R^{\downarrow}_{lwr}) \quad , \quad (5)$$

where $\sigma = 5.67 \times 10^{-8}$ W m^{-2} K^{-4} is the Stefan-Boltzman constant, $R^{\downarrow}_{lwr}$ is the downward long-wave radiation flux, and the factor of 0.97 corresponds to the broadband emissivity of the sea surface.

2.3.2 Net freshwater flux

In addition to the net heat flux, the surface net freshwater flux is also a necessary forcing at the model's surface. This flux is defined as evaporation minus precipitation, where positive and negative values correspond to salting (net evaporation) and freshening (net precipitation) of the sea surface, respectively. Thus, evaporation (E) releases both water vapor and latent heat to the atmosphere, hence it can be estimated as

$$E = \frac{Q_{lt}}{\rho_0 L_e} \quad , \quad (6)$$

once Eq. (4) has been evaluated (Yu, 2019).

2.3.3 Momentum flux

As in the flux calculations described above, the momentum flux at the air-sea interface is usually estimated by bulk formula, which is a function of a stress-transfer coefficient (normally referred to as drag coefficient) and the mean wind speed (*e.g.*, Fairall et al., 1996b; Yu, 2019; Qiao et al., 2021). Thus, the zonal (τ_x) and meridional (τ_y) wind-stress components can be estimated as

$$(\tau_x, \tau_y) = \rho_a C_d |\mathrm{U}_h| \mathrm{U}_h \quad , \quad (7)$$

where $\mathrm{U_h}$ is the horizontal wind vector and C_d is the drag coefficient; the contribution of the surface seawater velocity is neglected in this formulation. C_d can be estimated as a simple function of the wind speed and the air-sea thermal gradient (*e.g.*, Smith, 1988), or can be estimated by a more complex algorithm with refinement based on boundary-layer theory (*e.g.*, Fairall et al., 1996b).

3 Results

3.1 1997-98 El Niño's warm anomaly

Herein we use the SOI as an indicator of the ENSO activity. This conventional ENSO index is defined as the standardized difference in sea-level pressure anomalies between Tahiti and Darwin, Australia. Sustained episodes of negative values of SOI correspond to El Niño conditions, whereas episodes of positive values of SOI correspond to La Niña conditions. According to this index, the onset of El Niño conditions started in early 1997 and remained through early 1998 (Figure 2A), with values mostly<-1 and even reaching values<-2 from December 1997 to February 1998.

The strongest SST anomaly (SST') occurred in September-November 1997 (Figures 2B–D). This El Niño event induced an intense SST positive anomaly off BC peninsula, with a ~2°C peak in the spatially-averaged SST (Figure 2B) and a >3°C mean warm pool (Figure 2C). The GODAS reanalysis product used in the experiments described in Section 2.1 agrees with the satellite SST anomaly (Figure 2D).

The warm pool was linked to a near-surface atmospheric warming, consequence of an anomalous pattern in the synoptic atmospheric surface circulation. By July 1997, a weak and small surface-air warming tendency associated with horizontal heat flux divergence is observable off the southern half of BC Peninsula (23-25°N, 110-113°W, Figure 3A). This tendency is associated with a weakening of the monsoonal winds around the mouth of the Gulf of California and in its interior, and constrained in that zone by an anomalously southwestward wind impulsed by a relatively high pressure forming west of SCB (Figure 3A). This pattern prevails and intensifies by August (1997), when the surface-air warming is relatively stronger and more extensive, and it is constrained by the anomalous flow driven by the high pressure-anomaly which is now stronger and larger (Figure 3B). By September (1997), a large and intense low pressure anomaly dominates the atmospheric circulation west of Mexican waters. It induces a poleward along-shore enhanced flow that induces a surface-air cooling from the Mexican southern coast to the tip of BC Peninsula, and a surface-air warming off the middle portion of BC Peninsula (Figure 3C), resulting in a more intense SST anomaly in this region (Figure 2A). By October (1997), the combination of an elongated trough (linked to the low pressure anomaly which has moved to the southwest) and a small zone of relatively high pressure, features respectively located southwest and south of BC Peninsula, drive a northward flow that intensifies the surface-air warming off BC Peninsula (Figure 3D). This flow turns westward roughly following the isobars between the trough and a high pressure zone located off central California; this circulation also induces a surface-air warming south of Point Conception (Figure 3D). In November (1997), the pattern affecting the southern half of BC Peninsula is weaker, the surface-air warming remains but it is weaker; an enhanced eastward flow dominates the circulation north of 25°N, causing a surface-air cooling along its path onto SCB and the northern portion of BC Peninsula (Figure 3E). By December (1997), the winds around BC Peninsula are weaker, a surface-air cooling is now observed off BC Peninsula, and an intense air-surface warming occurs west of SCB (Figure 3F). By January 1998, the enhanced flow west of SCB reappears but its direction and surface-air cooling are mostly onto regions north of Point Conception. However, part of this flow is directed onto SCB and the northern half of BC Peninsula, forming an along-shore anticyclonic gyre which

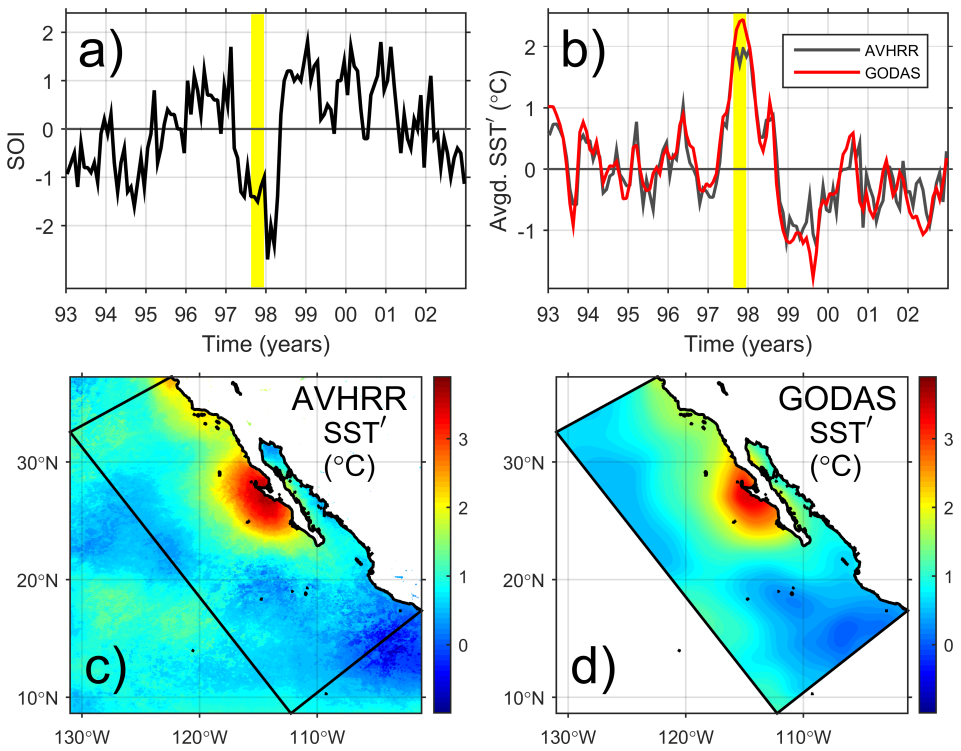

FIGURE 2
(A) Southern Oscillation Index (SOI), and **(B)** temporal evolution of monthly-mean, spatially-averaged (within the rectangle shown in panels **(C)** and **(D)**, which coincides with the model domain) SST anomaly (SST') from AVHRR satellite observations (gray line) and GODAS product (red line), for the 1993-2002 period. Yellow band indicates the September-November 1997 trimester, coincident with the maximum ENSO-induced warming, and period used to calculate the mean SST-anomaly maps shown for the AVHRR **(C)** and GODAS **(D)**.

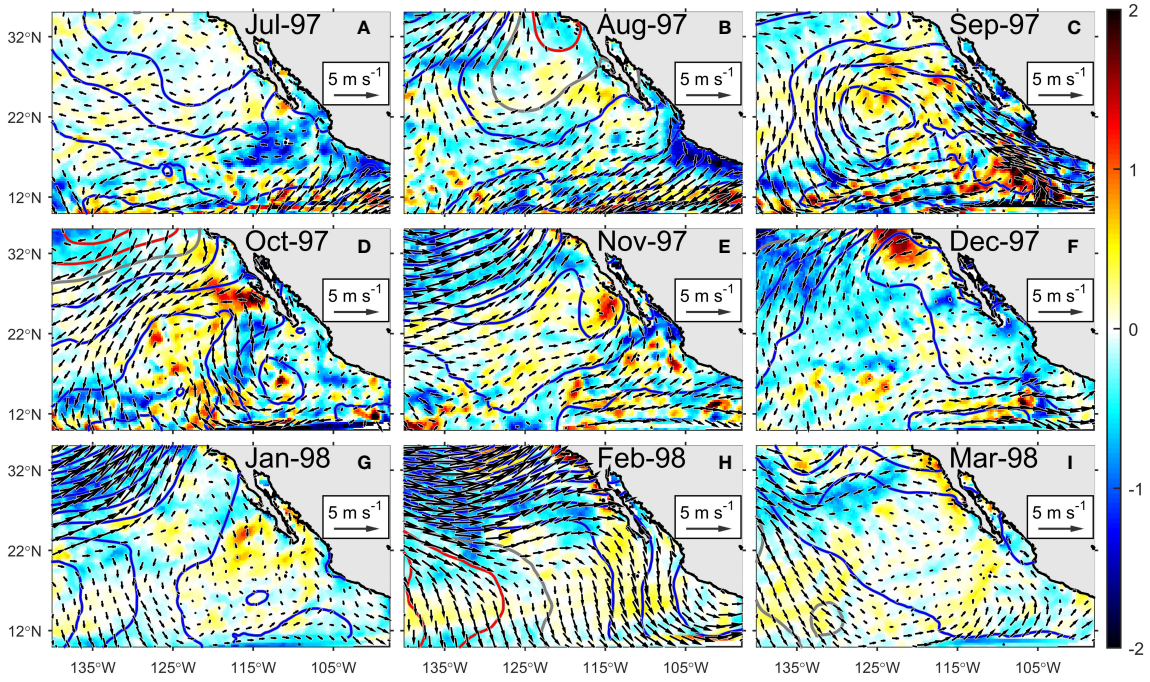

FIGURE 3
Time sequence of monthly-mean surface atmospheric anomalies from NARR before (**A, B**, July-August 1997), during (**C-E**, September-November 1997) and after (**F-I**, December 1997 – March 1998) the highest SST anomaly associated with the El Niño 1997-98 event. Color corresponds to the temperature-balance quantity $-\nabla \bullet (U_h T_a)$ in 10^{-5}°C s^{-1} (where U_h is horizontal wind velocity at surface and T_a is air temperature); positive values represent a warming tendency. Contour lines correspond to sea-level pressure (in intervals of 0.5 hPa; blue and red lines are for negative and positive values, respectively, gray line for zero); vectors correspond to surface wind.

induces a relatively weak surface-air warming off the southern portion of BC Peninsula (Figure 3G). By February (1998), the enhanced flow has moved southward and it is located west of BC Peninsula, flowing onto the northern half of the Peninsula and driving an along-shore equatorward flow off the southern half, which induces a surface-air cooling off the southern half of the Peninsula and the waters south of it (Figure 3H); the SST anomaly is weakening (Figure 2A). By March (1998), the circulation anomalies are weaker (Figure 3I) and the SST anomaly off BC Peninsula nearly disappeared (Figure 2A).

3.2 Downscaled reanalysis

We evaluate the capability of the numerical experiments to reproduce the observed SST anomalies. The experiment with prescribed surface fluxes,"ROMS-A" experiment, was unable to fully reproduce the temporal pattern of the SST anomaly (Figure 4A). ROMS-A experiment reproduces well the SST anomaly in its first months but starts to deviate from the observation that reaches its maximum in August 1997. It cools early and ultimately disappears in February 1998, three months before in the observations (Figure 4A). The spatial pattern of the SST anomaly diagnosed by ROMS-A experiment corresponds mostly to broad positive values but does not show the characteristic warm pool off BC Peninsula during September-November 1997, when SST' was the largest (Figure 4C). On the contrary, ROMS-B experiment successfully reproduced both the temporal and spatial patterns of the SST anomaly seen in the observation (Figure 4D).

ROMS-B experiment is generally better reproducing the SST anomaly than ROMS-A, as shown in the Taylor diagram (Taylor, 2001, see Figure 5). In the four evaluated regions, model-data correlations are higher in ROMS-B. As expected, the largest differences are found off BC Peninsula, where the correlation increases from 0.63 in ROMS-A to 0.91 in ROMS-B. Similarly, the correlation increases significantly in the rest of the regions: 0.83 to 0.91 in Southern California Bight (SCB), 0.71 to 0.88 in Tropical Eastern Pacific (TEP), and 0.77 to 0.90 in the Gulf of California (GoC). Standard deviation ratios are also improved in ROMS-B, with values closer to 1 expect for the TEP (where they are ~ 0.5 but still better than those in ROMS-A), and the RMSD values are also lower in this experiment.

These results emphasize the importance of the surface fluxes in reproducing the SST anomaly, as it is the only difference between the two experiments. The maximum differences in SST anomalies between the experiments are associated with large differences in heat-flux anomalies. These differences are maximum in November-December 1997, when ROMS-A simulation has a strong negative anomaly ~ -40 W m^{-2} that is 2 times greater than the negative anomaly ~ -20 W m^{-2} from ROMS-B simulation (Figure 4B). The mean net-heat flux anomaly (in September-November 1997) off BC Peninsula in the two experiments are opposite between each other, ROMS-A [prescribed fluxes] shows an intense upward flux (ocean's cooling) ~ -100 W m^{-2}, whereas ROMS-B [internally-calculated fluxes] shows a downward flux (ocean's heating) ~ 50 W m^{-2} (Figures 4E, F).

3.3 Controls on ENSO-driven SST anomalies

3.3.1 EOF analyses

As mentioned in the previous section, the SST warm anomaly localized off BC Peninsula, reproduced by ROMS-B experiment, is apparently linked to an anomalous surface-air warming driven by the synoptic circulation. In addition, the downward longwave-radiation anomaly must contribute to the modulation of the SST anomaly, although to a lesser extent. It shows high values (enhanced radiation flux *into* the ocean) in the last months of 1997 (not shown), when the SST anomaly was most pronounced, and reverse (radiation flux *out* of the ocean) in March-April 1998, when the SST anomaly decreases. Along-shore wind-stress anomaly are essentially the same in both experiments (*i.e.* minor changes in the internally-calculated drag coefficient) and it is mostly poleward through the year 1997 (Figure 3), which implies a weakening of upwelling favorable winds.

As described in Section 2.1, an EOF analysis was carried out in order to elucidate the most important atmospheric variables in the surface fluxes calculations. The 1^{st} variation mode of the SST anomalies, corresponds to a warming in the whole model domain with a warmer band perpendicular to the southern part of BC Peninsula, extending from the coast through the model's western boundary, and where the coastal area corresponds to the ENSO-induced warm pool (Figure 6A). This 1^{st} mode explains 54% of the variance contained in the SST anomalies.

The principal component (*i.e.* the eigenvalue or amplitude time series; PC) of the SST-anomaly 1^{st} mode described above was compared to those of the meteorological variables used to force the model, in order to explore their importance. Table 1 and Figures 6B–J show these correlation results. Air temperature 1^{st} PC, which explains 69% of variance of this variable's anomaly, has the highest correlation (r = 0.96) with that of the SST anomaly, and the highest values of its 1^{st} EOF coincide with those of the SST 1^{st} EOF (Figures 6B, E). The second most correlated 1^{st} PC (r = 0.69) is that of the downward longwave radiation anomaly explaining 48% of its variance, shows a spatial pattern consistent with those of air temperature and SST (Figures 6B, F). Atmospheric pressure 1^{st} PC (74% of its anomaly variance) has also a relatively high correlation with that of SST (r = 0.60). In this case the main features of its EOF was a low-pressure signal located northwest of BC Peninsula, consistent with that shown in Figure 3E. Results from the other three variables in Figure 6 show lower but still significant correlations (r < 0.50) with the SST 1^{st} mode (Figures 6C, D). Relative humidity shows a negative signal around BC Peninsula (Figure 6H), consequence of the less-saturated, warm-air signal mentioned above, and of the positive signal of downward long-wave radiation affecting the Peninsula (Figure 6J). The along-shore wind-stress signal occurs as an intensification west of Point Conception (Figure 6I), associated with the low-pressure signal in that region.

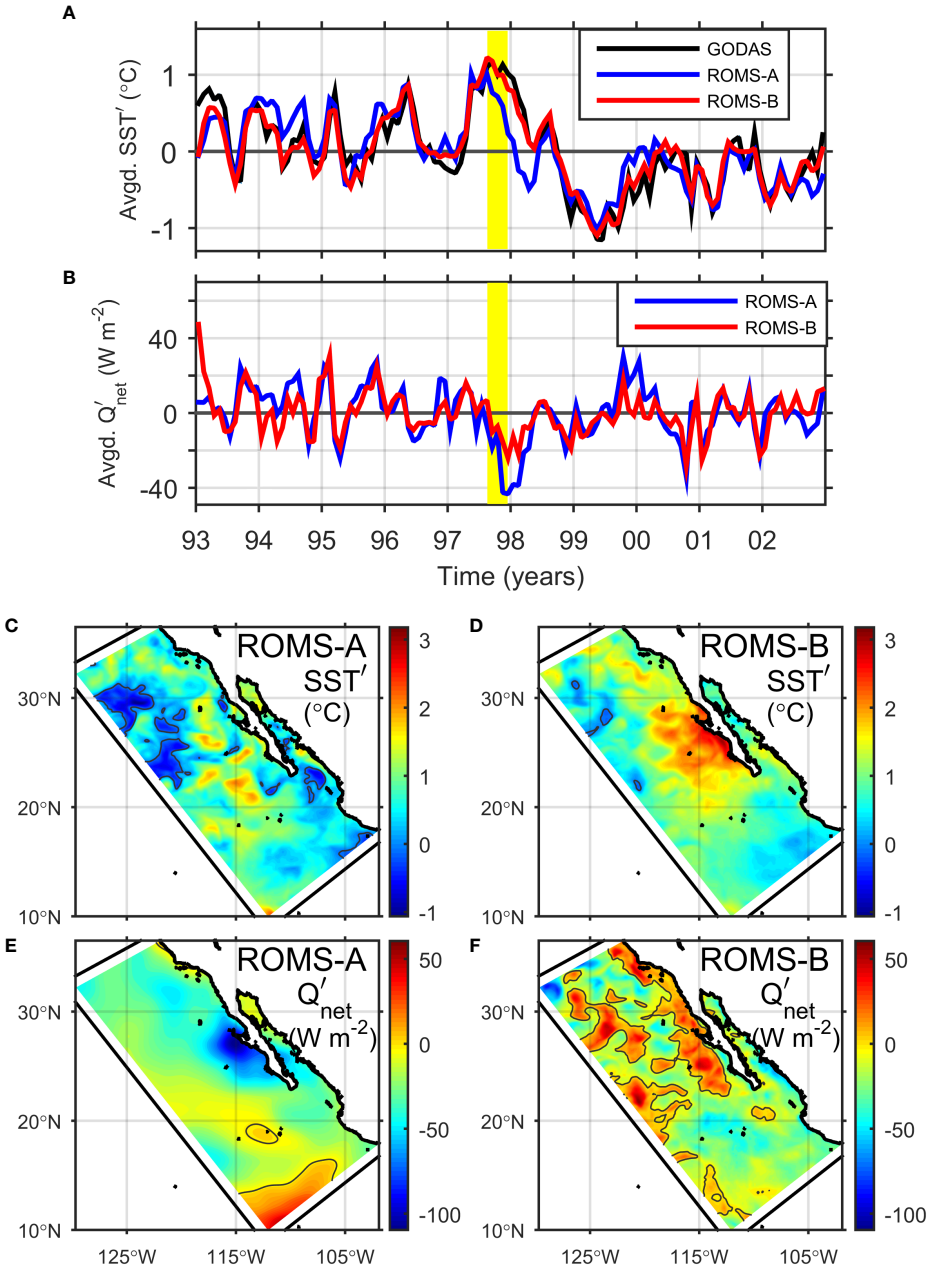

FIGURE 4
Temporal evolution of monthly-mean, spatially-averaged (within the whole model domain, except the nudging/sponge layer) anomalies of **(A)** SST and **(B)** net heat flux from the ROMS-A (blue line) and ROMS-B (red line) reanalysis-downscaling experiments (see Section 2.1), for the 1993-2002 period. Panel **(A)** also shows the SST anomaly from the GODAS (black line). Vertical yellow bands indicate the September-November 1997 trimester, period for which the mean SST-anomaly **(C, D)** and mean net heat-flux anomaly **(E, F)** were calculated for ROMS-A **(C, E)** and ROMS-B **(D, F)** experiments. Positive values in net heat-flux anomaly corresponds to an enhanced flux *into* the ocean.

3.3.2 Sensitivity to individual forcing fields

The EOF analysis described previously provides an insight about which atmospheric variables are important to reproduce the ENSO-induced warm pool, but the results relies on linear statistics. Therefore, herein we carried out sensitivity experiments in order to further evaluate the contribution of each atmospheric variable anomaly to the surface fluxes and hence to the ENSO-induced warming off BC Peninsula. As described in Section 2.1.1, shorter simulations (March 1997 - September 1998) were done in which the interannual variability of each atmospheric variable was removed by substituting its original values by its mean seasonal cycle. Correlations, RMS error, and MD between monthly SST anomaly from each sensitivity simulation and the original experiment were calculated for a coastal box located off BC Peninsula (purple box in Figure 1) that is centered on the region of maximum SST values. Lower correlations and larger RMS errors imply a higher importance of the analyzed forcing variable. Based on these criteria, air temperature and wind stress are the most important variables (Table 2). Similarly, for the 3-month period centered in the SST anomaly peak (September-November 1997) air

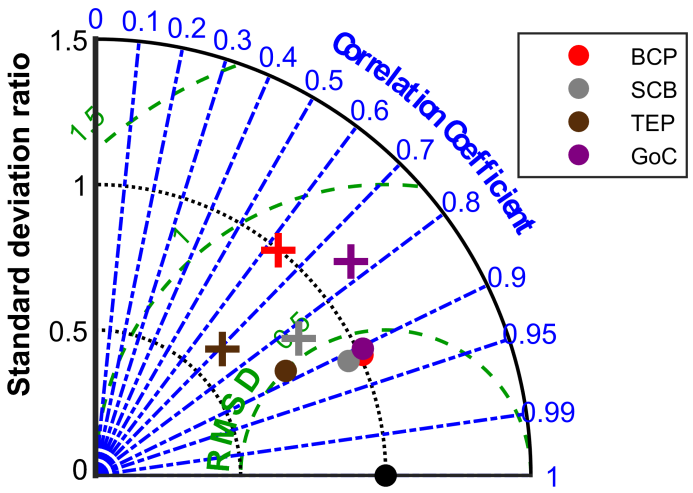

FIGURE 5
Taylor diagram for monthly SST-anomaly values located within the regions shown in Figure 1 during September-November 1997 (spatio-temporal arrays expressed as series of consecutive data), from ROMS-A (plus signs) and ROMS-B (dots) experiments. Radial distance represents the ratio of simulated to observe standard deviations and azimuthal angle represents model-observation correlation. All the correlation calculations satisfy $p < 0.05$. Observations coincide with the location defined by standard deviation ratio and correlation equal to one (black dots). Interior dashed contours show the root-mean-square deviation (RMSD). Marker colors indicate the data's regions: BC Peninsula (BCP), Southern California Bight (SCB), Tropical Eastern Pacific (TEP), and Gulf of California (GoC).

temperature and wind stress are still the most important variables but their order of importance changes (Table 3).

In spite of the results shown in Tables 2, 3, modifying only the wind field has a moderate effect on the simulation (Figures 7A, B), just increasing the magnitude of the SST peak (Figure 7A). Air temperature, on the other hand, shows a major effect on the warm pool (Figure 7C). Interestingly, the net heat flux is similar in both experiments, showing a positive anomaly off BC Peninsula (Figures 7D, E); this situation will be discussed in Section 4.

3.3.3 Surface heat-flux components

Further detail about the surface heat flux involved in the formation of the warm pool off BC is herein presented by the quantification of each of the air-sea heat-flux components in Eq. (2). Input/output variables from the model simulations were taken to quantify these heat-flux components, except for the net long-wave radiation flux which was not saved in the model's output files, hence it is estimated using Eq. (5) [with T_s = SST] for the case of ROMS-B experiment. Table 4 shows the mean flux anomalies within the coastal box off BC during the SST-anomaly peak. Notice that the values of Q_{net} do not exactly match the sum of four heat-flux components, these discrepancies can be associated with errors in averaging, interpolation (Reanalysis-to-model interpolation of input variables), and/or calculation (monthly-mean instead of instantaneous SST in Q_{lwr}).

In September 1997, when the maximum SST anomaly occurred, ROMS-A experiment presents a net heat loss (Q_{net} = −30.3 W m^{-2}) in contrast with ROMS-B which presents a net heat gain (Q_{net} = 20.4 W m^{-2}) [Table 4]. In both experiments the short-wave radiation flux is the same, in this case with a positive anomaly (Q_{sw} = 4.0 W m^{-2}) which corresponds to an anomalous heat input by the solar irradiance (Table 4). On top of this heat gain, there is a net gain by sensible heat flux (Q_{sn}) in both cases, but this is ~10 weaker in ROMS-A (1.2 W m^{-2}) with respect to ROMS-B (9.3 W m^{-2}). There is also a net heat gained by latent heat flux (Q_{lt}) in ROMS-B (3.6 W m^{-2}) but not in ROMS-A, where the latent flux is negative and remarkably strong (-23.8 W m^{-2}). In both experiments there is a heat loss by long-wave radiation flux (Q_{lw}), which is 2 times stronger in ROMS-A (-5.2 W m^{-2} vs. -2.7 W m^{-2} in ROMS-B); the downward long-wave radiation flux is the same in both experiments ($R^{\downarrow}_{lwr}$ = 9.5 W m^{-2}) [Table 4].

In the whole September-November 1997 trimester, the net heat loss in ROMS-A is stronger (-58.7 W m^{-2}) compared to the one mentioned above for September, and the net heat gain (4.2 W m^{-2}) in ROMS-B is weaker (Table 4). The remarkably strong heat loss in ROMS-A is responsible for the early decrease of the SST anomaly in that experiment. The anomaly of short-wave radiation flux is nearly null (Q_{sw} = −0.2 W m^{-2}) and has a negligible contribution to the heat budget. In ROMS-A the ocean surface losses heat by all the four heat-flux components, especially by latent flux which contributes to 85% of the lost heat. In ROMS-B there is a positive sensible-heat flux anomaly (Q_{sn} = 6.4 W m^{-2}) which compensates and even exceeds the negative net heat-flux anomaly (Q_{net}), but it is not strong enough to compensate the heat loss driven mostly by latent-heat flux (Q_{lt} = −10.1W m^{-2}). We note that although the budget residual is large, the dominance of Q_{lt} is illustrated in the Discussion.

3.4 2015-16 El Niño event

As shown in the previous sections, during intense warm conditions like those in the 1997-98 El Niño event, a model configuration with prescribed surface fluxes (ROMS-A

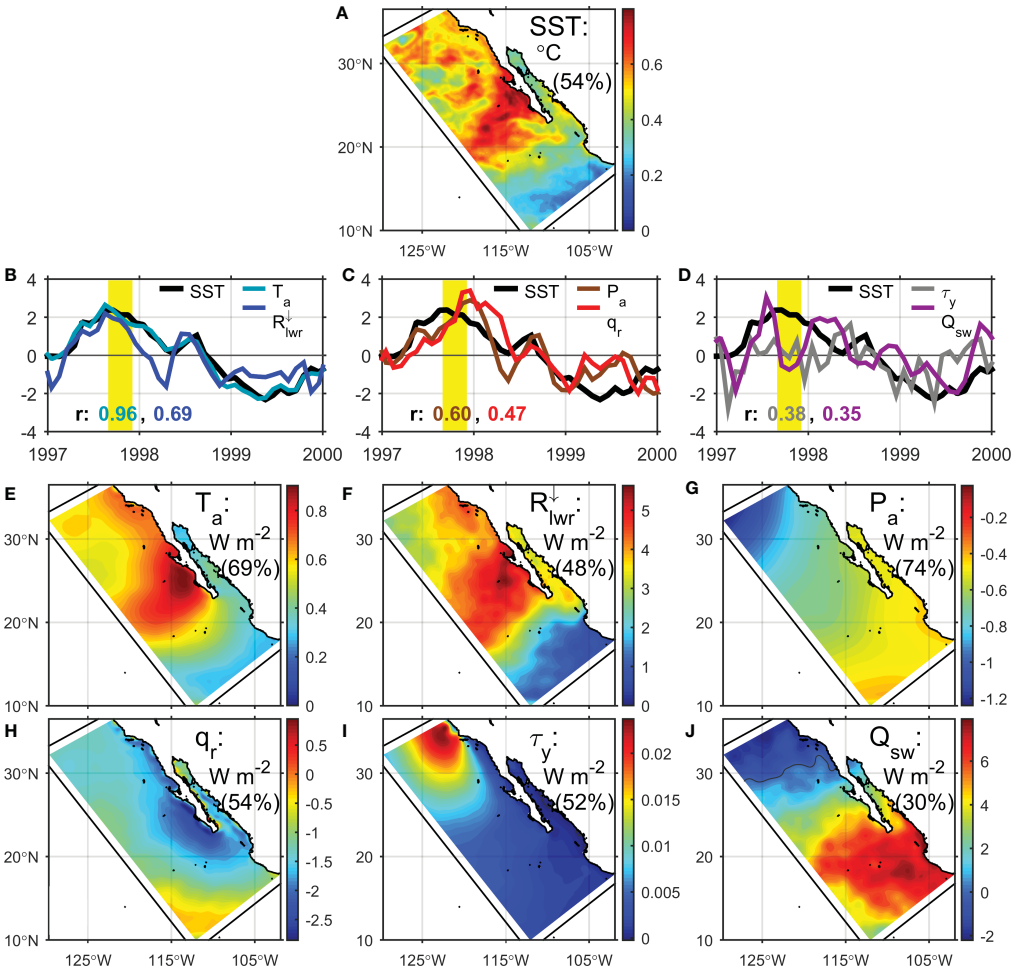

FIGURE 6
Comparison between the first EOF mode of the SST anomaly (see Section 2.1) from ROMS-B experiment **(A)** and those of the atmospheric fields provided to the model: air temperature (T_a; in °C), downwelling longwave radiation ($R^{\downarrow}_{lwr}$; in W m^{-2}), air pressure (P_a; in hPa), relative humidity (q_r; in percentage), along-shore wind stress (τ_y; in N m^{-2}), and net shortwave radiation (Q_{sw}; in W m^{-2}). Only those variables with a significant correlation ($p < 0.05$) are shown. Panels **(B-D)** shows comparisons of the principal components (time series of amplitudes), panels **(E-J)** shows the EOF spatial structures. Percentage of explained variance for each variable is indicated.

TABLE 1 Results from the EOF analysis described in Section 2.1.

Variable	Correl.	% var.
Air temperature (T_a)	0.96	69
Longwave rad. ($R^{\downarrow}_{lwr}$)	0.69	48
Atm. pressure (P_a)	0.60	74
Relative humidity (q_r)	0.47	54
Along-shore wind stress (τ_y)	0.38	52
Shortwave radiation (Q_{sw})	0.35	30
Rain rate	—	42
Net heat flux	—	19
Cross-shore wind stress	—	44

First column indicates the atmospheric variable from which the first principal component (from the first EOF mode) is obtained from its anomaly and correlated with that of the SST anomaly. Second column shows the results of this correlation (if significant; i.e. p<0.05). Third column shows the percentage of explained variance of the anomaly of each variable; it is 54% in the case of SST.

experiment) can present important limitations with respect to one where these fluxes are internally calculated (ROMS-B experiment), and that distinctive atmospheric patterns are associated with this warming. To establish whether these features are exclusive to the 1997-98 event or they occur in other ENSO-induced warm events, herein we diagnose the surface anomalies associated with the 2015-16 El Niño event, responsible for an intense warming off BC Peninsula (Dorantes-Gilardi and Rivas, 2019), from the extended ROMS-A and ROMS-B experiments described in Section 2.1.2. There are remarkable similarities between both El Niño events. In this more recent event (2015-16) the maximum SST anomaly off BC occurred in October 2015 (Dorantes-Gilardi and Rivas, 2019). This peak is reproduced by the ROMS-B experiment but not by the ROMS-A, since the latter experiment underestimates the SST anomaly from October 2015 to April 2016, even presenting negative anomalies from November 2015 to January 2016 (Figure 8A). This underestimation is associated with an excessively large heat-loss in ROMS-A with respect to that in

TABLE 2 Statistical results from the sensitivity reanalysis-downscaling experiments (see Section 2.1.1) for the period from March 1997 to September 1998.

Variable	Correl.	RMSE	MD
Air temperature	0.85	0.69	-0.54
Wind vector	0.88	0.39	0.07
Relative humidity	0.97	0.24	0.08
Longwave radiation	0.97	0.21	-0.08
Atmospheric pressure	0.98	0.17	-0.01
Rain rate	0.98	0.16	-0.02
Shortwave radiation	1.00	0.00	0.00

First column indicates the atmospheric variable that was modified (anomaly was removed) in each sensitivity experiment. Correlations, RMSE, and MD were calculated between the monthly mean SST anomaly from ROMS-B experiment and that of each sensitivity experiment. Units of RMSE and MD are °C.

ROMS-B (Figure 8B). The SST anomaly is more intense off the southern half of BC peninsula (Figures 8C, D) but it does not exist in the ROMS-A experiment which even shows negative values off the whole peninsula (Figure 8E). As in the 1997-98 El Niño event, distinctive features of the atmospheric circulation play an important role in the formation of the warm pool off BC in the 2015-16 event. In particular for the mean atmospheric anomalies in the last three months of 2015, a low pressure located south of BC peninsula, which drives winds coming from the south and the Gulf of California, together with a high pressure located northwest of the Peninsula driving wind from the SCB, cause a convergence of heat off the middle portion of the Peninsula (Figure 8F), which must supply heat onto the ocean surface to generate the characteristic warm pool. Then, all these anomalous patterns seem to be recurrent in intense ENSO-induced warm anomalies off BC, which strengthen the results presented in the previous sections.

4 Discussion

The localized and intense SST anomaly off BC Peninsula is mostly a response to an atmospheric pattern associated with the El Niño. During the months when the maximum SST anomaly is observed (September-November 1997) the eastern Pacific off Mexico was dominated by an sea-level pressure trough extending with a cyclonic circulation which favored an anomalous flow from near-equatorial regions. This anomaly weakened the coastal upwelling and also produced an advective warming of the surface air. As shown in our experiments, this near-surface atmospheric warming is of paramount importance in the heat fluxes off BC Peninsula. Also, anomalies in the local coastal upwelling (changes in sea surface temperature) would be associated with anomalies in the ocean-to-land air-moisture transports (Reimer et al., 2015), which must influence the local humidity (and low-level cloudiness) and hence the downward long-wave radiation, a secondary forcing field in our simulations. However, notice that even if the downward long-wave radiation ($R^{\downarrow}_{lwr}$) shows the second highest correlation

TABLE 3 Same as Table 2 but for the shorter period from September to November 1997.

Variable	Correl.	RMSE	MD
Wind vector	0.64	0.33	-0.05
Air temperature	0.76	1.11	-1.08
Relative humidity	0.93	0.25	0.20
Rain rate	0.96	0.11	-1.01
Longwave radiation	0.97	0.19	-0.16
Atm. pressure	0.98	0.08	0.00
Shortwave radiation	1.00	0.00	0.00

with the SST anomaly in our EOF analysis (Section 3.3.1), it is its difference with the outgoing (upward) long-wave radiation which contributes to the net heat flux. $R^{\downarrow}_{lwr}$ is correlated with the air temperature (r = 0.71), which is in turn highly correlated with the SST (r = 0.94); SST is also correlated with the outgoing long-wave radiation (r = 0.66), which results in that the remainder between this outgoing radiation and $R^{\downarrow}_{lwr}$ is not significantly correlated with the SST anomaly. On the other hand, the synoptic-scale near-surface circulation (enhanced westerly zonal winds in the eastern North Pacific), typical of strong El Niño conditions (Cavazos and Rivas, 2004), also plays an important role in the regional ENSO-induced warming since it modulates the advection of heat and moist from sub-tropical regions. From all the results, we can emphasize the need of a proper representation of the near-surface atmospheric patterns associated with the El Niño phenomenon.

Although our analysis is focused on the El Niño event that occurred in 1997-98, the results are applicable to other intense El Niño episodes, as shown by the additional simulation for the 2015-16 period (Section 3.4). This event shows a warm pool off BC, net heat-flux anomalies, and anomalous atmospheric patterns comparable to those in the 1997-98 event (Figure 8). Also in this 2015-16 event and like in the 1997-98 event, the numerical simulation based on the ROMS-A configuration presented limitations to fully reproduce the timing of the warm pool, showing an early decrease of the SST as it reached its maximum in the observational data (Figure 8A). A similar failure occurred in a previous numerical-modeling study for northwestern BC during this same 2015-2016 event (Dorantes-Gilardi and Rivas, 2019), which had a model configuration essentially similar to the ROMS-A experiment, and this failure limited the analysis of the effects of thermal anomalies on biogeochemical variables in that region. As in our analysis, an excessive heat loss (Figure 8B) may have been responsible for that failure, which could have been solved using internally-calculated surface fluxes (*i.e.*, ROMS-B configuration) to make the modeled warm pool more realistic (Figures 8C, D).

The evaluation of the surface heat-flux budget (Table 4) shows that the latent heat flux has a major role in the anomalous net air-sea heat exchange compared to the other heat-flux components. A simplified but illustrative calculation of the heat-flux components in Eq. (2) was carried out in order to understand the response of its components to a surface warming. To do this, Eqs. (3)-(5) were

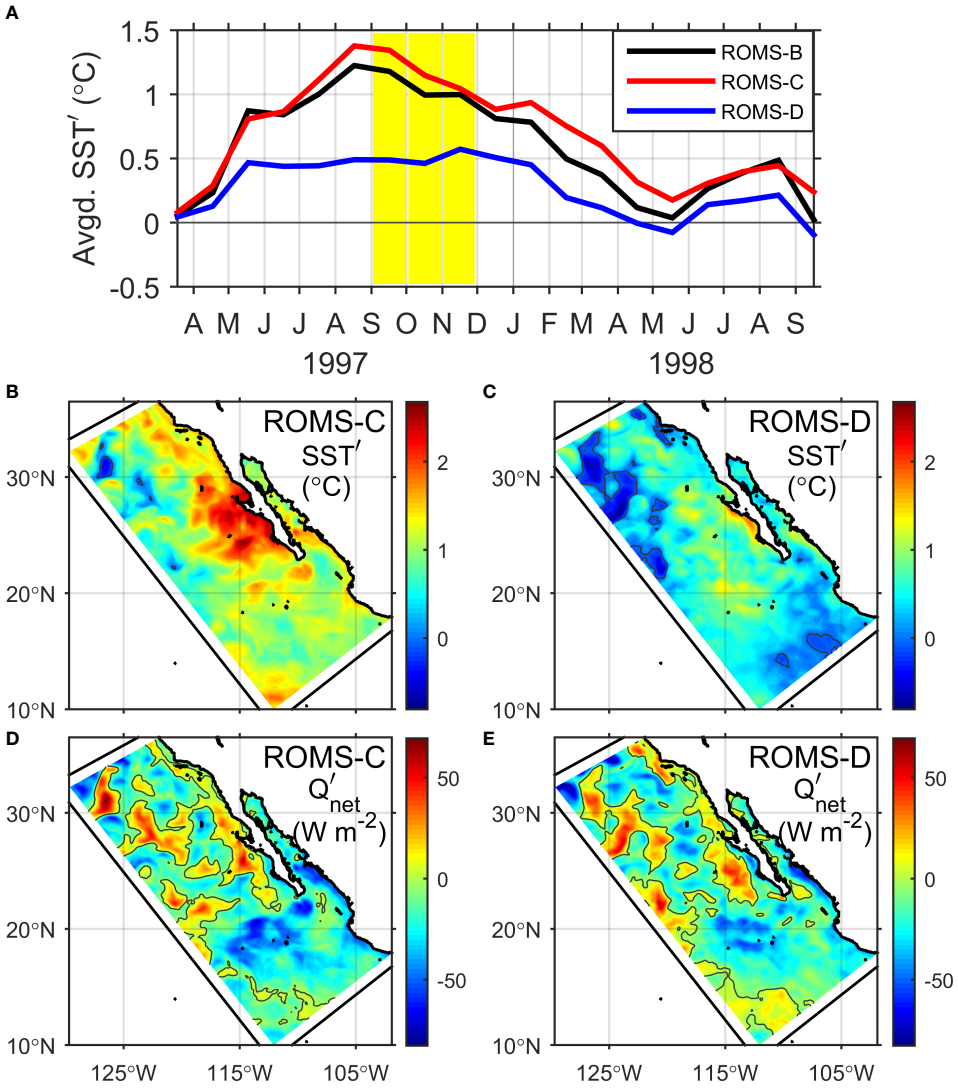

FIGURE 7
(A) Temporal evolution (from March 1997 to September 1998) of monthly-mean, spatially-averaged (within the whole model domain, except the sponge layer) SST anomaly from ROMS-B experiment (black line), and from two sensitivity reanalysis-downscaling experiments (see Section 2.1.1): removing the interannual variability of the wind (ROMS-C; red line) and the air temperature (ROMS-D; blue line). Yellow band indicates the September-November 1997 trimester, period for which the mean SST-anomaly **(B, C)** and mean net heat-flux anomaly **(D, E)** were calculated for ROMS-C **(B, D)** and ROMS-D **(C, E)** experiments.

evaluated for a constant, mean air-sea state within the coastal box off BC Peninsula (Figure 1) but with SST = $T_s + \Delta T$, with $-3°C \leq \Delta T \leq 3°C$. The values for the air-sea variables were taken from the input/output model variables for November 2001, when the monthly-mean SST anomaly was practically null and it could be a climatological state (at least in terms of SST) in which the SST anomaly would be set to ΔT. The results of these calculations are shown in Figure 9A. The latent-heat flux (Q_{lt}) has a more abrupt response to the thermal variation compared to the sensible-heat and long-wave radiation fluxes, it can be more than double when $|\Delta T|$ =

TABLE 4 Mean anomalies of the surface heat-flux budget (W m^{-2}) given by Eq. (2), spatially-averaged within the coastal box off BC Peninsula shown in Figure 1, from ROMS-A and ROMS-B experiments, for September 1997 and September-November 1997.

Experiment	Period	Q_{net}	Q_{sw}	$-Q_{sn}$	$-Q_{lt}$	$-Q_{lw}$	$R^{\downarrow}_{lwr}$
ROMS-A	Sep 97	-30.3	4.0	1.2	-23.8	-5.2	9.5
ROMS-B	Sep 97	20.4	4.0	9.3	3.6	-2.7	9.5
ROMS-A	Sep-Nov 97	-58.7	-0.2	-4.2	-47.2	-3.8	11.0
ROMS-B	Sep-Nov 97	4.2	-0.2	6.4	-10.1	-0.9	11.0

Positive values correspond to heat gained by the ocean.

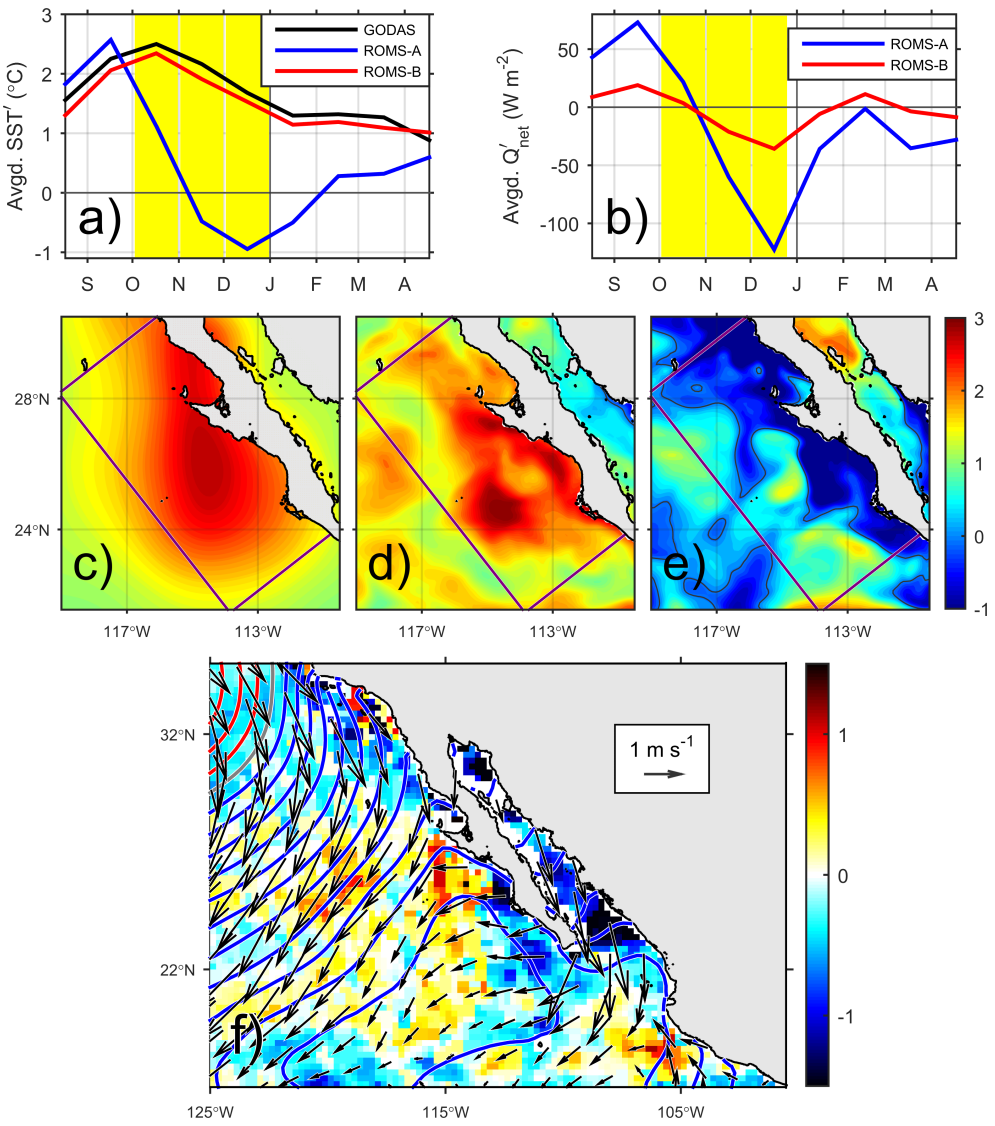

FIGURE 8
Upper row **(A, B)**: Same as Figure 4A, B, but spatially-averaged within the coastal box off BC Peninsula ("BCP" in Figure 1) and for the period from August 2015 to May 2016. Vertical yellow bands indicate the October-December 2015 trimester, period for which the mean SST anomaly (°C) was calculated from the GODAS product **(C)**, and ROMS-B **(D)** and ROMS-A **(E)** experiments. Lower row **(F)**: Similar to Figure 3, but for the October-December 2015 mean, and with pressure contour lines in intervals of 0.2 hPa. The anomalies are defined with respect the 1993-2002 climatology.

3°C (Figure 9A). This explains why the latent flux responds faster to the thermal variations and is more important during the formation of the warm pool, which implies that most of the heat lost to the atmosphere is driven by a vigorous evaporation triggered by surface warming.

Herein we have described the advantages of using internally-calculated surface fluxes in the model configuration, however, another important factor that contributes to obtain better numerical solutions (starting with SST) is the correction term Q_{cr} given by Eq. (1). As the surface heat flux is a strong function of temperature, this correction term is of paramount importance to update the net heat flux Q_{net} according to the instantaneous SST and to prevent the model to drift away from the reference temperature. Figure 9A shows the evaluation of Eq. (1) at SST = $Ts + \Delta T$, using the same air-sea "mean" state mentioned above. Compared to the heat fluxes, Q_{cr} varies about twice faster with the temperature, which can result in an efficient adjustment of Q_{net}. In spite of how efficient this correction can be, its contribution is limited. To show how Q_{cr} works in the two model configurations (ROMS-A and ROMS-B), here we solve the simplified temperature balance given by

$$\frac{\partial \mathrm{SST}}{\partial t} = \frac{1}{\rho_0 C_p}(Q_{net} + Q_{cr}), \tag{8}$$

where ρ_0 and $C_p = 4000$ J kg$^{-1\circ}$ C^{-1} are the density and the specific heat capacity of sea water; these results are shown in Figure 9B. Regardless of whether the initial temperature is higher ($\Delta T = 3$°C) or lower ($\Delta T = -3$°C) than its mean value, the instantaneous temperature converges to a nearly constant value after 8 days in the ROMS-A configuration, and only 4 days in the

ROMS-B configuration. More importantly, the final value obtained in ROMS-B approaches to the reference temperature at $\Delta T = T_{ref} - T_s = -0.04$°C, whereas the final value in ROMS-A presents a bias of ~ -3.7°C with respect to the reference temperature (Figure 9B). This bias results from the balance between the constant Q_{net} value, which makes the solution change indefinitely at a linear rate, and the Q_{cr} term, which approaches to T_{ref}. The relation among the heat fluxes and other variables involved in Q_{net} and Q_{cr} determines not just the amplitude of the bias in ROMS-A, but also the rate of change of the solution. Then, these results emphasize the possible limitations of the ROMS-A model configuration to prevent bias in the SST and thus in other physical variables.

As the model runs, the heat-flux components interact between each other to produce a net surface forcing that modifies the SST, and this change in turn modifies the heat-flux components. The combination of these forcings and feedbacks will determine the values of the resulting SST anomalies, which can be different in each experiment and not necessarily intuitive. For example, ROMS-C and ROMS-D experiments, in which the interannual variabilities of wind (ROMS-C) and air temperature (ROMS-D) were respectively removed, show a net heat flux that is similar in both cases even if the SST anomaly is different between each other (Figures 7D, E). Based on estimates with Eqs. (2)-(5) for September-November 1997 (using air-sea variables averaged for this period and within the coastal region off BC Peninsula) both increasing the wind speed and

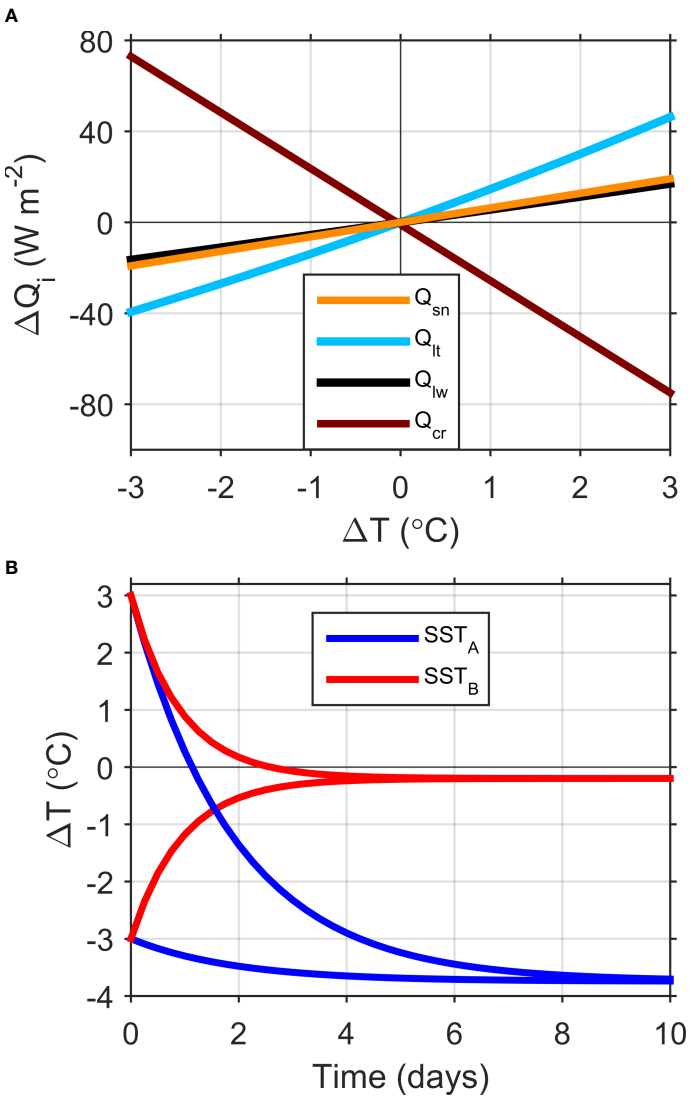

FIGURE 9
(A) Evaluation of the heat-flux components (Q_i; where $i = sn$ for sensible, $i = lt$ for latent, $i = lw$ for long-wave radiation, and $i = cr$ for bias-correction) in Eqs. (3)-(5) described in Section 2.3.1 for SST = $T_s + \Delta T$ (*i.e.*, adding a temperature variation to a "mean" state T_s), and the correction term defined by Eq. (1). The heat-flux results are expressed as variations with respect to the mean state, and as functions of the temperature change ΔT. **(B)** Solutions of the simplified temperature balance defined by Eq. (8), using the ROMS-A and ROMS-B model configurations, with two different initial values ($\Delta T = \pm 3$°C) in each case. In both panels **(A, B)**, The temperature results are expressed as deviations with respect the mean state, and as functions of the integration time. The following values were used for the air-sea variables: $T_s = 20.8$°C, $T_a = 17.0$°C, $q_a = 0.011$, $P_a = 1018.4$ hPa, $\rho_a = 1.22$ kg m^{-3}, $U = 5.2$ m s^{-1}, $R^{\downarrow}_{lwr} = 348.2$ W m^{-2}. $\rho_0 = 1024.4$ kg m^{-3}, $(dQ_{net}/dT_s)_{ref} = -24.6$ W m^{-2}°C^{-1}, and $T_{ref} = 20.7$°C.

reducing the air temperature (wind was 4% weaker and air temperature was 1°C higher than their climatological mean values in September-November 1997) cause an ocean heat loss [ΔQ_{net} = −3.3 W m^{-2} (ROMS-C), -5.1 W m^{-2} (ROMS-D)] and hence a decrease in SST [ΔSST = −0.2°C (ROMS-C), −0.3°C (ROMS-D)]. Based on the inverse ΔQ_i - ΔSST relation (Figure 9A), this negative SST change would cause a positive change in Q_{net} [ΔQ_{net} = +4.4 W m^{-2} (ROMS-C), +6.6 W m^{-2} (ROMS-D)], together with a positive Q_{net} compensation by Eq. (1) [Q_{cr} = +4.1 W m^{-2} (ROMS-C), +6.5 W m^{-2} (ROMS-D)], which in turn would cause a subsequent increase in SST. These rough estimates emphasize the fact that the cooling caused by the original wind and air-temperature anomalies can be compensated and even exceeded by a feedback warming. However, during the model's run these opposing processes act simultaneously to produce a continuously updated forcing which can result in a different final state. On the other hand, ROMS-C presents the relevant difference that modifying the wind causes changes in the sea surface circulation, which can be especially important in near-coastal areas. The anomalously weak wind would cause a decrease in the coastal upwelling and hence the offshore advection of colder water from subsurface levels. This dynamical factor, driven by the momentum flux applied by the surface wind, has direct effects on the SST and the air-sea exchanges, resulting in marked differences of its effects with respect to other atmospheric variables like the air temperature, as well as the magnitude of the SST anomalies.

The heat-flux calculation implemented in this paper has been previously used by other authors. Deutsch et al. (2021) were able to reproduce the 1997-98 El Niño event in the California Current System in a historical simulation with ROMS, computing also online surface heat fluxes and wind stress with instantaneous modeled fields (Renault et al., 2021). In contrast with our paper, these works lack an accurate analysis of ocean physical variables during the El Niño event and they do not identify that online computation of surface forcing with instantaneous modeled fields is critical for the reproduction of ENSO-driven phenomena in the ocean.

Intense El Niño events like the one analyzed in this paper (1997-98) has effects on other oceanic variables in addition to the SST. These effects can be directly or indirectly associated with the regional warming described in the previous sections. In our nested reanalysis, a positive sea-level anomaly ~5 cm - located along the coast from south of Cabo Corrientes to north of Point Conception, with greater values (8-10 cm) seaward from the shelf (Figure 10A) - occurred during the maximum SST event. This anomaly is consistent with coastal observations off central California which show positive sea-level anomalies associated with El Niño events, attributed to the passage of remotely generated and coastal trapped waves that were generated along the equator and propagated to the north along the west coast of North America (Ryan and Noble, 2002).

The physical anomalies described above can have important effects on the biogeochemical variables. As concluded from previous numerical-modeling results, an ENSO-induced regional warming strengthens the stratification that limits the vertical and onshore transport of nitrate onto the upper levels, and results in a subsurface reduction of nutrients (Dorantes-Gilardi and Rivas, 2019). This conclusion is consistent with hydrographic-observational results in the southern California Current System: a deepening of the nutricline off BC Peninsula has been reported during El Niño episodes, especially near the coast (Gaxiola Castro et al., 2010) and, specifically for the 1997-98 period, a deepening of the nutricline and nutrient depletion in the upper levels (from 80-m depth to the surface), associated with positive temperature anomalies at subsurface, was reported for central California from August 1997 through August 1998 (Castro et al., 2002). The chlorophyll field is consequently affected, as corroborated by *in-situ* observations of depth-integrated (0-100 m) chlorophyll-*a* anomalies off BC Peninsula, which showed a negative anomaly during the peak of the 1997-98 El Niño (McClatchie et al., 2016). It has been argued in previous literature (Dorantes-Gilardi and Rivas, 2019) that a regional warming deepens the thermocline and hence moving the subsurface chlorophyll maximum downwards, causing a reduction in the phytoplankton biomass. The oxygen field can be also affected by the regional warming, since its variability in the ocean upper levels is driven by changes in temperature and, in near-coastal areas, by changes in coastal upwelling (*e.g.* Turi et al., 2018). Thus, an anomalous downwelling (weakening of upwelling-favorable conditions) caused by the poleward coastal-wind anomaly like that in September-November 1997 (Figures 3C–E) must induce positive oxygen anomalies along the coast, given the reduced presence of oxygen-poor water from deeper levels. An opposite effect would be expected in offshore regions, where negative oxygen anomalies can occur, associated with a decreased oxygen solubility caused by the increased temperature. These results and notions are somewhat consistent with recent numerical results (Deutsch et al., 2021), which show that the amplitude of interannual variability in nitrate at the base of the photic zone and of oxygen in the thermocline are also both strongly correlated to undulations of the pycnocline, and the largest such anomalies in our simulation period were associated with the 1997-98 ENSO event.

Failing to reproduce the regional warming adequately implies an underestimation of the El Niño teleconnection on oceanic variables. For example, a comparison between two reanalysis-downscaling experiments (one using directly atmospheric forcing and once recomputing them with bulk formulae) suggests an underestimation of ~3 cm in the coastal sea level by the former experiment (Figure 10B), about 50% the coastal anomaly (Figure 10A). This underestimation will introduce large model biases in the biogeochemical fields.

5 Conclusions

Downscaling of global reanalysis products for a region of interest is a tractable alternative for reproducing many of the dynamical features typical of that region that are not resolved in coarse climate prediction and reanalysis systems. These local dynamics are associated with morphologic and physical characteristics of paramount importance. Here we demonstrate that one-way offline nesting of a three-dimensional regional model with global reanalysis products improves the

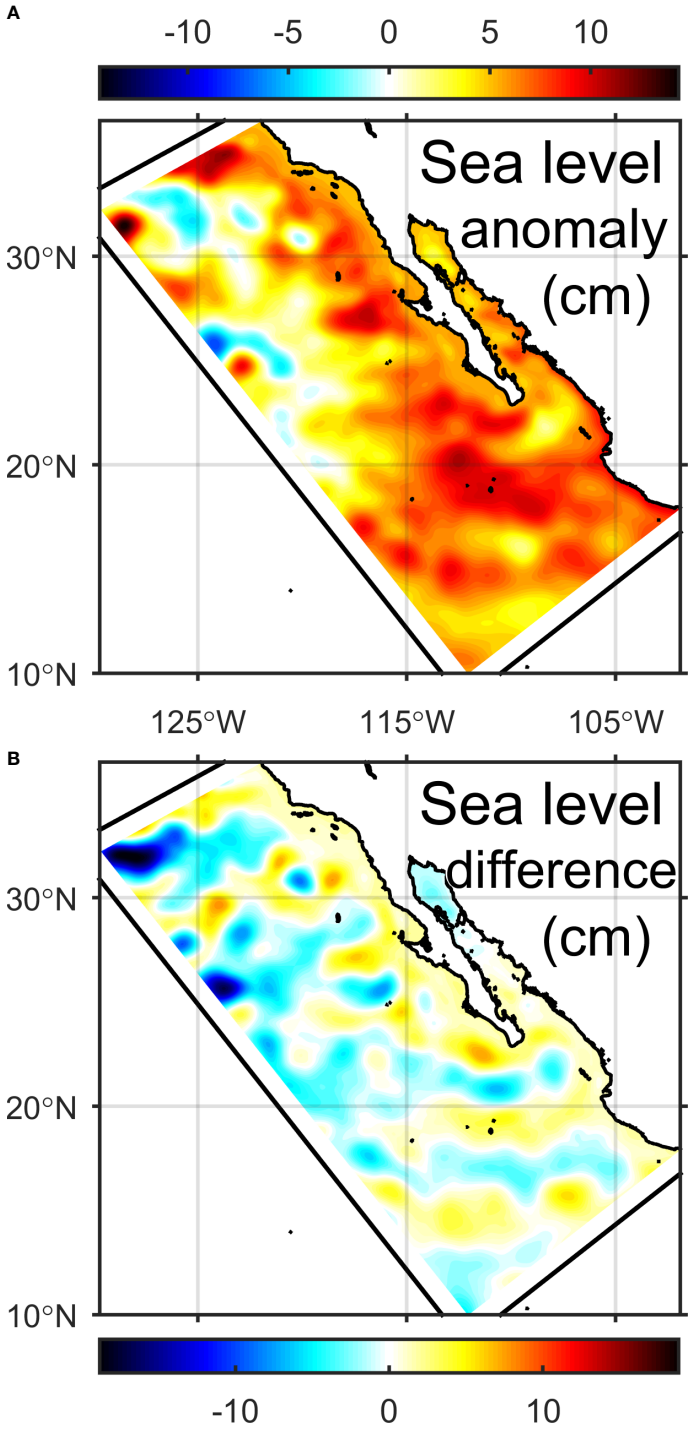

FIGURE 10
September-November 1997 means of **(A)** sea level anomaly from ROMS-B, and **(B)** sea level (climatology plus anomaly) from ROMS-B minus that from ROMS-A.

representation of the local anomaly for the warming off Baja California Peninsula associated with the 1997-98 El Niño event (results also corroborated for the 2015-16 El Niño event). This episode is one of the most intense El Niño episodes in the last decades. Given the important environmental effects of the ENSO on the Pacific Ocean and other regions, improving its representation in numerical simulations and its implication onto the coastal regions will enhance the usefulness of seasonal predictions (Kirtman et al., 2014). We have shown that an accurate representation of the surface fluxes is of paramount importance to reproduce the ENSO-induced SST anomalies. Prescribed heat fluxes can be inadequate for the regional model since they cannot "accommodate naturally" to the atmospheric conditions provided to the model. Internally-calculated surface fluxes provide the

possibility to the model to "adjust" to the atmospheric conditions, as the instantaneous SST is taken for the net heat flux calculation. Nonetheless, it is necessary that the atmospheric fields used to force the model are able to represent the ENSO-driven atmospheric circulation over the Northeastern Pacific, because it is responsible for the advection of warm and humid air onto the near-surface atmosphere off Baja California Peninsula, coming from near-equatorial regions and also from relatively warmer regions from the central Pacific. The atmospheric pattern, specifically the wind anomaly observed as an along-shore wind stream, would also cause weakened upwelling conditions along the Baja California coast during the period of the maximum SST anomaly, contributing to the coastal warming, and enhanced upwelling conditions by the end of the SST anomaly, counteracting the coastal warming and probably helping to cause the disappearance of the regional SST anomaly. Thus, the numerical exercises described in this paper will provide valuable insights to improve the reproducibility of ENSO thermal anomalies and similar signals and open the possibility to asses downscaling of seasonal prediction there.

Data availability statement

The raw data supporting the conclusions of this article will be made available by the authors, without undue reservation.

Author contributions

DR implemented and ran the numerical model, processed and analyzed the data, and wrote and edited the manuscript. FC was host and provided funding, helped with the model implementation, and revised the manuscript. NK was host and provided funding, revised the manuscript. All authors contributed to the article and approved the submitted version.

Acknowledgments

We thank the reviewers for their critical comments and suggestions to an earlier version of this manuscript, especially "Reviewer 1", whose thorough review really enriched this paper. This research was carried out during a sabbatical visit of DR to the NERSC and GFI-UiB in Bergen, Norway, which was funded by project CONACYT-ERC 297701 and from the Strategic Programme for International Research Collaboration from the University of Bergen 2019. During this visit, DR received funding from the Bjerknes fellowship and SPIRE 2019 programmes. DR was also supported by CICESE through the internal project 625118. FC and NK acknowledge the NFR-Climate Futures (309562) and the Trond Mohn Foundation, under project number BFS2018TMT01. This work has also received a grant for computer time from the Norwegian Program for supercomputing (NOTUR2, project number nn9039k) and a storage grant (NORSTORE, NS9039k). The work was also supported from the European Union's Horizon 2020 research and innovation programme under grant agreement No 817578 (TRIATLAS). The GODAS and NARR products were provided by the National Oceanic and Atmospheric Administration (NOAA) - Earth System Research Laboratory (ESRL) Physical Science Division (PSD) through its website: http://www.esrl.noaa.gov/psd/data/gridded/.

Conflict of interest

The authors declare that the research was conducted in the absence of any commercial or financial relationships that could be construed as a potential conflict of interest.

Publisher's note

All claims expressed in this article are solely those of the authors and do not necessarily represent those of their affiliated organizations, or those of the publisher, the editors and the reviewers. Any product that may be evaluated in this article, or claim that may be made by its manufacturer, is not guaranteed or endorsed by the publisher.

References

Adem, J. (1967). Parametrization of atmospheric humidity using cloudiness and temperature. *Mon. Wea. Rev.* 95, 83–88. doi: 10.1175/1520-0493(1967)095<0083:POAHUC>2.3.CO;2

Amante, C., and Eakins, B. W. (2009). ETOPO1 1 arc-minute global relief model: procedures, data sources and analysis. *NOAA Tech. Memorandum NESDIS NGDC-24*, 19.

Arellano, B., and Rivas, D. (2019). Coastal upwelling will intensify along the Baja California coast under climate change by mid-21st century: insights from a GCM-nested physical-NPZD coupled numerical ocean model. *J. Mar. Syst.* 199, 103207. doi: 10.1016/j.jmarsys.2019.103207

Barnier, B., Siefridt, L., and Marchesiello, P. (1995). Thermal forcing for a global circulation model using the three-year climatology of ECMWF analyses. *J. Mar. Syst.* 6, 363–380. doi: 10.1016/0924-7963(94)00034-9

Beckmann, A., and Haidvogel, B. (1993). Numerical simulation of flow around a tall isolated seamount. part I: problem formulation and model accuracy. *J. Phys. Oceanogr.* 23, 1736–1753. doi: 10.1175/1520-0485(1993)023<1736:NSOFAA>2.0.CO;2

Bograd, S. J., and Lynn, R. J. (2001). Physical-biological coupling in the California current during the 1997–99 El niño-la niña cycle. *Geophys. Res. Lett.* 28, 275–278. doi: 10.1029/2000GL012047

Castro, C. G., Collins, C. A., Walz, P., Pennington, J. T., Michisaki, R. P., Friederich, G., et al. (2002). Nutrient variability during El niño 1997-98 in the California current system off central California. *Prog. Oceanogr.* 54, 171–184. doi: 10.1016/S0079-6611(02)00048-4

Cavazos, T., and Rivas, D. (2004). Variability of extreme precipitation events in Tijuana, Mexico. *Clim. Res.* 25, 229–243. doi: 10.3354/cr025229

Chavez, F. (2002). Biogeochemical and ecological consequences of El niño in Eastern pacific upwelling ecosystems. *Investig. Mar.* 30 (suppl.), 102–103. doi: 10.4067/S0717-71782002030100018

Chavez, F. P., Pennington, J. T., Castro, C. G., Ryan, J. P., Michisaki, R. P., Schlining, B., et al. (2002). Biological and chemical consequences of the 1997–1998 El niño in central California waters. *Prog. Oceanogr.* 54, 205–232. doi: 10.1016/S0079-6611(02)00050-2

Cruz-Rico, J., and Rivas, D. (2018). Physical and biogeochemical variability in todos santos bay, northwestern Baja California, derived from a numerical NPZD model. *J. Mar. Syst.* 183, 63–75. doi: 10.1016/j.jmarsys.2018.04.001

Deutsch, C., Frenzel, H., McWilliams, J. C., Renault, L., Kessouri, F., Howard, E., et al. (2021). Biogeochemical variability in the California current system. *Prog. Oceanogr.* 196, 102565. doi: 10.1016/j.pocean.2021.102565

Dorantes-Gilardi, M., and Rivas, D. (2019). Effects of the 2013-2016 northeast pacific warm anomaly on physical and biogeochemical variables off northwestern Baja California, derived from a numerical NPZD ocean model. *Deep Sea Res. Part II* 169-170, 104668. doi: 10.1016/j.dsr2.2019.104668

Fairall, C. W., Bradley, E. F., Godfrey, J. S., Wick, G. A., Edson, J. B., and Young, G. S. (1996a). Cool-skin and warm-layer effects on sea surface temperature. *J. Geophys. Res.* 101, 1295–1308. doi: 10.1029/95JC03190

Fairall, C. W., Bradley, E. F., Rogers, D. P., Edson, J. B., and Young, G. S. (1996b). Bulk parameterization of air-sea fluxes for tropical ocean global atmosphere coupled-ocean atmosphere response experiment. *J. Geophys. Res.* 101, 3747–3764. doi: 10.1029/95JC03205

Gaxiola Castro, G., de la Cruz Orozco, M. E., Najera Martinez, S., Martínez Gaxiola, M. D. , and Rodríguez Gamboa, A. (2010). "Nutrientes: efectos de procesos locales y de gran escala," in *Dinámica del ecosistema pelágico frente a Baja california 1997-2007*. Eds. G. Gaxiola-Castro and R. Durazo (Mexico: Secretaría de Medio Ambiente y Recursos Naturales), 209–226.

Hess, S. L. (1959). *Introduction to theoretical meteorology*. Eds. Holt,, Rinehart, and Winston, (New York), 362.

Huang, B., Xue, Y., and Behringer, D. W. (2008). Impacts of argo salinity in NCEP global ocean data assimilation system: the tropical Indian ocean. *J. Geophys. Res.* 113, C08002. doi: 10.1029/2007JC004388

Jacox, M. G., Hazen, E. L., Zaba, K. D., Rudnick, D. L., Edwards, C. A., Moore, A. M., et al. (2016). Impacts of the 2015-2016 El Ni no on the California current system: early assessment and comparison to past events. *Geophys. Res. Lett.* 43, 7072–7080. doi: 10.1002/2016GL069716

Kahru, M., and Mitchell, B. G. (2000). Influence of the 1997–98 El niño on the surface chlorophyll in the California current. *Geophys. Res. Lett.* 27, 2937–2940. doi: 10.1029/2000GL011486

Kirtman, B. P., Min, D., Infanti, J. M., Kinter, J. L.III, Paolino, D. A., Zhang, Q., et al. (2014). The north American multimodel ensemble: phase-1 seasonal-tointerannual prediction; phase-2 toward developing intraseasonal prediction. *Bull. Am. Meteorol. Soc* 95, 585–601. doi: 10.1175/BAMS-D-12-00050.1

Lavaniegos, B. E., Gaxiola-Castro, G., Jiménez-Pérez, L. C., González-Esparza, M. R., Baumgartner, T., and García-Cordova, J. (2003). 1997-98 El niño effects on the pelagic ecosystem of the California current off Baja California, Mexico. *Geofísica Internacional* 42, 483–494. doi: 10.22201/igeof.00167169p.2003.42.3.939

Magaña, V., and Ambrizzi, T. (2005). Dynamics of subtropical vertical motions over the americas during El niño boreal winters. *Atmósfera* 18, 211–235.

Marchesiello, P., Debreu, L., and Couvelard, X. (2009). Spurious diapycnal mixing in terrain-following coordinate models: the problem and a solution. *Ocean Modell.* 26, 156–169. doi: 10.1016/j.ocemod.2008.09.004

McClatchie, S., Goericke, R., and Leising, A. W. (2016). State of the California current 2015-16: comparisons with the 1997-98 El niño. *Cal. Coop. Ocean Fish.* 57, 5–61.

Mellor, G. L., and Yamada, T. (1982). Development of a turbulence closure model for geophysical fluid problems. *Rev. Geophys. Space Phys.* 20, 851–875. doi: 10.1029/RG020i004p00851

Mesinger, F., DiMego, G., Kalnay, E., Mitchell, K., Shafran, P. C., Ebisuzaki, W., et al. (2006). North American regional reanalysis. *Bull. Am. Meteorol. Soc* 87, 343–360. doi: 10.1175/BAMS-87-3-343

Penven, P., Marchesiello, P., Debreu, L., and Lefèvre, J. (2008). Software tools for pre- and post-processing of oceanic regional simulations. *Environ. Model. Software* 22, 117–122. doi: 10.1016/j.envsoft.2007.07.004

Qiao, W., Wu, L., Song, J., Li, X., Qiao, F., and Rutgersson, A. (2021). Momentum flux balance at the air-sea interface. *J. Geophys. Res. Oceans* 126, e2020JC016563. doi: 10.1029/2020JC016563

Ravichandran, M., Behringer, D., Sivareddy, S., Girishkumar, M. S., Chacko, N., and Harikumar, R. (2013). Evaluation of the global ocean data assimilation system at INCOIS: the tropical Indian ocean. *Ocean Model.* 69, 1–13. doi: 10.1016/j.ocemod.2013.05.003

Reimer, J. J., Vargas, R., Rivas, D., Gaxiola-Castro, G., Hernandez-Ayon, J. M., and Lara-Lara, R. (2015). Sea Surface temperature influence on terrestrial gross primary production along the southern California current. *PloS One* 10, e0125177. doi: 10.1371/journal.pone.0125177

Renault, L., McWilliams, J. C., Kessouri, F., Jousse, A., Frenzel, H., Chen, R., et al. (2021). Evaluation of high-resolution atmospheric and oceanic simulations of the California current system. *Progr. Oceanogr.* 195, 102564. doi: 10.1016/j.pocean.2021.102564

Reyes Bonilla, H. (2001). Effects of the 1997-1998 El niño-southern oscillation on coral communities of the gulf of California, Mexico. *Bull. Mar. Sci.* 69, 251–266.

Rivas, D., and Samelson, R. M. (2011). A numerical modeling study of the upwelling source waters along the Oregon coast during 2005. *J. Phys. Oceanogr.* 41, 88–112. doi: 10.1175/2010JPO4327.1

Rutgersson, A., Carlsson, B., and Smedman, A.-S. (2007). Modelling sensible and latent heat fluxes over sea during unstable, very close to neutral conditions. *Boundary-Layer Meteorol.* 123, 395–415. doi: 10.1007/s10546-006-9150-9

Ryan, H. F., and Noble, M. (2002). Sea Level response to ENSO along the central California coast: how the 1997–1998 event compares with the historic record. *Prog. Oceanogr.* 54, 149–169. doi: 10.1016/S0079-6611(02)00047-2

Santoso, A., Hendon, H., Watkins, A., Power, S., Dommenget, D., England, M. H., et al. (2019). Dynamics and predictability of El niño–southern oscillation: an Australian perspective on progress and challenges. *Bull. Am. Meteorol. Soc* 100, 403–420. doi: 10.1175/BAMS-D-18-0057.1

Shchepetkin, A. F., and McWilliams, J. C. (2003). A method for computing horizontal pressure-gradient force in an oceanic model with a nonaligned vertical coordinate. *J. Geophys. Res.* 108, 3090. doi: 10.1029/2001JC001047

Shchepetkin, A. F., and McWilliams, J. C. (2005). The regional oceanic modeling system (ROMS): a split-explicit, free-surface, topography-following-coordinate oceanic model. *Ocean Modell.* 9, 347–404. doi: 10.1016/j.ocemod.2004.08.002

Smith, S. D. (1988). Coefficients for sea surface wind stress, heat flux, and wind profiles as a function of wind speed and temperature. *J. Geophys. Res.* 93, 15467–15472. doi: 10.1029/JC093iC12p15467

Taylor, K. E. (2001). Summarizing multiple aspects of model performance in single diagram. *J. Geophys. Res.* 106, 7183–7192. doi: 10.1029/2000JD900719

Trenberth, K. E. (1984). Signal versus noise in the southern oscillation. *Mon. Wea. Rev.* 112, 326–332. doi: 10.1175/1520-0493(1984)112<0326:SVNITS>2.0.CO;2

Turi, G., Alexander, M., Lovenduski, N. S., Capotondi, A., Scott, J., Stock, C., et al. (2018). Response of O_2 and pH to ENSO in the California current system in a high-resolution global climate model. *Ocean Sci.* 14, 69–86. doi: 10.5194/os-14-69-2018

Wilby, R. L., and Dawson, C. W. (2013). The statistical DownScaling model: insights from one decade of application. *Int. J. Climatol.* 33, 1707–1719. doi: 10.1002/joc.3544

Xu, Z., Han, Y., and Yang, Z. (2019). Dynamical downscaling of regional climate: a review of methods and limitations. *Sci. China Earth Sci.* 62, 365–375. doi: 10.1007/s11430-018-9261-5

Yu, L. (2019). "Sea Surface exchanges of momentum, heat, and freshwater determined by satellite remote sensing" in *Encyclopedia of ocean sciences, 3rd ed*. Eds. J. K. Cochran, H. J. Bokuniewicz and P. L. Yager (Amsterdam, Netherlands: Academic Press), 15–23. doi: 10.1016/B978-0-12-409548-9.11458-7

frontiers | Frontiers in Marine Science

TYPE Original Research
PUBLISHED 13 July 2023
DOI 10.3389/fmars.2023.1068134

OPEN ACCESS

EDITED BY
Francisco Machín,
University of Las Palmas de Gran Canaria, Spain

REVIEWED BY
David Rahn,
University of Kansas, United States
Xiaobiao Xu,
Florida State University, United States

*CORRESPONDENCE
José M. R. Alves
jose.alves@oom.arditi.pt

RECEIVED 12 October 2022
ACCEPTED 14 June 2023
PUBLISHED 13 July 2023

CITATION
Alves JMR, Miranda PMA and Caldeira RMA (2023) Low-level jets drive the summer intra-seasonal variability of the Canary upwelling system. *Front. Mar. Sci.* 10:1068134. doi: 10.3389/fmars.2023.1068134

Low-level jets drive the summer intra-seasonal variability of the Canary upwelling system

José M. R. Alves[1,2,3]*, Pedro M.A. Miranda[2] and Rui M.A. Caldeira[1,2]

[1]Oceanic Observatory of Madeira - Agência Regional para o Desenvolvimento da Investigação, Tecnologia e Inovação, Funchal, Portugal, [2]Faculdade de Ciências, Institute Dom Luiz, University of Lisbon, Lisboa, Portugal, [3]Faculty of Life Sciences, University of Madeira, Funchal, Portugal

The role of low-level jets in the intra-seasonal variability of the Canary upwelling system during summer is assessed with a fully coupled, high resolution (3km) ocean-atmosphere numerical simulation. Here, low-level jets include the main continental coastal jet, the tip jets of Madeira and the tip-jets of the steep Canary Islands. The coastline shape, orography of northwest Africa and the proximity of Canary islands lead to complex interactions between the jets, that result in strong surface wind intra-seasonal variability on the multiweek time scale. That variability is forced by oscillations in the shape and position of the Azores subtropical anticyclone, through a strong oscillation in the atmospheric boundary layer height. At the coast, coastal-trapped oscillations with a propagation speed, planetary boundary height, offshore extension, and surface pressure compatible with a Kelvin wave occasionally propagate northward, against the synoptic scale surface pressure. While similar processes have already been observed in California, the mechanisms here described appear to result from interactions of continental coastal processes with a set of steep islands close to the coast. The sensitivity of these dynamics to climate change is a challenging question.

KEYWORDS

Canary upwelling system, low-level jets, intra-seasonal variability, Kelvin waves, Azores anticyclone, numerical modelling

1 Introduction

The CANary Upwelling System (hereafter CANUS) extending from Cape Finisterre at the northwest tip of Iberia near 43 °N to Cape Blanc in the Africa northwest coast near 21° N (Figure 1A) is one of the major coastal upwelling systems in the world (e.g., Barton et al., 1998; Mason et al., 2011; Vazquez et al, 2022). Near its northern limit, offshore Iberia, upwelling only occurs in the boreal summer and is episodic, whereas it is restricted to the boreal winter near the southern edge (Aristegui et al., 2009). This seasonality is associated with a large-scale migration of the Azores subtropical anticyclone, reinforced by the variability of the continental Heat Low over the Sahara region, and of the non-permanent

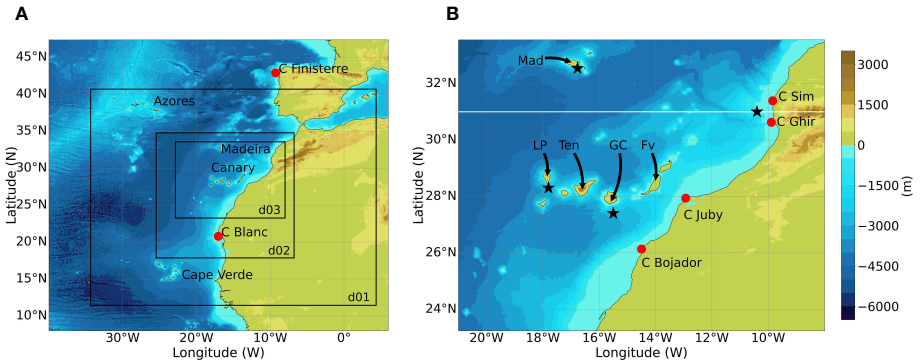

FIGURE 1
Topography and bathymetry from GEBCO (General Bathymetric Charts of the Oceans) 15 arc-second data. In panel **(A)** black rectangles represent geographic limits of the WRF domains. The outer domain (d01) with 27 km grid-spacing, and the inner ones with 9 (d02) and 3 kms (d03) grid spacing, respectively. The 9 and 3 kms grids are also common to ROMS. In panel **(B)** is shown the location of some islands (Mad- Madeira, LP- La Palma, Ten – Tenerife, GC- Gran Canaria, Fv- Fuerteventura). The location of main capes is shown with red points. White line at 31N parallel and black stars indicate regions where some analyses were done.

summer Heat Low in Iberia. The dynamics of these systems is not well understood. While the Heat Lows are essentially locked in position by geographical constraints, they can vary in intensity at sub-seasonal time scales. The anticyclone, however, can move freely in the NE-northeast Atlantic basin, responding to forcing from different external origins, and probably driving the regional variability in the CANUS.

In the CANUS, upwelling is triggered by an almost coast-parallel wind with an intense northerly component. Such wind is favored at the eastern edge of the subtropical anticyclone and will be reinforced by thermal wind equilibrium in the presence of a hot continent. The combination of these two processes leads to the development of a coastal narrow zone of persistent and intensified wind, that define a coastal low-level jet (Beardsley et al., 1987), which is essential for coastal upwelling development. In the presence of islands with significant topography, tip jets will be established without (or even against) a thermal wind forcing (Ólafsson and Bougeault, 1997; Alves et al., 2020). If islands are close enough to the coast, as is the case, tip-jets and coastal jets may interact. Low level wind will also modulate the atmosphere-ocean fluxes of momentum, sensible and latent heat, and is a driving force of the Canary current flowing south-westwards along the African coast. Variability of the jets, at the coast and near the island tips, will perturb the upper ocean. In extreme cases, jets can affect the deep ocean (Pickart et al., 2003), constituting one of the few processes able to trigger deep ocean convection. In the subtropical climate, one expects more modest impacts, but in regions of high ecological and economical value, close to the islands and across the highly productive CANUS.

The dynamics of the major upwelling systems have been the subject of much research, motivated by the need to understand its variability (from sub-seasonal to decadal scales), in the context of climate change. Bakun (1990) identified a positive trend in ship-based observations, within different upwelling systems, a conclusion that has been supported by other studies with different methodologies (e.g., Schwing and Mendelssohn, 1997; Demarcq, 2009; Narayan et al., 2010; Alves and Miranda, 2013), including in simulations of future climate (Miranda et al., 2013; Bakun et al., 2015). The presence of much spatial and time variability in such systems raises, however, many questions concerning their response to changes in the atmospheric circulation and the problem is still open to discussion (Barton et al., 2013; Bograd et al., 2023).

In coastal upwelling systems the atmospheric flow creates an intense positive coastal wind-stress curl that is far from being uniform along the coast. Instead, it is characterized by strong spatiotemporal heterogeneities, due to the compression bulges and the expansion fans frequently observed on the upwind and downwind sides of the main capes, respectively (Perlin et al., 2011). The cross-shore wind profile, sometimes described as the wind drop-off, responds to a combination of various thermodynamical processes (e.g., Boé et al., 2011; Perlin et al., 2011; Desbiolles et al., 2014). At the California coast, Renault et al. (2016a) identified a strong dependency of the offshore wind shape on the coastal orography, coastline orientation and land-sea drag contrast, and to a lower extent on the cooler coastal Sea Surface Temperature (hereafter SST), which may have a stabilizing effect on the lower layers of the air column. The coastal wind heterogeneities are frequently not well represented in satellite data or in atmospheric reanalyses, due to the lack of spatial and temporal resolution. Consequently, when these are used directly to force the ocean surface in high resolution ocean numerical simulations, they may lead to a misrepresentation of the Ekman pumping, offshore transport, associated eddy activity and consequently of the biogeochemical response (Capet et al., 2004; Renault et al., 2016b).

The atmosphere-ocean interaction around Madeira Island was studied with a coupled model, for conditions in the summer 2017 (Alves et al., 2020), which coincided with a period of stronger than usual summer wind. Simulations were performed at resolutions down to 1km, for both the atmosphere and ocean. Miranda et al. (2021) proceeded to an atmosphere-only simulation at 3km grid-spacing, forced by ERA5 boundary conditions for the entire 1979-2018 period, finding evidence of a strong intra-seasonal oscillation in the summer circulation around Madeira and, more importantly, of a multidecadal trend in the regional circulation associated with a

progressive lowering of the atmospheric boundary layer height. Alves et al. (2021) used results from the previous study to one-way force a 35-year ocean simulation and identified an asymmetric response of the local ocean to the atmospheric forcing.

Fully coupled atmosphere-ocean simulations at high resolution constitute the best tool to understand the processes driving the variability in CANUS, distinctive from others coastal upwelling systems. These include not only tip jets, but also island wakes (Caldeira et al., 2005; Grubišic´ et al., 2015), vortex shedding (e.g., Aristegui et al., 1994; Caldeira et al., 2002), and the corresponding wind and currents structures mutual interactions.

The main aim of this study is to assess the intra-seasonal variability of the Africa coastal low-level jet and of the tip-jets generated by the Canary and Madeira archipelagos, with a high resolution (3 km) ocean-atmosphere numerical simulation. This is particularly relevant in a region of intense gradients, for an improved knowledge of coastal thermodynamical processes linked to the jets. The impact of jets in the lower atmosphere and upper ocean variability is assessed through the analysis of oscillations in the PBL height, the occurrence of transient northward coastal trapped events along the NE Africa coast and oscillations in the Azores anticyclone.

While this study focuses on the regional circulation, it may also be relevant at a larger scale, as some of the effects with origin near the islands are observed in basin spatial scales (Xie et al., 2001). Moreover, it is estimated that upper ocean vertical velocities associated with small scale features, as those observed in the lee side of islands, are comparable in magnitude to the vertical velocities forced by the basin-scale wind stress curl (Chelton et al., 2004). The extended and lasting effects of isolated islands in the lower atmosphere and upper ocean may indicate that an upscale effect needs to be considered in global coupled simulations, which eventually would reduce some of the systematic errors observed in these simulations (Bock et al., 2020).

The study is organized as follows: section 2 describes the setup of numerical experiments; section 3 presents some comparisons against remote sensing and *in-situ* observations; section 4 discusses the main results; conclusions are presented in section 5.

2 Setup of numerical simulations

The simulation that follows uses the Coupled-Ocean-Atmosphere-Wave-Sediment-Transport (COAWST) modeling system (Warner et al., 2010), combining the atmospheric Weather Research and Forecasting model (WRF v4.2.2, Skamarock et al., 2008) with the Regional Ocean Modeling System model (ROMS v3.9, Shchepetkin and McWilliams, 2005). Before the 2-way coupled simulation, ROMS went through a 5-year (2014-2018) spin-up simulation forced by ERA5 atmospheric data (Hersbach et al., 2020), including 3-hourly fields of near surface wind, temperature, pressure, relative humidity, precipitation, net shortwave radiation and net longwave radiation.

Ocean boundary conditions (in both the spin-up and the main run) were taken every 24h from a global eddy resolving (1/12°) reanalysis (GLORYS12V1, Lellouche et al., 2021), which in 2019 was forced by ERA5. The coupled simulation started on 1st January 2019, but only the summer months July-August-September (hereafter JAS) were analyzed, due to the known jet's higher intensity during this season (Alves et al., 2021). ROMS used the HSMIT horizontal and vertical advection schemes (Wu and Zhu, 2010). For the boundaries a Chapman condition was used for the free surface (Chapman, 1985), a Shchepetkin condition (Mason et al., 2010) was applied to barotropic (2D) currents and a radiation-nudging condition (Marchesiello et al., 2001) to baroclinic (3D) currents. Tidal forcing was included with 10 tidal constituents (M2, S2, N2, K2, K1, O1, P1, Q1, Mf, Mm) from the TPX09 global model (Egbert and Erofeeva, 2002). WRF used the following parameterizations: the WRF Single-Moment 6-class microphysics scheme (Hong and Lim, 2006); the Kain-Fritch cumulus scheme (Kain and Fritsch, 1990; Kain, 2004) for convective parameterization; the rapid radiative transfer model (RRTM) (Mlawer et al., 1997) for longwave radiation; the Dudhia scheme for shortwave radiation (Dudhia, 1989); the Noah scheme (Chen and Dudhia, 2001) for land surface, the Monin-Obukhov Similarity scheme (Obukhov, 1946; Monin and Obukhov, 1954) for the surface layer and the Grenier-Bretherton-McCaa (GBM) scheme (Bretherton et al., 2004) for the planetary boundary layer. The latter was chosen due to its superior performance in ocean-atmosphere interaction studies (Perlin et al., 2014; Samelson et al., 2020).

The model was configured with 3 nested grids with approximately 27, 9 and 3 km horizontal grid-spacing for the atmosphere, and 2 nested grids with approximately 9 and 3 km, for the ocean. All grids use a Mercator projection. For the vertical discretization, WRF uses 50 hybrid vertical levels, and ROMS 40 sigma-levels, both with increasing resolution near the ocean surface. This grid-spacing and nesting permitted a smooth dynamical downscaling from the nearly 30 km atmospheric ERA5 data and from the 1/12° GLORYS ocean reanalysis, to the region of interest in this study, the 3 km inner domain, represented in Figure 1A. This domain encompasses a central section of the CANUS, and the Madeira and Canaries archipelagos. In WRF and ROMS the location of 9 and 3 km grids is very similar, but to account for minor differences between atmospheric and oceanic grid cells we used the Spherical Coordinate Remapping and Interpolation Package (SCRIP, Jones, 1999) to generate interpolation weights for remapping fields among computational grids. In the coupled simulation, the data is transferred every 30 minutes between models, with the Model Coupler Toolkit (MCT, Larson et al., 2005). For a description of the coupling procedures and of the variables exchanged between models, the reader is referred to Warner et al. (2008). To accurately represent the orography, we used the Shuttle Radar Topography Mission (SRTM) 3 arc-second data and for the bathymetry the 15 arc-second General Bathymetric Chart of the Oceans (GEBCO) data (Tozer et al., 2019).

In the model domain, the highest continental coastal orography is observed near 30°N, with maximum altitude around 2000 m within 100 km of the coastline, corresponding to the southwest limit of the Atlas Mountains (Figure 1). Besides this region, in the 3 km domain, the coastal orography is relatively smooth. Figure 1B shows

the location of the main capes (Sim, Ghir, Juby and Bojador), that in conjunction with the coastal orography and the presence of islands have a relevant role in coastal wind shape, as analyzed later. Madeira and some islands in the Canaries are steep obstacles to the atmospheric flow. In the ocean, their presence is associated with important bathymetric features in the coastal platform, and with steep subsurface slopes near the island edges and near some prominent submarine mountains. For instance, one major canyon is noted, near Cape Ghir. All these bathymetric features may be relevant for ocean eddy generation, by conservation of potential vorticity.

3 Simulations accuracy

3.1 Summer wind and SST

Remote sensed SST and surface wind are used to verify the model accuracy. Wind observations are from the Advanced Scatterometer (ASCAT) ascending path dataset, on an approximately 12 km grid (Verhoef et al., 2012). The analysis of SST uses the Multi-scale Ultra-high Resolution (MUR) dataset, that is made of foundation night SST values, with a daily periodicity, on a 0.01° grid. It comprises MODIS, AVHRR, microwave and *in-situ* retrievals. A comprehensive description of MUR can be found in Chin et al. (2017). Both wind and SST are compared on the model grid, by interpolating the 12 km satellite wind product and averaging the 0.01° SST satellite product.

Wind and SST results are presented, side by side, in Figure 2. Qualitatively, the mean WRF wind taken at 00h UTC (Figure 2B) is very similar to the ASCAT-12 km field (Figure 2A), with strong signatures of the coastal jet at Cape Ghir, and of tip jets downstream of Madeira and of the main Canary Islands. WRF wind speed bias (Figure 2C) is below ±0.5 m.s^{-1} away from the coasts, slightly negative in the wakes and the upstream blocked flow of the islands, slightly positive in the tip jets and on the African coast. These differences mean that WRF perceives a slightly higher impact from topography on the wind field than observed by ASCAT, which is consistent with its higher resolution and with known ASCAT sampling issues near the coast. It is important to mention that a gap free satellite product that is available on a 0.25° grid (Bentamy et al., 2021) fails to represent the tip jets in some islands, smoothing

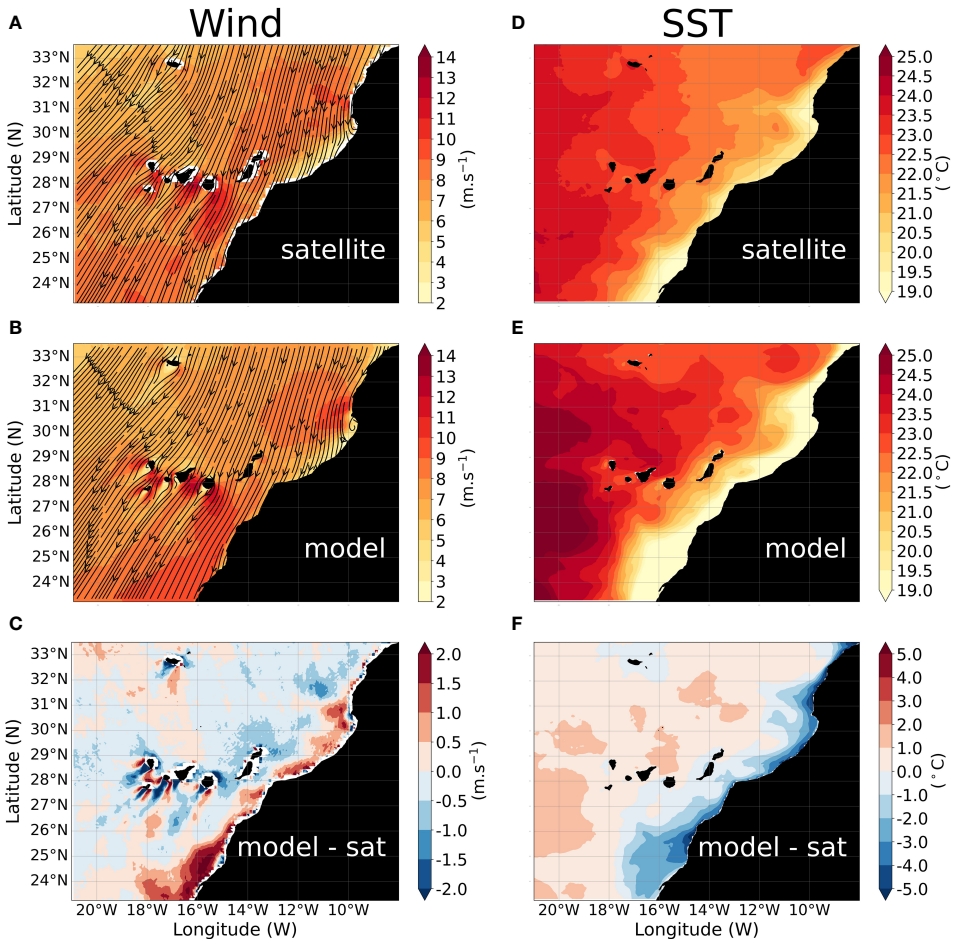

FIGURE 2
Mean surface wind in the model domain at 00 UTC: **(A)** remote sensing by ASCAT; **(B)** WRF at 3 km; **(C)** bias of the WRF simulation. Mean SST in the model domain at 00 UTC: **(D)** remote sensing by Multi-scale Ultra-high Resolution (MUR); **(E)** ROMS at 3 km; **(F)** bias of the ROMS simulation.

out almost all jet-like features (not shown). To further assess the realism of the simulated surface wind, we compared it with data from two meteorological stations of the Portuguese Institute for Sea and Atmosphere (IPMA) located near the East and West flanks of Madeira, which revealed a bias of -0.79 and -0.21 $m.s^{-1}$ and a time correlation of 0.8 and 0.7, for the East and West meteorological stations, respectively. Moreover, the *in-situ* observed wind was also compared with satellite values and showed a similar or a higher bias than the one obtained with simulated data. For instance, in the West flank meteorological station the satellite bias is almost 3 $m.s^{-1}$ higher than that of the modeling wind (see Figure S1). This seems to suggest that some of the difference between model and satellite based data, as seen in Figure 2C, could result from the lack of resolution of satellite data.

For SST, model results are taken at 00h UTC. Observations (Figure 2D) indicate a strong signature of coastal upwelling, with a persistent filament offshore Cape Ghir and a consistent zonal SST gradient perturbed by the presence of the islands. Coastal features in ROMS (Figure 2E) are qualitatively similar to observations (Figure 2D), but more intense. There is a small warm bias (Figure 2F) offshore, only slightly exceeding 1°C outside the Canary current. Near the coast there is, however, a stronger cold bias, exceeding -3°C, in places, that is consistent with the positive coastal wind bias, which result in an intensified upwelling. The coastal cold bias is possible also partially explained by the gap filling in the MUR dataset in the presence of low clouds, that tend to intensify in conditions of coastal upwelling (Samelson et al., 2021). Overall, the mean computed SST bias is +0.28°C. For SST validation, we also used *in-situ* data retrieved from oceanographic buoys maintained by Puertos del Estado Institute. The buoys are located near La Palma, Gran Canaria and Tenerife (see islands locations in Figure 1B), and revealed low cold biases of -0.30°C, -0.31°C and -0.54°C, respectively.

4 Discussion

4.1 Wind stress curl

The atmospheric flow drives the regional ocean circulation by wind stress, and the patterns of wind stress curl force regions of upwelling and downwelling in the coastal ocean. The simulated wind stress curl, represented in Figure 3, has a lot of small-scale noisy features, but is mostly characterized by a slight negative curl in regions away from coastal effects, a strong positive curl on the African coast, and strong dipolar features downstream of the islands. The background negative curl is the signature of the Azores subtropical anticyclone. The strong positive curl on the African coast is due to the cross-coast wind drop-off, as also found in other major upwelling systems, such as California (e.g., Renault et al., 2016a). A distinctive feature of the CANUS is the presence of islands with significant height, generating the strong curl dipoles, therefore confirming a rule of thumb in the upwelling near the islands by a -0.30 time-correlation between wind stress curl and SST nearby Gran Canaria west flank.

The offshore extension of the mean coastal positive curl anomaly is highly variable along the African coast, with potential impact in the regional ocean. Following Renault et al. (2016a), we define the wind drop-off extension as the distance from the coast of a reference contour line of the wind stress curl, here chosen as 3×10^{-7} $N.m^{-3}$ (cf. Figure 3). Different processes may control that extension: coastal topography, coastline orientation in relation to the prevailing wind, and maybe transient processes occurring along the coast (Dorman, 1985; Beardsley et al., 1987; Dorman, 1987) or larger scale subtropical processes unconfined to the coast (Taylor et al., 2008). The maximum drop-off extension is found south of Cape Ghir, coinciding both, with the wake of the southern edge of the Atlas Mountains, and a significant perturbation of the coastline geometry. The latter has a

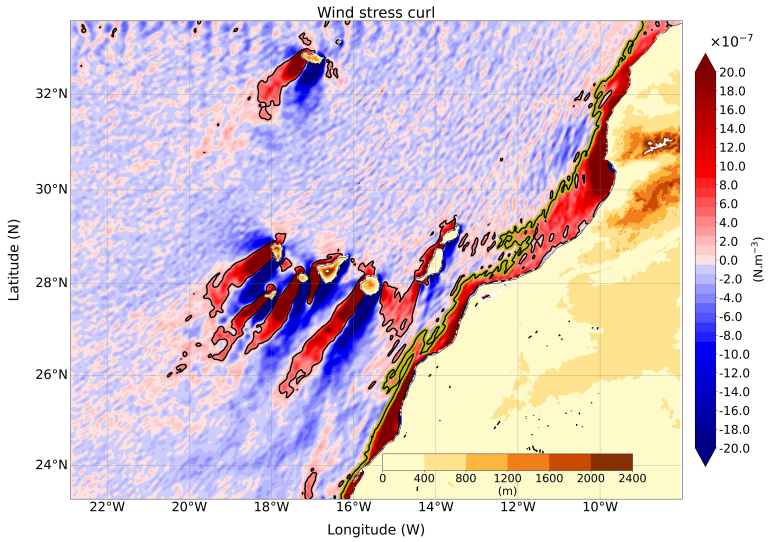

FIGURE 3
Mean summer (JAS) wind stress curl, after applying a 2D Gaussian filter, computed with simulated surface wind stress components at 00h UTC. Yellow-black line denotes the 3×10^{-7} $N.m^{-3}$ contour line, used to define the wind drop-off length. Topography is represented over the continent and islands.

direct impact on the wind direction relative to the coast, a parameter that will control the efficiency of Ekman pumping to generate upwelling. As shown in Figures 2A, B, C, E, the regions of intensified coastal upwelling coincide with sections of the coast which are almost parallel to the prevailing wind.

4.2 Heat fluxes

The spatial distributions of the summer mean latent and sensible heat fluxes (Figure 4) show the combined effect of coastal upwelling and low-level jets. Both fluxes are positive in the offshore region, where the ocean is warming and moistening the atmosphere. The latent heat flux presents maxima near most islands (except the two closest to the coast) coinciding with the tip jets and decreases to very low values close to the continental coast. The sensible heat flux is intensified in the Madeira eastern tip jet but is, however, very small near the Canaries and negative near the African coast, where the atmosphere is being cooled, indicating that the SST cooling by upwelling is more important than the increased transfer coefficients at the low-level jets.

4.3 Planetary boundary layer height and mixed layer depth

The strong signature of both, the African coast and of the different islands, in the atmospheric circulation, with quasi-permanent maxima of low-level jets at preferred locations, even with time varying oscillations in their intensity, suggests the need to look at the spatial structure of the atmosphere and of the ocean boundary layers. The atmosphere-ocean interactions lead to a strongly perturbed mean spatial distribution of the boundary layer in the atmosphere (Figure 5A) and ocean (Figure 5B). The atmospheric PBL height varies widely from near 200 m in the more active upwelling spots on the African coast to near 1400 m in the NW of the domain, with PBL subsidence downstream of the islands and main capes. The ocean Mixed Layer Depth (MLD) is roughly a mirror image of the former, with deeper MLD in regions of stronger wind, where PBL height is lower, an indication of the role of wind stress in driving the vertical mixing in the upper ocean.

4.4 Low-level jets variability

All major coastal upwelling systems develop low-level jets, usually observed at about 400m height (Lima et al., 2022), that eventually may interact with the islands jets. The focus here is in the intra-seasonal variability of those jets, directly associated with the corresponding variability of the underlying ocean. By intra-seasonal variability, we mean all variability with timescales less than 3 months. Miranda et al. (2021) found that, in the case of the Madeira tip jets, the variability is controlled by oscillations in the Azores Anticyclone, through a variability of the Planetary Boundary Layer (PBL) height at a time scale of weeks. Figures 6 and 7 show that such process extends throughout the Canary system, affecting both the tip jets of the different islands and the African coastal jet. While the jets are quasi-permanent features of the summer circulation, their intensity varies at week to multiweek time scales by a large factor.

The intra-seasonal variability of the jets is larger at Madeira, the island less affected by the African coastal jet, but all jets seem to oscillate at comparable timescales, and they all occasionally relax to low intensity (Figure 6). Considering the extension of CANUS, one would not expect a perfect synchronization between the jets, neither a simple connection to the PBL height at a single representative upstream location as found for Madeira (Miranda et al., 2021). Instead, Figure 7 proceeds to a more regionalized view by looking at composite means of the low-level wind speed for the lower tercile of the mean PBL height along the 31N parallel (Cape Ghir, cf. Figure 1B) and the corresponding upper tercile. With a lower PBL height (Figure 7A), the coastal jet widens throughout the CANUS almost to Madeira longitude, with strong tip jets in all islands; with higher PBL height (Figure 7B) all jets attenuate, and the continental coastal jet is more evident close to Cape Ghir and south of the Canaries. The intense dependence of surface wind on PBL height is also evident in the terciles differences to the mean wind speed (Figures 7C, D). In these panels the highest differences (about +- 2 $m.s^{-1}$) are observed near the islands, particularly the Canaries, revealing the importance of island orography on the PBL height and consequently on the surface wind. Moreover, it also shows the importance of a high-resolution simulation to assess the islands effect, otherwise the islands orography and its impact would be too smooth.

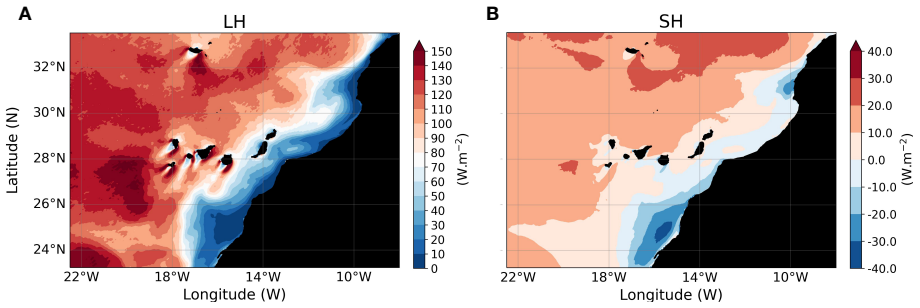

FIGURE 4
Summer (JAS) mean numerical simulated: **(A)** latent and **(B)** sensible heat fluxes at 00 UTC.

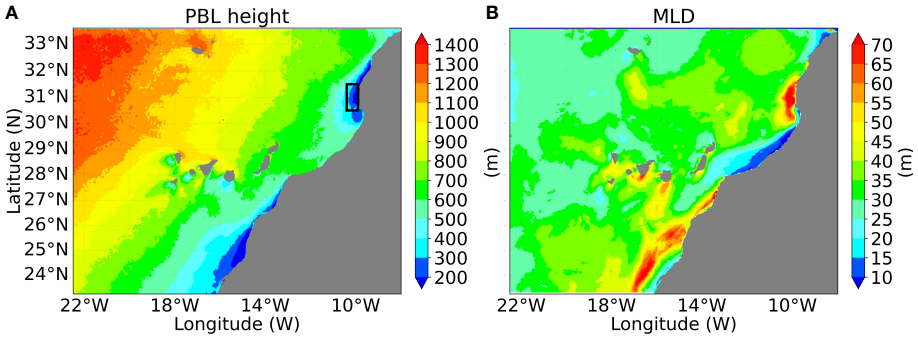

FIGURE 5
Summer (JAS) mean: **(A)** Planetary Boundary Layer height. Black rectangle near Cape Ghir shows region where the mean PBL height was taken to compute Kelvin wave phase speed; **(B)** Mixed Layer Depth. Values at 00h UTC. To compute the PBL height, it was considered the altitude where is attained the maximum of the square of Brunt-Väissälä frequency in the lower atmosphere. To compute the Mixed Layer Depth, it was considered a threshold of 0.3 kg.m^{-3} between the ocean surface density and the ocean density at the mixed layer depth.

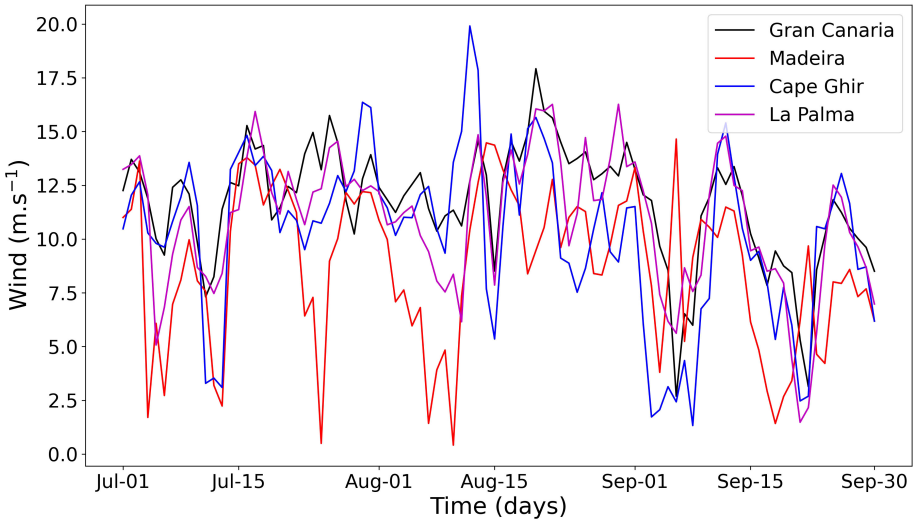

FIGURE 6
Time series of summer (JAS) numerical simulated (WRF) surface (10m) wind speed at 00h UTC at 4 locations representing jets in the Canary system. (Stars in Figure 1B show locations).

The wide oscillation that takes place at the multiweek time scale in CANUS, is even more evident in Figure 8, showing vertical wind speed composite means for the lower and upper terciles of PBL height at 31N and at 00h UTC. In these panels, the PBL height varies by a factor of 2 in the whole zonal section. The jet maximum always remains close to the top of the PBL. The abrupt lowering of the PBL near the coast fits the conceptual model proposed by Beardsley et al. (1987) from observations, at a time without the support of global reanalyses.

A more detailed view of the along coast wind (Figure 9A) reveals that most of the time the wind flows southwards along the African coast, with a clear diurnal cycle, apart from the bay south of Cape Ghir (30N) where a cyclonic circulation imposes a northward flow. Besides the diurnal cycle, visible in the power spectral density (Figure 10) by a peak at 1.16×10^{-5} Hz (24 h period) and of the two main sub-daily harmonics at 2.31×10^{-5} Hz (12 hours), at 3.52×10^{-5}Hz (8 hours), it is also noted a peak at 9.26×10^{-7} Hz, corresponding to a multi-weekly frequency. This latter peak is in agreement with the week and multi-week wind variability noted before in the surface wind time series (Figure 6). The cape Ghir nearby high orography and the regional strong coast veer lead to a high variability in the along coast wind at 31N, noted by modes of oscillation clearly more intense than at other latitudes (green line in Figure 10), and by computed standard deviation and variance local maximums (not shown). The computed narrow 90% confidence band of each line (not shown), demonstrate the peaks statistical accuracy.

The evolution of the along coast wind concerning the full JAS period of 2019 (Figure 9A) also shows at least 3 northward propagating wind reversals, from south of Cape Ghir to the

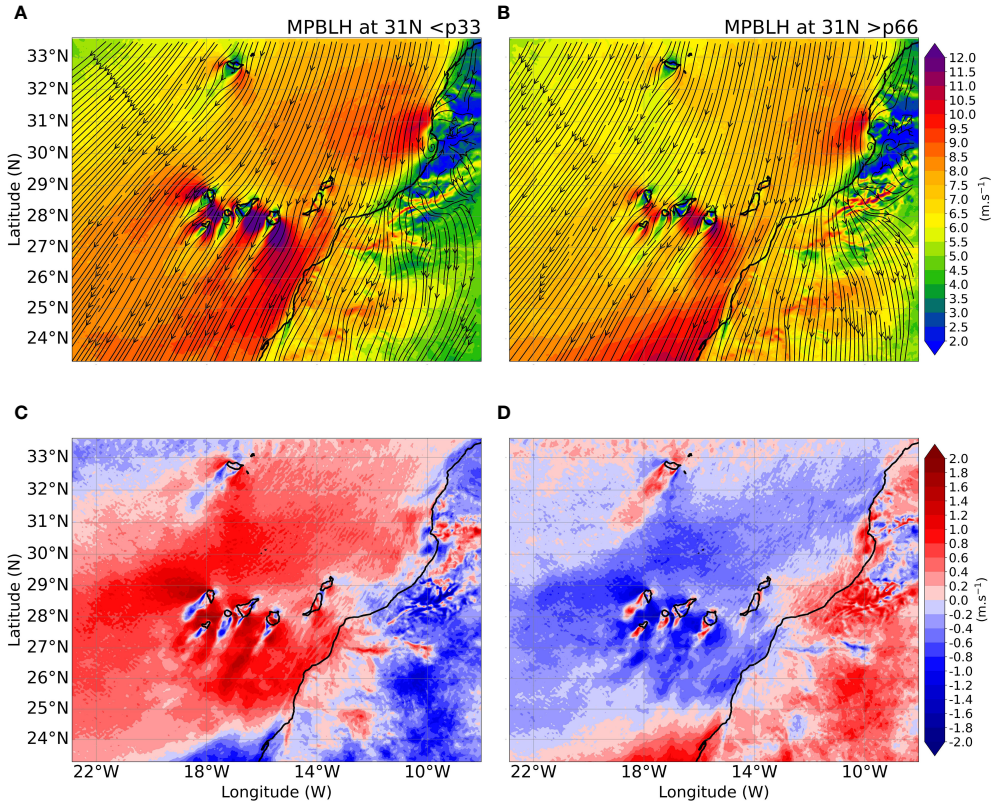

FIGURE 7
Composite of summer (JAS) mean surface (10m) wind speed for: **(A)** the lower tercile of planetary boundary layer height at 31 N (white line in Figure 1B); **(B)** the corresponding upper tercile. **(C, D)** the differences to the mean wind speed, respectively for **(A, B)**.

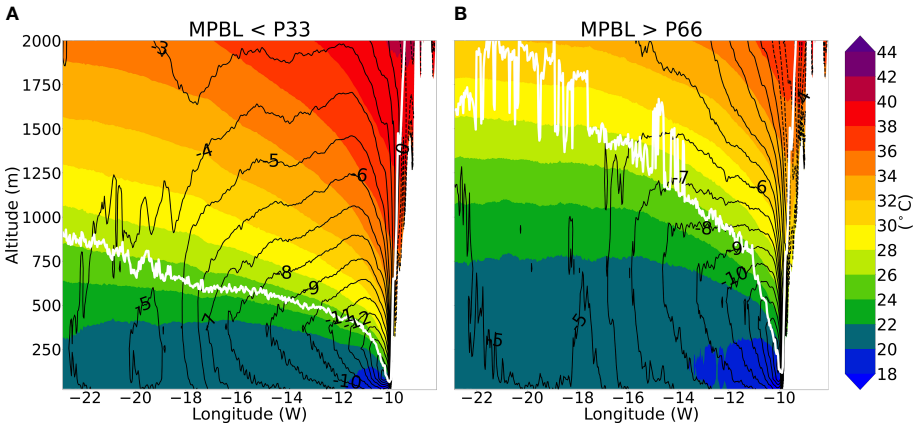

FIGURE 8
Composites of summer (JAS) mean wind in $m.s^{-1}$ (black isolines) at 31N, 00 UTC for: **(A)** lower tercile of PBL height and **(B)** upper tercile. Potential temperature represented by color shading and PBL height represented by white line.

northern limit of the domain, lasting a few days. From 1979 until 2018, the northwest Africa, summer (JAS) Hovmöllers of ERA5 surface wind along the coast, show 2-3 northward wind reversals per summer season (not shown) despite the 30 km data spatial resolution, which shows the recurrence of this phenomena in the studied region.

However, the wind reversal events are not simultaneously observed along the coast. Indeed, a detailed view of the July event (Figures 11A, B) puts in evidence a clear northward propagation of the wind reversal accompanied by a less clear, but still visible, corresponding propagation of a positive anomaly in the PBL height. The wind speed perturbation propagates relatively to the ground at

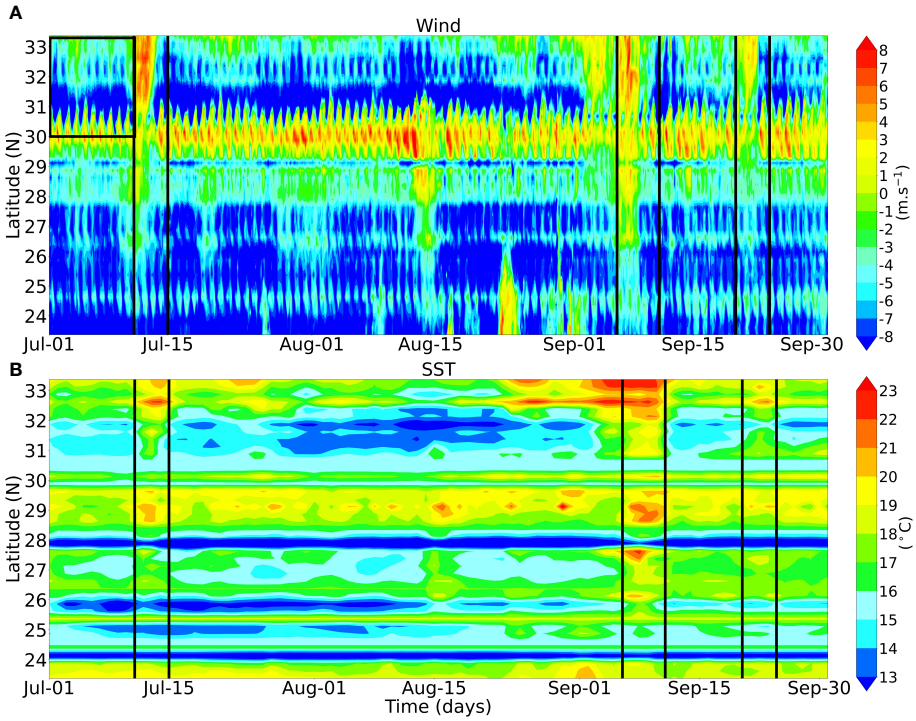

FIGURE 9
Hovmöllers of **(A)** along coast wind, and **(B)** along coast SST, during JAS 2019. Vertical lines show regions and dates where the Kelvin wave effect is noted. In panel **(A)** the black rectangle shows the area used to compute the mean upstream wind, before the July wind reversal.

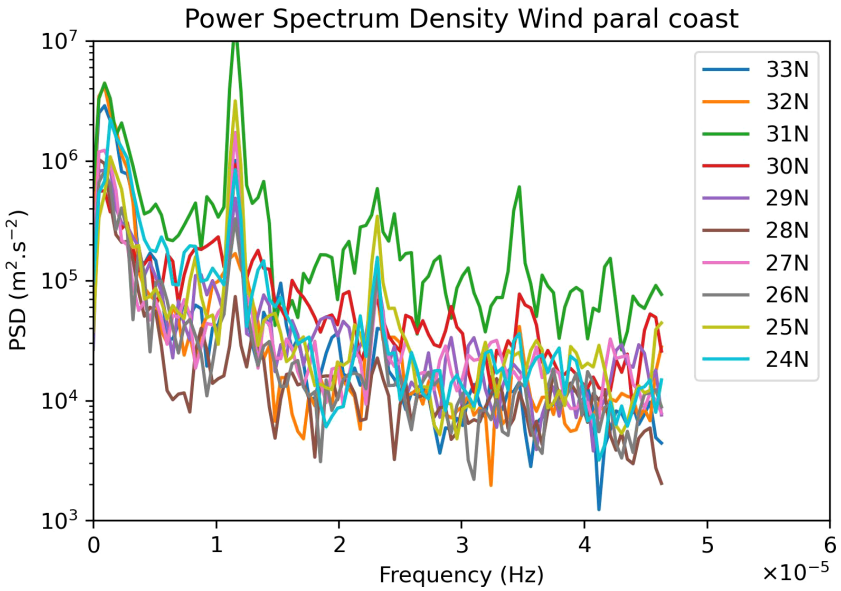

FIGURE 10
Power spectrum density of surface wind parallel to the coast every 3 hours, from 24N until 33N, during JAS 2019.

a mean speed of 3.8 m.s^{-1}, as shown by the star's positions, in panel 9A, that show the maximum wind northward propagation.

Dorman (1985; 1987) and Beardsley et al. (1987) identified in the California current upwelling system the occurrence of similar short-lived episodes of near coast wind reversal, accompanied by changes in the atmospheric PBL height, propagating northward. These were described as episodes of upwelling relaxation and were attributed to coastal trapped atmospheric events.

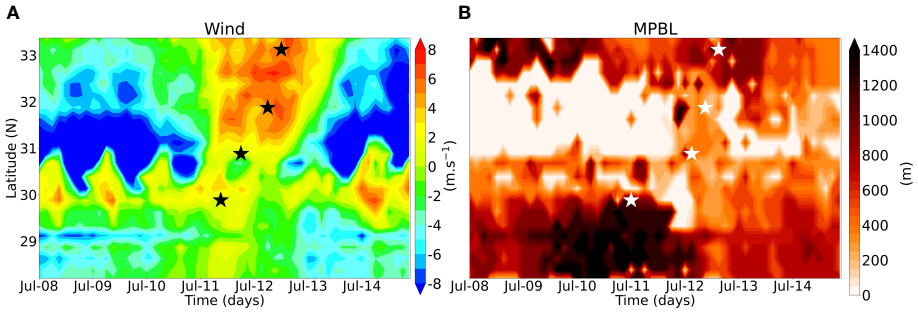

FIGURE 11
Hovmöllers of **(A)** surface (10m) along coast wind speed, and **(B)** near coast atmospheric boundary layer height, with data every 3 hour (00h, 03h, 06h, 09h, 12h, 15h, 18h and 21h UTC). Stars in panels **(A)** and **(B)** show the mean highest wind speed and PBL height at 30N, 31N, 32N and 33N, between 10-14 July.

Following the conceptual 2-layer model discussed in Dorman (1985), after analysis of potential temperature profiles in Cape Ghir zone, we computed a mean value of 293.5 K for the potential temperature of the lower layer (marine layer), that goes from ocean surface until a Brunt-Väisälä frequency square local maximum, and, a mean value of 302.5 K for the upper layer, that goes from the upper limit of the lower layer until an upper Brunt-Väisälä frequency square local maximum. These potential temperature mean layer values and the local mean 250 m PBL height, observed near cape Ghir (black rectangle in Figure 5A) permitted to compute the Kelvin wave phase speed, following eq 4 of Dorman (1985) (eq S1 in the supplementary material) with a value of 8.6 $m.s^{-1}$. But because the perturbation travels against a mean upstream flow of about 4.6 $m.s^{-1}$, between 30N and 33.2N, during the 10 days preceding the analyzed event (black rectangle in panel 9A), the perturbation ground-relative speed is near 4 $m.s^{-1}$, a value close to the simulated value (3.8 $m.s^{-1}$) of propagation to the north of maximum southerly wind.

Further evidence of a Kelvin wave is the geometry of the northward propagation event, clearly anchored at the coastline (Figure S2) excluding the hypothesis of a synoptic disturbance (like a front) as the cause of the wind anomaly. Moreover, the offshore extension of the coastal anomaly matches reasonably well the theoretical offshore extension of a Kelvin wave (eq.5 of Dorman, 1985 and eq S2 in supplementary material) that is about 53 km at 31N. Finally, the wind reversal coincides with transient positive anomalies of surface pressure (Figure S2) as would be expected for a Kelvin wave (Dorman, 1985).

4.5 The larger scale variability of the Azores anticyclone

The control of the PBL height in an extended region (Figure 5A) is certainly unrelated to coastal trapped perturbations, which, as mentioned before, decay exponentially in the cross-shore direction. Indeed, the larger scale environment driving the variability of the CANUS is predominantly dominated by the Azores anticyclone. As shown in Figure 12, built from 1979-2018 July-August-September ERA5 data, the lowering of the PBL height offshore Cape Ghir occurs when the anticyclone core is less intense, smoother and extends in ridge through the Bay of Biscay towards NE France and the English Channel, as noted by the displacement of 1020 hPa isobar, with an intensification of the geostrophic wind south-west of Iberia, leading to a stronger and wider coastal jet near Cape Ghir, extending almost to Madeira, and to intensified tip jets in both Madeira and the Canaries, as also clearly noted before in Figure 7. In contrast, higher PBL heights are associated with an anticyclone more intense in its core and more constrained in its zonal extension. These results are very similar to the 40-year mean shown in Miranda et al. (2021), but with a different compositing approach.

4.6 Variability in the upper ocean

Although not so intense as for surface wind, the coastal ocean surface temperature also shows variability, notably the one associated with wind reversals (Figure 9B). During the wind reversal event, of 11-13 July the coastal SST attains a relative maximum. Similarly, two other SST maxima in the same region, in the first and second fortnights of September are also coincident with the two other wind reversals events, with about one-two days of delay due to ocean inertia. In short, coastal trapped Kelvin waves are associated with periods of upwelling relaxation, as noted before in the California coast (Beardsley et al., 1987).

The cross-correlations of the SST at Cape Ghir with the surface wind at Cape Ghir, Gran Canaria, Madeira and La Palma (Figure 13A) show the co-variability of these two variables at four distinct locations where intense jets are usually observed. The maximum computed correlations, noted with a lag of one or two days, range from -0.37 at Madeira to -0.57 at La Palma. The lowest correlations are observed at Madeira jet, the one more distant from the Africa coast and consequently the less synchronized to the others, as noted before in surface wind time series (Figure 6). These values show that a significant part of the SST variability near the Africa coast is due to the jets variability. We hypothesized that some of the unexplained variability may be due to larger scale ocean and atmosphere dynamics, a research topic that is beyond the scope of the present study due to the constrains imposed by the geographic limits of the computational domain. Nevertheless, the impact on

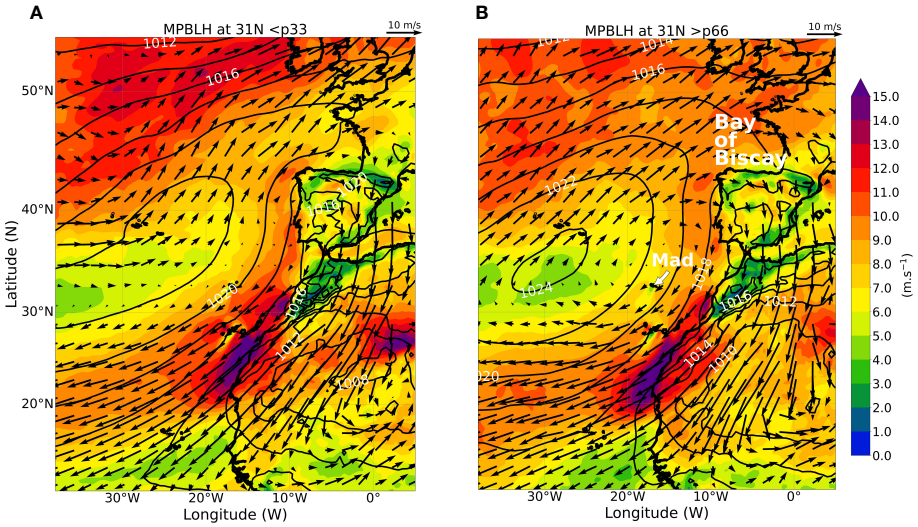

FIGURE 12
Summer (JAS) 10m wind (color shading and arrows) and surface pressure contours from 1979-2018 ERA5 data. Composite for the: **(A)** lower PBL height tercile at 31N and **(B)** upper tercile. In panel **(B)** are shown the Madeira Island and Bay of Biscay locations.

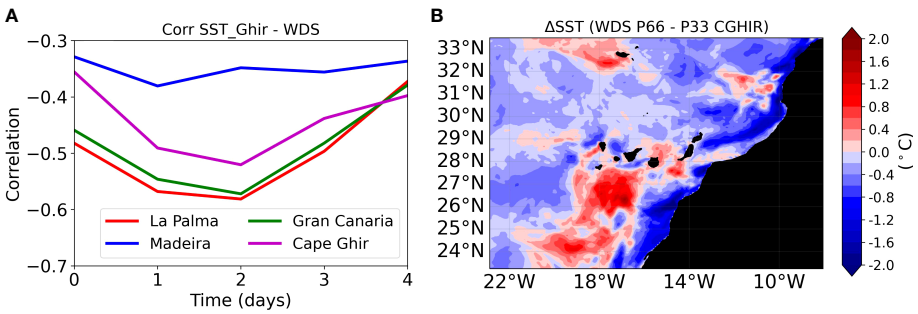

FIGURE 13
(A) Cross-correlation between SST and surface (10m) wind speed near Cape Ghir, Madeira, Gran Canaria and La Palma. For exact location of the time-series see stars positions in Figure 1B. **(B)** Mean SST difference between the surface wind speed upper tercile days (p66) and the lower tercile days (p33), near Cape Ghir.

ocean surface of the different wind regimes imposed by the jets is clearly noted in Figure 13B where is shown the SST difference between the wind speed upper tercile days and the lower tercile days at Cape Ghir. Similar figures for Madeira, Gran Canaria and La Palma jets show a similar pattern (not shown). As expected, near the coast a cooler ocean surface is observed when the jets are more intense, with values, as low as, -2°C. It is interesting to note that the cooler ocean surface is still verified near the west limit of the computational domain, a possible sign of the large-scale impact of the jets. The main exception to a cooler ocean surface during windy days occurs in the lee of the islands, due to a lower cloud cover that implies an intensified incident radiation, as verified in the simulated data (not shown).

The top-level ocean circulation (Figure 14) varies on longer timescales than its atmospheric counterpart, but is characterized by an intense mesoscale structure, with counterrotating eddies and offshore filaments, as noted in previous studies (e.g., Barton et al., 2004). Two main features, whose origin strongly depends on the jets, characterize that circulation: the southward Canary current along the African coast, and the eddy train propagating westwards in the subtropics north of 30N. The latter was identified by Sangrà et al. (2009) as the Madeira corridor. The Canary Islands, and to a lesser extent Madeira, mark the origin of eddy trains propagating south-westwards into the tropics. These eddies are a response to land-atmosphere-ocean interactions, which lead to atmosphere and ocean vortex shedding, in the most dynamic regions of the tip jets. It is well known that ocean eddies have an important role in the zonal transport of the properties of the upwelling zone to the oligotrophic open ocean. For instance, Sangrà et al. (2009) estimated that the total primary production related to westward eddies may be as high as the total primary production of the Canary upwelling system. Due to the estimated long life (>3 months) of these mesoscale eddies, we will no further analyse them here, but this is certainly a relevant issue to examine in a longer high-resolution ocean-atmosphere coupled simulation.

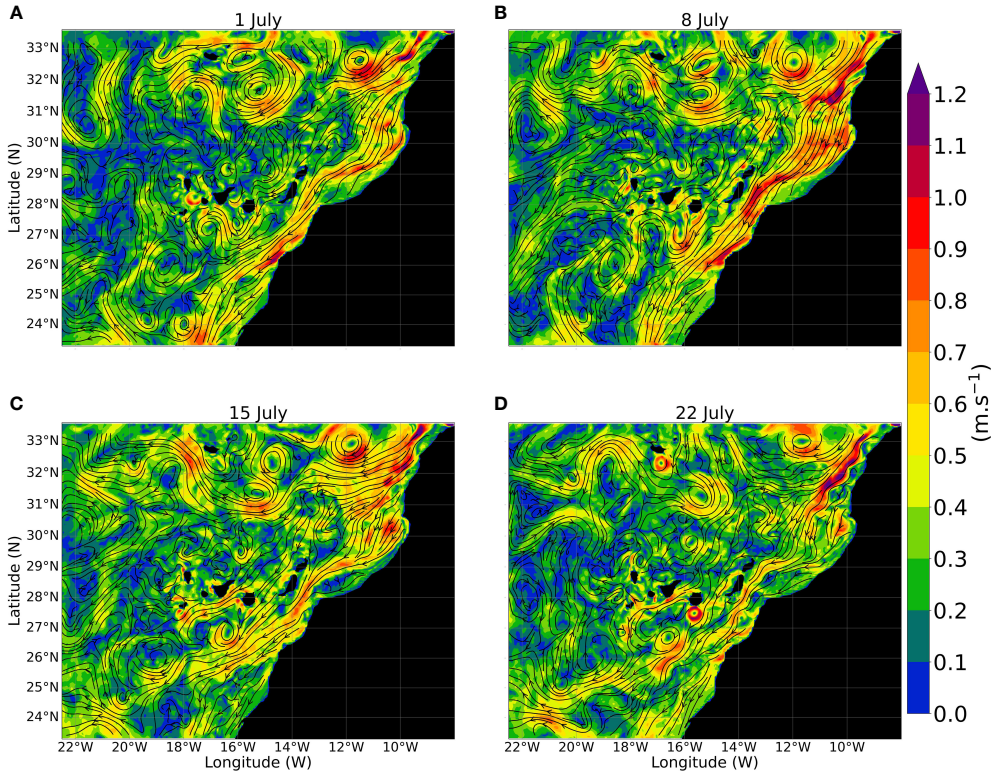

FIGURE 14
Weekly evolution (July 2019) of the ocean circulation. **(A)**1 July, **(B)** 8 July, **(C)** 15 July and **(D)** 22 July. Streamlines represent surface current direction and color shading indicates the currents intensity.

5 Conclusions

The complex mesoscale dynamics of coastal upwelling systems remain a source of uncertainty in the context of climate change. A realistic representation of the processes driving such dynamics, requires the development of fully coupled atmosphere-ocean simulations at high resolution. That was the approach followed here, attempting to test the applicability of proposed conceptual models in the conditions of the Canary system, and to explore specific issues that differentiate this from other upwelling regions. Due to computational constraints, the study was focused in one summer season and limited to the core of the CANUS, south of the Gulf of Cadiz, but in a domain that includes the impact of the SW limit of Atlas Mountains and the impact of the Madeira and Canary archipelagos.

The summer mean north-easterly atmospheric flow was found to be rather steady, along the edge of the Azores anticyclone, with persistent upwelling along the coast, except for the secluded bay south of Cape Ghir. At the intra-seasonal time scale, that flow varied significantly in strength, in a process that is driven by changes in the location and intensity of subtropical high and is accompanied by large oscillations in the height of the atmospheric boundary layer in a wide region, confirming a previous result from a much longer but uncoupled atmospheric simulation (Miranda et al., 2021). In the nearshore region, other oscillations that propagate against the synoptic scale surface pressure gradient, were identified, affecting the atmospheric flow near the coast. Occasionally these coastal trapped oscillations lead to a reversal of the along coast wind north of Cape Ghir associated with a northward surface wind and PBL height positive anomaly propagation at a speed, offshore extension, and surface pressure coastal anomaly compatible with an atmospheric Kelvin wave, that leads to coastal SST transient maximum, a process of upwelling relaxation already found in the California system (Dorman, 1985; Beardsley et al., 1987; Dorman, 1987).

As expected, the oceanic circulation in the region was found to vary on much slower time scales than the atmospheric circulation, but to be characterized by complex mesoscale structures, with counterrotating vortices propagating westward in the north of the domain, and south-westward in the wake of the islands, as noted in previous studies (eg. Barton et al., 1998; Sangrà et al., 2009). The ocean mixed layer was found to respond locally to both the coastal low-level atmospheric jet and the island tip-jets, by increased vertical mixing. The island tip jets were found to have a larger impact on the latent heat flux than on sensible heat flux, an impact that is asymmetric in the east-west direction, as also found in Alves et al. (2020).

The complex atmosphere-ocean circulation in the CANUS results from its geographic setting, including the coastal geometry and the presence of islands with significant height. Some of the processes are like the better studied California system, but others, as those linked to the nearby islands, are not comparable and require

high resolution simulations to accurately represent the intense coastal wind and PBL height gradients. The spatial and temporal details of those processes may have impact in the biogeochemical cycling throughout the system, affecting its productivity (Renault et al., 2016b). There is evidence of multidecadal variability in the intensity of the atmospheric flow in the Canary system (Miranda et al., 2021), which may be relevant in the context of climate change. Understanding the corresponding evolution of the ocean variability is an important target for future work.

Data availability statement

The raw data supporting the conclusions of this article will be made available by the authors, without undue reservation.

Author contributions

JA carried out the numerical simulations. JA and PM analyzed the data and wrote the manuscript in close collaboration with RC. All authors contributed to the article and approved the submitted version.

Funding

This study was funded by FCT (Fundação para a Ciência e a Tecnologia, I.P./MCTES) through national funds (PIDDAC) -UIDB/50019/2020. JA was financially supported by the Oceanic Observatory of Madeira Project (M1420-01-0145-FEDER-000001-Observatório Oceânico da Madeira-OOM).

Acknowledgments

The authors thank CESGA (Supercomputing Center of Galicia) for providing the necessary resources for the numerical simulations. ECMWF ERA5 data was downloaded from the Copernicus Climate Change Service. We acknowledge the *in-situ* data kindly provided by IPMA (Portuguese Institute for Sea and Atmosphere) and Puertos de Estado institute.

Conflict of interest

The authors declare that the research was conducted in the absence of any commercial or financial relationships that could be construed as a potential conflict of interest.

Publisher's note

Supplementary material

The Supplementary Material for this article can be found online at: https://www.frontiersin.org/articles/10.3389/fmars.2023.1068134/full#supplementary-material

References

Alves, J. M. R., Caldeira, R. M. A., and Miranda, P. M. A. (2020). Dynamics and oceanic response of the Madeira tip-jets. *Q. J. R. Meteorol. Soc* 146, 3048–3063. doi: 10.1002/qj.3825

Alves, J. M. R., and Miranda, P. M. A. (2013). Variability of Iberian upwelling implied by ERA-40 and ERA-interim reanalyses. *Tellus A: Dyn. Meteorol. Oceanogr.* 65, 1. doi: 10.3402/tellusa.v65i0.19245

Alves, J. M. R., Tomé, R., Caldeira, R. M. A., and Miranda, P. M. A. (2021). Asymmetric ocean response to atmospheric forcing in an island wake: a 35-year high-resolution study. *Front. Mar. Sci.* 8, 624392. doi: 10.3389/fmars.2021.624392

Aristegui, J., Barton, E. D., Alvarez-Salgado, X., Santos, M., Figueiras, F. G., Kifani, S., et al. (2009). Sub-Regional ecosystem variability in the canary current upwelling. *Prog. Oceanogr.* 83, 33–48. doi: 10.1016/j.pocean.2009.07.031

Aristegui, J., Sangrà, P., Hernandez-Leon, S., Cantón-Garbín, M., Hernández-Guerra, A., and Kerling, J. L. (1994). Island-induced eddies in the canary islands. *Deep Sea Res. I: Oceanogr. Res. Pap.* 41, 1509–1525. doi: 10.1016/0967-0637(94)90058-2

Bakun, A. (1990). Global climate change and intensification of coastal ocean upwelling. *Science* 247, 198–201. doi: 10.1126/science.247.4939.198

Bakun, A., Black, B. A., and Bograd, S. J. (2015). Anticipated effects of climate change on coastal upwelling ecosystems. *Curr. Clim. Change Rep.* 1, 85–93. doi: 10.1007/s40641-015-0008-4

Barton, E. D., Arístegui, J., Tett, P., and Navarro-Pérez, E. (2004). Variability in the canary islands area of filament-eddy exchanges. *Prog. Oceanogr.* 62, 71–94. doi: 10.1016/j.pocean.2004.07.003

Barton, E. D., Arıstegui, J., Tett, P., Cantón, M., Garcıa-Braun, J., Hernández-León, S., et al. (1998). The transition zone of the canary current upwelling region. *Prog. Oceanogr.* 41, 455–504. doi: 10.1016/S0079-6611(98)00023-8

Barton, E. D., Field, D., and Roy, C. (2013). Canary current upwelling: more or less? *Prog. Oceanogr.* 116, 167–178. doi: 10.1016/j.pocean.2013.07.007

Beardsley, R. C., Dorman, C. E., Friehe, C. A., Rosenfeld, L. K., and Winant, C. D. (1987). Local atmospheric forcing during the coastal ocean dynamics experiment: 1. a description of the marine boundary layer and atmospheric conditions over a northern California upwelling region. *J. Geophys. Res.* 92 (C2), 1467–1488. doi: 10.1029/JC092iC02p01467

Bentamy, A., Piollé, J. F., and Prevost, C. (2021). Global ocean wind L4 reprocessed 6 hourly observations. *Copernicus Mar. Service*. doi: 10.48670/moi-00185

Bock, L., Lauer, A., Schlund, M., Barreiro, M., Bellouin, N., Jones, C., et al. (2020). Quantifying progress across different CMIP phases with the ESMValTool. *J. Geophys. Res. Atmos.* 125, e2019JD032321. doi: 10.1029/2019JD032321

Boé, J., Hall, A., Colas, F., McWilliams, J. C., Qu, X., Kurian, J., et al. (2011). What shapes mesoscale wind anomalies in coastal upwelling zones? *Clim. Dyn.* 36 (11–12), 2037–2049. doi: 10.1007/s00382-011-1058-5

Bograd, S., Jacox, M., Hazen, E., Lovecchio, E., Montes, I., Buil, M., et al. (2023). Climate change impacts on Eastern boundary upwelling systems. *Annu. Rev. Mar. Sci.* 15, 1. doi: 10.1146/annurev-marine-032122-021945

Bretherton, C. S., McCaa, J. R., and Grenier, H. (2004). A new parameterization for shallow cumulus convection and its application to marine subtropical cloud-topped boundary layers. part I: description and 1D results. *Mon. Weather Rev.* 132, 864–882. doi: 10.1175/1520-0493(2004)132<0864:ANPFSC>2.0.CO;2

Caldeira, R. M. A., Groom, S., Miller, D., Pilgrim, P., and Nezlin, N. P. (2002). Sea-Surface signatures of the island mass effect phenomena around Madeira island, northeast Atlantic. *Remote Sens. Environ.* 80, 336–360. doi: 10.1016/S0034-4257(01)00316-9

Caldeira, R. M. A., Marchesiello, P., Nezlin, N. P., DiGiacomo, P. M., and McWilliams, J. C. (2005). Island wakes in the southern California bight. *J. Geophys. Res.* 110, C11012. doi: 10.1029/2004JC002675

Capet, X. J., Marchesiello, P., and McWilliams, J. C. (2004). Upwelling response to coastal wind profiles. *Geophys. Res. Lett.* 31, L13311. doi: 10.1029/2004GL020123

Chapman, D. C. (1985). Numerical treatment of cross-shelf open boundaries in a barotropic coastal ocean model. *J. Phys. Oceanogr.* 15, 1060–1075. doi: 10.1175/1520-0485(1985)0152.0.CO;2

Chelton, D. B., Schlax, M. G., Freilich, M. H., and Milliff, R. F. (2004). Satellite measurements reveal persistent small-scale features in ocean winds. *Science* 303, 978–983. doi: 10.1126/science.1091901

Chen, F., and Dudhia, J. (2001). Coupling an advanced land surface-hydrology model with the Penn state-NCAR MM5 modeling system. part I: model implementation and sensitivity. *Mon. Weather Rev.* 129, 569–585. doi: 10.1175/1520-0493(2001)129<0569:CAALSH>2.0.CO;2

Chin, T. M., Vazquez-Cuervo, J., and Armstrong, E. M. (2017). A multi-scale high-resolution analysis of global sea surface temperature. *Remote Sens. Environ.* 200, 154–169. doi: 10.1016/j.rse.2017.07.029

Demarcq, H. (2009). Trends in primary production, sea surface temperature and wind in upwelling systems, (1998–2007). *Prog. Oceanogr.* 83, 376–385. doi: 10.1016/j.pocean.2009.07.022

Desbiolles, F., Blanke, B., Bentamy, A., and Grima, N. (2014). Origin of fine-scale wind stress curl structures in the benguela and canary upwelling systems. *J. Geophys. Res. Oceans* 119, 7931–7948. doi: 10.1002/2014JC010015

Dorman, C. E. (1985). Evidence of kelvin waves in california's marine layer and related eddy generation. *Mon. Weather Rev.* 113.5, 827–839. doi: 10.1175/1520-0493(1985)113<0827:EOKWIC>2.0.CO;2>

Dorman, C. E. (1987). Possible role of gravity currents in northern California coastal summer wind reversals. *J. Geophys. Res. Oceans* 92 (C2), 1497–1506. doi: 10.1029/Jc092ic02p01497

Dudhia, J. (1989). Numerical study of convection observed during the winter monsoon experiment using a mesoscale two-dimensional model. *J. Atmos. Sci.* 46, 3077–3107. doi: 10.1175/1520-0469(1989)046<3077:NSOCOD>2.0.CO;2

Egbert, G. D., and Erofeeva, S. Y. (2002). Efficient inverse modeling of barotropic ocean tides. *J. Atmos. Ocean. Technol.* 19, 183–204. doi: 10.1175/1520-04262002019<0183:EIMOBO<2.0.CO;2

Grubišic´, V., Sachsperger, J., and Caldeira, R. M. (2015). Atmospheric wake of Madeira: first aerial observations and numerical simulations. *J. Atmos. Sci.* 72, 4755–4776. doi: 10.1175/JAS-D-14-0251.1

Hersbach, H., Bell, B., Berrisford, P., Hirahara, S., Horanyi, A., Munoz-Sabater, J., et al. (2020). The ERA5 global reanalysis. *Q. J. R. Meteorol. Soc* 146, 1999–2049. doi: 10.1002/qj.3803

Hong, S., and Lim, J. (2006). The WRF single-moment 6-class microphysics scheme (WSM6). *J. Korean Meteor. Soc.* 42, 129–151.

Jones, P. W. (1999). First- and second-order conservative remapping schemes for grids in spherical coordinates. *Mon. Weather Rev.* 127, 2204–2210. doi: 10.1175/1520-0493(1999)127<2204:FASOCR>2.0.CO;2

Kain, J. S. (2004). The kain–fritsch convective parameterization: an update. *J. Appl. Meteorol.* 43 (1), 170–181. doi: 10.1175/1520-0450(2004)043<0170:TKCPAU>2.0.CO;2

Kain, J. S., and Fritsch, J. M. (1990). A one-dimensional entraining/detraining plume model and its application in convective parameterization. *J. Atmos. Sci.* 47, 2784–2802. doi: 10.1175/1520-0469(1990)047<2784:AODEPM>2.0.CO;2

Larson, J., Jacob, R., and Ong, E. (2005). The model coupling toolkit: a new Fortran90 toolkit for building multiphysics parallel coupled models. *Int. J. High Perform. Comput. Appl.* 19 (3), 277–292. doi: 10.1177/1094342005056115

Lellouche, J. M., Greiner, E., Bourdallé-Badie, R., Garric, G., Melet, A., Drévillon, M., et al. (2021). The Copernicus global 1/12° oceanic and Sea ice GLORYS12 reanalysis. *Front. Earth Sci.* 9, 698876. doi: 10.3389/feart.2021.698876

Lima, D. C. A., Soares, P. M. M., Nogueira, M., and Semedo, A. (2022). Global coastal low-level wind jets revisited through the new ERA5 reanalysis. *Int. J. Climatol.* 2 (9), 4491–4507. doi: 10.1002/joc.7482

Marchesiello, P., McWilliams, J. C., and Shchepetkin, A. (2001). Open boundary conditions for long-term integration of regional oceanic models. *Ocean Model.* 3, 1–20. doi: 10.1016/S1463-5003(00)00013-5

Mason, E., Colas, F., Molemaker, J., Shchepetkin, A. F., Troupin, C., McWilliams, J. C., et al. (2011). Seasonal variability of the canary current: a numerical study. *J. Geophys. Res.* 116, C06001. doi: 10.1029/2010JC006665

Mason, E., Molemaker, J., Shchepetkin, A. F., Colas, F., McWilliams, J. C., and Sangrà, P. (2010). Procedures for offline grid nesting in regional ocean models. *Ocean Model.* 35, 1–15. doi: 10.1016/j.ocemod.2010.05.007

Miranda, P. M. A., Alves, J. M. R., and Serra, N. (2013). Climate change and upwelling: response of Iberian upwelling to atmospheric forcing in a regional climate scenario. *Clim. Dyn* 40, 2813–2824. doi: 10.1007/s00382-012-1442-9

Miranda, P. M. A., Tomé, R., Frois, L., Nogueira, M., Alves, J. M. R., Prior, V., et al. (2021). Speed-up of the Madeira tip jets in the ERA5 climate highlights the decadal variability of the Atlantic subtropics. *Q. J. R. Meteorol. Soc.* 147, 679–690. doi: 10.1002/qj.3940

Mlawer, E. J., Taubman, S. J., Brown, P. D., Iacono, M. J., and Clough, S. A. (1997). Radiative transfer for inhomogeneous atmosphere: RRTM, a validated correlated-k model for the long wave. *J. Geophys. Res.* 102, 16663–16682. doi: 10.1029/97JD00237D14

Monin, A. S., and Obukhov, A. M. (1954). Basic laws of turbulent mixing in the atmosphere near the ground. *Tr. Inst. Teor. Geofiz., Akad Nauk SSSR* 24, 1963–1987.

Narayan, N., Paul, A., Mulitza, S., and Schulz, M. (2010). Trends in coastal upwelling intensity. *Ocean Sci.* 6, 815–823. doi: 10.5194/os-6-815-2010

Obukhov, A. M. (1946). Turbulence in thermally non-homogeneous atmosphere. *Teor. Geofiz., Akad Nauk SSSR* 1, 95–115. doi: 10.1007/BF00718085

Ólafsson, H., and Bougeault, P. (1997). The effect of rotation and surface friction on orographic drag. *J. Atmos. Sci.* 54, 193–210. doi: 10.1175/1520-0469(1997)0542.0.CO;2

Perlin, N., Skyllingstad, E. D., and Samelson, R. M. (2011).). coastal atmospheric circulation around an idealized cape during wind-driven upwelling studied from a coupled ocean-atmosphere model. *Mon. Weather Rev.* 139, 3, 809–829. doi: 10.1175/2010MWR3372.1

Perlin, N., Szoeke, S. P., Chelton, D. B., Samelson, R. M., Skyllingstad, E. D., and O'Neill, L. W. (2014). Modeling the atmospheric boundary layer wind response to mesoscale sea surface temperature perturbations. *Mon. Weather Rev.* 142, 4284–4307. doi: 10.1175/MWR-D-13-00332.1

Pickart, R. S., Spall, M. A., Ribergaard, M. H., Moore, G. W. K., and Milliff, R. F. (2003). Deep convection in the irminger Sea forced by the Greenland tip jet. *Nature* 424, 152–156. doi: 10.1038/nature01729

Renault, L., Deutsch, C., McWilliams, Frenzel, H., Liang, J. H., and Colas, F. (2016b). Partial decoupling of primary productivity from upwelling in the California current system. *Nat. Geosci.* 9, 505–508. doi: 10.1038/ngeo2722

Renault, L., Hall, A., and McWilliams, J. C. (2016a). Orographic shaping of US West coast wind profiles during the upwelling season. *Clim. Dyn.* 46, 1–2, 273-289. doi: 10.1007/s00382-015-2583-4

Samelson, R. M., de Szoeke, S. P., Skyllingstad, E. D., Barbour, P. L., and Durski, S. M. (2021). Fog and low-level stratus in coupled ocean–atmosphere simulations of the northern California current system upwelling season. Mon. *Wea. Rev.* 149, 1593–1617. doi: 10.1175/MWR-D-20-0169.1

Samelson, R. M., O'Neill, L. W., Chelton, D. B., Skyllingstad, E. D., Barbour, P. L., and Durski, S. M. (2020). Surface stress and atmospheric boundary layer response to mesoscale SST structure in coupled simulations of the northern California current system. *Weather Rev.* 148, 1, 259–287. doi: 10.1175/MWR-D-19-0200.1

Sangrà, P., Pascual, A., Rodríguez-Santana, A., Machín, F., Mason, E., McWilliams, J. C., et al. (2009). The canary eddy corridor: a major pathway for long-lived eddies in the subtropical north Atlantic. *Deep Sea Res. I: Oceanogr. Res. Pap.* 56, 2100–2114. doi: 10.1016/j.dsr.2009.08.008

Schwing, F. B., and Mendelssohn, R. (1997). Increased coastal upwelling in the California current system. *J. Geophys. Res. Oceans* 102, 3421–3438. doi: 10.1029/96JC03591

Shchepetkin, A. F., and McWilliams, J. C. (2005). The regional oceanic modeling system (ROMS): a split-explicit, free-surface, topography-following-coordinate oceanic model. *Ocean Model.* 9 (4), 347–404. doi: 10.1016/j.ocemod.2004.08.002

Skamarock, W. C., Klemp, J. B., Dudhia, J., Gill, D. O., Barker, D., Duda, M. G., et al. (2008). *A description of the advanced research WRF version 3. NCAR technical note, 475 +STR.* (University Corporation for Atmospheric Research). doi: 10.5065/D68S4MVH

Taylor, S. V., Cayan, D. R., Graham, N. E., and Georgakakos, K. P. (2008). Northerly surface winds over the eastern north pacific ocean in spring and summer. *J. Geophys. Res.* 113, D02110. doi: 10.1029/2006JD008053

Tozer, B., Sandwell, D. T., Smith, W. H. F., Olson, C., Beale, J. R., and Wessel, P. (2019). Global bathymetry and topography at 15 arc sec: SRTM15+. *Earth Space Sci.* 6, 1847–1864. doi: 10.1029/2019EA000658

Vazquez, R., Parras-Berrocal, I., Cabos, W., Sein, D. V., Mañanes, R., and Izquierdo, A. (2022). Assessment of the canary current upwelling system in a regionally coupled climate model. *Clim. Dyn.* 58, 69–85. doi: 10.1007/s00382-021-05890-x

Verhoef, A., Portabella, M., and Stoffelen, A. (2012). High-resolution ASCAT scatterometer winds near the coast. *IEEE Trans. Geosci. Remote Sens.* 50, 7, 2481–2487. doi: 10.1109/TGRS.2011.2175001

Warner, J. C., Armstrong, B., He, R. Y., and Zambon, J. B. (2010). Development of a coupled ocean–atmosphere–wave–sediment transport (COAWST) modeling system. *Ocean Model.* 35, 230–244. doi: 10.1016/j.ocemod.2010.07.010

Warner, J. C., Perlin, N., and Skyllingstad, E. D. (2008). Using the model coupling toolkit to couple earth system models. *Environ. Model. Software* 23, 1240–1249. doi: 10.1016/j.envsoft.2008.03.002

Wu, H., and Zhu, J. (2010). Advection scheme with 3rd high-order spatial interpolation at the middle temporal level and its application to saltwater intrusion in changjiang estuary. *Ocean Model.* 33, 33–35. doi: 10.1016/j.ocemod.2009.12.001

Xie, S.-P., Liu, W. T., Liu, Q. Y., and Nonaka, M. (2001). Far-reaching effects of the Hawaiian islands on the pacific ocean–atmosphere system. *Science* 292 (5524), 2057–2060. doi: 10.1126/science.1059781

frontiers | Frontiers in Marine Science

TYPE Original Research
PUBLISHED 17 July 2023
DOI 10.3389/fmars.2023.1113879

OPEN ACCESS

EDITED BY
Weifeng (Gordon) Zhang,
Woods Hole Oceanographic Institution,
United States

REVIEWED BY
Jonathan Nash,
Oregon State University, United States
Shuang-Xi Guo,
Chinese Academy of Sciences (CAS), China

*CORRESPONDENCE
Sheila N. Estrada-Allis
sheila@cicese.mx

RECEIVED 01 December 2022
ACCEPTED 15 May 2023
PUBLISHED 17 July 2023

CITATION
Estrada-Allis SN, Rodríguez-Santana Á, Naveira-Garabato AC, García-Weil L, Arcos-Pulido M and Emelianov M (2023) Enhancement of turbulence and nutrient fluxes within an Eastern Boundary Upwelling Filament: a diapycnal entrainment approach.
Front. Mar. Sci. 10:1113879.
doi: 10.3389/fmars.2023.1113879

Enhancement of turbulence and nutrient fluxes within an Eastern Boundary Upwelling Filament: a diapycnal entrainment approach

Sheila N. Estrada-Allis[1]*, Ángel Rodríguez-Santana[2], Alberto C. Naveira-Garabato[3,4], Luis García-Weil[2], Mireya Arcos-Pulido[2] and Mikhail Emelianov[4]

[1]Department of Physical Oceanography, Ensenada Center for Scientific Research and Higher Education (CICESE), Ensenada, Baja California, Mexico, [2]Departamento de Física, Facultad de Ciencias del Mar, Universidad de Las Palmas de Gran Canaria (ULPGC), Las Palmas de Gran Canaria, Spain, [3]National Oceanography Centre, University of Southampton, Southampton, United Kingdom, [4]Physical and Technological Oceanography, Instituto de Ciencias del Mar (CSIC), Barcelona, Spain

The filaments of the African Eastern Boundary Upwelling System (EBUS) are responsible for feeding nutrients to the oligotrophic waters of the northeastern Atlantic. However, turbulent mixing associated with nutrient uplift in filaments is poorly documented and has been mainly evaluated numerically. Using microstructure profiler measurements, we detected enhanced turbulent kinetic energy dissipation rates (ε) within the Cape Ghir upwelling filament. In contrast to previous studies, this enhancement was not related to symmetrical instabilities induced by down-front winds but to an increase in vertical current shear at the base of the mixed layer (h_ρ). In order to quantify the impact of vertical shear and the influence of the active mixing layer depth (h_ε) in the filament, a simple one-dimensional (1D) turbulent entrainment approach was used. We found that the effect of turbulent enhancement, together with the isopycnal morphology of the filament front, drove the formation of local positive entrainment zones ($\Delta h = h_\varepsilon - h_\rho$), as h_ε was deeper than h_ρ. This provided suitable conditions for the entrainment of cold, nutrient-rich waters from below the filament pycnocline and the upward transport of biophysical properties to the upper boundary layer of the front. We also found that diapycnal nutrient fluxes in stations influenced by the filament (1.35 mmol m^{-2} d^{-1}) were two orders of magnitude higher than those of stations not affected by the filament front (0.02 mmol m^{-2} d^{-1}). Despite their importance, the effects of vertical shear and h_ε have often been neglected in entrainment parameterizations. Thus, a modified entrainment parameterization was adapted to include vertical shear and observed ε, which are overestimated by existing parameterizations. To account for the possible role of internal waves in the generation of vertical shear, we considered internal wave scaling to parameterize the observed dissipation. Using this adapted parameterization, the average entrainment velocities were six times (6 m d^{-1}) higher than those obtained with the classic parameterization (1 m d^{-1}).

KEYWORDS

upwelling filament, diapycnal mixing, active mixing, turbulent, entrainment, entrainment parameterization

1 Introduction

Phytoplankton productivity is limited by nutrient availability, especially in oligotrophic areas such as subtropical gyres. In Eastern Boundary Upwelling Systems (EBUS), filaments are examples of frontal systems that are able to supply nutrients from below the pycnocline to the upper boundary layer of the ocean. Moreover, cold and nutrient-rich water that is upwelled along the coast can be transported offshore by filaments, which are typically narrow $\mathcal{O}$ (10 km) and elongated $\mathcal{O}$ (100 km) structures with vertical extensions of ~100 m. These structures are often located near coastline irregularities (Hagen et al., 1996; Sangrà et al., 2015) and identifiable by low surface temperatures and high chlorophyll-a concentrations (Sangrà et al., 2015).

The pycnocline usually outcrops within filaments, producing sharp differences in the upper layer of the ocean with respect to the characteristics of the surrounding waters, which are generally well-mixed (Dewey and Moum, 1990; Pelegrí et al., 2005b; Arcos-Pulido et al., 2014). These thermohaline fronts affect the lateral buoyancy gradient, thus providing suitable conditions for diapycnal mixing through mechanisms such as vertical shear. Diapycnal mixing associated with submesoscale frontal systems is particularly important given that it involves the exchange of surface heat, buoyancy fluxes, and the vertical transport of tracers, such as nutrients, from below the pycnocline to surface waters (e.g., Hales et al., 2005; Li et al., 2012; Arcos-Pulido et al., 2014).

Despite the importance of these ubiquitous structures, few studies have analyzed how turbulence may be enhanced within filaments using turbulent kinetic energy (TKE) dissipation rates (ε_o) obtained with direct microstructure measurements. Dewey et al. (1993) observed elevated subsurface ε_o, which they attributed to mean shear turbulence generated within submesoscale structures known as minifilaments. Other observations of microstructures have suggested that surface-induced mixing may be enhanced by the proximity of filament fronts, resulting in strong horizontal density gradients that can help maintain the frontal system (Dewey and Moum, 1990). Other authors have suggested that two-dimensional turbulence is generated by symmetrical instabilities due to the low potential vorticity of down-front winds and/or atmospheric buoyancy loss (e.g., D'Asaro et al., 2011; Thomas et al., 2013; Peng et al., 2020). Collectively, these studies demonstrate that turbulence in the upper boundary layer may be notably enhanced within filaments; however, the mechanisms responsible for this enhanced turbulence remain unclear.

From a one-dimensional (1D) point of view, there are three primary TKE sources that control turbulence in the upper boundary layer (Niiler and Kraus, 1977): (*i*) wind stirring, (*ii*) convection forces, and (*iii*) vertical shear due to horizontal currents at the base of the mixed layer. These three sources are balanced by the dissipation term, which represents the main TKE sink. In order to close the system of equations of the 1D TKE budget, the entrainment rate (w_e) must be considered, which is a temporal rate of change of themixed layer depth (e.g., Niiler and Kraus, 1977; Cronin and McPhaden, 1997; Wade et al., 2011) that describes the turbulent and diapycnal velocity acting at the base of the mixed layer. Turbulent entrainment increases h_ρ, decreases temperature, and transports hydro-physical properties, such as heat, salinity, and nutrients, between the upper and lower ocean layers. This is particularly important in upwelling regions given that entrainment helps to upwell nutrient-rich waters from below the pycnocline to the nutrient-poor upper layers. Thus, entrainment can be viewed as a proxy of TKE sources and sinks that control turbulence from the pycnocline through the upper boundary layer.

The parameterization of entrainment through a 1D TKE budget has been widely used in many bulk mixed layer models (e.g., Deardorff, 1983; Gaspar, 1988; Jacob and Shay, 2003; Nagai et al., 2005; Samson et al., 2009; Liu et al., 2012; Giordani et al., 2013). However, the study of entrainment is itself challenging because its contributions are often overwhelmed by large-scale motions. In recent decades, considerable efforts have been made to elucidate entrainment behavior through laboratory experiments (e.g., Khanta et al., 1977; Deardorff, 1983; Fernando, 1991; Pelegrí and Richman, 1993; Jackson and Rehmann, 2014), modeling setups (e.g., Jacob and Shay, 2003; Sun and Wang, 2008) and observational studies (e.g., Dewey and Moum, 1990; Anis and Moum, 1994; Nagai et al., 2005). However, discrepancies in w_e values are apparent when comparing different entrainment parameterizations (Deardorff, 1983; Anis and Moum, 1994; Jacob and Shay, 2003).

Only a few studies have focused on the characterization of vertical turbulent entrainment in upwelling filament systems, and these have produced contradictory results. Dewey and Moum (1990) showed that wind-induced turbulent entrainment is less efficient in the warm sides of filaments than in their cold sides, where the pycnocline outcrops near the surface. These authors also suggested that entrainment could act to maintain a cool surface signature in upwelling filaments. In another study, Dewey et al. (1993) argued that diapycnal turbulent processes associated with minifilaments are less important than local upwelling or frontogenesis mechanisms. However, it is likely that both processes are related (Estrada-Allis et al., 2019). Indeed, the temporal evolution of vertical velocity suggests that vertical mixing can modulate the magnitude of the ageostrophic term, with elevated near-surface mixing enhancing the vertical velocity.

In another study, Grodsky et al. (2008) used satellite observations of equatorial Atlantic upwelling to demonstrate that thermocline shoaling associated with elevated wind strength increases the entrainment of cold, nutrient-rich water to the mixed layer, leading to phytoplankton blooms. Using a regional model, Giordani et al. (2013) found that entrainment does not contribute to the development of the Atlantic cold tongue. Although these studies have notably improved our understanding of entrainment, the sources that control the TKE balance in the upper boundary layer and consequently turbulent entrainment remain poorly understood.

In this study, we refer to the upper boundary layer as the region comprising both the mixed layer depth (h_ρ) and mixing layer depth (h_ε). The latter is the depth at which active mixing processes operate (Brainerd and Gregg, 1995). Some studies have indicated that h_ε may play an important role in highly dynamic areas like frontal systems. This is relevant because the vertical transport of heat,

momentum, and hydrophysical material within the upper boundary layer is controlled by turbulent mixing (Brainerd and Gregg, 1995; Cisewski et al., 2008; Inoue et al., 2010; Sutherland et al., 2014), with important and consequences for phytoplankton blooms (Franks, 2014).

This study focuses on the filament generated near Cape Ghir, which forms part of the African EBUS (e.g., Hagen, 2001). This recurrent filament is one of the major filaments of the Canary Current Upwelling System (Hagen et al., 1996; Pelegrí et al., 2005a; Pelegrí et al., 2005b) and is able to transport biogeochemical properties offshore more effectively than wind-driven Ekman transport (Álvarez Salgado et al., 2007). Moreover, the Cape Ghir filament is involved in both onshore and offshore export export (Santana-Falcón et al., 2020) and is responsible for up to 63% of the total annual primary production attributed to coastal upwelling (e.g., García-Muñoz et al., 2005). The long-lived (>3 months) westward-propagating mesoscale eddies generated in the Eddy Canary Corridor (Sangrà et al., 2009) can interact with the Cape Ghir filament, exporting nutrients and carbon to the oligotrophic interior regions of the northeastern Atlantic.

The generation of the Cape Ghir filament can be explained by the combined effects of baroclinic instability from the filament jet, seafloor topography, and wind near the cape, which act to deflect the filament offshore (Hagen, 2001; Pelegrí et al., 2005b; Troupin et al., 2012). Due to the enhancement of turbulent mixing within filaments, our primary objective was to investigate the primary TKE sources and sinks within and outside of the Cape Ghir upwelling filament in the upper ocean through an analysis of the bulk 1D TKE balance. Using novel observations of ε_o for this region, we analyzed where turbulent mixing takes place and how it relates to the three primary sources of turbulence at the surface by means of an entrainment parameterization. We also evaluated the importance of diapycnal nutrient fluxes at the base of the mixed layer and focused on vertical shear and dissipation as important TKE sources and sinks, respectively. These analyses were conducted using meteorological, hydrographic, and satellite data and microstructure turbulent profiles.

In this study, we show that actual turbulent entrainment parameterizations could be underestimating entrainment rates in highly dynamic areas dominated by mesoscale structures. These low diapycnal velocities will lead to an underestimation of the vertical transport of nutrients and physical properties from the base of the mixed layer to the upper boundary layer of Cape Ghir filament and other similar filaments associated with EBUS.

2 Materials and methods

2.1 Observational data

The hydrographic data used in this study were obtained from a survey of the Cape Ghir region in northwestern Africa, which formed part of the project "Mixing Processes in the Canary Basin (PROMECA)" (Figure 1). The survey was conducted aboard the *R/V García del Cid* in early fall (18–29 October 2010) when the Trade Winds typically weaken. Conductivity-temperature-depth (CTD), expendable bathythermograph (XBT), and microstructure data were collected at stations located approximately 10 km apart from one another along three transects (A, B, and C in Figure 1).

Wind speed, instantaneous wind speed, wind direction, air temperature, water temperature, relative humidity, air pressure, and incoming solar radiation were recorded at ~2-min intervals by a meteorological station installed onboard the ship. To remain consistent with hydrographic station measurements, the meteorological data were averaged over 2-h intervals (i.e., the time resolution of the CTD profiles).

During the cruise, current velocity data were also collected nearly continuously with a vessel-mounted 75 KHz Ocean Surveyor Acoustic Doppler Current Profiler (SADCP; Teledyne Technologies, Thousand Oaks, CA, USA). The data were processed with Common Ocean Data Access System (CODAS) software (Firing et al., 1995) to obtain vertical bin sizes of 10 m averaged over 2-h periods. An SBE911 plus CTD (Sea-Bird Scientific, Bellevue, WA, USA) was used to produce temperature, salinity, and density profiles (1 dbar vertical resolution). Between each CTD station, vertical temperature profiles were also obtained with XBT Sippican T5 probes (Lockheed Martin, Bethesda, MD, USA) that transmitted to 2000 m depth. The temperature profiles obtained with the XBT probes were smoothed using a classic, low-pass Butterworth filter. A comparison of the CTD and XBT temperature profiles revealed a discrepancy of approximately 10 m. Although uncommon, this offset has been observed in similar studies of the Cape Ghir filament (Pelegrí et al., 2005b). The results of this study are based on CTD rather than XBT vertical profiles.

A TurboMAP-L microstructure profiler Wolk et al., (2002) was used to obtain profiles of ε_o. The TurboMAP-L is a vertical free-fall profiler that carries microstructure sensors, including two shear probes and an FP07 thermistor, CTD sensors, and internally mounted accelerometers. The profiler freely falls at a speed of ~0.7 m s^{-1} while sampling at a rate of 512 Hz. All data were binned at 2-m intervals down to ~470 m depth and processed using TMTools v. 3.04 A.

The location, evolution, and coverage of the Cape Ghir upwelling filament during the survey were determined *via* sea surface temperature (SST) and chlorophyll-a (Chl) satellite images (Figure 2) obtained from the Moderate Resolution Imaging Spectroradiometer (MODIS) sensors of the AQUA and TERRA satellites. Satellite images were also downloaded from Ocean Color Web (http://oceancolor.gsfc.nasa.gov). Geostrophic surface currents were derived from the sea level anomaly provided by the AVISO altimeter products at a spatial resolution of 1/4° × 1/4°, which were downloaded with OpenDAP from the AVISO Website (http://www.aviso.altimetry.fr/en/home.html).

2.2 Microstructure data processing

To obtain ε_o, we first removed spikes from the turbulence profiles to obtain the shear fluctuation power spectrum, $\psi(k)$, from the fall speed of the profiler, where k is the wavenumber determined from its fall speed. Assuming isotropic turbulence

10.3389/fmars.2023.1113879

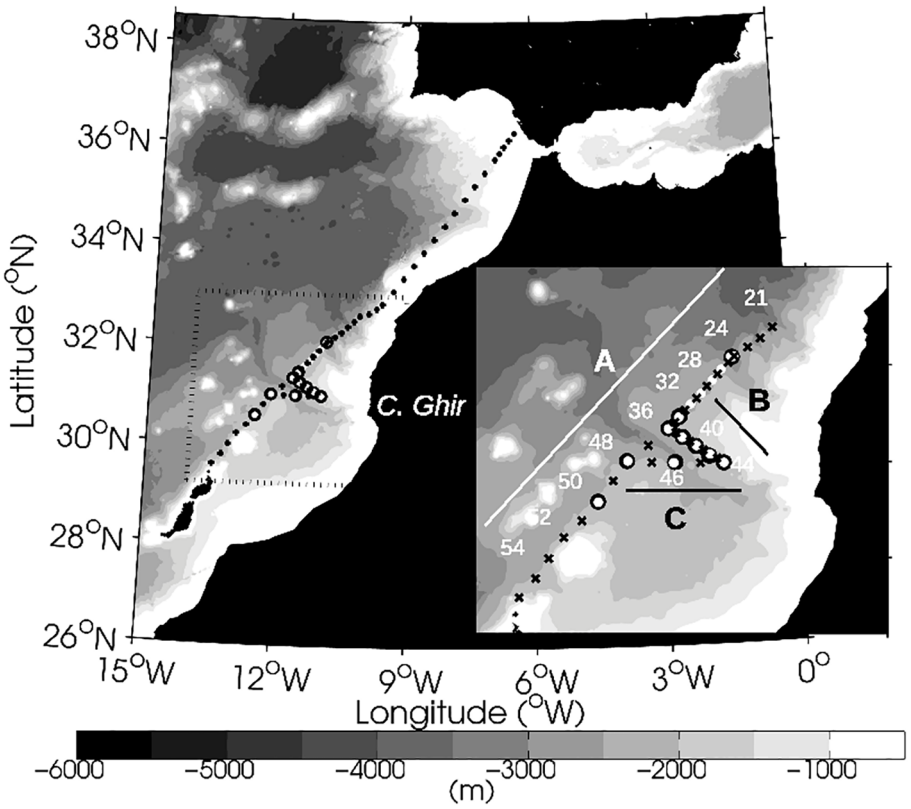

FIGURE 1
Bathymetry (500 m contour) of the Cape Ghir region and hydrographic sampling stations located around the upwelling filament during October 2010. The region delimited by the black dashed lines encompasses the hydrographic stations surveyed in this study and is shown in greater detail in the inset at the bottom right corner of the figure. Black squares indicate conductivity-temperature-depth (CTD) and Acoustic Doppler Current Profiler (ADCP) stations. White dots indicate microstructure stations. Black dots indicate expendable bathythermograph (XBT) stations. The station numbers appear next to each station, and the transects **(A–C)** are shown as solid lines.

Hinze, 1979, observed ε_o was estimated by integrating $\psi(k)$ within an appropriate wavenumber range following the methods of Oakey (1982):

$$\varepsilon_o = \frac{15}{2}\nu \int_{k_1}^{k_2} \psi(k)dk, \quad (1)$$

where ν is the molecular viscosity coefficient with a value of 1×10^{-6} m^2s^{-1} and k_1 is the lowest cutoff wavenumber, which was set to 1 cpm given the physical scale of the microstructure shear probe. In contrast, the upper limit of integration, k_2, is the highest vertical wavenumber free of noise and is usually taken to be the Kolmogorov wavenumber $k_c = (2\pi)^{-1}(\varepsilon\nu^{-3})^{1/4}$. After segmenting each microstructure profile within vertical bin sizes of 2 m, the observed shear spectrum was fitted to the Nasmyth empirical universal spectra for turbulence (Oakey, 1982; Wolk et al., 2002). This spectrum is considered to be representative of the spectral form of oceanic turbulence and is commonly used to verify shear spectrum measurements. An example of micro-shear power spectral density $\psi(k)$ and Nasmyth spectra can be seen in Figure 3 for a depth range of 43 to 45 m at station 24. Given that records of micro-scale velocity shear can be contaminated by noise (e.g., mechanical vibration of the instrument and the influence of the rope at the surface) until the probe reaches a quasi-constant free-falling velocity, the data within the first 16 m of the water column were removed. In addition, the vertical profiles of ε_o can exhibit large variability over short time periods. As such, the casts were repeated at least twice at each station.

2.3 Surface fluxes and meteorological-related quantities

To assess the relationship between atmospheric forcing and upper ocean turbulence, meteorological data were used to compute the net surface heat flux (J_q^o) as the sum of four individual components $J_q^o = J_q^{Sw} + J_q^{Lw} + J_q^{Se} + J_q^{La}$, where J_q^{Sw} is the net shortwave radiation flux, which is the main contributor to J_q^o during daytime and was directly obtained from the on-board meteorological station. Net longwave radiation (J_q^{Lw}) was determined with the equation of Berliand and Berliand (1952):

$$J_q^{Lw} = E_{Lw}\sigma T_{air}^4(0.39 - 0.5\sqrt{e_a})F_c - 4E_{Lw}\sigma T_{air}^3(T_{sw} - T_{air}), \quad (2)$$

where $E_{Lw} = 0.985$ is the longwave emissivity from from Dickey et al. (1994), $\sigma = 5.67 \times 10^{-8} m^2K^{-4}$ is the Stefan-Boltzman constant, T_{air} is the air temperature measured at a height of 10 m above the sea surface, T_{sw} is the surface water temperature, e_a is

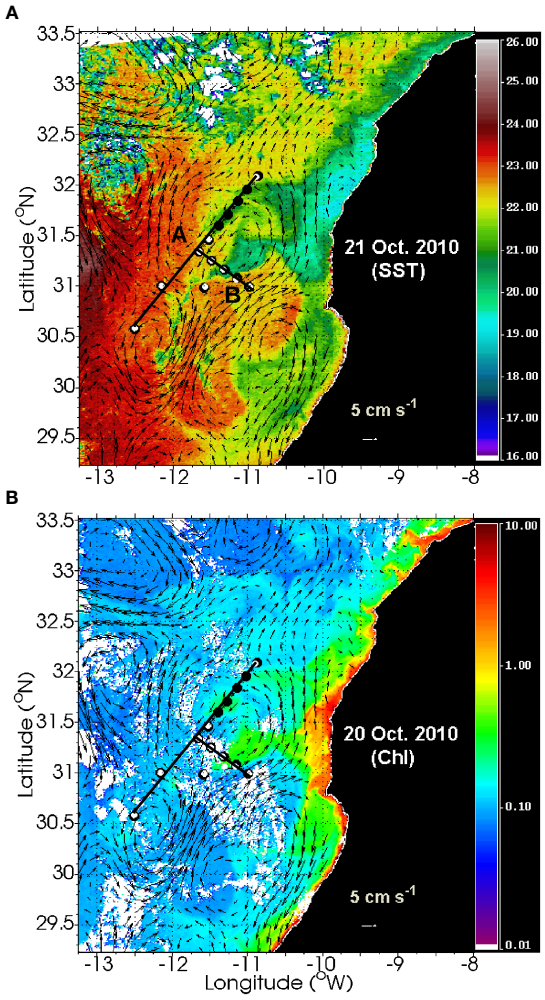

FIGURE 2
Snapshots of **(A)** sea surface temperature (SST, °C) from MODIS-Terra for 21 October 2010 at 14:25 h and **(B)** chlorophyll-a (Chl, mg m^{-3}) from MODIS-Aqua for 20 October 2010 at 13:45 h. Superimposed vectors denote the magnitude and direction of the geostrophic velocity field for the same days derived with AVISO Sea Level Anomaly data (1/4°horizontal resolution). Both transect A and B are shown as solid black lines. Black dots indicate conductivity-temperature-depth (CTD) and Acoustic Doppler Current Profiler (ADCP) stations. The white dots indicate microstructure stations.

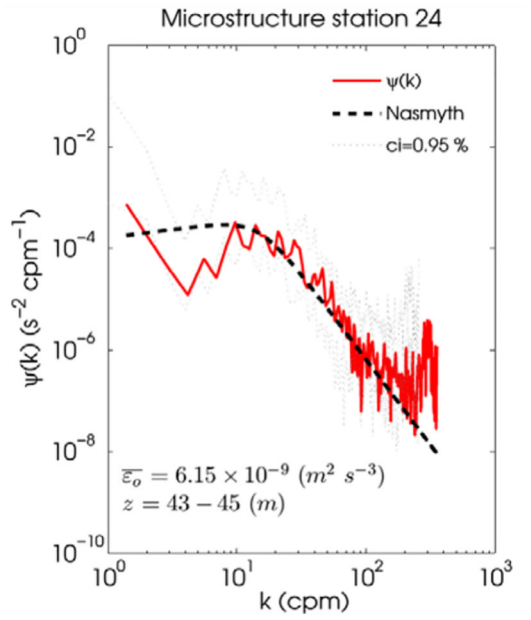

FIGURE 3
Shear power spectral density, $\psi(k)$ (red solid line), for station 24 from the PROMECA-cruise for a depth range (z) of 43 to 45 m. The Nasmyth universal spectra is shown as a dashed black line. The turbulent kinetic energy (TKE) dissipation rate, $\overline{\varepsilon_o}$, is averaged over the z range. The dotted thin lines indicate the 0.95% confidence interval for the power spectral density calculation. At the bottom, k represents the wavenumber in cycles per minute (cpm).

vapor pressure, and F_c is the cloud correction factor with values that range from 0.4 to 1 during daytime, as the sky was mostly clear throughout the study. The sensible heat flux (J_q^{Se}) and latent heat flux (J_q^{La}) were determined by using the Tropical Ocean Global Atmosphere Coupled Ocean-Atmosphere Response Experiment *TOGA-COARE* code available in the Matlab Air–Sea toolbox (version 3.0; http://sea-mat.whoi.edu) developed by the air-sea fluxes science group of the TOGA COARE project, which is a version of the bulk flux described in Fairall et al. (1996).

Once the net surface heat fluxes were obtained, we computed the net surface buoyancy flux (J_b^o) as:

$$J_b^o = \frac{g}{\rho_o}\left(\frac{\alpha J_q^o}{C_p}\right) + g\beta(E-P)So, \quad (3)$$

where g is acceleration due to gravity, C_p is the specific heat capacity of seawater ($\overline{C_p} = 3.98 \times 10^3 \pm 0.42 \text{J kg}^{-1}\,^\circ\text{C}^{-1}$), α is the thermal expansion coefficient of seawater ($\overline{\alpha} = 2.58 \times 10^{-4} \pm 6.92 \times 10^{-6} ^\circ\text{C}^{-1}$), β is the haline contraction coefficient of seawater ($\overline{\beta} = 7.44 \times 10^{-4} \pm 1.08 \times 10^{-6}\,^\circ\text{C}^{-1}$), and ρ_o is a density reference value (1026 kg m^{-3}). The first term corresponds to the thermal surface buoyancy flux (J_b^T), and the second term is related to the contribution of the haline surface buoyancy flux (J_b^S), as suggested by Dorrestein, 1979, where *So* is surface salinity and (E - P) is the difference between the evaporation and precipitation rates. Surface wind stress ($\boldsymbol{\tau}_o$) was computed as $\boldsymbol{\tau}_o = \rho_a C_d \boldsymbol{u}_r^2$, where ρ_a is the reference density of the air 10 m above the sea surface, and $\boldsymbol{u}_r$ is the wind speed. The drag coefficient (C_d) was derived from the equation of Large and Pond, 1981 with $C_d = 1.14 \times 10^{-1}$ for $\boldsymbol{u}_r <$ 10 m s^{-1} and $C_d = (0.49 + 0.065\boldsymbol{u}_r) \times 10^{-3}$ for $\boldsymbol{u}_r >$ 10 m s^{-1}. Note that only the meteorological-related quantities averaged over a window of 2 h were used for calculations in this study (denoted by superscript s in Figure 4). The window size of 2 h was chosen to include the hour before and the hour after the release of the CTD and reflects the time usually required to complete a CTD cast.

2.4 Entrainment parameterization of the 1D TKE budget

Entrainment rates can be parameterized by solving the turbulent closure scheme of the 1D TKE budget (Niiler and Kraus, 1977).

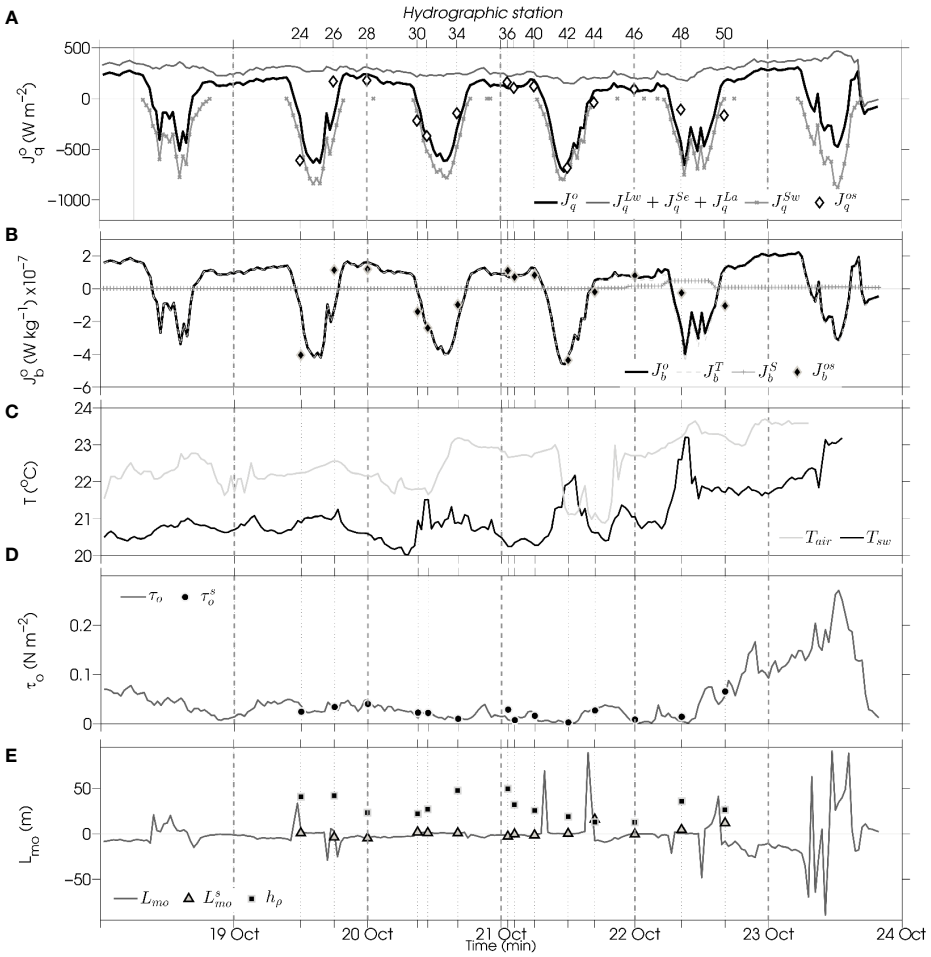

FIGURE 4
Half-hourly averaged meteorological data. **(A)** The net surface heat flux (J_q^o, W m^{-2}, defined positive upward) and the related components of the shortwave radiation flux (J_q^{Sw}), net longwave heat flux (J_q^{Lw}), latent heat flux (J_q^{La}), and sensible heat flux (J_q^{Se}). **(B)** The net surface buoyancy flux (J_b^o, W kg^{-1}), defined as the sum of the thermal surface buoyancy flux (J_b^T) and haline surface buoyancy flux (J_b^S). **(C)** Sea water temperature (T_{sw}) and air temperature (T_{air}, °C). **(D)** Wind stress (τ_o, N m^{-2}). **(E)** Monin-Obukhov length scale (L_{mo}, m) and mixed layer depth (h_ρ, m). Symbols superimposed on the time series denoted with a superscript *s* represent the exact values of each meteorological quantity obtained with the CTD casts from each hydrographic station. The thin vertical dashed lines at the top of the figure indicate the hydrographic stations. The thick dashed lines at the bottom of the figure indicate the end of each day.

Therefore, depending on the sources and sinks that balance the TKE budget of the mixed layer, an assessment of the entrainment parameterization can also help to elucidate which sources of energy drive mixing in the upper boundary layer.

The 1D TKE budget primarily depends on two sinks (i.e., the dissipation term and buoyancy fluxes during daytime) and three sources, namely (*i*) the production of TKE from mechanical stirring induced by wind stress whose velocity scale is the friction velocity $\boldsymbol{u}_\star = (\boldsymbol{\tau}_o/\rho_o)^{1/2}$; (*ii*) the generation of TKE by buoyancy forces during free-convection in which the velocity scale is the free-convection velocity $w_\star = (J_b^o h_\rho)^{1/3}$ (Deardorff, 1970); and (*iii*) TKE produced by shear, which is parameterized *via* the square of the vertical shear $Sh^2 = [(\partial u/\partial z)^2 + (\partial v/\partial z)^2]$ at the base of the mixed layer. In this study, this is represented by the Dynamic Instability Term, $DIT = 0.5 w_e(\delta u^2 + \delta v^2)$, where δu and δv represent velocity jumps at the base of the mixed layer calculated as the difference in velocity just below and above the mixed layer depth. All variables and parameters used in this study are summarized in Table 1. It should be noted that other entrainment sources can be included, such as internal waves breaking at the interface (Strang and Fernando, 2001) or Langmuir vortices within the mixed layer (Flór et al., 2010), although further research is required to elucidate the roles of additional sources in entrainment phenomena.

Several equations have been proposed to compute the entrainment rate as the effective vertical velocity that transports buoyancy across the base of the mixed layer. This study focuses on the parameterization of w_e following the widely used mixed layer bulk model of Gaspar (1988) (w_e^G, hereinafter), in which the evolution of the mixed layer can be computed as follows:

$$w_e^G = \frac{(m_1 + m_2)u_\star^3 + 0.5 h_\rho J_b^o - \overline{\varepsilon_p} h_\rho}{0.5(\delta b h_\rho)}, \tag{4}$$

where $m_1 = 2.6$ and $m_2 = 1.9$ are empirical constants, δb is the buoyancy jump at the base of the mixed layer calculated as the

TABLE 1 List of symbols and parameters that are relevant to the entrainment parameterization.

Symbol	Unit	Definition
group-F		stations within filament waters (26–32, 38–46)
group-nF		stations outside filament waters (24, 34–36, 48–50)
h_ρ	m	mixed layer depth
h_ε	m	mixing layer depth
Δh	m	entrainment zone $\Delta h = h_\varepsilon - h_\rho$
ε_o	$m^2\ s^{-3}$	observed TKE dissipation rate
ε_p	$m^2\ s^{-3}$	parameterized TKE dissipation rate following Gaspar (1988)
ε_{G89}	$m^2\ s^{-3}$	scaled TKE dissipation rate following Gregg (1989)
L_o	m	Ozmidov length scale
u_*	$m\ s^{-1}$	friction velocity
w_*	$m\ s^{-1}$	free-convection velocity
b	$m\ s^{-2}$	buoyancy $b = g(\rho_o - \rho)\rho_o^{-1}$
DIT	$m\ s^{-1}$	Dynamic instability Term, $DIT = 0.5 w_e\ (\delta u^2 + \delta v^2)$
w_e^G	$m\ s^{-1}$	TKE bulk-based entrainment rate from Gaspar (1988)
w_e^{DIT}	$m\ s^{-1}$	w_e^G + DIT term
$w_e^{\Delta h}$	$m\ s^{-1}$	new approach for a TKE bulk-based entrainment rate
w_e^{G89}	$m\ s^{-1}$	replaces ε_o by ε_{G89} in $w_e^{\Delta h}$
N^2	s^{-2}	buoyancy frequency squared
Sh^2	s^{-2}	vertical shear squared
τ_o	$N\ m^{-2}$	wind stress
L_{mo}	m	Monin-Obukhov length scale
J_q^o	$W\ m^{-2}$	surface net heat flux (downward negative)
J_q^{Lw}	$W\ m^{-2}$	surface long-wave heat flux
J_q^{Sw}	$W\ m^{-2}$	surface short-wave heat flux
J_q^{Se}	$W\ m^{-2}$	surface sensible heat flux
J_q^{La}	$W\ m^{-2}$	surface latent heat flux
J_b^o	$W\ kg^{-1}$	surface net buoyancy flux (downward negative)
J_b^T	$W\ kg^{-1}$	surface thermal buoyancy flux
J_b^S	$W\ kg^{-1}$	surface haline buoyancy flux
$(J_b^{\Delta h})_I$	$m^3\ s^{-3}$	turbulent diapycnal buoyancy flux integrated over Δh
T_{res}	minutes	Turbulent residence time
T_{air}	°C	air temperature at 10 m height
T_{sw}	°C	sea water temperature

difference in buoyancy just below and above the mixed layer depth, and ε_p is the parameterized TKE dissipation rate. This equation is similar to that of Niiler and Kraus (1977). The main difference between these expressions lies in how ε_p is parameterized. Equation (4) does not consider the effect of vertical shear at the base of the mixed layer as a relevant source of TKE. To take into consideration shear-driven turbulence (hereinafter w_e^{DIT}), we also employed the equation used in the modeling study of Samson et al. (2009):

$$w_e^{DIT} = \frac{(m_1 + m_2)u_*^3 + 0.5 h_\rho J_b^o - \overline{\varepsilon_p} h_\rho}{0.5[(\delta b h_\rho) - (\delta u^2 + \delta v^2)]}. \quad (5)$$

These authors included the DIT term to evaluate the response of the oceanic mixed layer during a hurricane. In this study, the effect of the DIT term was analyzed under normal wind conditions. In this case, vertical shear will be generated by other sources such as the baroclinicity of the filament front and/or breaking internal waves.

3 Results and discussion

3.1 Hydrographic background of the filament

Upwelling areas are highly dynamic systems (e.g., Barton et al., 1998; Hagen, 2001; Pelegrí et al., 2005b), and studying turbulent processes within these systems is understandably challenging. Unlike in laboratory or modeling experiments, the interactions between processes that operate on different spatiotemporal scales within upwelling systems makes isolating and analyzing a single process quite difficult. In order to describe the physical processes involved in the dynamics of an area, such as within frontal systems, mesoscale eddies, and submesoscale structures, a hydrographical description of the area is required.

The SST and Chl satellite images in Figure 2 show the extension and location of the Cape Ghir upwelling filament over a two-day period (20–21 October 2010). The meander-like structure is identifiable as a cool feature with a high Chl concentration that crosses the sampling stations in transects A and B (Figure 2). The filament waters exhibited a difference of ~2°C from the surrounding waters and were highly conditioned by the mesoscale dynamics of the area, as observed in the superimposed geostrophic currents from the AVISO product in Figure 2. Although representative images with low cloud coverage were chosen as examples, additional images indicated that the filament was present during the sampling period. The filament signal intensified after the last CTD station (i.e., station 50) when stronger wind speeds were recorded. The general description of this filament agrees with those of previous observational studies of African upwelling filaments (e.g., Barton et al., 2001; Hagen, 2001), especially that of Pelegrí et al. (2005b) for the same filament and season in 1995 and 1997.

The vertical sections of salinity (S) and the potential density anomaly (σ_θ) in Figure 5 show doming of isohalines and isopycnals in the northeastern stations of transect A (Figures 5A, B). In addition, the combined vertical CTD-XBT sections also show an elevation of isotherms at the same locations (Figure 6A). This dome-like structure seems to be well correlated with stations that cross the filament front according to satellite imagery (Figure 2).

Although it was not the aim of this study, it was interesting that the temperature-salinity ($T_\theta - S$) relationship (not shown) indicated the presence of a subsurface salinity maximum below the mixed layer (~50 m), with mean values of S = 36.55, T_θ = 19°C, and σ_θ = [26-26.5] kg m^{-3} in stations 38 and 40 of transect B (Figures 5C, D, 6B). This subsurface salinity maximum agrees with the one found by Pelegri et al. (2005b). In their study, these authors suggested that the presence of this subsurface maximum may indicate an interconnected horizontal recirculation cell in the Cape Ghir region. A $T_\theta - S$ diagram with the same data set used in this study can be found in Arcos-Pulido et al. (2014), which shows the subsurface salinity maximum (their Figure 1).

An abrupt upwelling of isohalines and isopycnals (Figures 5C, D) and isotherms (Figure 6B) from station 44 to 48 was apparent in transect B, which was located mostly onshore. The combined CTD-XBT vertical section allowed for the creation of an additional transect, C (Figure 6C), in which isotherm outcropping was smoother than that of transect B. This may have been due to the proximity of transect B to the filament.

In general, it appeared that the rising of isotherms and isopycnals was concentrated in the first 200 m of the water column, particularly in the stations located within the upwelling filament. This finding agrees with what was reported by Pelegrí et al. (2005b), who suggested that this filament originates at shallow depths within the water column. On the other hand, the area of interest was strongly influenced by strong mesoscale dynamics. In order to effectively show these structures, geostrophic velocities derived from AVISO altimeter products were superimposed on the satellite images (Figure 2). The current velocity revealed a cyclonic mesoscale structure, which seemed to induce northward along-front flow in transect A. A poleward geostrophic current crossed transect B in opposite direction to the filament flow as the result of an anticyclonic structure. The geostrophic currents revealed a cyclonic mesoscale structure, which seemed to induce southward along-front flow in transect A and northward along-front flow due to the interaction between a mesoscale cyclone and an anticyclone that crossed transect B.

Based on SST and Chl satellite imagery and its agreement with isopycnal shoaling, we concluded that the hydrographic stations could be separated into two groups: group-F, which was influenced by the upwelling filament and included stations 26–32 and 38–46, and group-nF, which included the remaining stations (24, 34–36, and 48–50). In a related study, Arcos-Pulido et al. (2014) indicated that group-F experienced enhanced nutrient concentrations below the mixed layer.

3.2 Meteorological conditions

Surface fluxes exhibited a regular diurnal cycle in which both J_q^o and J_b^o were positive when upward fluxes occurred during the night (Figures 4A, B). The J_q^o values varied between -3 W m^{-2} and -731 W m^{-2} during daytime and between 2 W m^{-2} to 309 W m^{-2} at night (Figure 4A), which resulted in convective conditions with mean values of 1.18 × 10^{-8} W kg^{-1} during the night (Figure 4B). In this regard, fluxes of J_b^S were always lower than those of J_b^T and differed by one order of magnitude. The main contributors to the net total heat flux during the night were J_q^{La} and J_q^{Lw} (Figure 4A).

The air temperature was generally higher than the sea water temperature except in CTD stations 30–32 and 42–44, which had comparable T_{air} and SST values (Figure 4C). This decrease in

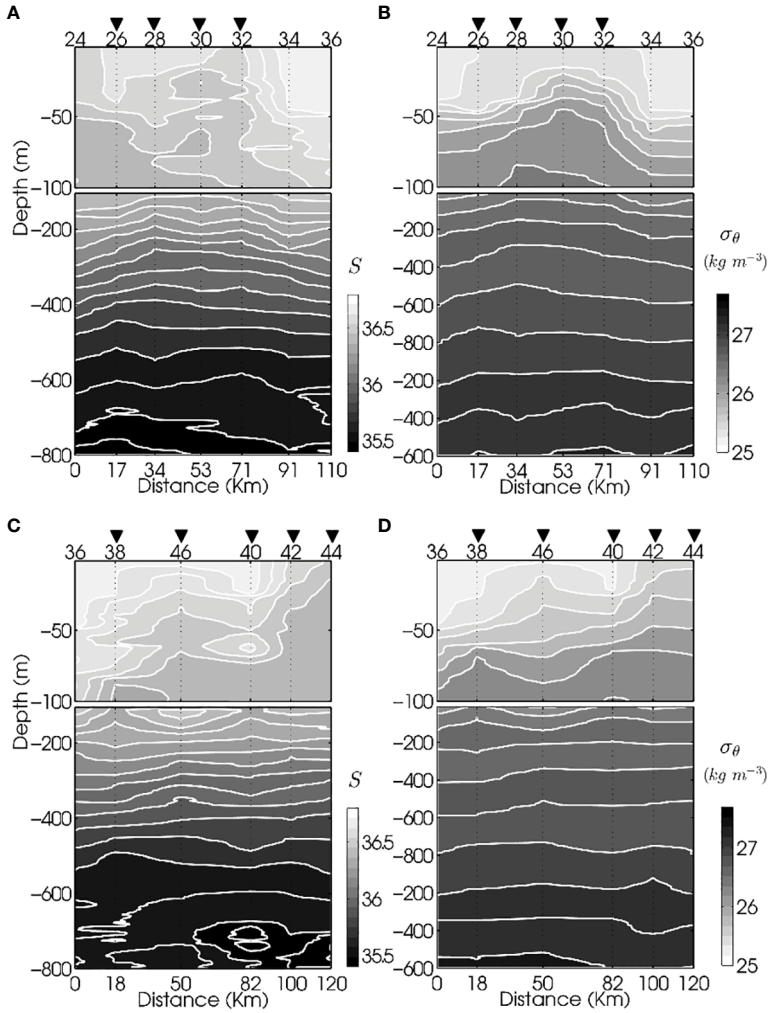

FIGURE 5
Vertical hydrographic sections derived from CTD profiles of **(A)** absolute salinity (*S*) and **(B)** potential density anomaly (σ_θ, m kg^{-3}) for transect A and **(C)** *S* and **(D)** σ_θ for transect B. Contours of *S* are plotted at 0.5 intervals, while σ_θ contours are plotted every 0.1 kg m^{-3}. The cumulative distance between stations in km is shown at the bottom of each panel. The hydrographic station numbers are shown at the top of each panel. Inverted triangles indicate stations influenced by the upwelling filament.

seawater temperature may be related to these stations being located within cool upwelling filament waters. It is noteworthy that the mean difference in temperature between waters within and outside of the filament was 1.09°C.

Weak northeasterly winds prevailed throughout the cruise (Figure 4D), with a mean speed of $\boldsymbol{u}_r$ = 3.78 m s^{-1} and $\boldsymbol{\tau}_o$ values that varied from 0.0026 N m^{-2} to 0.065 N m^{-2} on the last day of sampling. This wind pattern was characteristic of early fall when trade winds are relatively less intense in this region. A sudden increase in wind speed was observed on 24 October (Figure 4D), which interfered with observations. Thus, the measurements concluded on 23 October.

Given that both wind-stress and net surface heat fluxes can act as forcing mechanisms to enhance mixing at the base of the mixed layer and increase w_e, a meteorological-related quantity, such as the Monin–Obukhov length scale (L_{mo}) (Figure 4E), is useful for determining which forcing process dominates the dynamics of the upper ocean layer. To indicate the depth at which both mechanical and convection forces are comparable, this scale can take the following form:

$$L_{mo} = -\frac{u^{*3}}{\kappa J_b^o}, \tag{6}$$

where κ = 0.4 is the von Kármán constant (e.g., Huffman and Radshaw, 1972). Values of $L_{mo} > 0$ (Figure 4E) indicate that the turbulence generated by wind stirring is suppressed by the stable stratification present during daytime, while $L_{mo} < 0$ occurs under unstable conditions at night. Moreover, in our study, $|L_{mo}|$ was generally shallower than h_ρ (Figure 4E), which suggests that wind-induced mixing does not notably control the depth of the mixed layer.

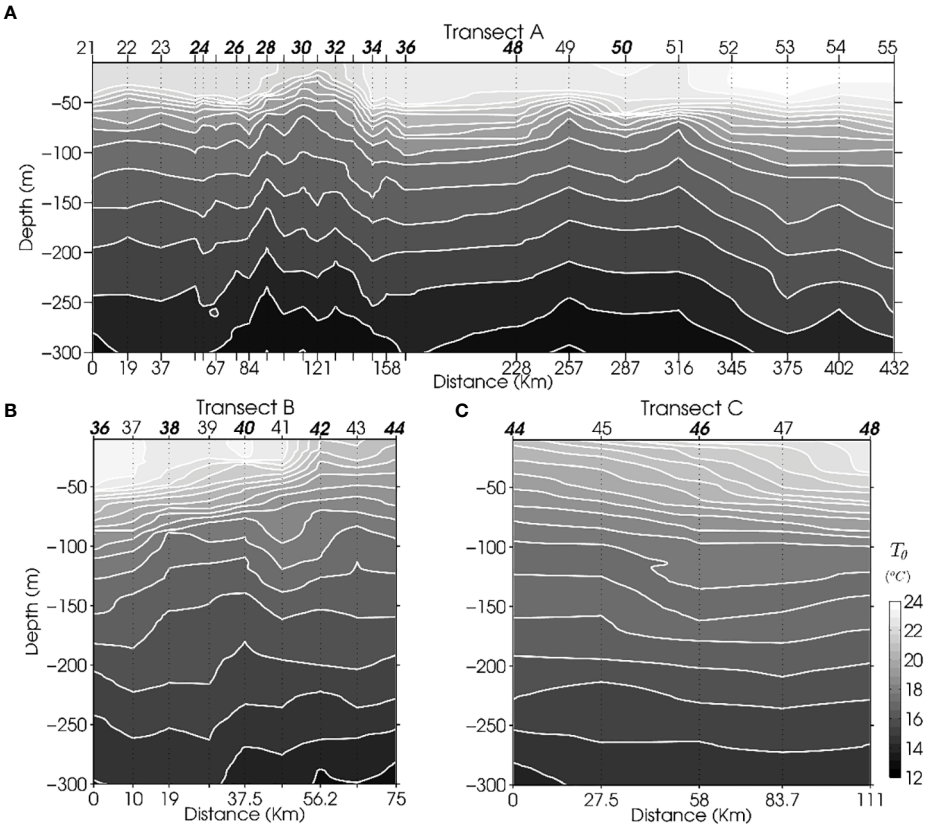

FIGURE 6
Vertical sections derived from CTD-temperature profiles combined with expendable bathythermograph (XBT) temperature profiles of transects **(A)** A, **(B)** B, and **(C)** C, which was an additional transect. Isotherms are spaced every 0.5°C, and an offset of approximately 10 m was applied to the XBT profiles to ensure consistency with CTD depth. At the top of each panel, numbers in bold italic font denote CTD stations, whereas numbers in Roman font denote XBT stations. Note that not all station numbers are displayed at the top to facilitate viewing. All CTD and XBT stations are taken into account in the vertical sections. The cumulative distance (km) is shown at the bottom of each panel.

3.3 Mixed layer depth, mixing layer depth, and entrainment zone

Bulk mixed layer models and consequently entrainment rates heavily depend on the depth of the mixed layer. This dependence has been attributed to velocity and buoyancy values across the mixed layer layer (Ravindran et al., 1999), which vary greatly with h_ρ. Therefore, we carefully determined h_ρ by comparing different methods (Figure 7).

The algorithm developed by Holte and Talley (2009) can be based on the shape of either the potential density or potential temperature profile of each hydrographic station. With the exception of station 50, we found that the σ_θ method from Holte and Talley (2009) resulted in an adequate fit to the observed h_ρ. For station 50, the T_θ method of Holte and Talley (2009) was more appropriate, which was largely due to the existence of salinity barriers around the area caused by the subsurface salinity maximum (Pelegrí et al., 2005b). This algorithm agrees rather well with the depth of the maximum gradient of the buoyancy frequency squared (N^2, rad^{2}s^{-2}) (Figure 7) and with the threshold method of $\Delta\sigma_\theta$ = 0.03 kg m^{-3} (de Boyer Montégut et al., 2004).

Further, we found that the algorithm given by Kara et al. (2000) tended to overestimate h_ρ, whereas the gradient methods of Dong et al. (2008) tended to underestimate h_ρ. These results agree with the findings of Holte and Talley (2009) for large databases of hydrographic profiles.

Several authors have emphasized the need to consider a boundary region of elevated and active mixing in the pycnocline at the base of the mixed layer (e.g., Dewey and Moum, 1990; Brainerd and Gregg, 1995; Nagai et al., 2005; Inoue et al., 2010; Sutherland et al., 2014), which is usually referred to as the mixing layer depth (h_ε). The difference between h_ρ and h_ε is that the latter is the depth at which turbulent processes are active and maintain the homogeneity of the mixed layer and entrain buoyancy across the pycnocline. In contrast, h_ρ represents the depth at which these surface fluxes have been mixed in the recent past (i.e., in a daily cycle or longer), thus h_ρ represents the history of several mixing events. Depending on the time scale and spatial resolution, the use of h_ε could be more appropriate when evaluating entrainment than h_ρ (Brainerd and Gregg, 1995). For example, fine-scale processes forced by transient mixing events in which flux conditions can change at any given moment of the day require measurements of

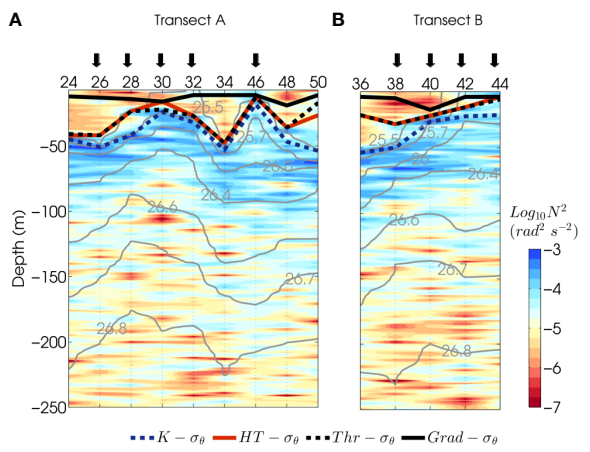

FIGURE 7
Vertical section of the buoyancy frequency squared (N^2, rad^2 s^{-2}) in logarithmic scale for all hydrographic stations of **(A)** transect A and **(B)** transect **(B)** Superimposed lines indicate mixed layer depths (h_ρ, m) computed with different methods. For the sake of clarity, only potential density-based algorithms are shown. Squares show h_ρ obtained with the methods of Kara et al. (2000). Red circles show h_ρ obtained with the Holte and Talley (2009) algorithm (except for station 50 where a T_θ-based algorithm was more appropriate). Black squares show the σ_θ threshold criteria of de Boyer Montégut et al. (2004). Yellow squares show h_ρ computed following the gradient method of Dong et al. (2008). The light gray contours are isopycnals (σ_θ, m kg^{-3}). The vertical black arrows denote the hydrographic stations of group-F, which were influenced by filament waters.

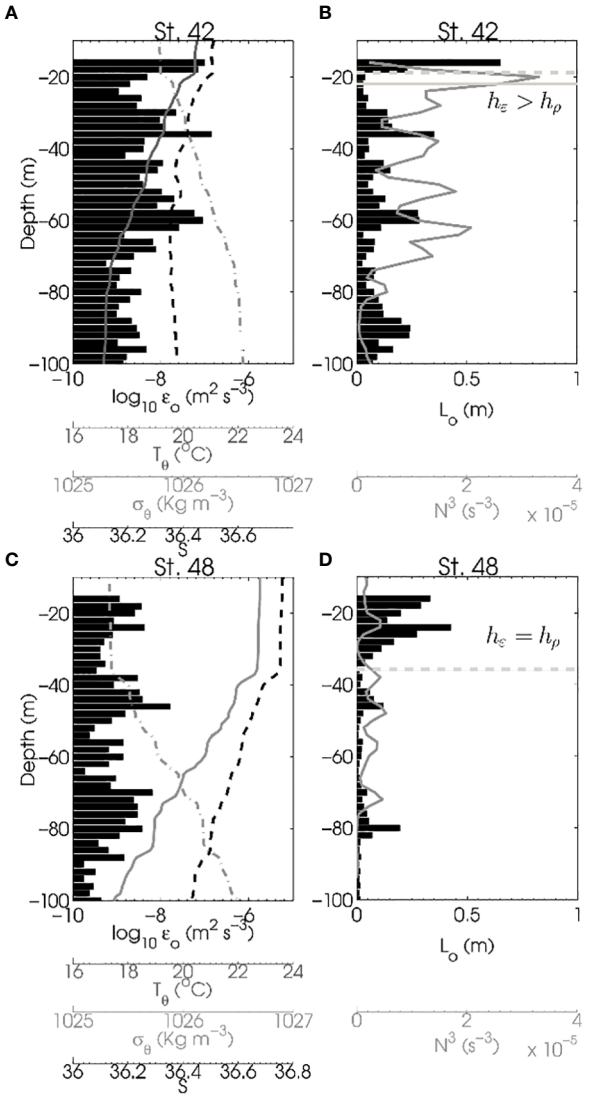

FIGURE 8
Vertical profiles of hydrographic and turbulent quantities. Left panels show potential temperature (T_θ °C, dark gray line), the potential density anomaly (σ_θ kg m^{-3}, dash-dot line), and absolute salinity (S, dashed black line) superimposed on turbulent kinetic energy (TKE) dissipation profiles (ε_o m^2 s^{-3}, black bars) for **(A)** station 42 of group-F (within the upwelling filament) and **(C)** station 48 of group-nF (outside the upwelling filament). Both stations were measured during stable daytime conditions. The right panels show Ozmidov scales (L_o, m, black bars) and vertical profiles of the buoyancy frequency cubed (N^3 s^{-3}, gray profiles) for **(B)** station 42 and **(D)** station 48. Horizontal dashed and thick lines denote the mixed layer depth (h_ρ, m) and mixing layer depth (h_ε, m), respectively.

the active mixing layer. As such, the definition of h_ε has important repercussions for Sverdrup's critical depth theory of phytoplankton blooms (Sverdrup, 1953). Franks (2014) revisited Sverdrup's critical depth theory and argued that h_ρ, defined by density gradients, may not always reflect the intensity of active turbulence or its vertical extension. In this sense, the critical turbulence hypothesis (Huisman and Weissing, 1999) suggests that active mixing described by the definition of h_ε must be considered, as it can act to reduce stratification in the upper layer, which may lead to favorable conditions that allow phytoplankton blooms to develop (e.g., Ferrari et al., 2015).

In general, h_ε can be directly obtained with the ε_o of microstructure data (Brainerd and Gregg, 1995; Inoue et al., 2010; Franks, 2014; Sutherland et al., 2014), microstructure temperature gradients (Nagai et al., 2005), or measurements of the largest turbulent overturning length scales such as Thorpe scales (Brainerd and Gregg, 1995). In this study, we determined the base of the mixing layer when the dissipation rate decreased by two orders of magnitude from the surface, which was similarly undertaken by Inoue et al. (2010). However, not all ε_o profiles exhibited clear transitions. Therefore, a turbulent length scale, such as the Ozmidov scale L_o (Ozmidov, 1965), could help clarify the extension of the active mixing or h_ε, where L_o takes the following form:

$$L_o = \sqrt{\varepsilon_o / N^3}\,. \tag{7}$$

In such a case, L_o is interpreted as the size of the largest turbulent eddy in a region of stable stratification. An example of h_ε and L_o can be viewed in Figure 8, in which the maximum vertical gradient of L_o agrees with a decrease in ε_o of one order of magnitude within the upper boundary layer.

Dewey and Moum (1990), in their examination of microstructure data in upwelling filaments off northern California, noted that entrainment can only take place when h_ε exceeds h_ρ; otherwise, when mixing is not strong enough to overcome the effects of stratification in the pycnocline, entrainment cannot occur. Inoue et al. (2010) also distinguished between h_ε and h_ρ to measure entrainment heat fluxes based on dissipation profiles across the Gulf Stream provided that h_ε was

deeper than h_ρ . The same approach was considered in this study by defining the entrainment zone or interface as $\Delta h = h_\varepsilon - h_\rho$.

3.4 Turbulence enhancement within upwelling filaments

When the active mixing layer extends deeper than the mixed layer, that is $h_\varepsilon > h_\rho$ (Dewey and Moum, 1990; Brainerd and Gregg, 1995; Inoue et al., 2010), non-turbulent fluid from the pycnocline is subject to sufficient mixing to break stratification at the pycnocline and enters the turbulent fluid.

Some authors have speculated that enhanced turbulence below h_ρ could be related to shear instabilities produced by internal waves as a result of impinging convective plumes from beneath the mixed layer (Moum et al., 1989). MacKinnon and Gregg (2005) found higher correlations between ε_o and internal wave energy than between ε_o and $\boldsymbol{\tau}_o$ below the mixed layer. Here, an example of this can be seen in Figure 8, in which h_ε is deeper than h_ρ for a station in group-F (Figures 8A, B). In contrast, h_ε and h_ρ exhibited the same depth in a station of group-nF (Figures 8C, D). Both stations were measured during daytime conditions (i.e., during the restratification of the mixed layer when convection forcing is absent).

A complete view of active turbulent mixing is given in Figure 9, which shows vertical profiles of ε_o and superimposed profiles of L_o scales computed for each microstructure station with their respective h_ρ and h_ε. Interestingly, h_ε was deeper than h_ρ (i.e., $\Delta h > 0$) in filament stations (thick profiles in Figures 9, 10A, B). This suggests that only filament stations are susceptible to diapycnal entrainment by surface-forced processes (Dewey and Moum, 1990; Fer and Sundfjord, 2007; Inoue et al., 2010). This may be the result of elevated ε_o at group-F stations and the shallow mixed layers produced by isopycnal outcropping due to the isopycnal morphology of the frontal filament system.

It is important to note the enhancement of ε_o below the mixed layer of filament waters, which can be seen in Figure 9. A weak wind regime during sampling days, as evidenced by the L_{mo} scales (Figure 4E), indicates that the turbulence generated within the upwelling filament by wind stress was likely small when compared to turbulent diapycnal buoyancy fluxes or vertical shear at the base of the mixed layer. However, this increase in turbulence has also often been linked with elevated vertical shear levels (Figure 11).

Vertical current shear was relatively high in areas associated with isopycnal outcropping, such as in group-F stations (Figure 11), thus we examined the nature of these shear values. To ensure consistency when comparing ADCP- Sh^2 with geostrophic shear (Sh_g^2), the ADCP velocities were rotated to the same reference system and interpolated between pairs of stations. Geostrophic shear was computed through the thermal wind relation by setting a reference level of no motion at 650 m (see Pelegrí et al., 2005b). In Figures 11A, C, it can be seen that the Sh^2 in group-F stations is mainly driven by the resolved component of the geostrophic velocity field in transect A. In transect B, the isopycnals outcropped towards the coast due to the presence of the filament and proximity to the coastal transition zone (Figure 11D). Here, the resolved geostrophic component became less relevant and ageostrophic effects arose to force total vertical shear in the stations of group-F (Figures 11B, D). These results were also supported by the geostrophic currents of altimetry data (see Figure 2). Further, the presence of a southward geostrophic current agreed with the predominance of geostrophic shear in transect A. In contrast, a departure from geostrophy appeared to take place in the coastal transition zone of transect B, in which the filament flowed southward in the opposite direction of geostrophic flow (Figure 11D), which was also observed by Dewey et al. (1993). As the filament moves offshore, it is balanced geostrophically, as was observed in transect A (Figure 11C). The enhancement of ε_o within the filament waters of group-F, the increase of vertical shear

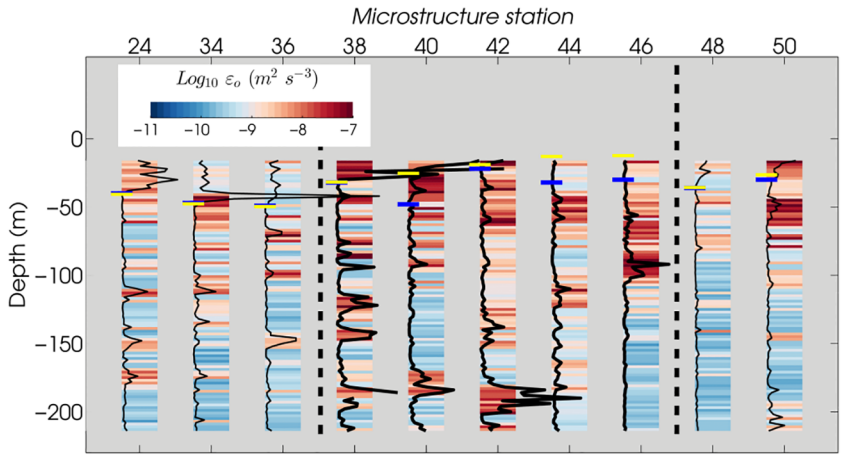

FIGURE 9
Vertical profiles of Ozmidov scales (L_o, m) for each microstructure station. The color columns are profiles of the observed TKE dissipation rates (ε_o, $m^2\ s^{-3}$). The maximum L_o value corresponds to 5.18 m for station 34 at 42 m depth. The minimum L_o of 0.0045 m corresponds to station 38 at 66 m depth. The thick black profiles show L_o for stations of group-F. The thin profiles show L_o for stations of group-nF. The horizontal lines indicate the mixed layer depths (h_ρ, yellow) and mixing layer depth (h_ε, blue) in meters. The vertical dashed lines show the limits of the group-F stations.

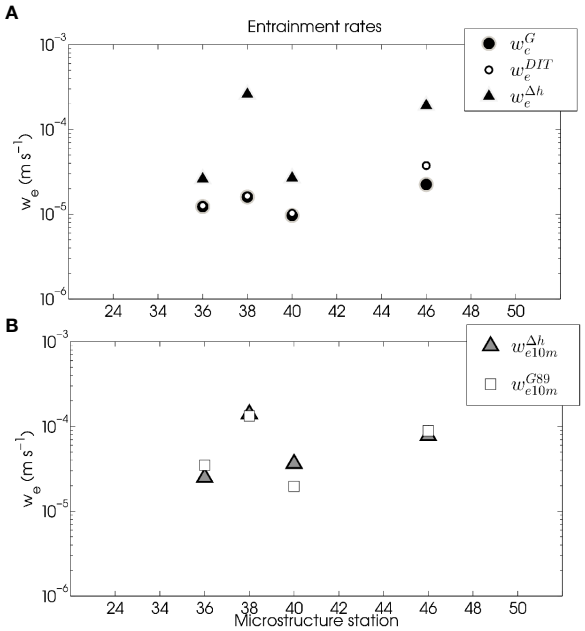

FIGURE 10
(A) Entrainment rates (w_e, m s^{-1}) following the methodology of Gaspar (1988) (w_e^G), entrainment rates adding the DIT term (w_e^{DIT}), and entrainment rates using the modifications proposed in this study ($w_e^{\Delta h}$) computed at a vertical resolution of 2 m. **(B)** Entrainment rates, $w_e^{\Delta h}$, averaged over 10 m for observable values ($w_{e10m}^{\Delta h}$), and entrainment rates scaled following the methodology of Gregg, (1989) (w_{e10m}^{G89}).

at the base of the mixed layer, and the resulting $\Delta h > 0$ are summarized in Figure 12.

In a modeling study, Small et al. (2012) argued that shear instability below the mixed layer may be generated in large part by propagating inertial waves, which ultimately increase the entrainment of cold waters from below the thermocline. Although it was not the aim of the present study to evaluate inertial wave activity, the lack of a time series of velocity currents did not allow for the presence of such near-inertial oscillations to be corroborated.

3.5 Implications of the entrainment process

The entrainment of cold, nutrient-rich waters from below the pycnocline to the surface layers and the subsequent deepening of the mixed layer are sensitive to turbulent mixing and the depth of the upper boundary layer. However, most bulk mixed layer models (Kraus and Turner, 1967; Niiler and Kraus, 1977; Gaspar, 1988) do not account for either (*a*) vertical shear as a source of TKE or (*b*) variable h_ε. Thus, such models are inappropriate for frontal areas with baroclinicity in which shallow h_ρ values are driven by the rising of the pycnocline and in which breaking internal waves may be important for the generation of strong sheared flows.

Accordingly, in the case of (*a*), we took into account the DIT term, which is described in Eq. (5). It is assumed that turbulent entrainment can occur only when active mixing in a stratified fluid is strong enough to overcome buoyancy effects and erode the pycnocline, that is when $\Delta_h > 0$ (Dewey and Moum, 1990; Inoue et al., 2010). Given that we had direct measurements of h_ε, we restricted our analysis to stations in which ε_o was available and $\Delta h > 0$. In the case of (*b*), we considered the diapycnal turbulent buoyancy flux integrated over the entrainment zone, $(J_b^{\Delta h})_I$. This term represents a TKE sink in the entrainment zone when $\Delta h > 0$, as the energy is consumed when stratification breaks down. The procedure to obtain $(J_b^{\Delta h})_I$ is described in Appendix A. Thus, the integration of the dissipation term over the entire active mixing layer $\int_{-h_\varepsilon}^{0} \varepsilon_o(dz) = \overline{\varepsilon_o} h_\varepsilon$ should also be considered, similarly to what can be observed in Dewey and Moum (1990). By including these considerations in Eq. (5), the TKE-based entrainment parameterization can be described by the following equation:

$$w_e^{\Delta h} = \frac{(m_2 + m_3)u_\star^3 + 0.5 h_\rho J_b^o + (J_b^{\Delta h})_I - \overline{\varepsilon_o} h_\varepsilon}{0.5[(\delta b h_\rho) - (\delta u^2 + \delta v^2)]}. \quad (8)$$

Unlike other entrainment parameterizations, Eq. (8) considers TKE sources and sinks due to mechanical stirring by means of $u_\star$, vertical shear at the base of h_ρ through the DIT term, buoyancy fluxes at the surface and turbulent buoyancy fluxes at the entrainment zone (i.e., J_b^o and $(J_b^{\Delta h})_I$), and TKE dissipation across the layer in which active mixing operates. The results from Eq. (8) yield mean entrainment rates of $\overline{w_e^{\Delta h}} = 6.99 \times 10^{-5} \pm 5 \times 10^{-5}$ m s^{-1} (~6 m d^{-1}), which differ by a factor of 6 when compared to those of $\overline{w_e^G} = 1.51 \times 10^{-5} \pm 5 \times 10^{-5}$m s^{-1} (1 m d^{-1}) (Figure 10). The addition of the DIT term resulted in a slight increase in the entrainment rates, with a mean value of $\overline{w_e^{DIT}} = 1.92 \times 10^{-5} \pm 1 \times 10^{-5} \pm$ m s^{-1} (~2 m d^{-1}).

It is important to note that although this analysis was based on a 1D approach, several scales can coexist within ocean fronts. Two-dimensional (2D) submesoscale processes in an upwelling filament may play major roles in mixing by serving as pathways that convey the kinetic energy extracted from the mean flow to the final dissipation range throughout the secondary instabilities of the submesoscale flow (Capet et al., 2008; D'Asaro et al., 2011; Thomas et al., 2013). To determine whether this type of process affected the front in this study, the vertical distributions of potential vorticity and submesoscale energy sources were evaluated (Appendix B). As a first approximation, our results indicate that at the moment of sampling, submesoscale 2D instabilities, such as symmetric instabilities, appeared to weakly affect the frontal structure. The cross-front wind in transect A (see Figure B.1 in Appendix B) was likely insufficient to induce Ekman transport, which would cause the front to be susceptible to symmetric instabilities (e.g., D'Asaro et al., 2011). Thus, a 1D perspective based on the TKE balance is appropriate in this study. Furthermore, D'Asaro et al. (2011) indicated that although turbulent mixing near fronts can arise from these instabilities, this does not seem to be responsible for the observed elevated mixing in the Cape Ghir upwelling filament front.

3.6 Implications of the dissipation term

The TKE budget and consequently entrainment are highly sensitive to the parameterization of the dissipation term, which

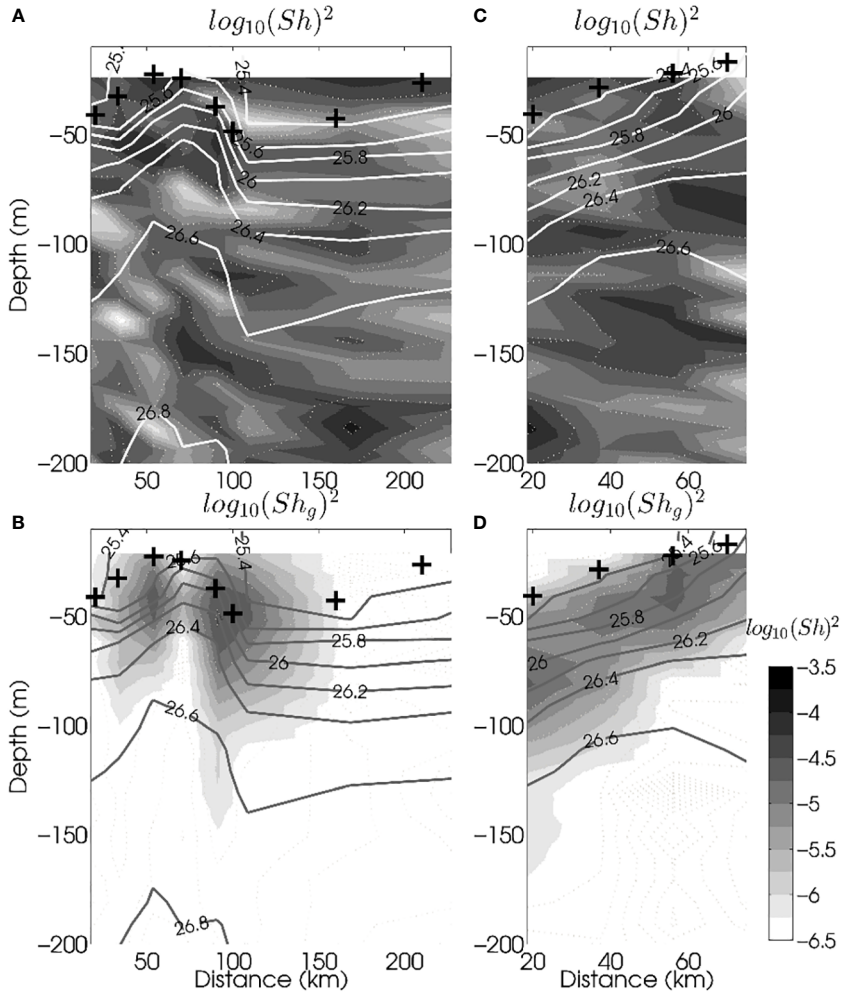

FIGURE 11
(A) Vertical sections of total vertical shear squared (Sh^2, s^{-2}) for transect A rotated to the reference system of geostrophic velocities and **(B)** geostrophic vertical shear squared (Sh_g^2, s^{-2}) with the level of no motion set to 650 m for transect **(A)** The same is shown in **(C, D)** for transect **(B)** Crosses represent the mixed layer depths (h_ρ, m) averaged between pairs of stations. Note the logarithmic scale. The isopycnals (kg m^{-3}) are also shown. The cumulative distance (km) between stations is shown at the bottom.

has proved to be a dominant sink in the energy balance (e.g., Deardorff, 1983; Gaspar, 1988; Wada et al., 2009). Our results highlight that the role of the dissipation term may be particularly important in frontal areas such as upwelling filaments. However, a dependence on observational ε_o values may make it difficult to include parameterizations of the dissipation term in bulk mixed-layer models.

We assumed a well-mixed upper ocean layer and averaged ε_o from the near-surface (far enough away from the effects of breaking waves at the surface ~16 m) to h_ε and compared this to the parameterized ε_G included in w_e^G following the methods of Gaspar (1988). Our results, which are shown in Table 2, indicate that the normalized parameterized dissipation term ($\overline{\varepsilon_G}|_{h_\rho}$) can be overestimated by two orders of magnitude with respect to the observed dissipation term ($\overline{\varepsilon_o}|_{h_\varepsilon}$).

In the context of a 1D TKE balance, most of the energy transferred to the interface is dissipated by viscosity. The remaining energy is stored in the form of potential energy that must work against buoyancy forces or as energy that will be subsequently converted to kinetic energy by entrainment. As a result of this 1D balance, the dissipation term may be overestimated due to entrainment velocities that are lower than expected, which suggests that the parameterized dissipation term extracts more energy from the system and leaves little energy for entrainment. Thus, decreasing the dissipation term in entrainment parameterizations to match the observed dissipation term will lead to an enhancement of w_e. This can be seen in Figure 10, in which $w_e^{\Delta h}$ exhibits velocities that are higher than those given by w_e^G and w_e^{DIT}. This suggests that the dissipation term within the entrainment parameterization of Gaspar (1988) might not be well resolved in frontal systems.

We also compared ε_o to the internal wave scaling (ε_{G89}) proposed by Gregg (1989), which takes the internal wave spectrum into account:

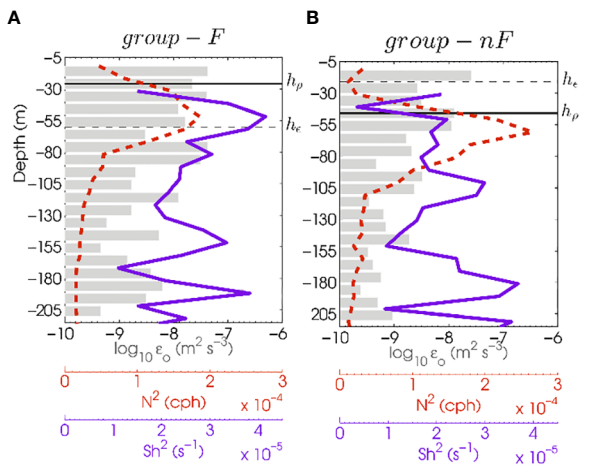

FIGURE 12
Horizontally averaged vertical profiles of turbulent kinetic energy (TKE) dissipation rates (ε_o, gray bars), buoyancy frequency squared (N^2 cph, dashed red profiles), and vertical shear squared (Sh^2 s^{-1}, violet profiles) for stations of **(A)** group-F (where $\Delta h > 0$) and **(B)** stations of group-nF (where $\Delta h > 0$). The horizontal dashed and solid lines represent the average mixed layer depth (h_ρ) and mixing layer depth (h_ε, m) for both transects, respectively. Note that ε_o and N^2 were vertically averaged to 10 m bins to ensure numerical consistency with the vertical resolution of Sh^2.

$$\varepsilon_{G89} = 1.8 \times 10^{-6} \left[\text{fcosh}^{-1} \left(\frac{No}{f} \right) \right] \left(\frac{N^2}{No^2} \right) \left(\frac{Sh^4}{S_{GM}^4} \right), \quad (9)$$

where $No = 5.2 \times 10^{-3}$ (rad s^{-1}), and $S_{GM} = 1.91 \times 10^{-5}$ (s^{-1}) is the Garret-Munk shear spectrum (Gregg, 1989).

Although the fine-scale parameterizations of ε_{G89} differ from the observed values of ε_o, when overestimating or underestimating ε_{G89} along the water column (Figure 13), the averaged dissipation term $\overline{\varepsilon_{G89}}|_{h_{\varepsilon 10}^{G89}}$ resembles the observed dissipation term $\overline{\varepsilon_o}|_{h_\varepsilon}$, particularly when this is averaged within 10 m depth intervals ($\overline{\varepsilon_{o10}}|_{h_{\varepsilon 10}}$) (Table 2). It is worth noting that the mixing layer depths obtained from ε_{G89} are quantitatively similar to those given by the observed ε_{o10} (Figure 10A). A comparison between mixing layer depths and the resulting entrainment zones is shown in Figures 10A, B. Note that for coarser resolutions, $h_{\varepsilon 10}$ is always deeper than the mixed layer depth, resulting in $\Delta h > 0$ for all stations. Moreover, the results also show agreement between ε_o and ε_{G89} in that both show enhanced turbulent mixing in stations of group-F (Figure 13 and Table 2).

These results indicate that the observed dissipation term in the proposed entrainment parameterization of Eq. (8) could be replaced by the scaling of Gregg (1989) (hereinafter w_e^{G89}). The mean value of w_e^{G89} was $6.91 \times 10^{-5} \pm 5 \times 10^{-5}$ m s^{-1} (6 m d^{-1}), which is similar to $w_e^{\Delta h}$, as indicated in Figure 10B. This result also suggests that the role of internal waves acting at the base of the mixed layer should not be ignored given the agreement between w_e^{G89} and $w_e^{\Delta h}$.

3.7 Implications of the nutrient fluxes

It is to be expected that the enhancement of diapycnal entrainment rates observed in group-F stations would favor the elevation of deep nutrient-rich water to the photic layer. In the same study region, Arcos-Pulido et al. (2014) observed that onshore stations, which belong to group-F, exhibited diapycnal nutrient fluxes, $F_z(Nut)$, which were one order of magnitude greater than those observed in offshore stations calculated at a reference layer located 20 to 30 m below the mixed layer.

To verify that the enhancement of entrainment rates in the upwelling filament contributed to increasing nutrient availability below the mixed layer, we computed $F_z(Nut)$ immediately below h_ρ for each microstructure station with the following equation:

$$F_z(Nut) = -K_z \frac{\partial N}{\partial z}, \quad (10)$$

where K_z is the diapycnal diffusivity coefficient given by the classic expression ($K_z = \Gamma \varepsilon_o / N^2$) of Osborn (1980). Buoyancy diffusivity and heat were assumed to be of the same order. The

TABLE 2 Turbulent kinetic energy dissipation terms (ε) averaged horizontally for stations of group-F (within the filament), group-nF (outside the filament), and all microstructure stations.

Averaged ε (m^3 s^{-3})	group-F	group-nF	Total
$\overline{\varepsilon_G}\|_{h_\rho}$	1.14×10^{-6}	2.82×10^{-6}	1.98×10^{-6}
	($\pm$ 1.09×10^{-6})	($\pm$ 2.06×10^{-6})	($\pm$ 1.79×10^{-6})
$\overline{\varepsilon_o}\|_{h_\varepsilon}$	3.37×10^{-8}	9.53×10^{-9}	2.16×10^{-8}
	($\pm$ 3.07×10^{-8})	($\pm$ 1.01×10^{-8})	($\pm$ 2.50×10^{-8})
$\overline{\varepsilon_{G89}}\|_{h_{\varepsilon 10}^{G89}}$	7.07×10^{-8}	3.36×10^{-7}	2.03×10^{-7}
	($\pm$ 8.62×10^{-8})	($\pm$ 3.32×10^{-7})	($\pm$ 2.68×10^{-7})
$\overline{\varepsilon_{o10}}\|_{h_{\varepsilon 10}}$	1.01×10^{-6}	3.10×10^{-7}	6.59×10^{-7}
	($\pm$ 1.60×10^{-6})	($\pm$ 3.42×10^{-7})	($\pm$ 1.51×10^{-6})

ε (either observed or parametrized) was vertically averaged from the surface to different layers as follows: $\overline{\varepsilon_G}|_{h_\rho}$ is the parameterized dissipation term following Gaspar (1988) averaged up to the mixed layer depth; $\overline{\varepsilon_o}|_{h_\varepsilon}$ is the observed dissipation term averaged until mixing layer depth; $\overline{\varepsilon_{G89}}|_{h_{\varepsilon 10}^{G89}}$ is the parameterized dissipation term [ε] averaged up to a mixing layer depth identified at a vertical resolution of 10 m following the scaled dissipation profile of Gregg (1989); $\overline{\varepsilon_{o10}}|_{h_{\varepsilon 10m}}$ is the observed dissipation term averaged up to an observed mixing layer depth identified at a vertical resolution of 10 m. Standard deviations appear in parenthesis.

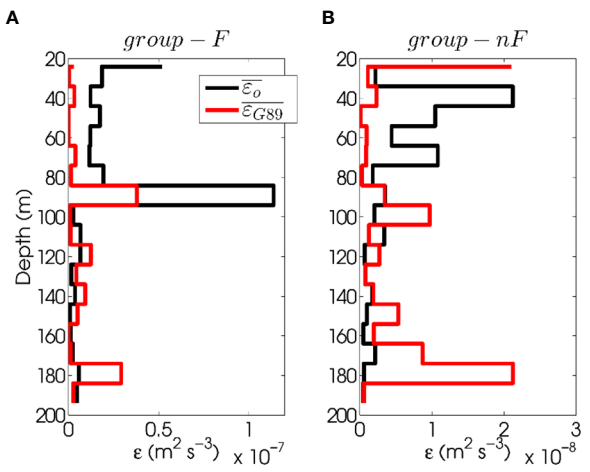

FIGURE 13
Comparison of turbulent kinetic energy dissipation rates, ε ($m^2\ s^{-3}$), spatially averaged for stations of **(A)** group-F (within the filament) and **(B)** group-nF (outside the filament). Black profiles are the observed dissipation rates, $\overline{\varepsilon_o}$ ($m^2\ s^{-3}$). The red profiles are the dissipation rates obtained following the methodology of Gregg (1989), $\overline{\varepsilon_{G89}}$ ($m^2\ s^{-3}$). Note the different scales of the x-axis.

mixing efficiency (Γ) is the ratio between the vertical buoyancy flux and ε_o set to 0.2 (Oakey, 1982). The nutrient concentration, which consists of the sum of nitrites and nitrates (*Nut*), was linearly interpolated to a vertical 2-m grid given the microstructure vertical resolution.

Nutrient gradients ($\partial Nut/\partial z$) were calculated over depths ranging from 5 m to 20–30 m below h_ρ depending on the availability of nutrient (Schafstall et al., 2010). This differs from what was reported by Arcos-Pulido et al. (2014), who calculated fluxes for a reference layer far below h_ρ. Then, K_z was averaged for the same depth range over which $\partial N/\partial z$ was calculated. Positive values of $F_z(Nut)$ imply an upward transport of nutrients from the pycnocline to the surface layers, where they may then be assimilated by phytoplankton.

The diapycnal nutrient fluxes (Table 3) indicated that stations of group-F exhibited large $F_z(Nut)$ immediately below the mixed layer associated with maximal diapycnal mixing, which was three times larger than those of group-nF stations. However, station 34 was an exception to this pattern. Station 34 was located adjacent to the filament edge (see Figure 6A) and was surveyed under weak wind, non-favorable convection, and low δV conditions. Station 34 also exhibited more intense *Lo* at the mixed layer depth (Figure 9) and high nutrient gradients (Table 3) when compared to the other stations in its group. In this case, Δh was nearly zero at station 34, indicating that both h_ρ and h_ε were similar. Stations of group-F that were near station 34 (i.e., 30, 32, and 36) also exhibited high vertical nutrient gradients (not shown). This suggests that it cannot be ruled out that station 34 was influenced by either the upwelling filament or other processes, such as breaking internal waves or Langmuir cells, capable of promoting intense vertical mixing at the base of the mixed layer (Flór et al., 2010; Schafstall et al., 2010). However, the lack of microstructure observations and time series of physical variables did not allow for an evaluation of the underlying causes. Stations 48 and 50 also exhibited positive $F_z(Nut)$. Despite forming part of group-nF, these stations exhibited $\Delta h > 0$, indicating that favorable entrainment conditions were present, yet their fluxes were lower than those of group-F stations

In general, stations of group-F exhibited diapycnal nutrient fluxes that were two orders of magnitude larger than those of group-nF stations. The values of $F_z(Nut)$ for stations of group-F were at the upper end of those reported for the North Atlantic (Bahamón et al., 2003; Dietze et al., 2004; González-Dávila et al., 2006; Mouriño-Carballido et al., 2011) but of the same order of magnitude as those of other EBUS sites (Hales et al., 2005; Hales et al., 2009; Li et al., 2012). Most studies conducted in the North Atlantic have not included calculations of nutrient fluxes immediately below the mixed layer using direct microstructure observations nor in highly turbulent environments such as frontal systems. The values reported for frontal systems in other EBUS range from 5.2 (mmol m^{-2} d^{-1}) in the California Current EBUS to 19.11 (mmol m^{-2} d^{-1}) in the Chilean EBUS (Hales et al., 2005; Hales et al., 2009; Li et al., 2012; Corredor-Acosta et al., 2020). The latter values agree with our maxima of 8.34 (mmol m^{-2} d^{-1}) for station 42 (group-F) and average of 1.35 (mmol m^{-2} d^{-1}) for all stations influenced by the upwelling filament front.

4 Conclusions

We analyzed the sources and sinks of TKE that control the upper boundary layer through a simple 1D TKE-balance. This study was conducted in the submesoscale upwelling filament of Cape Ghir using satellite imagery and *in-situ* hydrographic measurements, including novel ε_o measurements from a microstructure profiler. The main results of this study are summarized as follows:

- Microstructure profiles revealed an enhancement of turbulent mixing within the upwelling filament front where pycnoclines shoal. The absence of strong winds and the presence of moderate buoyancy and heat fluxes enabled us to consider vertical shear as a relevant source of TKE, which is usually neglected in entrainment parameterizations.
- Enhanced turbulence and the morphology of the front promoted the formation of regions of active mixing, which were identified by the depth of the mixing layer exceeding the depth of the mixed layer, resulting in local areas of $\Delta h > 0$ (Figures 8, 9, 12). This created optimal conditions for the entrance of nutrient-rich waters from the pycnocline to the upper boundary layer *via* entrainment. This theory is supported by positive Δh values in areas directly affected by the upwelling filament in which the pycnocline is close to the surface. In such cases, turbulent mixing becomes more efficient within a smaller volume of water in the upper ocean layer. This highlights the importance of distinguishing between h_ρ and h_ε.
- To quantify the role of entrainment, we included observed values of ε_o and considered h_ρ, h_ε, and shear at the base of the mixed layer. We found that the entrainment rates

TABLE 3 Average values of the diapycnal diffusivity coefficient (K_z, $m^2\ s^{-1}$), vertical nutrient gradient (nitrite + nitrate, $\partial Nut/\partial z$, $mmol\ m^{-4}$), and diapycnal nutrient flux $F_z(Nut)$ $mmol\ m^{-2}\ d^{-1}$) below the mixed layer for each microstructure station.

Station	K_z	∂N/∂z	$F_z(Nut)$
24	0.34×10^{-4} ($\pm 0.53 \times 10^{-4}$)	+0.003 (±0.013)	-0.02 (±0.05)
34	0.58×10^{-4} ($\pm 0.73 \times 10^{-4}$)	-0.02 (±0.01)	+0.10 (±0.12)
36	0.55×10^{-4} ($\pm 0.69 \times 10^{-4}$)	+0.002 (±0.003)	-0.02 (±0.04)
38*	2.21×10^{-4} ($\pm 7.01 \times 10^{-4}$)	-0.007 (±0.007)	+0.21 (±0.78)
40*	8.78×10^{-4} ($\pm 8.85 \times 10^{-4}$)	-0.02 (±0.02)	+1.21 (±1.58)
42*	6.27 V× 10^{-4} ($\pm 8.64 \times 10^{-4}$)	-0.06 (±0.002)	+3.87 (±4.47)
44*	0.52×10^{-4} ($\pm 0.45 \times 10^{-4}$)	-0.23 (±0.14)	+0.57 (±0.87)
46*	2.56×10^{-4} ($\pm 3.14 \times 10^{-4}$)	-0.03 (±0.01)	+0.87 (±1.33)
48	0.57×10^{-4} ($\pm 0.87 \times 10^{-4}$)	-0.003 (±0.007)	+0.01 (±0.01)
50	7.86×10^{-4} ($\pm 12.0 \times 10^{-4}$)	-0.002 (±0.009)	+0.01 (±0.06)
group-nF	1.98×10^{-4} ($\pm 3.29 \times 10^{-4}$)	-0.002 (±001)	+0.02 (±0.05)
group-F	4.27×10^{-4} ($\pm 3.26 \times 10^{-4}$)	-07 (±0.09)	+1.35 (±1.465)

Standard deviation is shown in parenthesis.
(*) Microstructure stations impacted by the upwelling filament (i.e., Group-F).

changed considerably ($w_e^{\Delta h} = 6\mathrm{m\ d^{-1}}$) and were six times greater than those of other parameterizations. We also found that the dissipation term is often overestimated. The resulting low turbulent entrainment velocities could lead to an overestimation of SST in numerical models that include such mixing schemes.

- One of the most important results of this study can be summarized by Figure 12. We found that enhanced turbulent mixing within the upwelling filament is associated with an increase in vertical shear. One possible cause of the increase in vertical shear could be the effects of internal waves, which might be particularly effective when the filament is near the coast (transect B) and vertical shear exhibits ageostrophic behavior. This also allows for ε_o to be replaced by simple scaling based on the internal wave model of Gregg (1989), ε^{G89} , in the new proposed entrainment parameterization approach. This suggestion is supported by our result of w_e^{G89} being similar to the mean value of $w_e^{\Delta h}$.
- The diapycnal nutrient fluxes presented in this study reinforce the idea that enhanced diapycnal entrainment in upwelling filaments with $\Delta h > 0$ associated with high levels of diapycnal mixing favors the uplift of deep, nutrient-rich waters to the photic layer in submesoscale frontal systems.

This study aimed to establish a basis for future research that includes *in situ* data with proper spatiotemporal resolution and numerical simulations. The inclusion of additional TKE sources in entrainment studies, such as the energy of breaking internal waves that affects Δh and turbulent Langmuir circulation, may improve our understanding of turbulence in the upper boundary layer of submesoscale fronts.

Data availability statement

The raw data supporting the conclusions of this article will be made available by the authors, without undue reservation.

Author contributions

SE-A: Write the manuscript, processing of turbulence data, atmospheric data, data analysis, parameterization, figures, and tables. ÁR-S: Expert in the diapycnal mixing process, supervised the manuscript and the processing of the data, analysis, and parameterizations. AN-G: Expert in turbulence ocean process, advised about the symmetrical instabilities process that improves the original idea and in consequence the manuscript and supervised the manuscript. LG-W: Satellite Data access and its processing of sea surface temperature and surface chlorophyll. ME: Processing of ADCP data. All authors contributed to the article and approved the submitted version.

Acknowledgments

This study was made possible by a PhD grant awarded to the first author, which was supported by the Universidad de Las Palmas de

Gran Canaria. The hydrographic data necessary to reproduce this study were provided by projects PROMECA-2010 (CTM2009-06993-448 E/MAR) and PROMECA (CTM2008-04057) of Universidad de Las Palmas de Gran Canaria, co-founded by European Union (FEDER) and Ministerio de Ciencia e Inovación of Spain. The data are available from the corresponding authors upon request (angel.santana@ulpgc.es; sheila.estrada103@doctorandos.ulpgc.es). Satellite imagery were downloaded from NASA's Ocean Color Web for Moderate Resolution Imaging Spectroradiometer (MODIS) at NASA's Goddard Space Flight Center. Eds. Kuring, N., Bailey, S. W. (http://oceancolor.gsfc.nasa.gov/). The altimeter products were produced by Ssalto/Duacs and distributed by Aviso, with support from Cnes (http://www.aviso.altimetry.fr/duacs/). The comments of the reviewers and editor greatly improved the manuscript. The authors also thank the captain and crew of *R/V García del Cid* (CSIC) as well as all participating scientists for their support during the field survey.

Conflict of interest

The authors declare that the research was conducted in the absence of any commercial or financial relationships that could be construed as a potential conflict of interest.

Publisher's note

References

Álvarez Salgado, X., Arístegui, J., Barton, E., and Hansell, D. (2007). Contribution of upwelling filaments to offshore carbon export in the subtropical northeast atlantic ocean. *Limnol. Oceanogr.* 3 (52), 1287–1292. doi: 10.4319/lo.2007.52.3.1287

Anis, A., and Moum, J. (1994). Prescriptions for heat flux and entrainment rates in the upper ocean during convection. *J. Phys. Oceanography* 24, 2142–2155. doi: 10.1175/1520-0485(1994)024<2142:PFHFAE>2.0.CO;2

Arcos-Pulido, M., Rodríguez-Santana, A., Emelianov, M., Paka, V., Benavides, M., Sangrà, P., et al. (2014). Diapycnal nutrient fluxes on the northern boundary of cape ghir upwelling region. *Deep-Sea Res. Part I* 84, 100–109. doi: 10.1016/j.dsr.2013.10.010

Bahamón, N., Velasquez, Z., and Cruzado, A. (2003). Chlorophyll a and nitrogen flux in the tropical north Atlantic ocean. *Deep-Sea Res. Part I* 50, 1189–1203. doi: 10.1016/S0967-0637(03)00145-6

Barton, E. D., Arístegui, J., Tett, P., Cantón, M., García-Braun, J., Hernández-León, S., et al. (1998). The transition zone of the canary current upwelling region. *Prog. Oceanography* 41, 455–504. doi: 10.1016/S0079-6611(98)00023-8

Barton, E., Inall, M., and Sherwin, T. J. (2001). Vertical structure, turbulent mixing and fluxes during Lagrangian observations of an upwelling filament system off Northwest Iberia. *Prog. Oceanography* 51, 249–268. doi: 10.1016/S0079-6611(01)00069-6

Berliand, M. E., and Berliand, T. G. (1952). Measurement of the effective radiation of the earth with varying cloud amounts. *Izvestiya Akademii Nauk SSSR Seriya Geofiz* 1.

Brainerd, K. E., and Gregg, M. C. (1995). Surface mixed and mixing layer depths. *Geophysical Res. Lett.* 42, 1521–1543. doi: 10.1016/0967-0637(95)00068-H

Capet, X., McWilliams, J. C., Molemaker, M. J., and Shchepetkin, A. F. (2008). Mesoscale to submesoscale transition in the California current system. part III: energy balance and flux. *J. Phys. Oceanography* 38, 2256–2269. doi: 10.1175/2008JPO3810.1

Cisewski, B., Strass, V. H., Losch, M., and Prandke, H. (2008). Mixed layer analysis of a mesoscale eddy in the Antarctic polar front zone. *J. Geophysical Research: Oceans* 113. doi: 10.1029/2007JC004372

Corredor-Acosta, A., Morales, C. E., Rodríguez-Santana, A., Anabalón, V., Valencia, L., and Hormazabal, S. (2020). The influence of diapycnal nutrient fluxes on phytoplankton size distribution in an area of intense mesoscale and submesoscale activity off concepción, Chile. *J. Geophysical Research: Oceans* 125. doi: 10.1029/2019JC015539

Cronin, M. F., and McPhaden, M. J. (1997). The upper ocean heat balance in the western equatorial pacific warm pool during september–december 1992. *J. Geophysical Research: Oceans* 102, 8533–8553. doi: 10.1029/97JC00020

D'Asaro, E., Lee, C. M., Rainville, L., Harcourt, R., and Thomas, L. N. (2011). *Enhanced turbulence Energy dissipation at ocean fronts. Sci.* 332, 318–332. doi: 10.1126/science.1201515

Deardorff, J. W. (1970). Preliminary results from numerical integrations of the unstable boundary layer. *J. Atmospheric Sci.* 27, 1209–1231. doi: 10.1175/1520-0469(1970)027<1209:PRFNIO>2.0.CO;2

Deardorff, J. W. (1983). A multi-limit mixed-layer entrainment formulation. *J. Phys. Oceanography* 13, 988–1002. doi: 10.1175/1520-0485(1983)013<0988:AMLMLE>2.0.CO;2

de Boyer Montégut, C., Madec, G., Fischer, A. S., Lazar, A., and Iudicone, D. (2004). Mixed layer depth over the global ocean: an examination of profile data and a profile-based climatology. *J. Geophysical Res.* 109. doi: 10.1029/2004JC002378

Dewey, R. K., and Moum, J. N. (1990). Enhancement of fronts by vertical mixing. *J. Geophysical Res.* 95, 9433–9445. doi: 10.1029/JC095iC06p09433

Dewey, R. K., Moum, J. N., and Caldwell, D. R. (1993). Microstructure activity within a minifilament in the coastal transition zone. *J. Geophysical Res.* 98, 14457–14470. doi: 10.1029/93JC01127

Dickey, T. C., Manov, D. V., Weller, R. A., and Seigel, D. (1994). Determination of longwave heat flux at the air–sea interface using measurements from buoy platforms. *J. Atmospheric Oceanic Technol.* 11, 1057–1078. doi: 10.1175/1520-0426(1994)011<1057:DOLHFA>2.0.CO;2

Dietze, H., Oschlies, A., and Kähler, P. (2004). Internal-wave-induced and double-diffusive nutrient fluxes to the nutrient-consuming surface layer in the oligotrophic subtropical north atlantic. *Ocean Dynamics* 54, 1–7. doi: 10.1007/s10236-003-0060-9

Dong, S., Sprintall, J., Gille, S. T., and Talley, L. (2008). Southern ocean mixed-layer depth from argo float profiles. *J. Geophysical Res.* 113. doi: 10.1029/2006JC004051

Dorrestein, R. (1979). On the vertical buoyancy flux below the sea surface as induced by atmospheric factors. *J. Phys. Oceanography* 9, 229–231. doi: 10.1175/1520-0485(1979)009<0229:OTVBFB>2.0.CO;2

Estrada-Allis, S. N., Barceló-Llull, B., Pallàs-Sanz, E., Rodríguez-Santana, A., Souza, J. M. A. C., Mason, E., et al. (2019). Vertical velocity dynamics and mixing in an anticyclone near the canary islands. *J. Phys. Oceanography* 49, 431–451. doi: 10.1175/JPO-D-17-0156.1

Fairall, C. W., Bradley, E. F., Rogers, D. P., Edson, J. B., and Young, G. S. (1996). Bulk parameterization of air-sea fluxes for tropical ocean-global atmosphere coupled-ocean atmosphere response experiment. *J. Geophysical Res.* 101, 3747–3764. doi: 10.1029/2010JC006884

Fer, I., and Sundfjord, A. (2007). Observations of upper ocean boundary layer dynamics in the marginal ice zone. *J. Geophysical Res.* 112. doi: 10.1029/2005JC003428

Fernando, H. J. (1991). Turbulent mixing in stratified fluids. *Annu. Rev. Fluid Mechanics* 23, 455–493. doi: 10.1146/annurev.fl.23.010191.002323

Ferrari, R., Merrifield, S. T., and Taylor, J. R. (2015). Shutdown of convection triggers increase of surface chlorophyll. *J. Mar. Syst.* 147, 116–122. doi: 10.1016/j.jmarsys.2014.02.009

Firing, E., Ranada, J., and Caldwell, P. (1995). *Processing ADCP data with the CODAS software system version 3.1* (Joint Institute for Marine and Atmospheric Research/NODC).

Flór, J. B., Hopfinger, E. J., and Guyez, E. (2010). Contribution of coherent vortices such as langmuir cells to wind-driven surface layer mixing. *J. Geophysical Res.* 115. doi: 10.1029/2009JC005900

Franks, P. J. (2014). Has sverdrup's critical depth hypothesis been tested? mixed layers vs. turbulent layers. *ICES J. Mar. Sci.* 72, 1897–1907. doi: 10.1093/icesjms/fsu175

García-Muñoz, M., Arístegui, J., Pelegrí, J., Antoranz, A., Ojeda, A., and Torres, M. (2005). Exchange of carbon by an upwelling filament off cape ghir (NW Africa). *J. Mar. Syst.* 54, 83–95. doi: 10.1016/j.jmarsys.2004.07.005

Gaspar, P. (1988). Modeling the seasonal cycle of the upper ocean. *J. Phys. Oceanography* 18, 161–180. doi: 10.1175/1520-0485(1988)018<0161:MTSCOT>2.0.CO;2

Giordani, H., Caniaux, G., and Voldoire, A. (2013). Intraseasonal mixed-layer heat budget in the equatorial atlantic during the cold tongue development in 2006. *J. Geophys. Res. Oceans* 118, 650–671. doi: 10.1029/2012JC008280

González-Dávila, M., Santana-Casiano, M., Demetrio de Armas, J., Escánez,, and Suarez-Tangil, M. (2006). The influence of island generated eddies on the carbon dioxide system, south of the canary islands. *Mar. Chem.* 99, 177–190. doi: 10.1016/j.marchem.2005.11.004

Gregg, M. C. (1989). Scaling turbulent dissipation in the thermocline. *J. Geophys. Res.* 94, 9686–9698. doi: 10.1029/JC094iC07p09686

Grodsky, S. A., Carton, J. A., and McClain, C. R. (2008). Variability of upwelling and chlorophyll in the equatorial Atlantic. *Geophysical Res. Lett.* 35. doi: 10.1029/2007GL032466

Hagen, E. (2001). Northwest African Upwelling scenario. *Oceanology Acta* 24, 113–128. doi: 10.1016/S0399-1784(00)01110-5

Hagen, E., Zülicke, C., and Feistal, R. (1996). Near surface structures in the cape ghir filament off Morocco. *Oceanology Acta* 19, 577–598.

Hales, B., Hebert, D., and Marra, J. (2009). Turbulent supply of nutrients to phytoplankton at the new england shelf break front. *J. Geophysical Res.* 114. doi: 10.1029/2008JC005011

Hales, B., Moum, J. N., Covert, P., and Perlin, A. (2005). Turbulent supply of nutrients to phytoplankton at the new england shelf break front. *J. Geophysical Res.* 110. doi: 10.1029/2004JC002685

Hinze, J. O. (1979). *Turbulence. 2nd ed.* (New York), 790.

Holte, J., and Talley, L. (2009). A new algorithm for finding mixed layer depths with applications to argo data and subantarctic mode water formation. *J. Atmospheric Oceanic Technol.* 26, 1920–1939. doi: 10.1175/2009JTECHO543.1

Huffman, G. D., and Radshaw, B. P. (1972). A note on von kármán's constant in low reynolds number turbulent flows. *J. Fluid Mechanics* 53, 45–60. doi: 10.1017/S0022112072000035

Huisman, J., and Weissing, F. J. (1999). Biodiversity of plankton by species oscillations and chaos. *Nature* 402, 407–410. doi: 10.1038/46540

Inoue, R., Gregg, M. C., and Harcourt, R. R. (2010). Mixing rates across the gulf stream, part 1: on the formation of eighteen degree water. *J. Mar. Res.* 68, 643–671. doi: 10.1357/002224011795977662

Jackson, P. R., and Rehmann, C. R. (2014). Experiments on differential scalar mixing in turbulence in a sheared, stratified flow. *J. Phys. Oceanography* 44, 2661–2680. doi: 10.1175/JPO-D-14-0027.1

Jacob, S. D., and Shay, L. K. (2003). The role of oceanic mesoscale features on the tropical cyclone-induced mixed layer response: a case study. *J. Phys. Oceanography* 33, 649–676. doi: 10.1175/1520-0485(2003)332.0.CO;2

Kara, A. B., Rochford, P. A., and Hurlburt, H. E. (2000). An optimal definition for ocean mixed layer depth. *J. Geophysical Res.* 105, 803–1682. doi: 10.1029/2000JC900072

Khanta, L. H., Phillips, O. M., and Azadp, R. S. (1977). On turbulent entrainment at a stable density interface. *J. Fluid Mechanics* 79, 753–768. doi: 10.1017/S0022112077000433

Kraus, E. B., and Turner, J. S. (1967). A one-dimensional model of the seasonal thermocline II. the general theory and its consequences. *Tellus* 19, 98–106.

Large, W. G., and Pond, S. (1981). Open ocean momentum flux measurements in moderate to strong winds. *J. Phys. Oceanography* 11, 324–336. doi: 10.1175/1520-0485(1981)011<0324:OOMFMI>2.0.CO;2

Li, Q. P., Franks, P. J., Ohman, M. D., and Landry, M. R. (2012). Enhanced nitrate fluxes and biological processes at a frontal zone in the southern California current system. *J. Plankton Res.* 39, 790–801. doi: 10.1093/plankt/fbs006

Liu, Y., Lee, S. K., Muhling, B. A., Lamkin, J. T., and Enfield, D. B. (2012). Significant reduction of the loop current in the 21st century and its impact on the gulf of Mexico. *J. Geophysical Res.* 117. doi: 10.1029/2011JC007555

MacKinnon, J. A., and Gregg, M. C. (2005). Spring mixing: turbulence and internal waves during restratification on the new England shelf. *J. Phys. Oceanography* 35, 2425–2443. doi: 10.1175/JPO2821.1

Moum, J. N., Caldwell, D. R., and Paulson, C. A. (1989). Mixing in the equatorial surface layer and thermocline. *J. Geophysical Res.* 94, 2005–2022. doi: 10.1029/JC094iC02p02005

Mouriño-Carballido, B., Graña, R., Fernández, A., Bode, A., Varela, M., Domínguez, J. F., et al. (2011). Importance of N2 fixation vs. nitrate eddy diffusion along a latitudinal transect in the Atlantic ocean. *Limnol. Oceanogr.* 56, 999–1007. doi: 10.4319/lo.2011.56.3.0999

Nagai, T., Yamazaki, H., Nagashima, H., and Kantha, L. H. (2005). Field and numerical study of entrainment laws for surface mixed layer. *Deep-Sea Res. Part II* 52, 1109–1132. doi: 10.1016/j.dsr2.2005.01.011

Niiler, P. P., and Kraus, E. B. (1977). *One-dimensional model ofthe upper ocean. modelling and prediction of the upper layers of the ocean.* Ed. E. B. Kraus (Pergamon Press.), 143–172.

Oakey, N. S. (1982). Determination of the rate of dissipation of turbulent energy from simultaneous temperature and velocity shear microstructure measurements. *J. Phys. Oceanography* 12, 256–271. doi: 10.1175/1520-0485(1982)012<0256:DOTROD>2.0.CO;2

Osborn, T. R. (1980). Estimates of the local rate of vertical diffusion from dissipation measurements. *J. Phys. Oceanography* 10, 83–89. doi: 10.1175/1520-0485(1980)010<0083:EOTLRO>2.0.CO;2

Ozmidov, R. V. (1965). On the turbulent exchange in a stably stratified ocean. *Atmospheric Oceanic Phys.* 8, 853–860.

Pelegrí, J. L., Arístegui, J., Cana, L., González-Dávila, M., Hernández-Guerra, A., Hernández-León, S., et al. (2005a). Coupling between the open ocean and the coastal upwelling region off Northwest Africa: water recirculation and offshore pumping of organic matter. *J. Mar. Syst.* 54, 3–37. doi: 10.1016/j.jmarsys.2004.07.003

Pelegrí, J. L., Marrero-Díaz, A., Ratsimandresy, A., Antoranz, A., Cisneros-Aguirre, J., Gordo, C., et al. (2005b). Hydrographic cruises off Northwest Africa: the canary current and the cape ghir region. *J. Mar. Syst.* 54, 39–63. doi: 10.1016/j.jmarsys.2004.07.001

Pelegrí, J. L., and Richman, J. G. (1993). On the role of shear mixing during transient coastal upwelling. *Continental Shelf Res.* 13, 1363–1400. doi: 10.1016/0278-4343(93)90088-F

Peng, J., Holtermann, P., and Umlauf, L. (2020). Frontal instability and energy dissipation in a submesoscale upwelling filament. *J. Phys. Oceanography* 7. doi: 10.1175/JPO-D-19-0270.1

Ravindran, P., Wright, D. G., Platt, T., and Sathyendranath, S. (1999). A generalized depth-integrated model of the oceanic mixed layer. *J. Phys. Oceanography* 29, 791–806. doi: 10.1175/1520-0485(1999)029<0791:AGDIMO>2.0.CO;2

Samson, G., Giordani, H., Caniaux, G., and Roux, F. (2009). Numerical investigation of an oceanic resonant regime induced by hurricane winds. *Ocean Dynamics* 59, 565–586. doi: 10.1007/s10236-009-0203-8

Sangrà, P., Pascual, A., Rodríguez-Santana, A., Machín, F., Mason, E., McWilliams, J. C., et al. (2009). The canary eddy corridor: a major pathway for long-lived eddies in the subtropical north Atlantic. *Deep Sea Res. Part I* 56, 2100–2114. doi: 10.1016/j.dsr.2009.08.008

Sangrà, P., Troupin, C., Barreiro-González, B., Barton, D. E., Abdellatif, O., and Arístegui, J. (2015). The cape ghir filament system in august 2009 (NW Africa). *J. Geophysical Research: Oceans* 120, 4516–4533. doi: 10.1002/2014JC010514

Santana-Falcón, Y., Mason, E., and Arístegui, J. (2020). Offshore transport of organic carbon by upwelling filaments in the canary current system. *Prog. Oceanography* 186, 2100–2114. doi: 10.1016/j.pocean.2020.102322

Schafstall, J., Dengler, M., Brandt, P., and Bange, H. (2010). Tidal induced mixing and diapycnal nutrient fluxes in the Mauritanian upwelling region. *J. Geophysical Res.* 115, 1978–2012. doi: 10.1029/2009JC005940

Small, R. J., Carniel, S., Campbell, T., Teixeira, J., and Allard, R. (2012). The response of the ligurian and tyrrhenian seas to a summer mistral event: a coupled atmosphere–ocean approach. *Ocean Model.* 48, 30–44. doi: 10.1016/j.ocemod.2012.02.003

Strang, E. J., and Fernando, H. J. S. (2001). Entrainment and mixing in stratified shear flows. *J. Fluid Mechanics* 428, 349–386. doi: 10.1017/S0022112000002706

Sun, J., and Wang, Y. (2008). Effect of the entrainment flux ratio on the relationship between entrainment rate and convective Richardson number. *Boundary-Layer Meteorology* 126, 237–247. doi: 10.1007/s10546-007-9231-4

Sutherland, G., Reverdin, G., Marié, L., and Ward, B. (2014). Mixed and mixing layer depths in the ocean surface boundary layer under conditions of diurnal stratification. *Geophysical Res. Lett.* 41, 8469–8476. doi: 10.1002/2014GL061939

Sverdrup, H. U. (1953). On conditions for the vernal blooming of phytoplankton. *J. du Conseil Int. pour l'Exploration la Mer* 18, 287–295.

Thomas, L. N., Taylor, J. R., Ferrari, R., and Joyce, T. M. (2013). Symmetric instability in the gulf stream. *Deep-Sea Res. Part II* 91, 96–110. doi: 10.1016/j.dsr2.2013.02.025

Troupin, C., Mason, E., Beckers, J. M., and Sangrà, P. (2012). Generation of the cape ghir upwelling filament: a numerical study. *Ocean Model.* 41, 1–15. doi: 10.1016/j.ocemod.2011.09.001

Wada, A., Niino, H., and Nakano, H. (2009). Roles of vertical turbulent mixing in the ocean response to typhoon Rex, (1998). *J. Oceanography* 65, 373–396. doi: 10.1007/s10872-009-0034-8

Wade, M., Caniaux, G., duPenhoat, Y., Dengler, M., Giordani, H., and Hummels, R. (2011). A one-dimensional modeling study of the diurnal cycle in the equatorial atlantic at the pirata buoys during the egee–3 campaign. *Ocean Dynamics* 61, 1–20. doi: 10.1007/s10236-010-0337-8

Wolk, F., Yamazaki, H., Seuront, L., and Lueck, R. G. (2002). A new free-fall profiler for measuring biophysical microstructure. *J. Atmospheric Oceanic Technol.* 19, 780–793. doi: 10.1175/1520-0426(2002)019<0780:ANFFPF>2.0.CO;2

Zaron, E. D., and Moum, J. N. (2009). A new look at Richardson number mixing schemes for equatorial ocean modeling. *J. Phys. Oceanography* 39, 2652–2664. doi: 10.1175/2009JPO4133.1

Appendix A. $(J_b^{\Delta h})_I$

According to Osborn (1980), the diapycnal turbulent buoyancy flux ($\overline{w'b'}$) can be scaled as:

$$\overline{w'b'} = \Gamma\varepsilon_o, \tag{A.1}$$

where the mixing efficiency (Γ) is the ratio of the vertical buoyancy flux to ε_o. We employed a constant value of 0.2 (e.g., Zaron and Moum, 2009). To consider the diapycnal turbulent buoyancy flux that contributes to the TKE budget in the entrainment zone, a parameterization derived from Osborn (1980) was integrated over the entrainment zone, Δh (i.e., from $-h_\varepsilon$ to $-h_\rho$) to obtain $(J_b^{\Delta h})_I$:

$$\int_{-h_\varepsilon}^{-h_\rho} \overline{w'b'}(dz) = -\int_{-h_\varepsilon}^{-h_\rho} 0.2\varepsilon_o(dz) = (J_b^{\Delta h})_I (m^3 s^{-3}). \tag{A.2}$$

Due to the dependence on Δh, $(J_b^{\Delta h})_I$ is only a TKE sink when $\Delta h > 0$, thus it will be a sink in filament waters given that energy is consumed to break stratification below the mixed layer.

Appendix B. Submesoscale Processes

Turbulence is a three-dimensional (3D) process. To restrict the entrainment analysis to a 1D approach, we required a prior examination of 2D instabilities that could occur in frontal structures.

Following the analysis of Thomas et al. (2013), potential vorticity (q) can be determined as $q_A = (f - \partial v/\partial x)N^2 - (\partial b/\partial x)^2 f^{-1}$ for transect A and similarly as $q_B = (f - \partial u/\partial y)N^2 - (\partial b/\partial y)^2 f^{-1}$ for transect B. Despite the lack of synoptic measurements, an analysis of q revealed positive values for along-front q_A (Figure B.1A, indicating stable conditions (e.g., D'Asaro et al., 2011). Transect B (Figure B.1B) exhibited a similar pattern to that of transect A in the along-front q_B, with slightly near zero values at locations where isopycnals outcropped to the surface and $\Delta h > 0$ (i.e., at the upwelling filament). These results provide no immediate evidence for symmetric instabilities, which was supported by the presence of cross-front winds in transect A (Figure B.1). This indicates that a 1D turbulent approach is appropriate for this case study.

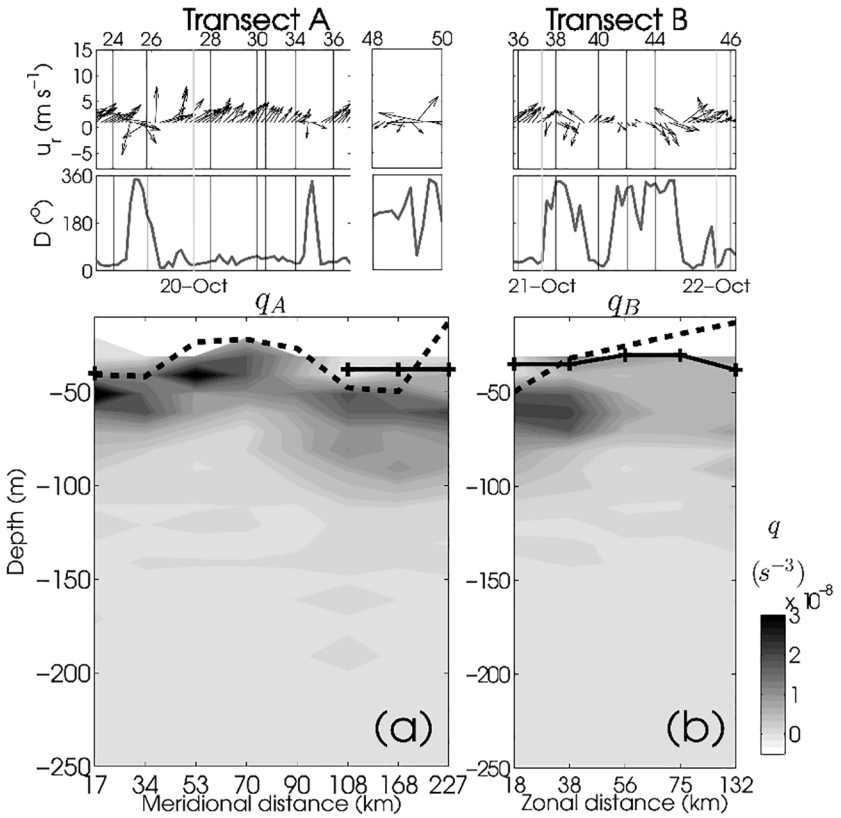

FIGURE B.1
Upper panels: wind speed (u_r, m s^{-1}) with the respective wind direction (clockwise from North). Lower panels: cross-stream sections of potential vorticity (q, s^{-3}) for (A) transect A and (B) transect B. The dashed lines correspond to mixed layer depths (h_ρ). The solid lines denote mixing layer depths (h_ε, m).

frontiers | Frontiers in Marine Science

TYPE Original Research
PUBLISHED 19 July 2023
DOI 10.3389/fmars.2023.1087980

OPEN ACCESS

EDITED BY
Francisco Machín,
University of Las Palmas de Gran Canaria, Spain

REVIEWED BY
Giulia Bonino,
Foundation Euro-Mediterranean Center on Climate Change (CMCC), Italy
Eduardo Zorita,
Helmholtz Centre for Materials and Coastal Research (HZG), Germany

*CORRESPONDENCE
Sadegh Yari
sadegh.yari@io-warnemuende.de

RECEIVED 02 November 2022
ACCEPTED 30 June 2023
PUBLISHED 19 July 2023

CITATION
Yari S, Mohrholz V and Bordbar MH (2023) Wind variability across the North Humboldt Upwelling System.
Front. Mar. Sci. 10:1087980.
doi: 10.3389/fmars.2023.1087980

Wind variability across the North Humboldt Upwelling System

Sadegh Yari*, Volker Mohrholz and Mohammad Hadi Bordbar

Department of Physical Oceanography and Instrumentation, Leibniz Institute for Baltic Sea Research Warnemünde (IOW), Rostock, Germany

Surface wind is taken as the primary driver of upwelling in the eastern boundary upwelling systems. The fluctuation of momentum flux associated with the variation in wind regulates the nutrient supply to the euphotic surface layer via changing the properties of oceanic mixed layer depth, the coastal and offshore upwelling, and horizontal advection. Here, the spatial and temporal variability of the surface wind field over the last seven decades across the Peruvian upwelling system is investigated. Strong fluctuations in seasonal to decadal timescales are found over the entire upwelling system. A semi-periodic wind fluctuation on an interannual timescale is found, which is closely related to the regional sea surface temperature and can be attributed to the El Niño Southern Oscillation (ENSO). However, the wind anomaly patterns during positive and negative phases of ENSO are not opposite, which suggests an asymmetric response of local wind to ENSO cycles. In addition, a semi-regular fluctuation on the decadal timescale is evident in the wind field, which can be attributed to the Interdecadal Pacific Oscillation (IPO). Our results show that the sea surface temperature over the Humboldt Upwelling System is closely connected to local wind stress and the wind stress curl. The SST wind stress co-variability seems more pronounced in the coastal upwelling cells, in which equatorward winds are very likely accompanied by robust cooling over the coastal zones. Over the past seven decades, wind speed underwent a slightly positive trend. However, the spatial pattern of the trend features considerable heterogeneity with larger values near the coastal upwelling cells.

KEYWORDS

Humboldt Upwelling System, Eastern Boundary Upwelling Systems (EBUS), climate change, coastal alongshore winds, Interdecadal Pacific Oscillation (IPO), El Niño Southern Oscillation (ENSO)

1 Introduction

The Humboldt Upwelling System (HUS), located in the Southeastern Pacific, is one of the most productive marine ecosystems worldwide. The Peruvian Upwelling System (PUS; 4°S–19°S), as the equatorial portion of the HUS, is recognized with perennial tongue-shaped cold water near the coast resulting from a pronounced coastal upwelling (Guillen, 1983). Despite comparable upwelling intensities, the fisheries in the HUS considerably exceed that in other major Eastern Boundary Upwelling Systems (Chavez and Messié, 2009). The high level of biological productivity has been largely attributed to the presence of regional equatorward alongshore wind stress, which persists throughout the year and facilitates the nutrient supply to the euphotic surface layers.

The upwelling in the PUS covers a wide range of variability from short-term (few days) to long-term (decadal) variations, which sometimes undergo systematic shifts associated with different modes of regional climate variabilities.

The timing, duration, and intensity of upwelling-favorable winds across the PUS are modulated by the intensity and displacement of the South Pacific atmospheric anti-cyclonic system, which is largely affected by modes of climate variability such as the El Niño Southern Oscillation (ENSO), and the Interdecadal Pacific Oscillation (IPO) (Bakun, 1990; Montecinos et al., 2003; García-Reyes et al., 2015; Barros et al., 2014; Bakun et al., 2015). Several studies investigated the effects of climate change on EBUS functionality (Bakun, 1990; Narayan et al., 2010; Echevin et al., 2011; Belmadani et al., 2013; Jacox et al., 2014; Bakun et al., 2015; Rykaczewski et al., 2015; Varela et al., 2015; Oyarzún and Brierley, 2019; Taboada et al., 2019). In a conceptual notion, Bakun (1990) hypothesized that global warming would very likely continue causing enhanced continent–ocean surface atmospheric pressure gradient. With more signature in warm seasons of the year, the alongshore (equatorward) winds across the major EBUS are intensified, and consequently, the upwelling intensity is enhanced. He showed that the observed wind stress (τ) in the Peruvian coastal area (4.5°S–14.5°S) underwent an upward trend during 1945–1985 (Figures 1D, E in Bakun, 1990).

The results of Sydeman et al. (2014) support Bakun's hypothesis by performing a meta-analysis of the results of various studies on the upwelling-favorable winds over EBUSs. They synthesized the results of 22 published studies in the period of 1990–2012, and their result confirms Bakun's hypothesis in the Humboldt current system. This was supported by both observational and simulated data.

Most recently, Rykaczewski et al. (2015), using the result of 21 models, demonstrated that projected changes in upwelling-favorable winds are not exclusively due to the enhanced surface temperature contrast between the land and adjacent ocean. They suggested an alternate hypothesis; anthropogenic changes in the intensity of upwelling-favorable winds will be associated with shifts in the seasonal development and geographic positioning of the four major atmospheric high-pressure systems.

At the same time, the proximity of the PUS to the Eastern Pacific and its dominant modes of climate variability (i.e., ENSO and IPO) may hinder the detection of anthropogenic climate change signals. ENSO cycles are semi-regular with a periodicity of 3–7 years and have rapidly varying and long-lasting effects on the PUS ecosystems (Chavez et al., 2003; Taylor et al., 2008; Dewitte et al., 2012; Espinoza-Morriberon et al., 2017; Chamorro et al., 2018). The IPO is not necessarily independent of the ENSO. It shows a basin-wide horseshoe-like pattern that is virtually

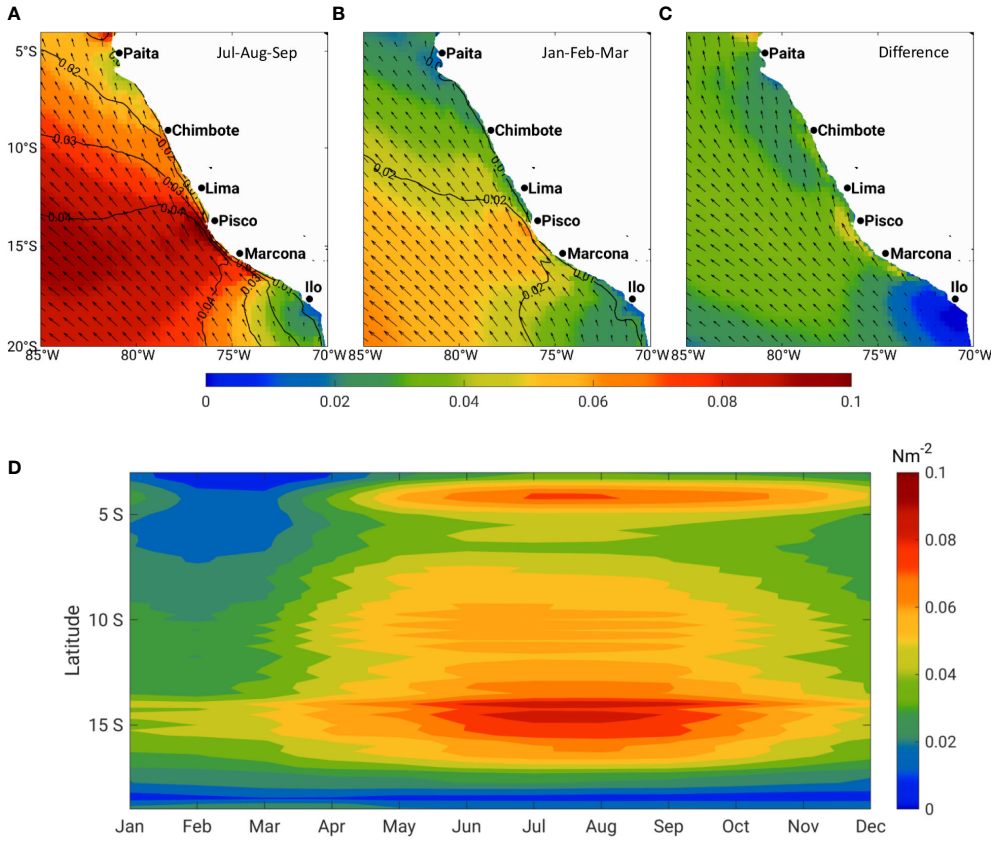

FIGURE 1
Mean τ (color shaded, N/m^2) and direction (arrows, every third vector shown) and corresponding variability in terms of standard deviation (isolines) for **(A)** winter (July–September), **(B)** summer (January–March), and **(C)** difference between winter and summer, calculated using ERA5 wind over 1950–2019. Hovmöller diagram of the annual cycle of alongshore wind stress across the PUS **(D)**. The alongshore wind stress is obtained over the first baroclinic Rossby radius distance from the coastline.

symmetric about the equator with 15–20 years of oscillation (Meehl and Hu, 2006; Parker et al., 2007; Ding et al., 2013; Henley et al., 2015 and Meehl et al., 2016). The IPO phase transitions have large influences on the wind field over the PUS.

The temporal and spatial variations of the wind field are largely affected by several local factors such as coastline geometry and orography, coastal breeze, atmosphere stability, and small-scale air–sea interactions (Renault et al., 2016). Overall, these factors tend to weaken the wind speed toward the coast, which is known as the wind drop-off phenomenon (Capet et al., 2004; Renault et al., 2012; Desbiolles et al., 2014, and Renault et al., 2015). The combination of mountain orography with a cape shape coastline has a large influence on the wind drop-off (Renault et al., 2015). This transitional area is approximately several 10 km wide and features a significant divergence in the offshore transport driven by the alongshore winds (Boe et al., 2011). The upwelling associated with the divergence of the offshore transport is known as Ekman pumping/suction and covers a larger area compared with the coastal upwelling. Thus, it is considered almost equally important as coastal upwelling for the regional marine ecosystem.

Understanding long-term variations and trends of the wind field, as a primary driver of the coastal upwelling, and their connections to the dominant modes of climate variability (e.g., ENSO and IPO) are of great importance for understanding historical changes in the PUS. So far, there have been attempts to study the PUS utilizing modeling and observational data analysis on seasonal to decadal timescales. However, given the systematic biases in the models and lack of long-term observation-based data sets with sufficiently high resolution, the model's results on a multi-decadal timescale are subject to large uncertainty.

This study aims to analyze the wind stress field as the primary atmospheric forcing for upwelling across the PUS using 70 years of wind data provided by the European Centre for Medium-Range Weather Forecasts (ECMWF). We put special emphasis on the impacts of the IPO and the ENSO as primary modes of regional climate variability. We additionally investigate SST and the surface wind field co-variabilities across the region. In addition, we provide a detailed overview of the mean state, the seasonal cycle, and the long-term trends of the surface winds, which are of great importance for marine ecosystem communities.

The paper is organized as follows: materials and methods are described in *Section 3*. *Section 4* presents the results, and *Section 5* is dedicated to discussions and conclusions.

2 Materials and methods

2.1 Data

Among other available reanalysis products, the ERA5 product is used mainly due to its spatial resolution (0.25°×0.25°) and extended temporal coverage (1950–2020; Hersbach et al., 2020). The ERA5 surface level wind field and sea surface temperature (SST) products for the period of 1950–2019 are used. The data sets consist of two major reanalysis periods. Over 1950–1978, it was reconstructed from the assimilation of early satellite-derived data and reprocessed conventional observations (Bell et al., 2020). In contrast, vast amounts of historical observations are used after 1979, which are available a few days behind real time (Hersbach et al., 2018). ERA5 hourly products with global coverage are publicly accessible on a 0.25° × 0.25° grid. In this study, the daily mean values of wind components were computed from the hourly data.

The time series of the ENSO index (NINO 3.4) was taken from the climate prediction center of the National Oceanic and Atmospheric Administration[1] (NOAA), which was obtained from the 3-month running mean of monthly SST. The IPO index was also taken from the NOAA Physical Sciences Laboratory (PSL)[2].

2.2 Data analysis

The daily τ is calculated using the bulk formula:

$$\vec{\tau} = \rho \times C_D^N \times |U_{10}| \overrightarrow{U_{10}} \quad (1)$$

where ρ is the air density (1.2 kg.m^{-3}), C_D^N is the neutral drag coefficient (Trenberth et al., 1990), and U_{10} is the wind velocity at 10 m height above the sea surface.

Considering the impacts of wind speed on the drag coefficient is sometimes essential to accurately estimate momentum flux into the ocean over the coastal area (Brodeau et al., 2017; Bonino et al., 2022). Since the momentum flux associated with the wind is of central importance for the upwelling process in EBUSs, we used the approach of Trenberth et al. (1990), which is based on the drag coefficient varying by wind speed. This method is widely used by marine researchers.

Theory suggests that the coastal upwelling is bounded to a coastal zone in the order of the first baroclinic Rossby radius of deformation (R_i). We consider the wind over 100 km from the coastline, which is within the range of R_i across the PUS. The temporal evolution of the τ at the 100 km coastal band is calculated by zonal averaging at each latitude.

The monthly, seasonal, and annual mean of the τ and the corresponding anomaly of monthly and annual τ with the reference period of 1981–2010 are calculated. The climatological cycle of τ is calculated as well.

The anomaly of mean monthly SST is calculated using ERA5 products for 1950–2019. To estimate the wind-stress-curl-driven upwelling, we computed the curl of τ divided by the Coriolis parameter (f) as follows:

$$curl(\tau) = \left(\frac{\partial \tau_y}{\partial x} - \frac{\partial \tau_x}{\partial y}\right)$$

$$f = 2\Omega \,.\, sin(\varphi)$$

where τ_x, τ_y, f, Ω, and φ are zonal and meridional wind stresses, the Coriolis parameter, the angular speed of the earth, and the

1 https://origin.cpc.ncep.noaa.gov/products/analysis_monitoring/ensostuff/ONI_v5.php

2 https://psl.noaa.gov/data/timeseries/IPOTPI/

latitude, respectively. The climatological cycle for 1950–1979 and 1990–2019 is calculated. These two periods are compared to investigate the long-term trend of wind stress.

To understand the SST and surface wind field co-variability, we implement joint Empirical Orthogonal Function (EOF) analysis using ERA5 wind and SST from NOAA satellite OIv2 measurements (Kutzbach, 1967; Reynolds et al., 2007). Before conducting the EOF analysis, the climatological annual cycle was subtracted from each variable. Then, given the fact that wind and SST have different physical units and scales, we normalized them with the areal average of the standard deviation of monthly anomalies over the entire domain (85°W–70°W, 20°S–2°S). In this way, the EOF modes and their principal components (PCs) can be interpreted as the co-variability of the normalized surface wind field and SST in space and time, respectively.

3 Results

Here, we discuss the long-term mean, seasonal cycle, and interannual variability of wind stress (speed) off Peru. We also address the impacts of dominant modes of regional climate variability on the wind field. We discuss also the SST-wind stress co-variability and the long-term trend of the wind.

3.1 Long-term mean

The long-term mean and variability of wind stress (τ) are shown in Figure 2. The variability is expressed as the standard deviation of daily mean wind stress. A distinct maximum τ of approximately 0.08 N/m^2 is observed off Pisco, which is reduced seaward. The strong τ off Pisco–Marcona is attributed to the local effect of coastal geometry and headland. The τ shows a high variation in the Pisco–Marcona area with a standard deviation of approximately 0.03 N/m^2. The variability is reduced across the northern and southern coasts.

The alongshore component of τ shows a large variation in seaward (i.e., zonal) direction across different cells (Figure 2B). Due to the headland effect of the coastline, there is a strong wind close to the coastline of the Pisco and Marcona cells, with a steep reduction toward the land. The wind off Paita shares several similarities with that off Pisco but with a smaller magnitude. This may come down to the similar orographic and headland pattern in these two upwelling

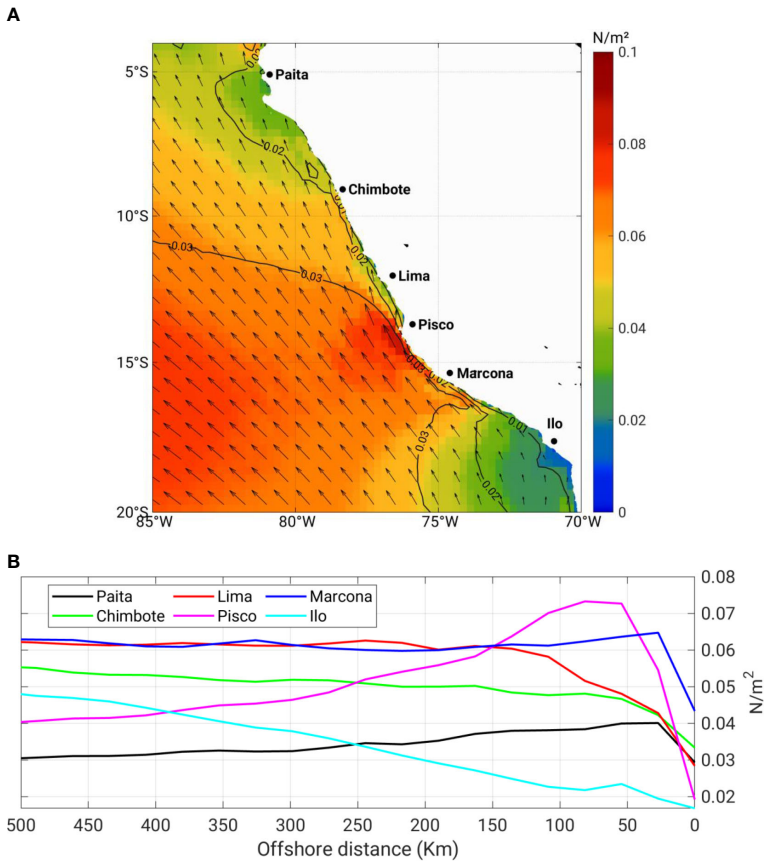

FIGURE 2
(A) Mean surface τ (color shading; N/m^2), direction (arrows, every third vector shown), and its variability (contours; N/m^2) across the Peruvian upwelling system. The variability was computed as the standard deviation of daily mean values. **(B)** Zonal profiles of the long-term mean τ_y for different upwelling cells across the PUS. The curves were obtained from the meridional average over a 1.0° band from the coastline to 500 km offshore distance in a zonal direction.

cells. Unlike the central and northern portions of the HUS, τ profile shows a stepwise enhancement with the coastal distance in the sector south of Marcona.

3.2 Seasonality

In austral summer (January–March) concurrent with the southernmost position of the intertropical convergence zone, τ experiences its seasonal minimum in the entire PUS with values of approximately 0.02–0.05 Nm^{-2} in the coastal band. The standard deviation is almost uniform, approximately 0.01–0.02 Nm^{-2} in the coastal area and enhanced seaward (Figure 1). The τ is more intensified in the austral autumn (April–June) and reaches the seasonal maximum in winter (July–September). Except in the southernmost portion of the HUS, the intensity of τ exceeds 0.04 Nm^{-2} over the entire region in winter. It reaches approximately 0.1 Nm^{-2} in the Pisco and Marcona cells. A positive seaward gradient in the τ is evident near the coast, which is more pronounced at the Pisco and Marcona. The offshore gradient becomes steeper in the Austral winter. It is important to highlight the fact that the presence of distinct maximum τ off the Pisco and Marcona cells persists throughout the year.

The annual cycle of the alongshore τ over the coastal zones with a width of R_i shows a high seasonal variation with a seasonal maximum in Austral winter (July–September) and a seasonal minimum in Austral summer (January–March). The seasonal pattern shows a non-uniform geographical distribution with a strong seasonal peak off Pisco–Marcona (13°–16°S) diminishing north- and southward (Figure 1).

3.3 ENSO events

As mentioned in previous studies (Chavez et al., 2003; Taylor et al., 2008; Dewitte et al., 2012; Espinoza-Morriberon et al., 2017; Chamorro et al., 2018), the Pacific El Niño and La Niña events exert profound impacts on the wind field in the HUS. The mean τ during El Niño and La Niña events in 1950–2019 is calculated using monthly mean and plotted in Figure 3. The criterion for selecting El Niño and La Niña events is the Nino3.4 SST anomalies. When the SST anomaly is higher (cooler) than >0.5°C and persistent for longer than 5 consecutive months, it is considered El Niño (La Niña). During the El Niño, the magnitude of τ shows higher values concerning the long-term mean, particularly along the coastal area, with a maximum of ~0.09 Nm^{-2} in the Pisco upwelling cell (Figures 3A, C). On the contrary, the La Niña events are associated with reduced τ mainly in the central and northern parts (Figures 3B, D). The higher τ during the El Niño does not mean stronger upwelling and productivity. The deeper thermocline and thicker warmer water cause weaker upwelling and less nutrients and consequently lower primary production. On the contrary, during La Niña, the thermocline is shallower concerning normal conditions, which causes more nutrient supply to surface waters and higher primary production.

3.4 Coastal domain

The time evolution of yearly mean alongshore τ anomalies over the 100-km coastal band is displayed in Figure 4. It shows fluctuations on interannual to decadal time scales. A year-to-year oscillation with more signatures in the central and southern sectors of the PUS is obvious, which is likely associated with the ENSO events. Robust positive (equatorward) anomalies in 1983, 1995, 1998, 2002, 2010, and 2015 coincide with pronounced El Niño events. Moreover, a transition from negative to positive anomalies was evident around 1997. A mirror-like pattern is observed around 2015. However, the center of large positive and negative anomalies during these two events does not appear at the same location. It might be connected to the asymmetric behavior of the ENSO and the IPO. During 1997–2015, the anomaly of τ is positive over the entire coastal domain. This situation is not only dominated in the coastal domain but also appears in the offshore area (not shown here). In addition, there is a relatively weak decadal negative anomaly period for 1972–1983, which is followed by another negative in 1984–1995 after a positive signal in 1983–1984. These systematic decadal changes resemble the transition phase of the IPO.

We applied low pass filters (1- and 5-year running average) to the time series of monthly mean alongshore τ anomalies over the coastal stripe of the Peruvian coast (5S–18S) (Figure 5). The presence of fluctuations in interannual and interdecadal timescales in the time series is evident. The interannual fluctuation of the wind stress is in phase with ENSO cycles. The same is true for the long-term fluctuations of τ and the IPO cycle, but they are out of phase. The pronounced shift from negative to positive τ anomalies in 1996 and from positive to negative in 2015 is apparent in the time series, which is in good agreement with IPO phase transitions. The negative phase of the IPO, which is a basin-wide La Niña-like pattern, is observed concurrent with the positive wind stress anomalies. This is also true for the period from 1975 to 2019.

The linear correlation between the time series is also examined. The correlation coefficient of monthly τ and ENSO is approximately 0.28. Considering the entire period, the correlation coefficient of monthly τ and the IPO is not statistically significant. Therefore, the time series of IPO is divided into two periods; the first period is 1950–1978, and the second period is 1979–2015. The monthly τ anomalies show a small correlation of approximately 0.09 with the first period (1950–1978). In contrast, it is anti-correlated with the second period of IPO with a correlation coefficient of approximately −0.36. The 1-year filtered data have correlation coefficients of 0.27, 0.22, and −0.57 with ENSO and with the first and second periods of IPO, respectively. The 5-year filtered data show a high negative correlation coefficient with the second period of IPO as −0.73 and 0.32 with the first period of IPO (Table 1).

To investigate the co-variation of the rotation wind stress and SST, the cross-correlation between monthly mean anomalies of SST and $curl(\tau)/f$ is examined (Figure 6). Since the dominant driver of upwelling near the coastal band of about the first baroclinic Rossby radius of deformation is the alongshore wind-driven upwelling

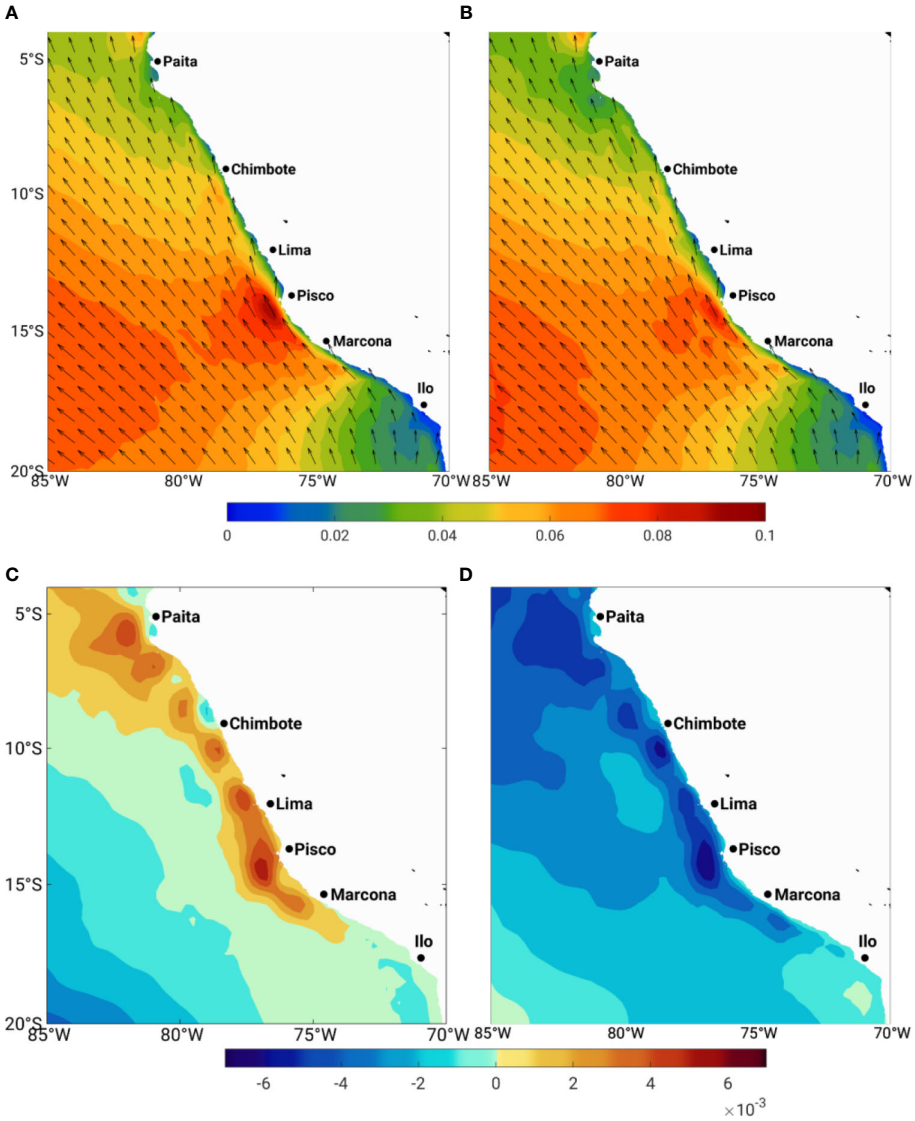

FIGURE 3
Mean τ (N/m^2) for El Niño and direction (arrows, every third vector shown) **(A)** and its difference from the mean state **(C)**, and La Niña and direction (arrows, every third vector shown) **(B)** and its difference from mean state **(D)** off Peru. It is obtained from ERA5 wind data from 1950 to 2019.

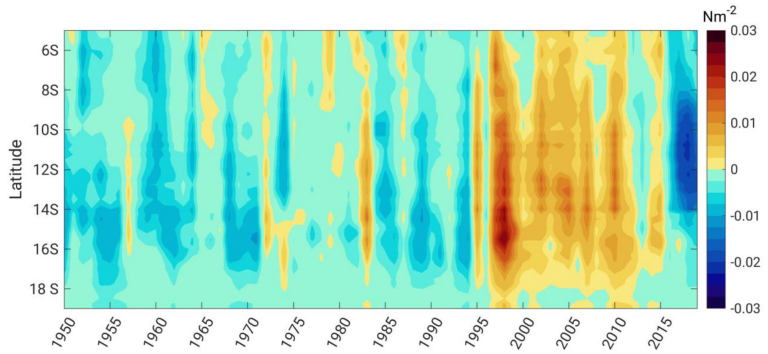

FIGURE 4
Hovmöller diagram of the yearly mean of alongshore wind stress anomaly over the 100 km coastal band across the PUS. Note that the long-term mean was subtracted before computing the yearly mean.

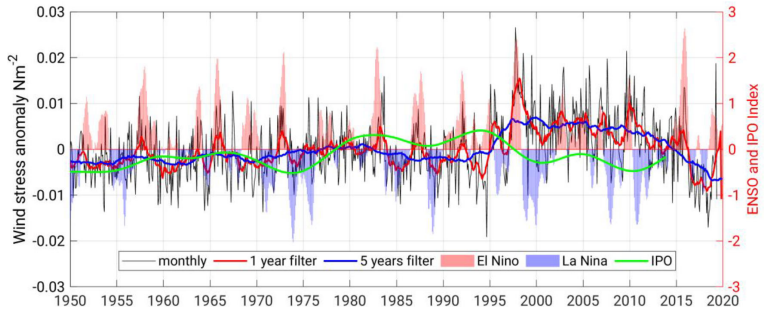

FIGURE 5
Anomaly of mean monthly (black curves), 1-year (red curve), and 5-year (blue curve) running means of alongshore wind stress across the PUS (coastal stripe over 5S–18S). The time series of the IPO index is shown by green lines. Red and blue shadings indicate El Niño and La Niña events, respectively. Note that alongshore wind stress is averaged over a coastal distance of 100 km.

(Bordbar et al., 2021), we do not show the correlation over the coastal zone. The higher value is obtained with *curl(τ)/f* leading by 1 month. The *curl(τ)/f* is proportional to the offshore vertical transport. Since the main driver of upwelling near the coast is along-shore wind-driven upwelling, we only discuss the aforementioned correlation offshore (>100km off coast). It is shown that the *curl(τ)/f*, and SST is widely anti-correlated: implying that the enhanced *curl(τ)/f* is very likely followed by SST cooling. A higher correlation is observed off the upwelling cells.

To understand the coherent variation in surface wind and SST variability, we conducted joint wind-SST EOF analysis using the monthly SST and wind anomalies (Figure 7). In this way, the co-variability of the surface wind and SST is reflected in the spatial pattern of the EOFs. Here, we show the results of our analysis for the first four EOF modes. The remaining modes appear less significant, with the percentage of explained variability typically<3.5%. The first mode (Figure 7A) explains more than 47% of the total variability. It features northwesterly/southeasterly anomalies in the surface wind, almost the same magnitude over the entire domain. The pronounced phase transition occurred around 1995 (Figure 7E), which was nearly coincident with the phase transition of the IPO. The correlation of PC1 with the IPO is approximately 0.42. However, the SST variation in this mode is small relative to that for the wind. The second and third modes seem to be related to the ENSO fluctuations and explain more than 28% of the total variability (Figures 7B, C). The corresponding PCs display fluctuations on interannual timescales (Figures 7F, G). The pronounced peaks in 1982–1983, 1987–1988, 1997–1998, and 2015–2016 in the second PC reminds the strong El Niño events. The correlation between the second PC and Nino3.4 index is approximately 0.60. The wind anomaly associated with the second mode is small compared with other modes. The warming during the El Niño-like phase is associated with the local deepening of the thermocline and elevated sea level driven by upper ocean heat content transported from the western tropical Pacific. Thus, the local wind plays rather a minor role in this mode. However, the third mode, which seems to be ENSO related, suggests a cooling associated with equatorial winds with more signature near the coast. A close connection between the spatial pattern of SST and wind is viewed in the fourth mode. However, this mode explains only 4.3% of the total variability.

To investigate the influence of El Niño and La Niña on the meridional wind stress, we regressed the monthly mean wind stress onto the monthly ENSO index. It shows higher coefficients off the upwelling cells with a maximum of 0.42 in the Pisco area (Figure 8). This coefficient is particularly larger off the Pisco cell. We additionally applied the regression for the El Niño and La Niña episodes separately. The coefficients are 0.61 and 0.28 for El Niño and La Niña, respectively. The El Niño and La Niña events are decomposed based on the SST anomalies over the Nino3.4 index. The anomalies larger (smaller) than 1.0 (−1.0) are considered El Niño (La Niña) events. During El Niño, wind over the coastal zones is intensified, which is more pronounced off Pisco, Lima, Chimbote, and Paita. The weakening of the wind over the coastal zone is evident during La Niña. However, the impact of La Niña appears to be not mirror-like of El Niño. For example, wind over the central and southern portion of the PUS appears to be anti-correlated with the Nino3.4 SST during La Niña. In contrast, the wind over these sectors is marginally affected by the Nino3.4 SST during El Niño. It reminds the asymmetric features of ENSO cycles. Overall, coastal upwelling is more affected during warm (i.e., El Niño) than cold (i.e., La Niña) episodes.

TABLE 1 Correlation coefficients between time series presented in Figure 5.

	ENSO	IPO (1950–1978)	IPO (1979–2015)
Monthly	0.28	0.09	−0.36
1 year	0.27	0.22	−0.57
5 years	−0.05	0.32	−0.73

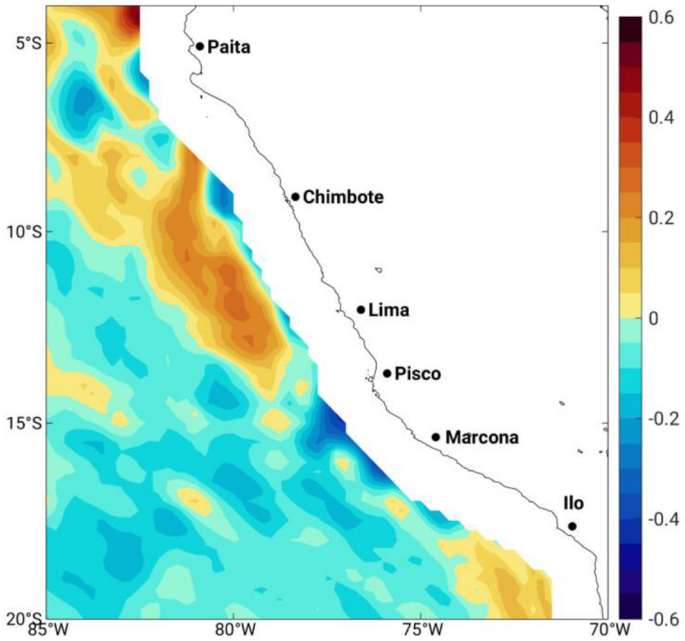

FIGURE 6
Spatial pattern of the correlation coefficient between anomalies of monthly SST and *curl(τ)/f*. Please note that *curl(τ)/f* is leading SST by 1 month.

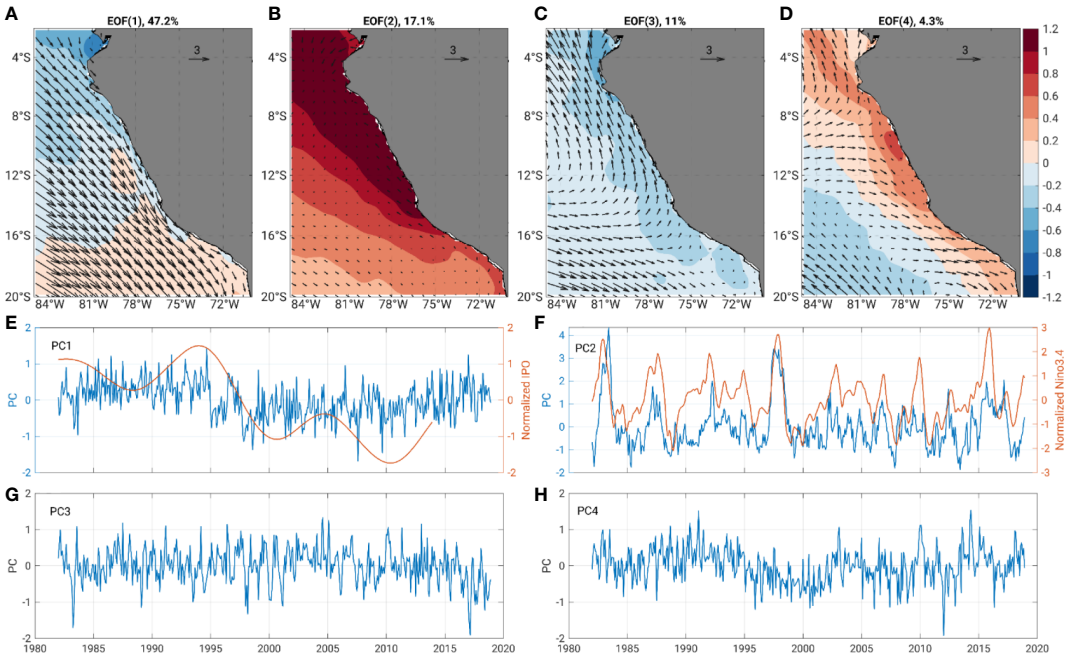

FIGURE 7
The results of joint wind-SST EOF analysis over the PUS. The spatial patterns of EOF1-4 are shown in panel **(A–D)**. The explained variability by each EOF is shown on the top of panels **(A–D)**. The time series of the corresponding PCs are displayed in panel **(E–H)**. The red curves in panels (**E, F**) represent the normalized time series of the IPO and Niño3.4 index. We used the monthly mean SST and surface wind from OISST and ERA5 data sets from 1982 to 2019, respectively. The climatological monthly mean values were subtracted before computing the EOFs.

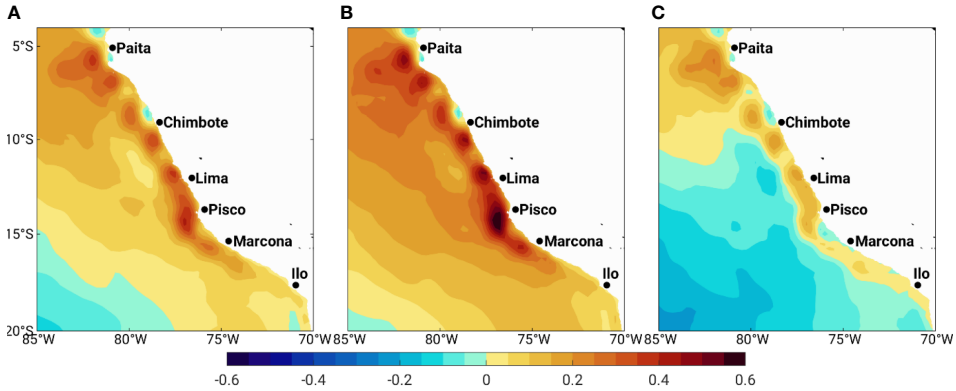

FIGURE 8
Spatial pattern of the regression coefficient (N/m^{2}C) between meridional wind stress and ENSO **(A)**, El Niño **(B)**, and La Niña **(C)** events. In the regression, the predicted parameter is wind stress.

3.5 Long-term trend

The long-term trend of meridional wind stress over the coastal domain and offshore areas shows a positive trend. The climatological mean over the periods of 1950–1979 and 1990–2019 and the difference between the two periods are shown in Figure 9. The distribution of trend (Figure 9C) shows positive values in almost all areas except the northernmost of the domain (above 5° S) with the maximum value in the Pisco area. The long-term wind intensification across the PUS can be largely attributed to the strengthening and southwest migration of the Pacific Subtropical Anticyclone (Ancapichún and Garcés-Vargas, 2015). Detailed information on the connection between the Pacific subtropical anticyclone and wind-driven upwelling across the PUS would be very beneficial for improving regional decadal prediction, which is beyond the current study.

In addition, the trend of the meridional wind stress over the coastal zone is calculated. First, the linear trend for the austral winter (July–September) wind stress over the coastal band (100 km) is computed. Given the phase locking of the ENSO cycle, the winter-time wind stress is slightly affected by the ENSO-related oscillations. This shows a positive trend in the entire coastal domain with higher values off the Pisco upwelling cell (Figure 10). The meridional wind stress shows a long-term upward trend of approximately ~0.001 Nm^{-2} per decade. Second, the impact of ENSO is subtracted from the monthly wind stress using linear regression. Again, the result shows an upward trend, which is comparable with the previous trend.

4 Discussions and conclusions

Using the ERA5 reanalysis, we assessed wind stress' temporal and spatial variations in the Peruvian Upwelling System (PUS) over the last seven decades. The long-term mean and seasonal cycle of wind stress were shown and discussed. On the long-term average,

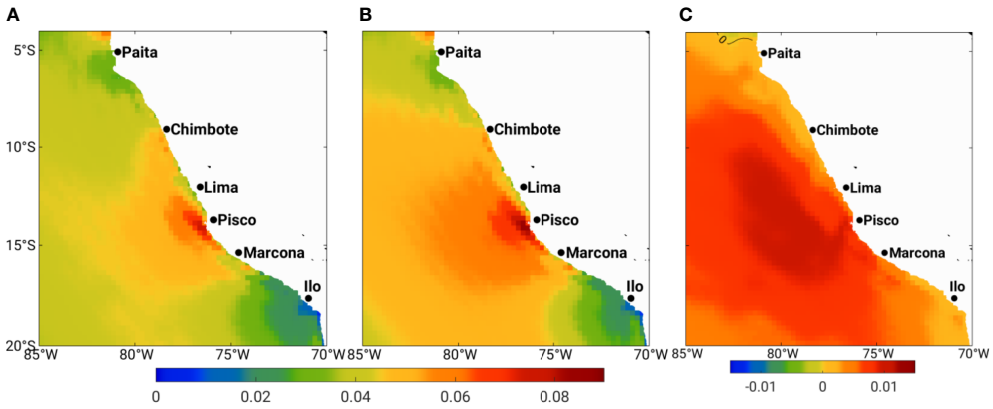

FIGURE 9
The climatology of the meridional wind stress (N/m^2) over the entire study area for the period of 1950–1979 **(A)**, 1990–2019 **(B)**, and the difference between two periods, 1990–2019 minus 1950–1979 **(C)**, calculated using ERA5 wind data. The isoline on **(C)** shows zero wind stress.

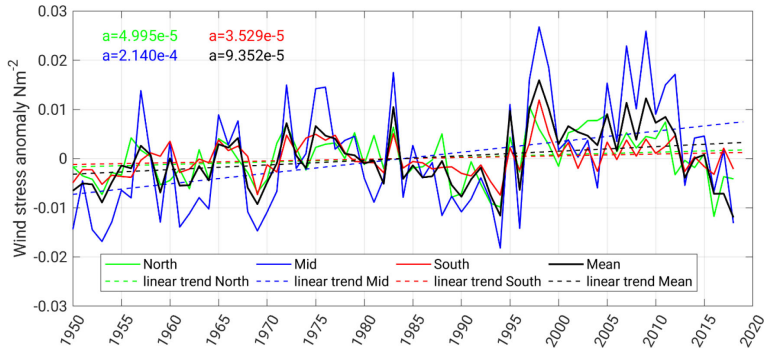

FIGURE 10
The yearly mean anomaly of the meridional wind stress for winter (July–September) over the coastal 100-km domain. The red, blue, green, and black lines represent the wind stress over the northern, central, and southern portions of the domain, respectively. Black lines indicate the wind averaged over the entire domain. The dashed lines are the linear trend. The linear trend coefficients (Nm^{-2}/year) are given with similar colors.

wind over the central PUS is intensified, which can be attributed to the headland effect. In general, the coastal and offshore winds over the southern portion of the PUS undergo more variability than the northern portion. The exception is the wind off the Paita upwelling cell in the northern portion of the PUS, which features a large variation. ENSO cycles exert profound impacts on the wind across the entire PUS. El Niño episodes feature intensified winds with more signature off Pisco. Interestingly, the wind anomaly during La Niña is not the opposite of that for El Niño, highlighting the asymmetric feature of the ENSO cycle. Our findings show a semi-regular variation on the decadal timescale and beyond, closely followed by the Interdecadal Pacific Oscillation cycles. For example, the transition of IPO from the negative to a positive phase in the late 1970s was concurrent with the weakening of the winds across the PUS. In contrast, the IPO phase reversal in the late 1990s was accompanied by the strengthening the PUS winds, which lasted for almost two decades. However, the ERA5 time span (~70 years) is insufficient to discuss the detailed structure of wind anomaly associated with the IPO. Our analysis indicates a long-term intensification of wind over the entire PUS. This intensification is more pronounced in the upwelling zones, consistent with previous studies, and very likely associated with the intensification of the South Pacific Anticyclone.

In addition, we conducted the joint wind-SST Empirical Orthogonal Function. The first mode is on a decadal timescale, explains more than 40% of variability, and is more related to the wind than SST. The wind anomaly associated with this mode is directed northwesterly/southeasterly and almost uniform across the entire domain. The associated principal component (PC) fluctuations are almost in phase with the IPO. This further highlights the teleconnection between climate variability over the extratropical Pacific and wind variability across the BUS. The second and third modes and their PCs share many similarities with ENSO cycles. In general, local wind variability tends to be more affected by the IPO, whereas the SST appears more related to the ENSO. The wind anomaly during El Niño is equatorward. However, the SST anomaly is pronounced and negative. It is likely due to the deepening of the thermocline and eastward propagation of upper ocean heat content during El Niño.

Data availability statement

The original contributions presented in the study are included in the article/supplementary material. Further inquiries can be directed to the corresponding author.

Author contributions

VM is the head of the project and designed the study. SY performed the whole data analysis and all authors contributed to the writing and revision. All authors contributed to the article and approved the submitted version.

Acknowledgments

This study was conducted within the frame of the CUSCO project sponsored by the Federal Ministry of Education and Research (BMBF) with the reference number CUSCO-03F0813E. The ERA5 data sets were obtained from ECMWF. We appreciate the reviewer for his/her constructive comments and suggestions, which helped to improve the manuscript.

Conflict of interest

The authors declare that the research was conducted in the absence of any commercial or financial relationships that could be construed as a potential conflict of interest.

Publisher's note

References

Ancapichún, S., and Garcés-Vargas, J. (2015). Variability of the southeast pacific subtropical anticyclone and its impact on sea surface temperature off north-central Chile. *Cienc. Marinas* 41 (1), 1–20. doi: 10.7773/cm.v41i1.2338

Bakun, A. (1990). Global climate change and intensification of coastal ocean upwelling. *Science* 247, 198–201. doi: 10.1126/science.247.4939.198

Bakun, A., Black, B. A., Bograd, S. J., García-Reyes, M., Miller, A. J., Rykaczewski, R. R., et al. (2015). Anticipated effects of climate change on coastal upwelling ecosystems. *Curr. Clim. Change Rep.* 1, 85–93. doi: 10.1007/s40641-015-0008-4

Barros V. R., Field C. B., Dokken D. J., Mastrandrea M. D., Mach K. J., Bilir T. E., et al (2014). Climate change 2014: impacts, adaptation, and vulnerability. part b: regional aspects. *Contribution Working Group II to Fifth Assess. Rep. ofthe Intergovernmental Panel Climate Change* (Cambridge; New York, NY), 688.

Bell, B., Hersbach, H., Berrisford, P., Dahlgren, P., Horányi, A., Muñoz Sabater, J., et al. (2020) *ERA5 hourly data on single levels from 1950 to 1978 (preliminary version)* (Copernicus Climate Change Service (C3S) Climate Data Store (CDS). Available at: https://cds.climate.copernicus-climate.eu/cdsapp#!/dataset/reanalysis-era5-single-levels-preliminary-back-extension?tab=overview (Accessed 25-01-2021).

Belmadani, A., Echevin, V., Codron, F., Takahashi, K., and Junquas, C. (2013). What dynamics drive future wind scenarios for coastal upwelling off Peru and Chile? *Clim. Dyn* 43, 1893–1914. doi: 10.1007/s00382-013-2015-2

Boe, J., Hall, A., Colas, F., McWilliams, J., Qu, X., Kurian, J., et al. (2011). What shapes mesoscale wind anomalies in coastal upwelling zones? *Clim. Dyn.* 36, 2037–2049. doi: 10.1007/s00382-011-1058-5

Bonino, G., Iovino, D., Brodeau, L., and Masina, S. (2022). The bulk parameterizations of turbulent air-sea fluxes in NEMO4: the origin of Sea surface temperature differences in a global model study. *Geoscientific Model. Dev. Discussions*, 1–20.

Bordbar, M. H., Mohrholz, V., and Schmidt, M. (2021). The relation of wind-driven coastal and offshore upwelling in the benguela upwelling system. *J. Phys. Oceanogr.* 51, 3117–3133. doi: 10.1175/JPO-D-20-0297.1

Brodeau, L., Barnier, B., Gulev, S. K., and Woods, C. (2017). Climatologically significant effects of some approximations in the bulk parameterizations of turbulent air–sea fluxes. *J. Phys. Oceanography* 47 (1), 5–28.

Capet, X. J., Marchesiello, P., and McWilliams, J. C. (2004). Upwelling response to coastal wind profiles. *Geophys. Res. Lett.* 3, L13311. doi: 10.1029/2004GL020123

Chamorro, A., Echevin, V., Colas, F., Oerder, V., Tam, J., and Quispe-Ccalluari, C. (2018). Mechanisms of the intensification of the upwelling-favorable winds during El niño 1997–1998 in the Peruvian upwelling system. *Climate Dynamics* 51, 3717–3733. doi: 10.1007/s00382-018-4106-6

Chavez, F. P., and Messié, M. (2009). A comparison of eastern boundary upwelling ecosystems. *Prog. Oceanogr.* 83, 80–96. doi: 10.1016/j.pocean.2009.07.032

Chavez, F. P., Ryan, J., Lluch-Cota, S., and Miguel Ñiquen, C. (2003). From anchovies to sardines and back: multidecadal change in the pacific ocean. *Science* 299 (5604), 217–221. doi: 10.1126/science.1075880.

Desbiolles, F., Blanke, B., Bentamy, A., and Grima, N. (2014). Origin of fine-scale wind stress curl structures in the benguela and canary upwelling systems. *J. Geophys. Res.* 119 (11), 7931–7948. doi: 10.1002/2014JC010015

Dewitte, B., Vazquez-Cuervo, J., Goubanova, K., Illig, S., Takahashi, K., Cambon, G., et al. (2012). Change in El nino flavours over 1958-2008: implications for the long-term trend of the upwelling off Peru. *Deep-Sea Res. Pt. II* 77–80, 143–156. doi: 10.1016/j.dsr2.2012.04.011

Ding, H., Greatbatch, R., Latif, M., Park, W., and Gerdes, R. (2013). Hindcast of the 1976/77 and 1998/99 climate shifts in the pacific. *J. Climate* 26, 7650–7661. doi: 10.1175/JCLI-D-12-00626.1

Echevin, V., Colas, F., Chaigneau, A., and Penven, P. (2011). Sensitivity of the northern Humboldt current system nearshore modeled circulation to initial and boundary conditions. *J. Geophys. Res.* 116, C07002. doi: 10.1029/2010JC006684

Espinoza-Morriberon, D., Echevin, V., Colas, F., Tam, J., Ledesma, J., Vasquez, L., et al. (2017). Impacts of El niño events on the Peruvian upwelling system productivity. *J. Geophys. Res. Oceans* 122, 5423-5444. doi: 10.1002/2016JC012439

García-Reyes, M., Sydeman, W. J., Schoeman, D. S., Rykaczewski, R. R., Black, B. A., Smit, A. J., et al. (2015). Under pressure: climate change, upwelling, and Eastern boundary upwelling ecosystems. *Front. Mar. Sci.* 2. doi: 10.3389/fmars.2015.00109

Guillen, O. (1983). Condiciones oceanognificas y sus fluctuaciones en el pacifico sur oriental. *FAO Fish Rep.* 3, 607–658.

Henley, B., Gergis, J., Karoly, D., Power, S., Kennedy, J., and Folland, C. (2015). A tripole index for the interdecadal pacific oscillation. *Climate Dynamics* 45, 3077–3090. doi: 10.1007/s00382-015-2525-1

Hersbach, H., Bell, B., Berrisford, P., Biavati, G., Horányi, A., Muñoz Sabater, J., et al. (2018) *ERA5 hourly data on single levels from 1979 to present* (Copernicus Climate Change Service (C3S) Climate Data Store (CDS) (Accessed 11.09.2019).

Hersbach, H., Bell, B., Berrisford, P., Hirahara, S., Horányi, A., Muñoz-Sabater, J., et al. (2020). The ERA5 global reanalysis. *Q. J. R. Meteorol. Soc* 146 (2020), 1999–2049. doi: 10.1002/qj.3803

Jacox, M. G., Moore, A. M., Edwards, C. A., and Fiechter, J. (2014). Spatially resolved upwelling in the California current system and its connections to climate variability. *Geophys. Res. Lett.* 41, 3189–3196. doi: 10.1002/2014GL059589

Kutzbach, J. E. (1967). Empirical eigenvectors of sea-level pressure, surface temperature and precipitation complexes over north America. *J. Appl. Meteorol. Climatol.* 6 (5), 791–802. doi: 10.1175/1520-0450(1967)006<0791:EEOSLP>2.0.CO;2

Meehl, G. A., and Hu, A. (2006). Megadroughts in the Indian monsoon region and southwest north America and a mechanism for associated multi-decadal pacific sea surface temperature anomalies. *J. Climate* 19, 1605–1623. doi: 10.1175/JCLI3675.1

Meehl, G., Hu, A., and Teng, H. (2016). Initialized decadal prediction for transition to positive phase of the interdecadal pacific oscillation. *Nat. Commun.* 7, 11718. doi: 10.1038/ncomms11718

Montecinos, A., Purca, S., and Pizarro, O. (2003). Interannual-to-interdecadal sea surface temperature variability along the western coast of south America. *Geophys. Res. Lett.* 30, 1570. doi: 10.1029/2003GL017345

Narayan, N., Paul, A., Mulitza, S., and Schulz, M. (2010). Trends in coastal upwelling intensity during the late 20th century. *Ocean Sci.* 6, 815–823. doi: 10.5194/os-6-815-2010

Oyarzún, D., and Brierley, C. M. (2019). The future of coastal upwelling in the Humboldt current from model projections. *Clim. Dyn* 52, 599–615. doi: 10.1007/s00382-018-4158-7

Parker, D., Folland, C., Scaife, A., Knight, J., Colman, A., Baines, P., et al. (2007). Decadal to multidecadal variability and the climate change background. *J. Geophys. Res.* 112, D18115. doi: 10.1029/2007JD008411

Renault, L., Deutsch, C., McWilliams, J. C., Frenzel, H., Liang, J. H., and Colas, F. (2016). Partial decoupling of primary productivity from upwelling in the California current system. *Nat. Geosci.* 9 (7), 505–508. doi: 10.1038/ngeo2722

Renault, L., Dewitte, B., Marchesiello, P., Illig, S., Echevin, V., Cambon, G., et al. (2012). Upwelling response to atmospheric coastal jets off central Chile: a modeling study of the October 2000 event. *J. Geophys. Res.* 117, C02030. doi: 10.1029/2011JC007446

Renault, L., Hall, A., and McWilliams, J. C. (2015). Orographic shaping of US West coast wind profiles during the upwelling season. *Clim. Dyn.* 46, 273–289. doi: 10.1007/s00382-015-2583-4

Reynolds, R. W., Smith, T. M., Liu, C., Chelton, D. B., Casey, K. S., Schlax, M. G., et al. (2007). Daily high-resolution blended analyses for sea surface temperature. *J. Climate* 20, 5473–5496. doi: 10.1175/2007JCLI1824.1

Rykaczewski, R. R., Dunne, J. P., Sydeman, W. J., García-Reyes, M., Black, B. A., and Bograd, S. J. (2015). Poleward displacement of coastal upwelling-favorable winds in the ocean's eastern boundary currents through the 21st century. *Geophys. Res. Lett.* 42, 6424–6431. doi: 10.1002/2015GL064694

Sydeman, W. J., García-Reyes, M., Schoeman, D., Rykaczewski, R. R., Thompson, S. A., Black, B. A., et al. (2014). Climate change and wind intensification in coastal upwelling ecosystems. *Science* 345, 77–80. doi: 10.1126/science.1251635

Taboada, F. G., Stock, C. A., Griffies, S. M., Dunne, J., John, J. G., Small, R. J., et al. (2019). Surface winds from atmospheric reanalysis lead to contrasting oceanic forcing and coastal upwelling patterns. *Ocean Modeling* 133, 79–111. doi: 10.1016/j.ocemod.2018.11.003

Taylor, M. H., Wolff, M., Mendo, J., and Yamashiro, C. (2008). Changes in trophic flow structure of independence bay (Peru) over an ENSO cycle. *Prog. Oceanogr.* 79 (2-4), 336–351. doi: 10.1016/j.pocean.2008.10.006

Trenberth, K., Large, W., and Olson, J. (1990). The mean annual cycle in global ocean wind stress. *J. Phys. Oceanogr.* 20, 1742–1760. doi: 10.1175/1520-0485(1990)020<1742:TMACIG>2.0.CO;2

Varela, R., Álvarez, I., Santos, F., deCastro, M., and Gómez-Gesteira, M.. (2015). Has upwelling strengthened along worldwide coasts over 1982-2010? *Sci. Rep.* 5, 10016. doi: 10.1038/srep10016

frontiers | Frontiers in Marine Science

TYPE Original Research
PUBLISHED 04 September 2023
DOI 10.3389/fmars.2023.1158472

OPEN ACCESS

EDITED BY
Donald B. Olson,
University of Miami, United States

REVIEWED BY
Salvador E. Lluch-Cota,
Centro de Investigación Biológica del Noroeste (CIBNOR), Mexico
Francisco Machín,
University of Las Palmas de Gran Canaria, Spain

*CORRESPONDENCE
Marisol García-Reyes
marisolgr@faralloninstitute.org

RECEIVED 03 February 2023
ACCEPTED 15 August 2023
PUBLISHED 04 September 2023

CITATION
García-Reyes M, Koval G, Sydeman WJ, Palacios D, Bedriñana-Romano L, DeForest K, Montenegro Silva C, Sepúlveda M and Hines E (2023) Most eastern boundary upwelling regions represent thermal refugia in the age of climate change.
Front. Mar. Sci. 10:1158472.
doi: 10.3389/fmars.2023.1158472

Most eastern boundary upwelling regions represent thermal refugia in the age of climate change

Marisol García-Reyes[1]*, Gammon Koval[1], William J. Sydeman[1], Daniel Palacios[2], Luis Bedriñana-Romano[3], Kelly DeForest[4], Carlos Montenegro Silva[5], Maritza Sepúlveda[6] and Ellen Hines[4]

[1]Farallon Institute, Petaluma, CA, United States, [2]Marine Mammal Institute, Oregon State University, Newport, OR, United States, [3]Centro de Investigación Oceanográfica en el Pacífico Sur-Oriental (COPAS) Coastal, Universidad de Concepción, Concepción, Chile, [4]Estuary and Ocean Science Center, San Francisco State University, Tiburon, CA, United States, [5]Departamento Evaluación de Pesquerías, Instituto de Fomento Pesquero (IFOP), Valparaíso, Chile, [6]Centro de Investigación y Gestión de Recursos Naturales (CIGREN), Instituto de Biología, Universidad de Valparaíso, Valparaíso, Chile

Eastern Boundary Upwelling Systems (EBUS) are regions where wind-driven coastal upwelling brings deep cold, nutrient-rich water to the surface and may be characterized by a coastal 'footprint' of sea surface temperature (SST) cooler than their surroundings. Previous studies have shown that EBUS coastal temperatures are responding differently to global ocean warming, warming slowly or not at all. However, the spatial dynamics of coastal upwelling footprints have yet to be investigated. In this paper, we use 20 years of high-resolution SST data derived from satellites (MUR SST) to test the null hypothesis that the extent of coastal upwelling footprints have remained stable over the period 2002–2022, consistent with the idea that these regions are thermal refugia. We investigate linear trends at different time scales, finding that the Humboldt and Iberian/Canary EBUS show no contraction of this footprint on annual or seasonal scales. The Benguela EBUS shows no change in its central and poleward subregions, but it exhibits contraction of the footprint in the equatorward subregion in the austral winter and spring. The California EBUS behaves differently: on the annual scale only the equatorward subregion shows contraction of the SST footprint, while on the seasonal scale, the entire EBUS show contraction during the fall or summer/fall. Summarizing the last two decades, most coastal habitats of EBUS (>80% of the areas tested) are remaining cool and may be acting as regional refugia from global warming, but this is true for some regions only during certain seasons. However, the declines in areal extent of upwelling in subregions of the California and Benguela EBUS indicate potential consequences for marine life and may help to explain changes in abundance, productivity, and redistributions of populations in these regions.

KEYWORDS

thermal refugia, spatial trends, MURSST, seasonal variation, upwelling footprint

Introduction

The four major Eastern Boundary Upwelling Systems (EBUS) - Humboldt, Benguela, California, and Iberian/Canary - are characterized by a narrow coastal band (~50–150 km) of surface temperatures that are cooler than temperatures offshore (Bakun and Parrish, 1982; Chavez and Messié, 2009). This is caused by wind-driven coastal upwelling that brings deep, cold water to the surface at the coast. Cool, nutrient-rich upwelled waters fuel large phytoplankton blooms that sustain the rich marine ecosystems of EBUS (Kämpf and Chapman, 2016), including 20% of world fisheries catch (Pauly and Christensen, 1995; Bindoff et al., 2019) and high biodiversity of upper trophic level species (Chavez and Messié, 2009; *Watermeyer et al., 2020*]. Furthermore, the cool coastal sea surface temperature (SST) footprint is important to adjacent terrestrial ecosystems in driving low clouds (fog), low temperature, and high humidity (Johnstone and Dawson, 2010) that are favorable to forested and agricultural areas (Black et al., 2014). Overall, EBUS provide services to ~80 million people (García-Reyes et al., 2015). On a global scale, the cool EBUS SST footprint affects climate through air-sea interactions (Large and Danabasoglu, 2006; Curchitser et al., 2011; Bakun et al., 2015), as well as CO_2 outgassing (as upwelled water is high in CO_2 content) and capture (through enhanced primary productivity) (Mackas et al., 2006; Ikawa et al., 2013; Brady et al., 2019).

Changes in the cold footprint of upwelling have not been studied extensively as have changes in temperatures along EBUS, although they are clearly related. For example, Santora et al. (2020) quantified the upwelling footprint as the coastal area below a temperature threshold associated with upwelled water, calling it the habitat compression index (HCI). Impacts of warm conditions along EBUS are well documented, for example, during El Niño events along the Pacific EBUS (Chavez et al., 2002; Escribano et al., 2004; Jacox et al., 2016; Diaz-Astudillo et al., 2022), or a marine heatwave (MHW) in the Northeast Pacific in 2014–2016 (Gentemann et al., 2017; Santora et al., 2020); both types of events caused large negative consequences for coastal socio-ecological systems. In the California, variability in the HCI has been associated with changes in zooplankton and forage indices (Schroeder et al., 2022), as well as the risk of humpback whale entanglement in fishing gear due to reduction of cold favorable habitat, which leads to redistribution and overlap of whale prey into crab fishing grounds (Santora et al., 2020). The HCI has demonstrated that changes in upwelling footprint is a good indicator of suitable habitat.

Anthropogenic global climate change is impacting EBUS similarly to other oceanic regions by increasing global ocean temperatures (Cooley et al., 2022; Bograd et al., 2023), stratification (Bakun et al., 2015; Li et al., 2020), and frequency of extreme events such as MHWs (Gentemann et al., 2017; Varela et al., 2021; Izquierdo et al., 2022; Thoral et al., 2022). On the other hand, upwelling-favorable winds are predicted to strengthen in poleward regions of EBUS (Sydeman et al., 2014; Bakun et al., 2015; Rykaczewski et al., 2015; Wang et al., 2015; Abrahams et al., 2021; Bograd et al., 2023), potentially counteracting increasing temperature trends. However, how temperatures in coastal upwelling regions are and will respond to these counteracting drivers has been a subject of debate, with unclear or contradicting trends (Bograd et al., 2023) depending on dataset, period of study, and spatial scale (Sydeman et al., 2014; Bakun et al., 2015; García-Reyes et al., 2015). Few studies have examined SST trends at the spatial scales at which coastal upwelling occurs. Varela et al. (2018) and Seabra et al. (2019) showed that decadal trends in SST along EBUS have changed little, or even cooled, at nearshore locations (within ~50 km) due to the cooling effects of upwelling. For these reasons, EBUS have been hypothesized to be "thermal refugia" from global warming (Bakun et al., 2015; Hu and Guillemin, 2016; Lourenço et al., 2016; Barceló et al., 2018; Varela et al., 2018; Lourenço et al., 2020), but observed regional and seasonal changes in the spatial extent of the surface expression (i.e., "footprint") of coastal upwelling has yet to be investigated.

A general question of interest is, therefore: as global ocean temperatures rise and marine heatwaves become more frequent (Bindoff et al., 2019), are the upwelling-derived cool-water habitats in EBUS coastal areas changing in a manner that may be detrimental to marine life and coastal societies? This question has yet to be asked across all EBUS. In particular, trends in the upwelling footprint would depend on the relative importance and rate of change of different mechanisms driving temperature change in different regions (see review in Bograd et al., 2023 and in the IPCC's Cooley et al., 2022). In this study, we address this question by investigating changes in spatial extent of cool SST footprints in EBUS using high-resolution observations collected over the last two decades. We test the null hypothesis of no significant change (expansion or contraction) in the cool-water SST footprint over time, consistent with the concept that EBUS coastal habitat represents thermal refugia to global warming due to the effects of upwelling.

Data & methods

In this study we used an area of 300 km from shore (approximately the extent of national exclusive economic zones (EEZ); see Figures 1, 2) along the EBUS to fully capture variability in the SST associated with upwelling coastal process. This occurs mostly in a narrow band of ~30 km from shore, corresponding to the Rossby radius of deformation (Allen, 1973; Carr and Kearns, 2003), but the cooler SST upwelled can extend to 150 km or more due to offshore transport, especially downstream of upwelling centers like promontories or capes (Chavez and Messié, 2009; Hutchings et al., 2009). These 300-km subregions are embedded in the equatorward eastern boundary currents that occur year-round and can extend hundreds of kilometers offshore (Thiel et al., 2007; Checkley and Barth, 2009; Mason et al., 2011). We selected three subregions within each EBUS (Figure 1, Table 1) based on subregions identified in the literature as dynamically coherent (Tarazona and Arntz, 2001; Thiel et al., 2007; Arístegui et al., 2009; Checkley and Barth, 2009; Hutchings et al., 2009). The subregions were identified by their distinctive seasonality and magnitude in upwelling-favorable winds and sea temperature, with equatorial subregions exhibiting larger temperatures and year-round winds, and poleward

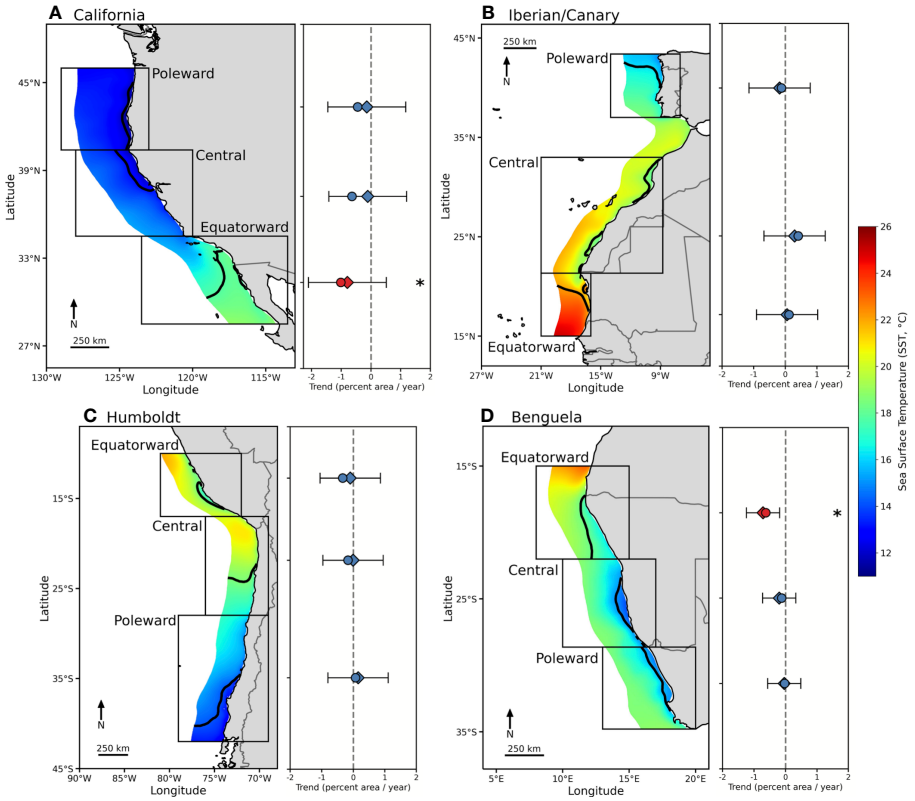

FIGURE 1
Mean SST (2002-2022, MURSST) in the four major EBUS (**(A)** California, **(B)** Iberian/Canary, **(C)** Humboldt, **(D)** Benguela), within an area extending 300 km from the shore. Selected subregions within each EBUS are delineated. The black line delimits the threshold SST_T for each subregion that identifies the cool SST footprint. To the right of each map are the trends in annual SST footprint from the GLS model (diamond) and the GLM (circle) for each subregion represented as the percent of the total area per year. Statistically significant trends, based on the two-tail Monte Carlo test, are colored in red and denoted with an asterisk (See Table 1). 95% confidence intervals are shown from the GLS model and indicated by black lines.

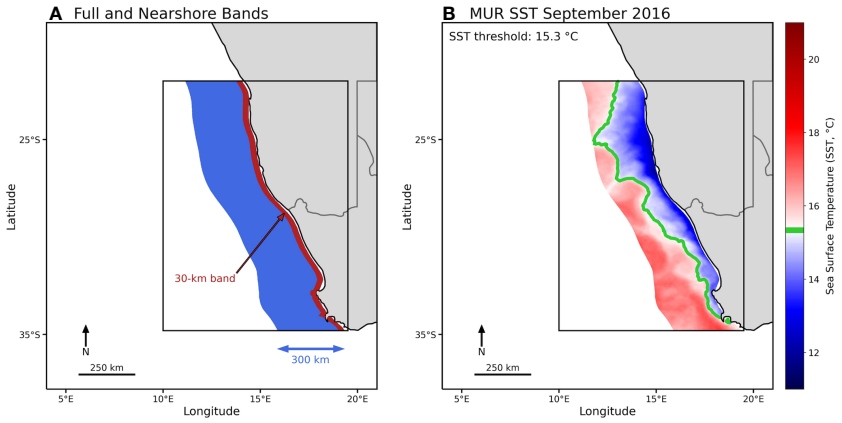

FIGURE 2
(A) Map of the poleward Benguela subregion illustrating the method of study area delineation. Subregion broad boundaries are shown as a black box, the total area of study is delimited by the 'blue' area from the coast to 300 km offshore (this area represents 100% of the possible area of the SST footprint), and the 30-km 'red' coastal band is where upwelling occurs and where the SST threshold (SST_T) was calculated as the mean SST within it. **(B)** Cool SST footprint for September 2016, with color representing monthly SST and the green contour line indicating the subregion SST threshold (SST_T = 15.6°C); the portion of the total area with temperature below the SST_T (green line) is defined as the SST footprint for this month.

TABLE 1 Latitudinal range, SST threshold (SST_T) for each subregion (defined mean SST of the coastal band within 30 km from shore for each EBUS), and for comparison, the entire subregion mean SST (from shore to 300 km away from the coast).

EBUS - Subregion	Latitudinal range	SST_T (°C)	Subregion SST (°C)
California-Poleward	40.40 – 46.00°N	11.88	13.02
California-Central	34.50 – 40.40°N	13.07	14.05
California-Equatorward	28.50 – 34.50°N	17.78	17.34
Humboldt-Poleward	28.00 – 42.00°S	14.12	14.97
Humboldt-Central	17.00 – 28.00°S	19.07	19.71
Humboldt-Equatorward	10.00 – 17.00°S	18.27	19.99
Iberian/Canary-Poleward	37.00 – 43.39°N	16.21	17.25
Iberian/Canary-Central	21.33 – 30.00°N	19.26	20.54
Iberian/Canary-Equatorward	15.00 – 21.33°N	22.57	23.34
Benguela-Poleward	28.63 – 34.80°S	15.34	17.25
Benguela-Central	22.00 – 28.63°S	15.07	17.0
Benguela-Equatorward	15.00 – 22.00°S	18.18	19.33

subregions with lower temperatures and stronger seasonality in winds. Central subregions in most EBUS exhibit a strong center of seasonal upwelling.

We used Multi-scale Ultra-high Resolution (MUR) SST V4.1 data (JPL Mur MEaSUREs Project, 2015; Chin et al., 2017) for a 20-year period (June 1, 2002 to May 31, 2022). MUR SST data are gap-free at daily temporal scales and have a spatial resolution of 1x1 km, which is ideal for this analysis; the fine spatial resolution can most accurately capture the SST footprint extension and its changes. We aggregated the SST data monthly to increase the signal to noise ratio, as we were interested in interannual and longer time scale changes. Another advantage of using MUR SST, despite its relatively short temporal reach, was that it is available worldwide, allowing a comparison across EBUS in recent times. Subregions of SST were then delimited (masked) by the latitudinal range shown in Table S1, the coast, and a longitudinal line 300 km away from the shore. This masked area (colored in Figures 1, 2) constituted the 100% of the area for each subregion.

Inspired by the HCI Index definition from Santora et al. (2020), we defined an indicator of the EBUS cool SST footprint: an area with SST below a given threshold proxying a coastal cool habitat associated with upwelling and mixing of cool and nutrient-rich waters, and therefore biological productivity (Schroeder et al., 2022). This threshold (SST_T) was calculated as the long-term mean SST value of the 30-km coastal band within each subregion (Table 1, red band in Figure 2A) where coastal upwelling occurs. The SST_T used in this research might differ from one more specifically derived based on local upwelling measurements that factor in wind stress or nutrient content, but this one-size-fits-all definition is an objective way to compare SST footprint variability for all subregions, and it was necessary given the heterogeneity in coastal upwelling among and within EBUS. Coastal upwelling shows heterogeneity in phenology, magnitude, and sign of winds and SST through the year (Figure 3) (Bakun and Nelson, 1991; Carr and Kearns, 2003; Escribano and Schneider, 2007; Bograd et al., 2009). However, we used the same subregional threshold SST_T value for the entire subregion, as it is representative of the local upwelling along the subregion coast.

The monthly cool SST footprint extension was then calculated as the number of 1x1-km pixels in a given subregion that were below its threshold SST_T (see Figure 2B), and was expressed as a percent of the subregion area (masked) to standardize it. Because the threshold SST_T was based on the SST of the cool 30-km coastal band, the total subregion area was seldom below that value; however, winter temperatures, not necessarily associated with upwelling but not distinguishable from them, could be below the threshold SST_T. Finally, we calculated seasonal and annual averages of the SST footprint. The annual average spanned winter to fall for both hemispheres, covering an entire upwelling season. Winter was defined as December to February for the northern hemisphere and June to August for the southern hemisphere, and so on.

We tested our hypothesis through two methods. First, we used a generalized least square model (GLS) to calculate linear trends for the subregions within each EBUS. To build the GLS, the subregion's annual SST footprint time series acts as the response variable, year as the time covariate, and EBUS and subregions as categorical values (See supplementary material). Following the methodology laid out by Zuur et al. (2009), the GLS included a weight parameter to help control for heteroskedasticity in the residuals. For this model, a constant variance function was used in which each EBUS was allowed to vary independently. The GLS also included a correlation term that corrected for the non-independence of the residuals, necessary given the relatively short span of the time series. A first order autoregressive structure was fit to the residuals of the model with year as the continuous covariate, and the significance is represented in the results by the confidence intervals. This method allowed us to estimate the linear trends with larger statistical power by increasing the degrees of freedom when combining data together from all subregions. The second approach used generalized linear models (GLM) to individually calculate the trend for each EBUS/

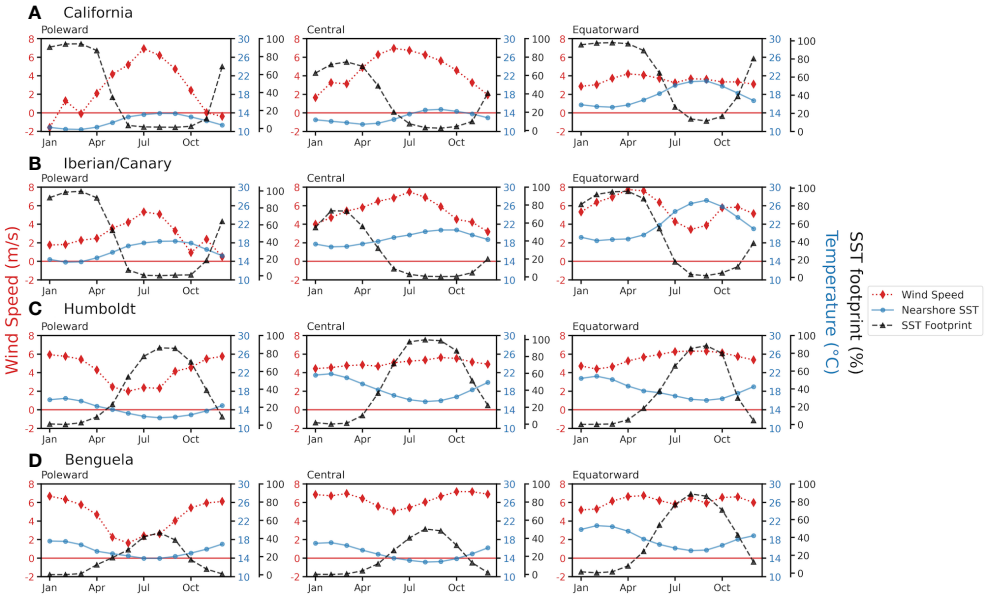

FIGURE 3
Seasonal cycle of upwelling-favorable meridional wind speed (red diamonds: ERA5 data), SST from the coastal 30-km band (blue dots: MURSST), and cool SST footprint percentage (black triangles; MURSST). Values were based on monthly means for the period 2002-2022, for **(A)** California, **(B)** Iberian/Canary, **(C)** Humboldt, and **(D)** Benguela EBUS.

subregion time series, and therefore had fewer degrees of freedom given by the length of each time series. These GLMs had a similar formula as the GLS, with percent of the area below SST_T as the response variable and year as a continuous covariate. For the GLM trends a two-tail Monte-Carlo test was used to calculate p-values from a randomized set of similarly distributed data to avoid overestimating statistical significance ($p < 0.025$ for the two-tail test) due to autocorrelation and length of time series. Both model methods provide similar information, but have different statistical capabilities and we consider them complementary to address the length of the time series and the large interannual variability in some regions. Furthermore, each subregion is large enough to be considered independent from each other (given the smaller Rossby radius of deformation (Huyer, 1983) and the offshore extent of upwelling compared to the distance to the next subregion), therefore, we are not concerned with inflation of p-values by the number of linear regressions calculated.

To investigate changes in the timing of the SST footprint, we calculated linear trends in seasonal means in each subregion's footprint. Seasonal means were chosen over monthly to avoid over-calculating trends on data that did not necessarily show large changes month to month. In addition, we calculated linear trends of seasonal SST within each EBUS to further describe the spatial distribution of cool SST footprint changes. We used the GLM and Monte-Carlo tests to calculate trends and p-values for these time series. The Python and R code used to generate the indices and analyze the data can be found in a Github repository [https://github.com/farallon-institute/Garcia-Reyes_etal_2023_EBUSFootprint].

Additionally, to illustrate the seasonality of upwelling-favorable wind and SST, we used the monthly seasonality of SST in the 30-km coastal bands and the meridional wind (V) over each EBUS subregion (Figure 3). Meridional wind speed (m/s) was extracted from the ERA5 dataset (Hersbach et al., 2020) for the period 2002–2022. Wind data were provided at 10 m over the sea surface with an hourly temporal resolution and a 31-km spatial resolution. SST was extracted from MUR SST for the same period.

Results

The extent of cool SST footprints in all EBUS subregions show differences in timing and magnitude through their seasonal cycles (Figure 3), with magnitudes varying from 0% to 40–100% (area below the threshold SST_T). The largest cool footprints occur between February and April in the northern hemisphere, and between July and September in the southern hemisphere. The meridional wind and SST seasonalities shown in Figure 3 are consistent with those reported in the literature (Shannon, 2001; Carr and Kearns, 2003; Chavez and Messié, 2009; Montecino and Lange, 2009), but note that the peaks of the SST footprint do not occur simultaneously with the peaks in meridional wind speed (upwelling-favorable) in most subregions (Figure 3). The difference in peak timing indicates that the strong seasonality in temperature due to the solar cycle dominates the timing of the coastal SST annual cycle, rather than upwelling-induced cooling, independently of the cooler SST magnitudes at the coast due to upwelling. In winter, temperatures are below the mean SST threshold, and the SST footprint is large. This is not necessarily due to upwelling (although in equatorial subregions upwelling occurs year-round), but SST values are below those typical of the upwelling season anyway, so they still represent a cool habitat.

The seasonality of the SST footprint unfolds, in general, as follows. During the peak of upwelling-favorable winds, nearshore waters are cooler than offshore. As summer unfolds, the SST footprint contracts, even if upwelling-favorable winds are still present, as deep cool water no longer reaches the surface due to the increasing stratification of the water column caused by the seasonal warming of upper layers of the ocean (Jacox and Edwards, 2011). The poleward Benguela subregion shows the narrowest SST footprint due to the warm influence of the portion of the Agulhas Current that enters the South Atlantic as mesoscale eddies (Hutchings et al., 2009), which leads to a strong cross-shore SST gradient year-round (Figure 1D). In any season, SST footprints can contract for other reasons, such as the occurrence of a marine heatwave, as occurred in 2014–2016 in the California EBUS (Figure S1) (Gentemann et al., 2017).

Linear trends for the annual SST footprint show similar results for the GLS and GLM (Table 2, Figure 1), with no significant trends for 10 of 12 EBUS subregions ($p < 0.025$ in the two-tail Monte Carlo test in the GLM or $p < 0.05$ in the GLS); the exceptions are the equatorward Benguela and California subregions, which show a contraction of their annual SST footprints. The equatorward California subregion shows a significant negative large trend in the GLM, but not in the GLS due to the autocorrelation and large interannual variability of the time series (Figure S1). The central California subregion shows a significant negative trend in the GLM, but the Monte Carlo test removes the significance and the trend is small and largely not significant in the GLS (Figure 1) due to autocorrelation and large interannual variability. It is worth noting that despite the lack of statistical significance ($p > 0.025$ on the Monte Carlo test), trends in other subregions show negative trends of significant magnitude, like central and poleward California in the GLM, and a positive trend in central Iberian/Canary in both models.

Seasonal linear trends in SST footprints for each EBUS subregion from the GLM are shown in Figure 4 and Table S1, while the time series are plotted in Figure S2. Trends vary in magnitude, and in some subregions in sign, across seasons. Humboldt and Iberian/Canary show no significant trends in any season (based on the Monte Carlo test), although they show not significant trend in all seasons, especially a positive trend in the fall in central Iberian/Canary and negatives ones in winter and summer in central Humboldt. The Benguela EBUS shows negative trends in winter (significant only in the equatorward subregion), and is more neutral in other seasons for the poleward and central subregions, although the equatorward subregion also shows a negative trend in spring. The California EBUS exhibits the largest negative trends among EBUS, in both its central and equatorward subregions. In the fall, all subregions show contracting (negative) trends in the Monte Carlo test, with the equatorward subregion having the largest trend, and the poleward the smallest. Central and equatorward California regions also show significant negative (contracting) trends in the summer, again, with the equatorward subregion exhibiting the largest negative trend, and the largest interannual variability in all seasons. It is worth noting that the central California spring season has a very small positive trend, the only one in this EBUS for any season.

Seasonal SST trends show narrow coastal regions of decreased temperatures in the central and poleward Benguela, Humboldt, and central Canary subregions, and warming trends in equatorward Benguela and California EBUS (Figures S3–S6). While the trends in most areas were not statistically significant ($p>0.05$, significance directly from the linear trend calculation at each grid point), the Iberian-Canary and Humboldt EBUS had a mix of small negative and positive trends offshore of the coastal band, while the Benguela and California EBUS had more ubiquitous warming trends, except during the spring season, which were negative. Any negative trend in the EBUS areas is opposed to the warming global SST trends (see Table S2 for global and hemispheric SST trend magnitudes), however, EBUS warming trends, when significant, can be larger than global or hemispherical trends by up to an order of magnitude.

TABLE 2 Linear trends of annual SST footprint area in %/year for generalized least squared (GLS) model and generalized linear model (GLM).

EBUS	Subregion	GLS trend (%/year)	GLS p-value	GLM trend (%/year)	Monte Carlo test p-value
California	Poleward	-0.308	0.572	-0.446	0.132
	Central	-0.366	0.502	-0.637	0.110
	Equatorward	-0.893	0.103	-1.012	0.009*
Iberian/Canary	Poleward	-0.146	0.696	-0.119	0.221
	Central	0.209	0.576	0.238	0.198
	Equatorward	0.094	0.801	0.119	0.315
Humboldt	Poleward	0.104	0.791	0.071	0.365
	Central	-0.090	0.819	-0.168	0.177
	Equatorward	-0.238	0.546	-0.335	0.169
Benguela	Poleward	-0.021	0.925	-0.027	0.432
	Central	-0.157	0.472	-0.121	0.166
	Equatorward	-0.672	0.002*	-0.625	0.001*

P-values and their statistical significance (marked with an asterisk) are shown for the GLS trends directly from the model, and for the GLM trends from a two-tail Monte Carlo test ($p < 0.025$).

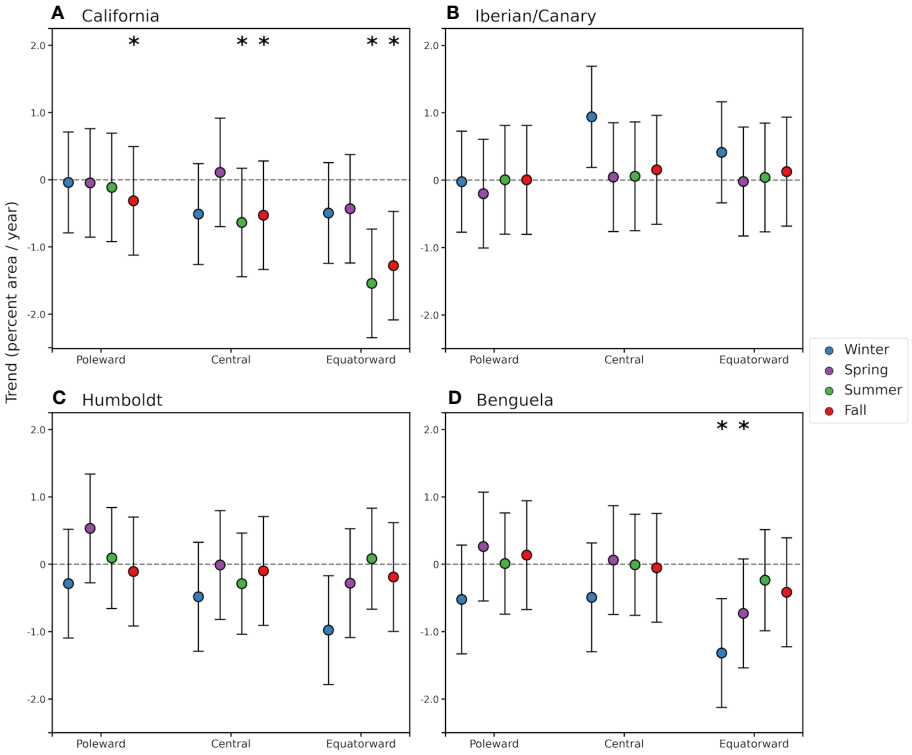

FIGURE 4
Linear trends of seasonal means of SST footprint (%/year) for each EBUS subregion with 95% confidence intervals from the GLM. Colors indicate seasons; winter is defined as December to February for the northern hemisphere and June to August for the southern hemisphere. Significant trends ($p < 0.025$ based on two-tail Monte Carlo test) are represented with an asterisk, and confidence intervals are based on the linear regression model. **(A)** California, **(B)** Iberian/Canary, **(C)** Humboldt, and **(D)** Benguela EBUS.

For example, the central and equatorward California subregions in the fall and the equatorial Benguela subregions in winter show large patches of significant warming up to 1°C/decade (from 2002 to 2022), while the global SST trend is 0.14°C/decade and the trend for the northern hemisphere is 0.21°C/decade (See Table S2) change into (NOAA Climate at a Glance). Note, however, that SST trends in Figures S3–S6 are representative of the change in temperatures in the region, but their magnitudes are based on pixels of 1 km x 1 km, as per the resolution of the data; smaller trends (and with different statistical significance) would be obtained if spatial averages were considered (as done for global or California EBUS scale analysis).

Discussion

In this paper, we quantify the changes in the coastal cool SST footprint that characterize EBUS. We test if 20-year linear trends in the extension of these footprints are contracting at annual and seasonal scales across EBUS (Table 3). We found that, taken into account the autocorrelation and variability of the time series, 10 out of 12 EBUS subregions support the hypothesis that the extension of the footprint, on annual scales, has not contracted in the last 20 years, despite the continued warming of the global oceans (Fox-Kemper, 2021). This result is in agreement with the idea that EBUS could be considered thermal refugia, and consistent with results from Seabra et al. (2019) showing that coastal areas in EBUS are responding differently to global warming, mostly warming at lower rates than offshore areas. Two subregions, equatorward California and Benguela, however, exhibit a contraction of their annual SST footprint in the period of study, with the former being the largest trend across all subregions. The large interannual variability in the equatorward California, plus the autocorrelation in the time series, removes the statistical significance in the trend in the GLS model, however, as we discuss later, diverging seasonal trends play an important role. Although not significant, the equatorward Humboldt subregion exhibits a contracting trend (negative), but on the contrary, equatorward Iberian/Canary shows an expanding trend. Interestingly, despite the lack of statistical significance, there is a pattern in the trends in which the equatorward regions exhibit the largest contraction trends (negative) and the poleward the smallest or zero (Figure 1), except in the Iberian/Canary EBUS.

This latitudinal pattern appears to be consistent with the weakening of upwelling, stronger water column stratification, and warmer temperatures in equatorward regions of EBUS predicted under climate change (Bakun et al., 2015; García-Reyes et al., 2015; Rykaczewski et al., 2015; Wang et al., 2015). The reported strengthening of upwelling-favorable winds in recent decades (Sydeman et al., 2014; Varela et al., 2015; Bindoff et al., 2019; Bograd et al., 2023) and predicted under climate change (Bakun, 1990; Rykaczewski et al., 2015; Wang et al., 2015; Bindoff et al., 2019) is not reflected in an expansion of cool SST footprints, although we observe cooling of coastal waters during the study

TABLE 3 Were used in. Summary of locations and timing of statistically significant trends in the annual and seasonal cool SST footprint (downward arrow: contraction; upward arrow: expansion).

EBUS	Subregion	Annual SST Footprint Trend	Seasonal SST Footprint Trend			
			Winter	Spring	Summer	Fall
California	Poleward	–	–	–	–	↓
	Central	–	–	–	↓	↓
	Equatorward	↓	–	–	↓	↓
Iberian/Canary	Poleward	–	–	–	–	–
	Central	–	–	–	–	–
	Equatorward	–	–	–	–	–
Humboldt	Poleward	–	–	–	–	–
	Central	–	–	–	–	–
	Equatorward	–	–	–	–	–
Benguela	Poleward	–	–	–	–	–
	Central	–	–	–	–	–
	Equatorward	↓	↓	↓	–	–

Statistical significance is based on GLS for annual footprint trends, and the Monte Carlo test for seasonal footprint trends.

period across EBUS, except California. It is possible, however, that the lack of expansion is caused by the increasing offshore temperatures (Seabra et al., 2019; Fox-Kemper, 2021), pressing on EBUS coastal footprints.

The lack of contraction of annual SST footprints in most EBUS, however, is encouraging, and it is supported from previous studies showing that in coastal areas of the EBUS, upwelling appears to mitigate or counteract the global ocean warming trend observed elsewhere (Santos et al., 2012; Varela et al., 2018; Seabra et al., 2019; Abrahams et al., 2021; Izquierdo et al., 2022). This suggests that, for the period 2002–2022, local processes like coastal upwelling, winter mixing, and longwave cooling have been strong or stable enough to counteract global warming trends and/or regional climate processes that drive low-frequency variability in EBUS conditions (Bonino et al., 2019; Marin et al., 2021). Notably, for the period of this study, the Humboldt EBUS does not show the reported cooling (corresponding to contraction of the SST footprint) trends observed in other datasets with longer time series (Varela et al., 2018; Seabra et al., 2019; Abrahams et al., 2021), while California shows significant contraction and warming at seasonal scales (see below).

Given the short length of the time series in climate time-scales, the observed trends might not be a reflection of climate change only, but also of basin-scale decadal climate oscillations. This is particularly the case of the Iberian/Canary poleward subregion, which exhibits opposite trends (positive, expansion) in annual SST footprint to other EBUS, although not statistically significant, and the California EBUS where the largest variability is observed (Figures S1, S2). However, the Iberian/Canary trends are consistent with previous results showing trends in upwelling-associated indicators divergent from other EBUS (Sydeman et al., 2014; Varela et al., 2015; Abrahams et al., 2021; Bograd et al., 2023). These differences among EBUS trends (in sign and magnitude) are addressed in a modeling study by Bonino et al. (2019) which shows that different regional mechanisms drive SST variability in each basin: California and Humboldt systems respond largely and synchronously to El Niño variability, Benguela responds to long-term anthropogenic climate change, and Iberian/Canary responds to North Atlantic multi-decadal variability. While results presented here are mostly consistent with Bonino et al. (2019), (seen for example in the large interannual variability in the California EBUS, associated with El Niño in 2016 and the preceding large marine heatwave in 2014–2015 that impacted the trends and their significance), in the poleward Humboldt cooling has been associated with strengthening upwelling-favorable winds and regional cooling temperatures (Varela et al., 2015; Abrahams et al., 2021), rather than the large interannual variability associated with El Niño observed in the equatorial subregion and in the California EBUS. As global ocean warming is expected to continue (Fox-Kemper, 2021), it is likely, however, that warming trends might become significant in all subregions, despite upwelling-favorable wind trends or regional multi-decadal oscillations, due to increased offshore SST, increased ocean temperature at depth, and increased stratification that limits the efficacy of upwelling to bring deeper, cooler waters to the surface (Bakun et al., 2015; Li et al., 2020).

Since coastal upwelling is mostly a seasonal process in EBUS, we further investigate changes in SST footprints by calculating linear trends of seasonal means of SST footprint for each EBUS subregion (Figure 4, Table S1) and of spatially explicit seasonal SST along EBUS (Figures S3–S6). Corroborating the results for the annual SST footprint analyses, no statistically significant trends in seasonal SST footprint were found in the Humboldt and Iberian/Canary subregions in any season. However, in the Humboldt EBUS

winter footprint trends are negative and larger in magnitude than in the other seasons, particularly in the equatorward subregion, which correspond to larger warming in this region in Figure S5. The lack of significance in the Monte Carlo test, despite the large magnitude of the winter footprint trend, is likely caused by the large interannual variability and magnitude of the SST footprint in this season. Winter also exhibits patches of significant warming in all subregions. In the Iberian/Canary EBUS, trends in all seasons in the poleward and equatorward subregions are close to zero, while in the central subregion, the fall shows a small expanding trend, also represented in a coastal band of significant cooling SST (Figure S4). Winter also shows an expanding trend that is larger but not significant, which corresponds to more widespread but not significant cooling. In the Benguela, the central and poleward subregions show no significant trends in all seasons, although winter trends are negative. Figure S6 also shows how for these subregions, a coastal cooling occurs in spring in both regions, and in the poleward regions also in summer and fall, while winter show more warming patches offshore. Therefore, the SST footprints in the Humboldt and Iberian/Canary EBUS and the central and poleward Benguela subregions are not significantly contracting at seasonal scales during the period of study, supporting the hypothesis, and consistent with the idea that these EBUS coastal areas can act as thermal refugia, as offshore areas exhibit warming.

On the other hand, the equatorial Benguela shows increasing trends in SST in winter and spring (June–November, Figure 4, Table S1), consistent with the contracting trends in the annual footprint (Figure S6). This warming trend is in agreement with the large warming (largest among EBUS) reported by Seabra et al. (2019) on a longer time scale in this region, and with a study (Bonino et al., 2019) showing that the driver of low-frequency variability in the Benguela EBUS is related to anthropogenic global change. Moreover, in the other Benguela subregions, non-significant negative footprint and positive SST trends occur in the same season, which are consistent with the findings of Bonino et al. (2019) as well. It is worth noting that the warming SST trends occur during seasons when the cool SST footprint is largest (austral winter, Figure 3), thus, the contracting trend in footprint represents a significant loss of cool habitat area in this EBUS (Table 2).

Similarly, the California EBUS exhibits statistically significant decreasing SST footprint trends and SST warming trends in all its subregions during the fall, as well as in the summer in the equatorward and central subregions (Figures 4, S3, Table S1). This appears to contradict the lack of change in the annual SST footprint in the central and poleward subregions in the GLM and in all regions in the GLS, but this is most likely due to the fact that the SST footprint is usually fully contracted during the warm seasons (Figures 3, S2), and therefore does not have a large influence on the expanded footprint during winter and spring. In the equatorward subregion, extent of the SST footprint in summer and fall is larger than in the central subregion, likely the reason for having an impact on the annual SST footprint. Therefore, the California EBUS, despite showing no significant trend in annual SST footprint, does not qualify as a thermal refugia year-round, as it shows strong and widespread coastal warming in the fall, and to a lesser extent in the summer. The significant contracting footprint and warming SST trends in the summer/fall in the California EBUS are likely due to the large interannual variability and autocorrelation in SST associated with the strong MHW and El Niño events in this EBUS during this period (Gentemann et al., 2017) (Figures S1, S2). The large trend in the equatorward California subregion can also be due to the dominance of temperature processes and advection from the south that can overtake the weak coastal upwelling (Checkley and Barth, 2009; Di Lorenzo et al., 2005).

Finally, it is interesting to note that the contracting trends in seasonal SST footprints that are larger toward the equatorial subregions, occur in different seasons in each hemisphere—summer and fall in the northern hemisphere (California EBUS), and winter and spring in the southern hemisphere EBUS—but at the same time of year (June–November), suggesting that these trends are related to a more global response than regional/seasonal drivers.

While there has been a significant global warming trend during our study period (Table S2, Fox-Kemper, 2021), the observed trends (or lack thereof) in SST footprint and in SST could reflect decadal trends due to basin-scale oscillations (Bonino et al., 2019) such as the Pacific Decadal Oscillation (Mantua and Hare, 2002) in the California EBUS or the Atlantic Multidecadal Oscillation and the North Atlantic Oscillation in the Iberian/Canary EBUS (Pardo et al., 2011). Furthermore, large interannual variability and autocorrelation, as seen in the California EBUS due to an extreme MHW (Gentemann et al., 2017), could impact linear trend calculations on short time series. Aware of the potential issues with the limited time series, large interannual variability, and autocorrelation mentioned previously, we trade longer SST data products in this study for a shorter time period of MUR SST due to its high resolution. At this scale, we can observe change in upwelling-related SST footprints. While the use of the GLS model and Monte Carlo test aims to address these caveats, results should be carefully interpreted in the timeframe they represent. Another consideration for the interpretation of our results is the definition of subregions and threshold SST_T for the cool footprint. A latitudinal redefinition of the boundaries by a few degrees does not change the sign or statistical significance of SST footprint trends (not shown), therefore, the results are not sensitive to the chosen subregion margins. The threshold SST_T was designed to represent temperatures in coastal upwelling regions and facilitate its comparison across EBUS, but does not take into account the influence of local processes and characteristics of individual subregions. For example, the SST footprint of the equatorward California and Iberian/Canary and poleward Humboldt and Iberian/Canary subregions show the influence of upstream cold currents and latitudinal gradients in SST (Figure 1), not only the coastal signature typical of upwelling regions as in poleward California and Benguela. This study aims to evaluate the cool SST footprint as objectively as possible across EBUS and subregions, as well as across their different upwelling seasonalities, and thus it is recommended to consider local processes, and *in situ* data when available, in the interpretation of the results for particular locations along any EBUS.

Implications for ecosystems

Marine species that inhabit or migrate through EBUS are adapted to their variable, cold, and nutritious conditions (Kämpf and Chapman, 2016). We have shown that the Humboldt and Iberian/Canary EBUS, as well as the poleward and central Benguela and California subregions, are consistent with the idea of thermal refugia habitats for their ecosystems as their cool annual SST footprints have not contracted over the past two decades in a rapidly warming ocean [see for example Medellín-Mora et al., 2016). Species can still be impacted by changes in extent or phenology of the cool habitat, however, as they are during MHWs when warm conditions can have significant negative impacts (Sanford et al., 2019; Smale et al., 2019; Santora et al., 2020; Varela et al., 2021).

EBUS, as other oceanic systems, are subject to a wide array of anthropogenic pressures that might elicit major ecosystem modifications (Watermeyer et al., 2008; Lima et al., 2020; Rivadeneira and Nielsen, 2022). In addition, EBUS are also experiencing increased ocean acidification and hypoxic and marine heatwave events (Gruber et al., 2021) that add to the pressure of long-term overfishing and marine pollution, impacts that might be challenging to disentangle from favorable temperature conditions (see for example Yemane et al., 2014). However, EBUS are potentially significant marine thermal refugia due to the richness of the ecosystems they sustain, which is disproportionate to the world ocean's area that they cover (<1%) (Pauly and Christensen, 1995). This remains true even in those areas showing contractions of SST footprint, as they warm at a slower rate than other coastal and offshore areas (Bakun et al., 2015; Hu and Guillemin, 2016; Varela et al., 2018; Seabra et al., 2019; Lourenço et al., 2016; Lourenço et al., 2020).

Regional differences in SST footprint trends could represent habitat changes for the species they support. Contractions of the cool SST footprint can negatively impact the abundance, health, and distribution of cold-water affinity foundational species (such as macroalgae, euphausiid crustaceans, or forage fish) as well as the higher trophic level organisms they sustain (Soto et al., 2004; Ralston et al., 2015; Pérez-Matus et al., 2017; Becker et al., 2019; Santora et al., 2020; Cárdenas-Alayza et al., 2022; Schroeder et al., 2022). SST trends in EBUS may also have direct physiological effects on cold-water species as contractions result from warm conditions (Smale et al., 2019), as well as synergistic impacts due to combined stressors (Lima et al., 2020). These conditions can 'push' species out of the contracting and warming regions into areas that remain cool (Poloczanska et al., 2013; Poloczanska et al., 2016). For example, warming might disrupt the coping mechanisms of forage fish beyond the stability that ecological trade-off grants in the long-term, yielding habitat loss for some species (Deutsch et al., 2015; Howard et al., 2020). Contractions of the cool SST footprint can also lead to changes in habitat use by top predators which alters trophic interactions through spatial overlap among top species and also fisheries (Santora et al., 2020; Cimino et al., 2022; Schroeder et al., 2022).

These impacts have been observed particularly during warming episodes, like the 2014–2016 MHW that drastically contracted the cool SST footprint in the California EBUS (Gentemann et al., 2017). It is worth noting that these warming events can have a large impact on the ecosystem, even when thermal refugia protect these ecosystems from larger negative impacts to some degree (Varela et al., 2021; Izquierdo et al., 2022). This is of particular importance in the California EBUS as this system exhibits large variability in SST footprint during all seasons.

As the equatorward Benguela EBUS has little interannual variability, we would expect to observe evidence of ecosystem impacts from changes in the SST footprint, however, fishing pressure in that area has largely impacted stocks and it is difficult to disentangle the role of the environmental change (Blamey et al., 2015). Furthermore, expansion in the poleward direction towards refugia areas is challenged by the Luderitz upwelling cell off the coast of Namibia that acts as an ecological barrier for fish due to its strong offshore transport (Hutchings et al., 2009). On the other hand, warming areas can attract and better support species with warm-water affinities, as seen in marine species shifts with ocean warming trends (Perry et al., 2005; Poloczanska et al., 2016; Mason et al., 2019).

An interesting result is the timing at which contraction of SST footprints happens in the equatorward California and Benguela EBUS, as it has potentially different consequences for each ecosystem. In California, little impact is seen from the annual cool SST footprint, as seasonal changes occur after the peak of upwelling and during the warm seasons (spring and summer). This might result in disparate impacts to organisms, being a thermal refugia for species that migrate into the region during the cool seasons or have life stages that are more sensitive to temperature and nutrients during the cool season (Black et al., 2011; García-Reyes et al., 2013; Black et al., 2014; Ralston et al., 2015), but a negative impact for those species that are sensitive to temperatures during the summer and fall (Doney et al., 2012; Harley et al., 2012), particularly in the equatorward subregion. On the other hand, in the equatorward Benguela subregion, contraction of the cool SST footprint occurs when the footprint is largest (winter and spring), therefore, any contraction represents a significant habitat loss for species that rely on the cool temperatures and entrainment of nutrients due to upwelling and the productivity that follows. In this subregion, species that are more resilient to summer warm conditions are bound to be less impacted than those responding to winter/spring cool conditions.

Conclusion

We used high-resolution SST data and found that the coastal cool SST footprints characterizing EBUS did not exhibit contracting annual trends in 10 of the 12 subregions analyzed, in agreement with the thermal refugia concept. However, in the Benguela and California EBUS, the equatorward subregions show contraction of the cool SST footprint (by 0.6% and 1.0% of their areas respectively). These contractions occur in the austral winter/spring for Benguela and boreal summer/fall for California, corresponding to regions with significant warming during these seasons. EBUS could be important areas of conservation for marine

ecosystems, as they are areas of disproportionally high productivity for local and migrating species, especially as surrounding areas warm faster.

Data availability statement

The original contributions presented in the study are included in the article/Supplementary Material. Further inquiries can be directed to the corresponding author.

Author contributions

MG-R, WS, and EH conceived and designed the study. GK, WS, and MG-R conducted the statistical analyses and prepared the manuscript figures. All authors wrote and reviewed the manuscript. All authors contributed to the article and approved the submitted version.

Funding

MG-R, GK, KD, and EH were supported by The Pew Charitable Trusts Contract ID 0034562. MG-R and GK were also supported by NASA award 80NSSC20K0768. LB-R was supported by COPAS Coastal ANID FB210021.

Acknowledgments

Multi-Scale Ultra High Resolution (MUR) Sea Surface Temperature (SST) was downloaded from AWS https://registry.opendata.aws/mur from 2002–2020 [dataset accessed 08 July 2022], and from the ECMWF Reanalysis v5 (ERA5) wind data was downloaded from PO.DAAC https://doi.org/10.5067/GHGMR-4FJ04 from 2020–2022 [dataset accessed 10 August 2022]. The authors thank Chelle Gentemann for making the MUR SST dataset available in Zarr format on Amazon Web Services (AWS), Bian Hoover and Helen Killeen for the helpful discussions on statistics, and Sarah Ann Thompson for editing assistance. We thank the reviewers for their comments that helped us improve the manuscript.

Conflict of interest

The authors declare that the research was conducted in the absence of any commercial or financial relationships that could be construed as a potential conflict of interest.

Publisher's note

Supplementary material

The Supplementary Material for this article can be found online at: https://www.frontiersin.org/articles/10.3389/fmars.2023.1158472/full#supplementary-material

References

Abrahams, A., Schlegel, R. W., and Smit, A. J. (2021). Variation and change of upwelling dynamics detected in the world's eastern boundary upwelling systems. *Front. Mar. Sci.* 8, 626411. doi: 10.3389/fmars.2021.626411

Allen, J. S. (1973). Upwelling and coastal jets in a continuously stratified ocean. *J. Phys. Oceanogr.* 3 (3), 245–257. doi: 10.1175/1520-0485(1973)003<0245:UACJIA>2.0.CO;2

Arístegui, J., Barton, E. D., Álvarez-Salgado, X. A., Santos, A. M. P., Figueiras, F. G., Kifani, S., et al. (2009). Sub-regional ecosystem variability in the Canary Current upwelling. *Prog. Oceanogr.* 83 (1-4), pp.33–pp.48. doi: 10.1016/j.pocean.2009.07.031

Bakun, A. (1990). Global climate change and intensification of coastal ocean upwelling. *Science* 247 (4939), 198–201. doi: 10.1126/science.247.4939.198

Bakun, A., Black, B. A., Bograd, S. J., Garcia-Reyes, M., Miller, A. J., Rykaczewski, R. R., et al. (2015). Anticipated effects of climate change on coastal upwelling ecosystems. *Curr. Climate Change Rep.* 1 (2), 85–93. doi: 10.1007/s40641-015-0008-4

Bakun, A., and Nelson, C. S. (1991). The seasonal cycle of wind-stress curl in subtropical eastern boundary current regions. *J. Phys. Oceanogr.* 21 (12), 1815–1834. doi: 10.1175/1520-0485(1991)021<1815:TSCOWS>2.0.CO;2

Bakun, A., and Parrish, R. H. (1982). Turbulence, transport, and pelagic fish in the California and Peru current systems. *California. Cooperative. Oceanic. Fisheries. Investigations.* 23, 99–112.

Barceló, C., Ciannelli, L., and Brodeur, R. D. (2018). Pelagic marine refugia and climatically sensitive areas in an eastern boundary current upwelling system. *Global Change Biol.* 24 (2), 668–680. doi: 10.1111/gcb.13857

Becker, E. A., Forney, K. A., Redfern, J. V., Barlow, J., Jacox, M. G., Roberts, J. J., et al. (2019). Predicting cetacean abundance and distribution in a changing climate. *Diversity Distributions.* 25 (4), 626–643. doi: 10.1111/ddi.12867

Bindoff, N. L., Cheung, W. W., Kairo, J. G., Arístegui, J., Guinder, V. A., Hallberg, R., et al. (2019). "Changing ocean, marine ecosystems, and dependent communities," in *IPCC special report on the ocean and cryosphere in a changing climate* (Cambridge, UK and New York, NY, USA: Cambridge University Press), 477–587. doi: 10.1017/9781009157964.007

Black, B. A., Schroeder, I. D., Sydeman, W. J., Bograd, S. J., Wells, B. K., and Schwing, F. B. (2011). Winter and summer upwelling modes and their biological importance in the California Current Ecosystem. *Global Change Biol.* 17 (8), 2536–2545. doi: 10.1111/j.1365-2486.2011.02422.x

Black, B. A., Sydeman, W. J., Frank, D. C., Griffin, D., Stahle, D. W., García-Reyes, M., et al. (2014). Six centuries of variability and extremes in a coupled marine-terrestrial ecosystem. *Science* 345 (6203), 1498–1502.

Blamey, L. K., Shannon, L. J., Bolton, J. J., Crawford, R. J., Dufois, F., Evers-King, H., et al. (2015). Ecosystem change in the southern Benguela and the underlying processes. *J. Mar. Syst.* 144, 9–29. doi: 10.1016/j.jmarsys.2014.11.006

Bograd, S. J., Jacox, M. G., Hazen, E. L., Lovecchio, E., Montes, I., Pozo Buil, M., et al. (2023). Climate change impacts on eastern boundary upwelling systems. *Annu. Rev. Mar. Sci.* 15, 303–328. doi: 10.1146/annurev-marine-032122-021945

Bograd, S. J., Schroeder, I., Sarkar, N., Qiu, X., Sydeman, W. J., and Schwing, F. B. (2009). Phenology of coastal upwelling in the California Current. *Geophys. Res. Lett.* 36 (1), L01602. doi: 10.1029/2008GL035933

Bonino, G., Di Lorenzo, E., Masina, S., and Iovino, D. (2019). Interannual to decadal variability within and across the major Eastern Boundary Upwelling Systems. *Sci. Rep.* 9 (1), 1–14. doi: 10.1038/s41598-019-56514-8

Brady, R. X., Lovenduski, N. S., Alexander, M. A., Jacox, M., and Gruber, N. (2019). On the role of climate modes in modulating the air–sea CO2 fluxes in eastern boundary upwelling systems. *Biogeosciences* 16 (2), 329–346. doi: 10.5194/bg-16-329-2019

Cárdenas-Alayza, S., Adkesson, M. J., Edwards, M. R., Hirons, A. C., Gutiérrez, D., Tremblay, Y., et al. (2022). Sympatric otariids increase trophic segregation in response to warming ocean conditions in Peruvian Humboldt Current System. *PloS One* 17 (8), e0272348. doi: 10.1371/journal.pone.0272348

Carr, M. E., and Kearns, E. J. (2003). Production regimes in four Eastern Boundary Current systems. *Deep. Sea. Res. Part II: Topical. Stud. Oceanogr.* 50 (22-26), 3199–3221. doi: 10.1016/j.dsr2.2003.07.015

Chavez, F. P., and Messié, M. (2009). A comparison of eastern boundary upwelling ecosystems. *Prog. Oceanogr.* 83 (1-4), 80–96. doi: 10.1016/j.pocean.2009.07.032

Chavez, F. P., Pennington, J. T., Castro, C. G., Ryan, J. P., Michisaki, R. P., Schlining, B., et al. (2002). Biological and chemical consequences of the 1997–1998 El Niño in central California waters. *Prog. Oceanogr.* 54 (1-4), 205–232. doi: 10.1016/S0079-6611(02)00050-2

Checkley, D. M. Jr, and Barth, J. A. (2009). Patterns and processes in the california current system. *Prog. Oceanogr.* 83 (1-4), 49–64. doi: 10.1016/j.pocean.2009.07.028

Chin, T. M., Vazquez-Cuervo, J., and Armstrong, E. M. (2017). A multi-scale high-resolution analysis of global sea surface temperature. *Remote Sens. Environ.* 200, 154–169. doi: 10.1016/j.rse.2017.07.029

Cimino, M. A., Shaffer, S. A., Welch, H., Santora, J. A., Warzybok, P., Jahncke, J., et al. (2022). Western gull foraging behavior as an ecosystem state indicator in Coastal California. *Front. Mar. Sci.* 8, 790559. doi: 10.3389/fmars.2021.790559

Cooley, S., Schoeman, D., Bopp, L., Boyd, P., Donner, S., Ito, S. I., et al. (2022). "Oceans and coastal ecosystems and their services," in *IPCC AR6 WGII* (Cambridge, UK and New York, NY, USA: Cambridge University Press).

Curchitser, E., Small, J., Hedstrom, K., and Large, W. (2011). "3.7 Up-and down-scaling effects of upwelling in the California Current System," in *Report of working group 20 on evaluations of climate change projections* (Canada: North Pacific Marine Science Organization (PICES)), 98.

Deutsch, C., Ferrel, A., Seibel, B., Pörtner, H. O., and Huey, R. B. (2015). Climate change tightens a metabolic constraint on marine habitats. *Science* 348 (6239), 1132–1135. doi: 10.1126/science.aaa160

Diaz-Astudillo, M., Riquelme-Bugueno, R., Bernard, K. S., Saldias, G. S., Rivera, R., and Letelier, J. (2022). Disentangling species-specific krill responses to local oceanography and predator's biomass: The case of the Humboldt krill and the Peruvian anchovy. *Front. Mar. Sci.* 9, 979984. doi: 10.3389/fmars.2022.979984

Di Lorenzo, E., Miller, A. J., Schneider, N., and McWilliams, J. C. (2005). The warming of the California Current System: Dynamics and ecosystem implications. *J. Phys. Oceanogr.* 35 (3), 336–362. doi: 10.1175/JPO-2690.1

Doney, S. C., Ruckelshaus, M., Emmett Duffy, J., Barry, J. P., Chan, F., English, C. A., et al. (2012). Climate change impacts on marine ecosystems. *Annu. Rev. Mar. Sci.* 4, 11–37. doi: 10.1146/annurev-marine-041911-111611

Escribano, R., Daneri, G., Farías, L., Gallardo, V. A., González, H. E., Gutiérrez, D., et al. (2004). Biological and chemical consequences of the 1997–1998 El Niño in the Chilean coastal upwelling system: a synthesis. *Deep. Sea. Res. Part II: Topical. Stud. Oceanogr.* 51 (20-21), 2389–2411. doi: 10.1126/science.aaa160

Escribano, R., and Schneider, W. (2007). The structure and functioning of the coastal upwelling system off central/southern Chile. *Prog. Oceanogr.* 75 (3), 343–347. doi: 10.1016/j.pocean.2007.08.020

Fox-Kemper, B. (2021). "Ocean, cryosphere and sea level change (Ch. 9 of climate change 2021: the physical science basis)," in *Contribution of working group I to the sixth assessment report of the intergovernmental panel on climate change* (Cambridge, United Kingdom and New York, NY, USA: Cambridge University Press), 1211–1362. doi: 10.1017/9781009157896.011

García-Reyes, M., Sydeman, W. J., Schoeman, D. S., Rykaczewski, R. R., Black, B. A., Smit, A. J., et al. (2015). Under pressure: Climate change, upwelling, and eastern boundary upwelling ecosystems. *Front. Mar. Sci.* 2, 109. doi: 10.3389/fmars.2015.00109

García-Reyes, M., Sydeman, W. J., Thompson, S. A., Black, B. A., Rykaczewski, R. R., Thayer, J. A., et al. (2013). Integrated assessment of wind effects on Central California's pelagic ecosystem. *Ecosystems* 16 (5), 722–735. doi: 10.1007/s10021-013-9643-6

Gentemann, C. L., Fewings, M. R., and García-Reyes, M. (2017). Satellite sea surface temperatures along the West Coast of the United States during the 2014–2016 northeast Pacific marine heat wave. *Geophys. Res. Lett.* 44 (1), 312–319. doi: 10.1002/2016GL071039

Gruber, N., Boyd, P. W., Frölicher, T. L., and Vogt, M. (2021). Biogeochemical extremes and compound events in the ocean. *Nature* 600 (7889), 395–407. doi: 10.1038/s41586-021-03981-7

Harley, C. D., Anderson, K. M., Demes, K. W., Jorve, J. P., Kordas, R. L., Coyle, T. A., et al. (2012). Effects of climate change on global seaweed communities. *J. Phycol.* 48 (5), 1064–1078. doi: 10.1111/j.1529-8817.2012.01224.x

Hersbach, H., Bell, B., Berrisford, P., Hirahara, S., Horányi, A., Muñoz-Sabater, J., et al. (2020). The ERA5 global reanalysis. *Q. J. R. Meteorol. Soc.* 146 (730), 1999–2049. doi: 10.1002/qj.3803

Howard, E. M., Penn, J. L., Frenzel, H., Seibel, B. A., Bianchi, D., Renault, L., et al. (2020). Climate-driven aerobic habitat loss in the California Current System. *Sci. Adv.* 6 (20), eaay3188. doi: 10.1126/sciadv.aay3188

Hu, Z. M., and Guillemin, M. L. (2016). Coastal upwelling areas as safe havens during climate warming. *J. Biogeogr.* 43 (12), 2513–2514. doi: 10.1111/jbi.12887

Hutchings, L., van der Lingen, C. D., Shannon, L. J., Crawford, R. J. M., Verheye, H. M. S., Bartholomae, C. H., et al. (2009). The Benguela Current: An ecosystem of four components. *Prog. Oceanogr.* 83 (1-4), 15–32. doi: 10.1016/j.pocean.2009.07.046

Huyer, A. (1983). Coastal upwelling in the California Current system. *Prog. Oceanogr.* 12 (3), 259–284. doi: 10.1016/0079-6611(83)90010-1

Ikawa, H., Faloona, I., Kochendorfer, J., Paw U, K. T., and Oechel, W. C. (2013). Air–sea exchange of CO 2 at a Northern California coastal site along the California Current upwelling system. *Biogeosciences* 10 (7), .4419–.4432. doi: 10.5194/bg-10-4419-2013

Izquierdo, P., Taboada, F. G., González-Gil, R., Arrontes, J., and Rico, J. M. (2022). Alongshore upwelling modulates the intensity of marine heatwaves in a temperate coastal sea. *Sci. Total. Environ.* 835, 155478. doi: 10.1016/j.scitotenv.2022.155478

Jacox, M. G., and Edwards, C. A. (2011). Effects of stratification and shelf slope on nutrient supply in coastal upwelling regions. *J. Geophys. Res.: Oceans.* 116 (C3), C03019. doi: 10.1029/2010JC006547

Jacox, M. G., Hazen, E. L., Zaba, K. D., Rudnick, D. L., Edwards, C. A., Moore, A. M., et al. (2016). Impacts of the 2015–2016 El Niño on the California Current System: Early assessment and comparison to past events. *Geophys. Res. Lett.* 43 (13), 7072–7080. doi: 10.1002/2016GL069716

Johnstone, J. A., and Dawson, T. E. (2010). Climatic context and ecological implications of summer fog decline in the coast redwood region. *Proc. Natl. Acad. Sci.* 107 (10), 4533–4538. doi: 10.1073/pnas.0915062107

JPL Mur MEaSUREs Project (2015). *GHRSST level 4 MUR global foundation sea surface temperature analysis (v4. 1). PO* (Jet Propulsion Laboratory, Pasadena, CA, USA: NASA PO(DAAC)).

Kämpf, J., and Chapman, P. (2016). "The functioning of coastal upwelling systems," in *Upwelling systems of the world* (Cham: Springer), 31–65.

Large, W. G., and Danabasoglu, G. (2006). Attribution and impacts of upper-ocean biases in CCSM3. *J. Climate* 19 (11), 2325–2346. doi: 10.1175/JCLI3740.1

Li, G., Cheng, L., Zhu, J., Trenberth, K. E., Mann, M. E., and Abraham, J. P. (2020). Increasing ocean stratification over the past half-century. *Nat. Climate Change* 10 (12), 1116–1123. doi: 10.1038/s41558-020-00918-2

Lima, M., Canales, T. M., Wiff, R., and Montero, J. (2020). The interaction between stock dynamics, fishing and climate caused the collapse of the Jack Mackerel stock at Humboldt Current Ecosystem. *Front. Mar. Sci.* 7, 123. doi: 10.3389/fmars.2020.00123

Lourenço, C. R., Nicastro, K. R., McQuaid, C. D., Krug, L. A., and Zardi, G. I. (2020). Strong upwelling conditions drive differences in species abundance and community composition along the Atlantic coasts of Morocco and Western Sahara. *Mar. Biodiversity.* 50 (2), 1–18. doi: 10.1007/s12526-019-01032-z

Lourenço, C. R., Zardi, G. I., McQuaid, C. D., Serrão, E. A., Pearson, G. A., Jacinto, R., et al. (2016). Upwelling areas as climate change refugia for the distribution and genetic diversity of a marine macroalga. *J. Biogeogr.* 43 (8), 1595–1607. doi: 10.1111/jbi.12744

Mackas, D. L., Strub, P. T., Thomas, A. C., and Montecino, V. (2006). "Eastern ocean boundaries pan-regional overview," in *The sea, vol. 14: the global coastal ocean*. Eds. A. R. Robinson and R. Brink (. Cambridge, MA: Harvard Univ. Press), 21–60.

Mantua, N. J., and Hare, S. R. (2002). The Pacific decadal oscillation. *J. Oceanogr.* 58 (1), 35–44. doi: 10.1023/A:1015820616384

Marin, M., Bindoff, N. L., Feng, M., and Phillips, H. E. (2021). Slower long-term coastal warming drives dampened trends in coastal marine heatwave exposure. *J. Geophys. Res.: Oceans.* 126 (11), e2021JC017930. doi: 10.1029/2021JC017930

Mason, J. G., Alfaro-Shigueto, J., Mangel, J. C., Brodie, S., Bograd, S. J., Crowder, L. B., et al. (2019). Convergence of fishers' knowledge with a species distribution model in a Peruvian shark fishery. *Conserv. Sci. Pract.* 1 (4), e13. doi: 10.1111/csp2.13

Mason, E., Colas, F., Molemaker, J., Shchepetkin, A. F., Troupin, C., McWilliams, J. C., et al. (2011). Seasonal variability of the Canary Current: A numerical study. *J. Geophys. Res.: Oceans.* 116 (C6). doi: 10.1029/2010JC006665

Medellín-Mora, J., Escribano, R., and Schneider, W. (2016). Community response of zooplankton to oceanographic changes, (2002–2012) in the central/southern upwelling system of Chile. *Prog. Oceanogr.* 142, 17–29. doi: 10.1016/j.pocean.2016.01.005

Montecino, V., and Lange, C. B. (2009). The Humboldt Current System: Ecosystem components and processes, fisheries, and sediment studies. *Prog. Oceanogr.* 83 (1-4), 65–79. doi: 10.1016/j.pocean.2009.07.041

NOAA. (2023). Climate at a Glance: Global Time Series, Available at: https://www.ncei.noaa.gov/access/monitoring/climate-at-a-glance/global/time-series.

Pardo, P. C., Padín, X. A., Gilcoto, M., Farina-Busto, L., and Pérez, F. F. (2011). Evolution of upwelling systems coupled to the long-term variability in sea surface temperature and Ekman transport. *Climate Res.* 48 (2-3), 231–246. doi: 10.3354/cr00989

Pauly, D., and Christensen, V. (1995). Primary production required to sustain global fisheries. *Nature* 374 (6519), 255–257. doi: 10.1038/374255a0

Pérez-Matus, A., Carrasco, S. A., Gelcich, S., Fernandez, M., and Wieters, E. A. (2017). Exploring the effects of fishing pressure and upwelling intensity over subtidal

kelp forest communities in Central Chile. *Ecosphere* 8 (5), e01808. doi: 10.1002/ecs2.1808

Perry, A. L., Low, P. J., Ellis, J. R., and Reynolds, J. D. (2005). Climate change and distribution shifts in marine fishes. *science* 308 (5730), 1912–1915. doi: 10.1126/science.1111322

Poloczanska, E. S., Brown, C. J., Sydeman, W. J., Kiessling, W., Schoeman, D. S., Moore, P. J., et al. (2013). Global imprint of climate change on marine life. *Nat. Climate Change* 3 (10), 919–925. doi: 10.1038/nclimate1958

Poloczanska, E. S., Burrows, M. T., Brown, C. J., García Molinos, J., Halpern, B. S., Hoegh-Guldberg, O., et al. (2016). Responses of marine organisms to climate change across oceans. *Front. Mar. Sci.* 3, 62. doi: 10.3389/fmars.2016.00062

Ralston, S., Field, J. C., and Sakuma, K. M. (2015). Long-term variation in a central California pelagic forage assemblage. *J. Mar. Syst.* 146, 26–37. doi: 10.1016/j.jmarsys.2014.06.013

Rivadeneira, M. M., and Nielsen, S. N. (2022). Deep anthropogenic impacts on benthic marine diversity of the Humboldt Current Marine Ecosystem: Insights from a Quaternary fossil baseline. *Front. Mar. Sci.* 9. doi: 10.3389/fmars.2022.948580

Rykaczewski, R. R., Dunne, J. P., Sydeman, W. J., García-Reyes, M., Black, B. A., and Bograd, S. J. (2015). Poleward displacement of coastal upwelling-favorable winds in the ocean's eastern boundary currents through the 21st century. *Geophys. Res. Lett.* 42 (15), 6424–6431. doi: 10.1002/2015GL064694

Sanford, E., Sones, J. L., García-Reyes, M., Goddard, J. H., and Largier, J. L. (2019). Widespread shifts in the coastal biota of northern California during the 2014–2016 marine heatwaves. *Sci. Rep.* 9 (1), 1–14. doi: 10.1038/s41598-019-40784-3

Santora, J. A., Mantua, N. J., Schroeder, I. D., Field, J. C., Hazen, E. L., Bograd, S. J., et al. (2020). Habitat compression and ecosystem shifts as potential links between marine heatwave and record whale entanglements. *Nat. Commun.* 11 (1), 1–12. doi: 10.1038/s41467-019-14215-w

Santos, F., Gomez-Gesteira, M., Decastro, M., and Alvarez, I. (2012). Differences in coastal and oceanic SST trends due to the strengthening of coastal upwelling along the Benguela current system. *Continental. Shelf. Res.* 34, 79–86. doi: 10.1016/j.csr.2011.12.004

Schroeder, I. D., Santora, J. A., Mantua, N., Field, J. C., Wells, B. K., Hazen, E. L., et al. (2022). Habitat compression indices for monitoring ocean conditions and ecosystem impacts within coastal upwelling systems. *Ecol. Indic.* 144, 109520. doi: 10.1016/j.ecolind.2022.109520

Seabra, R., Varela, R., Santos, A. M., Gómez-Gesteira, M., Meneghesso, C., Wethey, D. S., et al. (2019). Reduced nearshore warming associated with eastern boundary upwelling systems. *Front. Mar. Sci.* 6, 104. doi: 10.3389/fmars.2019.00104

Shannon, L. V. (2001). "Benguela current," in *Encyclopedia of ocean sciences*. Eds. J. H. Steele, S. A. Thorpe and K. K. Turekian (San Diego, Calif: Academic Press), 255–267.

Smale, D. A., Wernberg, T., Oliver, E. C., Thomsen, M., Harvey, B. P., Straub, S. C., et al. (2019). Marine heatwaves threaten global biodiversity and the provision of ecosystem services. *Nat. Climate Change* 9 (4), 306–312. doi: 10.1038/s41558-019-0412-1

Soto, K. H., Trites, A. W., and Arias-Schreiber, M. (2004). The effects of prey availability on pup mortality and the timing of birth of South American sea lions (Otaria flavescens) in Peru. *J. Zool.* 264 (4), .419–.428. doi: 10.1017/S0952836904005965

Sydeman, W. J., García-Reyes, M., Schoeman, D. S., Rykaczewski, R. R., Thompson, S. A., Black, B. A., et al. (2014). Climate change and wind intensification in coastal upwelling ecosystems. *Science* 345 (6192), 77–80. doi: 10.1126/science.1251635

Tarazona, J., and Arntz, W. (2001). "The Peruvian coastal upwelling system," in *Coastal marine ecosystems of Latin America* (Berlin, Heidelberg: Springer), 229–244.

Thiel, M., Castilla, J. C., Fernández Bergia, M. E., and Navarrete, S. (2007). "The Humboldt current system of northern and central Chile," in *Oceanography and Marine Biology: An annual review* (Berlin, HeidelbergBoca Raton, USA: CRC Press), 45.

Thoral, F., Montie, S., Thomsen, M. S., Tait, L. W., Pinkerton, M. H., and Schiel, D. R. (2022). Unraveling seasonal trends in coastal marine heatwave metrics across global biogeographical realms. *Sci. Rep.* 12 (1), 1–13. doi: 10.1038/s41598-022-11908-z

Varela, R., Álvarez, I., Santos, F., DeCastro, M., and Gómez-Gesteira, M. (2015). Has upwelling strengthened along worldwide coasts over 1982-2010? *Sci. Rep.* 5 (1), 1–15. doi: 10.1038/srep10016

Varela, R., Lima, F. P., Seabra, R., Meneghesso, C., and Gómez-Gesteira, M. (2018). Coastal warming and wind-driven upwelling: a global analysis. *Sci. Total. Environ.* 639, 1501–1511. doi: 10.1016/j.scitotenv.2018.05.273

Varela, R., Rodríguez-Díaz, L., de Castro, M., and Gómez-Gesteira, M. (2021). Influence of Eastern Upwelling systems on marine heatwaves occurrence. *Global Planetary. Change* 196, 103379. doi: 10.1016/j.gloplacha.2020.103379

Wang, D., Gouhier, T. C., Menge, B. A., and Ganguly, A. R. (2015). Intensification and spatial homogenization of coastal upwelling under climate change. *Nature* 518 (7539), 390–394. doi: 10.1038/nature14235

Watermeyer, K. E., Shannon, L. J., Roux, J. P., and Griffiths, C. L. (2008). Changes in the trophic structure of the northern Benguela before and after the onset of industrial fishing. *Afr. J. Mar. Sci.* 30 (2), 383–403. doi: 10.2989/AJMS.2008.30.2.12.562

Yemane, D., Kirkman, S. P., Kathena, J., N'siangango, S. E., Axelsen, B. E., and Samaai, T. (2014). Assessing changes in the distribution and range size of demersal fish populations in the Benguela Current Large Marine Ecosystem. *Rev. Fish. Biol. Fisheries.* 24 (2), 463–483. doi: 10.1007/s11160-014-9357-7

Zuur, A. F., Ieno, E. N., Walker, N. J., Saveliev, A. A., and Smith, G. M. (2009). *Mixed effects models and extensions in ecology with R* (New York: springe), 574.

frontiers | Frontiers in Marine Science

TYPE Original Research
PUBLISHED 23 October 2023
DOI 10.3389/fmars.2023.1244643

OPEN ACCESS

EDITED BY
Francisco Machín,
University of Las Palmas de Gran Canaria, Spain

REVIEWED BY
Samiran Mandal,
Indian Institute of Technology Delhi, India
Sadegh Yari,
Niedersächsische Landesbetrieb für Wasserwirtschaft, Küsten- und Naturschutz (NLWKN), Germany

*CORRESPONDENCE
Māris Skudra
maris.skudra@lhei.lv

RECEIVED 22 June 2023
ACCEPTED 05 October 2023
PUBLISHED 23 October 2023

CITATION
Skudra M, Väli G, Ikauniece A and Papirtis M (2023) Upwelling characteristics in the Gulf of Riga (Baltic Sea): multiple data source approach.
Front. Mar. Sci. 10:1244643.
doi: 10.3389/fmars.2023.1244643

Upwelling characteristics in the Gulf of Riga (Baltic Sea): multiple data source approach

Māris Skudra[1]*, Germo Väli[2], Anda Ikauniece[1] and Miks Papirtis[1]

[1]Department of Marine Monitoring, Latvian Institute of Aquatic Ecology, Riga, Latvia, [2]Department of Marine Systems, Tallinn University of Technology, Tallinn, Estonia

Upwellings are characteristic for the Baltic Sea region including the Gulf of Riga, although the current knowledge is rather limited with only few research conducted in the Gulf itself. Upwelling events in the Gulf of Riga in 2010–2022 were studied by analyzing sea surface temperature time series from coastal stations and SmartBuoy, together with satellite data, model data, and CTD (conductivity, temperature, and depth) surveys. The starting/end point, active, and relaxation phases were defined in each event to describe the characteristics and length of each phase. Upwellings were less frequent (41%) on the eastern coast but lasted longer and had higher temperature drops than on the western coast. On the western coast, a variety of upwelling characteristics between stations only 30 km apart were found with the likely reason being the different orientations of the coastline with respect to the wind direction. Satellite data revealed that on the western coast of the Gulf, rather small upwelling events form along specific sections of the coastline. Of all upwelling events, 30% were characterized by an immediate temperature increase after reaching the minimum temperature, and we suggest that this is related to a distinct change in wind direction. The results from the simulations indicated smaller lateral density and salinity gradients in the sea surface than in larger Baltic Sea gulfs. It signals that conditions for the occurrence of baroclinic instabilities are rather small; thus, we suggest that weaker gradients could explain quite fast upwelling relaxation in the basin if compared to, e.g., the Gulf of Finland.

KEYWORDS

upwelling, SST, Gulf of Riga, SmartBuoy, GETM, Baltic Sea, mesoscale

1 Introduction

Upwelling is a globally vital process, which is governed by Ekman's theory that describes the rotation of the flow direction over horizontal layers with depth and explains the relation between offshore currents initiated by alongshore winds with perpendicular surface water motion (Ekman, 1905). Coastal wind-driven upwelling mainly occurs when the wind is blowing alongshore with the coast on its left/right side in the Northern/Southern Hemisphere (e.g., Lehmann and Myrberg, 2008; Lehmann et al., 2012). Considering that winds in the Baltic Sea (BS) region blow from all directions and, at some point, parallel to the coast, upwelling can occur everywhere.

The Gulf of Riga (GoR) is a semi-enclosed basin located in the eastern part of the BS. The GoR covers an area of approximately 17,913 km^2 with a volume of 405 km^3 (Leppäranta and Myrberg, 2009). The average depth of the GoR is 26 m, which is approximately two times smaller than that of the Baltic Sea. It is connected to the BS *via* two shallow straits—Irbe Strait in the west (with a sill depth of 25 m and cross-section of 0.4 km^2) and Suur Strait in the north (with a sill depth of 5 m and cross-section of 0.04 km^2). The majority (70%–80%) of water exchange occurs *via* the Irbe Strait (Petrov, 1979).

The catchment area of the GoR is 134,000 km^2. Five major rivers (Daugava, Gauja, Lielupe, Salaca, and Pärnu) bring freshwater to the GoR, with the majority of the freshwater (86%) discharging in the southern part of the gulf (Berzinsh, 1995), mostly due to the contribution of Daugava river, which gives approximately 70% of the overall river input in the GoR (Yurkovskis et al., 1993). Due to the excessive river runoff to the gulf (henceforth GoR or the gulf) and limited water exchange with the open BS, a salinity gradient can be observed from the Irbe Strait to the south and southeast of the GoR.

As the GoR is often perceived as an estuary-type water basin, the common understanding of the gulf is that the outflow/inflow occurs through surface/bottom layers *via* the Irbe Strait with cyclonic (anti-clockwise) mean surface circulation within the gulf (e.g., Elken et al., 2003; Leppäranta and Myrberg, 2009). Nevertheless, research from historical surveys (e.g., Berzinsh, 1980; Lips et al., 1995) and model analysis (e.g., Soosaar et al., 2014; Lips et al., 2016a; Lips et al., 2016b) have revealed that variations exist to this "common understanding" showing that a cyclonic and anticyclonic circulation pattern can be persistent in the GoR depending on the seasonality and forcing factors.

The water temperature in the GoR has a seasonal pattern. Cooling of the whole water column occurs during October/November–February. March/April marks the start of the water column warming. The temperature reaches its maximum in August, which is again followed by a steady cooling during September–October. Seasonal changes in thermal stratification are consistent with the annual cycle of air–sea heat exchange (Raudsepp, 2001). Further details on stratification in the GoR can be obtained in the research by, e.g., Stipa et al. (1999) and Skudra and Lips (2017).

In the summer, upwellings are usually associated with lower temperatures as well as nutrient abundance (necessary for biological productivity) at surface layers, which is a direct result of vertical mixing where bottom layer waters are shifted to the surface layers (e.g., Lehmann et al., 2012; Omstedt et al., 2014; Krek et al., 2021).

Bychkova et al. (1988) identified 22 typical areas of upwelling in the BS based on corresponding general weather conditions, out of which two were identified in the GoR, namely, the eastern and western coasts of the GoR. Previous investigations regarding upwelling in the GoR have been considered mainly in the context of the whole BS region based on satellite data (e.g., Uiboupin and Laanemets, 2015; Dabuleviciene et al., 2018; Zhang et al., 2022), model data (e.g., Myrberg and Andrejev, 2003; Wu et al., 2019), or a combination of both (e.g., Lehmann et al., 2012; Gurova et al., 2013; Kowalewska-Kalkowska and Kowalewski, 2019). In addition to that, more detailed investigations have been performed concentrating on specific gulfs (e.g., Kikas and Lips, 2016—the Gulf of Finland), parts, or regions (Bednorz et al., 2018 and Bednorz et al., 2019—South-Eastern Baltic Sea) of the Baltic Sea and explore various aspects of upwelling-related topics, e.g., atmospheric forcing (Bednorz et al., 2021), submesoscale structures (Väli et al., 2017), surface transport (Delpeche-Ellmann et al., 2017 and Delpeche-Ellmann and Soomere, 2018), excess of phosphorus in surface layer (e.g., Laanemets et al., 2011; Väli et al., 2011), chlorophyll *a* variability (Dabuleviciene et al., 2020), and heat waves (Suursaar, 2020). Previous studies of the GoR region have been general and descriptive (e.g., Bychkova et al., 1988; Lehmann et al., 2012; Bednorz et al., 2021), focused on identifying the main upwelling areas and giving frequency estimates.

This research aims to provide more detail and focus specifically on the GoR upwelling events, their characteristics, and dynamics, as within the BS region many papers about upwellings mostly consider other regions (e.g., Gulf of Finland, Gdansk Bay, and Baltic Proper). The main goal of the present study is to detect upwelling events in the GoR in 2010–2022 and describe their characteristics (e.g., length and frequency). To achieve this, multiple *in-situ* data acquisition methods —historical monitoring and coastal measurement data, SmartBuoy data, satellite data, model data, and *in-situ* measurement campaigns —are combined. Motivation also included the targeted approach to capture coastal upwelling events with *in-situ* CTD (conductivity, temperature, and depth) measurements (biological and chemical samples were also taken), and two events in current research were described more in detail as case studies.

Such research furthers the current understanding of upwelling events in the GoR. It reveals their types, phases and lengths, and typical locations within the basin, which subsequently sets the basis to explore how upwellings influence regional/local biogeochemical processes. This study concentrates on *in-situ* data, which makes it the first such analysis in the GoR and will be relevant for other, rather shallow, semi-enclosed water basins.

2 Material and methods

We applied a wide range of data sources, and each one is described in detail in this section. Surface water temperature measurements from four coastal monitoring stations (Salacgriva, Skulte, Mersrags, and Roja; see Figure 1) collected in May–September 2010–2022 were analyzed using a freely available online database by the Institute of Food Safety, Animal Health and Environment. Data from Salacgriva were used only for quantitative analysis due to the large variability. All data had a temporal resolution of 1 h, and the dataset was smoothed (5 h moving average) before further analysis. An event qualified as upwelling if the following conditions were observed: a temperature drop of ≥5.0°C. It was possible to empirically define the start/end, relaxation phase (RP), and/or the active upwelling phase (AUP) of each event. The start of the upwelling event was defined as a point (with the highest temperature) from which temperature decreased consecutively by ≥0.05°C, reaching a temperature drop of at least 5.0°C. The point where consecutive temperature decrease criteria were not met was defined as the start of the AUP. Consequently, the AUP endpoint

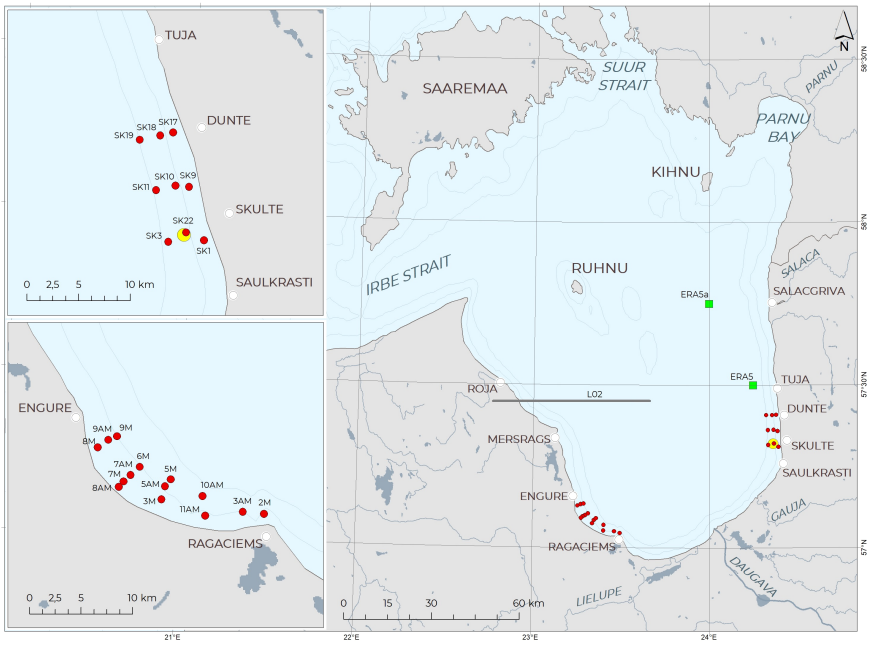

FIGURE 1
Map of the Gulf of Riga with red dots representing the performed CTD (conductivity, temperature, and depth) casts on July 13 (eastern coast) and August 17 (western coast), 2021. Yellow circle shows the location of SmartBuoy. Coastal temperature measurements were available from Roja, Mersrags (wind data as well), Skulte (wind data as well), and Salacgriva. ERA5 and ERA5a denote the location of wind data. Gray line marked with L02 represents the model transect presented in Figure 13.

corresponds to the start of the RP, which was defined as the point from which the temperature increased consecutively by ≥0.02°C. The end of the RP corresponds to the end of the upwelling event itself and was defined as a point with the maximum temperature value during the increase (please, refer to Figure 2 for a more schematic view regarding the defined upwelling phases). Due to the high temperature variability in some events (even with data smoothing), the parameterization criteria had to be adjusted—every event where the overall temperature dropped by at least 5.0°C during the event was used for quantitative analysis. If during the temperature drop there was an alternate, short (≤5 h) temperature increase, the start of the AUP was defined manually. Likewise, if during the RP there was an alternate, short temperature decrease, the end of the event was also defined manually. In very rare cases, we neglected the temperature variability if it was obvious from the overall time series where exactly the specific phase starts/ends. As we further analyzed purely the length of defined phases and fixed the temperature values at phase start/end points, temperature variability itself had no direct impact on our results (which would be the case if we analyzed the temperature within the respective phase) with the only exception of calculated

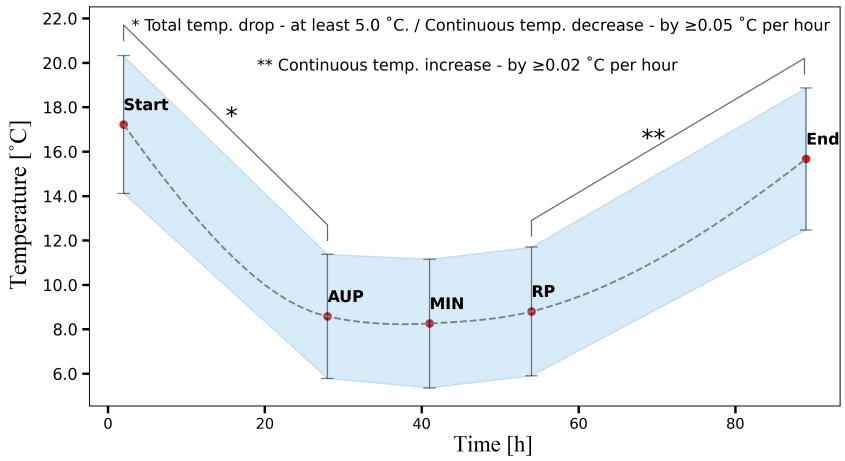

FIGURE 2
Mean upwelling event features derived from detected and parameterized upwelling events in 2010–2022.

average temperature in AUP. Those events where temperature variability did not allow to define the respective phase start/end points were excluded from further data analysis.

To sum up, each upwelling event was characterized by the length (days/hours) of the whole event, the RP, the AUP, and how rapidly the upwelling evolved together with the average temperature in the AUP (as simple mean), and the maximum temperature drop during the event.

Targeted CTD measurement surveys using an SBE 19plus V2 SeaCAT CTD probe (Sea-Bird Electronics, Bellevue, WA, USA) were performed on the southern (S), southeastern (SE), and southwestern (SW) coasts of the GoR in July and August of 2021 and 2022 inside and outside of the area affected by the upwelling. After data processing, all CTD profiles were stored with a vertical resolution of 0.5 m. In addition, during the surveys, water samples were taken with a horizontal water sampler (Van Dorn) from the surface and bottom layers inside and outside of upwelling areas for nutrient analysis. Phytoplankton (5-m and 10-m integral tubes; Van Dorn water sampler) and zooplankton (WP-2 net; mesh size 100 μm) samples from surface and bottom layers were also taken in some of these locations.

The historical sea surface temperature (CTD) data collected by the Latvian Institute of Aquatic Ecology (2010–2022) and the Institute of Food Safety, Animal Health and Environment (2010–2012) during the summer monitoring cruises from the long-term CTD dataset (Skudra and Lips, 2017) were also analyzed for upwelling events.

SmartBuoy data were obtained in 2021–2022 from the SmartBuoy system deployed on the eastern coast of the GoR near the Skulte port, approx. 2.5 km offshore with coordinates of 57.31998 N latitude and 24.36355 E longitude (see Figure 1). The dataset consisted of surface water temperature measurements (temperature sensor mounted on Wave and Tide Sensor 5218, Aanderaa, Norway) primarily used in this research during May–September. All data from SmartBuoy had a temporal resolution of 1 h, and the temperature dataset was smoothed (5 h moving average) before further analysis similarly as with coastal measurements.

Satellite data (The BACC II Author Team, 2015) were analyzed during May–September using Landsat 7 (2010–2012) and Landsat 8 (2013–2022) with resolutions of 60 m and 100 m per pixel, respectively, and Sentinel-3 Level-2 data (2017–2022) with a resolution of 1 km per pixel data. To manage data volume, only data with a cloud cover of less than 40% over the GoR area were used. Landsat 7 and Landsat 8 data were extracted from https://earthexplorer.usgs.gov/; for Sentinel-3, data were extracted from archive.eumetsat.int, and subsequent conversion from Kelvin to degree Celsius for sea surface temperature (SST) was performed using ESA SNAP API for Python. The satellite data were further analyzed in Quantum GIS to visualize and select the datasets where the upwelling signal was evident with emphasis on those events, which were confirmed from *in-situ* measurements in order to analyze the spatial distribution.

The General Estuarine Transport Model (GETM; Burchard and Bolding, 2002) was applied to simulate the physical conditions in the GoR from 2010 until 2021 in order to find out how well the model is capable of simulating the coastal upwelling events compared to *in-situ* and satellite data. The horizontal resolution of the model grid is 0.5 nautical miles (approximately 926 m) with 60 adaptive layers (e.g., Gräwe et al., 2015; Klingbeil et al., 2018) in the vertical direction. Initial conditions for temperature and salinity for April 1, 2010, were taken from Copernicus Marine Service re-analysis for the period 1989–2015, with meteorology input from atmospheric re-analysis dataset ERA5 (Hersbach et al., 2020) with hourly resolution in time and 0.28 × 0.28 degrees (31 km) in space. Climatological T/S values in Kattegat and observed sea-level elevation from Gothenburg station were used for the open boundary condition in the Kattegat region. More information about the model setup can be found in Liblik et al. (2020) and Liblik et al. (2022) and Zhurbas et al. (2018). The output parameters included snapshots of surface parameters in the GoR along with the daily mean 3D thermohaline and current fields.

Wind data (direction and speed) were collected from Mersrags and Skulte coastal stations (see Figure 1) as background data from a freely available online database hosted by the Latvian Institute of Food Safety, Animal Health and Environment. In addition, wind series from selected locations (see Figure 1, green rectangles) from ERA5 were used for additional analysis of wind conditions. Sea surface temperature and vertical temperature distribution was analyzed using freely available software "Ocean Data View" (Schlitzer 2018).

3 Results

3.1 Detected upwelling events

Quantitative results of detected upwelling events from *in-situ* data and satellite data are presented in Table 1. A total of 116 separate upwelling events were determined from the time series of water temperature in four coastal monitoring stations—Mersrags, Roja, Skulte, and Salacgriva. In five cases, an upwelling signal was observed from historical monitoring surveys performed in August. SmartBuoy (Skulte) measurements performed in 2021 and 2022 revealed three and two upwelling events, respectively. As for the satellite data, a total number of 562 satellite images were processed with an upwelling signal detected in 28 (Sentinel-3) and 10 (Landsat) cases, which yielded a total number of 164 upwelling events detected by all methods. As there were cases when one individual upwelling event was detected by multiple data acquisition methods, it was afterward determined that the total number of separate individual upwelling events was 131.

Regarding coastal measurements in each monitoring station, 52, 37, 30, and 24 upwelling events were observed in Mersrags, Roja, Skulte, and Salacgriva, respectively, which represent a frequency of 4.0, 2.8, 2.3, and 1.8 events/per year on average, respectively. In 20 cases, upwelling events overlapped between Mersrags and Roja; in seven cases, between Skulte and Salacgriva, there was a total of 116 (from 143) separate events. It has to be noted that measurements were not performed in 2010 (Roja), 2013 (Skulte, May), and 2014–2016 (Skulte).

Between the years 2010 to 2022, upwelling events varied between 5 and 20 events/per year (Table 2). There was an average of 9 events/per year with 59% of all events detected on the western

10.3389/fmars.2023.1244643

TABLE 1 Detected upwelling events in May–September 2010–2022 in the Gulf of Riga.

Year	Coastal measurements (4 monitoring stations)	Historical monitoring data (CTD)	SmartBuoy measurements	Satellite data		Total
				Sentinel-3	Landsat 7 and 8	
2010	8*	0	–	–	0	8
2011	20	0	–	–	2	22
2012	10	1	–	–	1	12
2013	8*	1	–	–	0	9
2014	9*	0	–	–	1	10
2015	10*	0	–	–	2	12
2016	6*	0	–	–	0	6
2017	5	1	–	3	0	9
2018	11	1	–	8	1	21
2019	7	0	–	6	3	16
2020	5	0	–	2	0	7
2021	11	1	3	7	0	22
2022	6	0	2	2	–	10
Total	116	5	5	28	10	164

CTD, conductivity, temperature, and depth.
*No measurements: 2010 (Roja), 2013 (Skulte, May), and 2014–2016 (Skulte).

(W) coast as opposed to the eastern (E) coast. On a monthly basis, the total count of upwelling events was roughly two times scarcer in May and September than in June, July, and August. No upwelling events were detected in 6 out of the 13 years for May and in 4 out of the 13 years for September. The total number of upwelling events during June–August was distributed evenly, and only in June 2017, July 2019, and August 2013 was no upwelling event detected.

3.2 Characteristics of upwelling events (from coastal data)

From defined main points or phases in upwelling events in 2010–2022 (May–September), we derived that the mean length of evolvement (from Start to AUP), active upwelling phase (from AUP to RP), relaxation phase (from RP to End), and total upwelling length for the GoR was 26 h, 26 h, 36 h, and 88 h, respectively (Figure 2). The mean temperature at the start of an upwelling was 17.2°C, the mean minimum value during the upwellings was 8.2°C, and the mean maximum temperature drop was 9.0°C. At the end of the upwelling events, the mean temperature was 15.7°C. On a monthly basis, the length of the whole event and the RP length gradually increased during May–September by between 74–101 h and 17–48 h, respectively. The length of the AUP and the length of the evolvement were variable between the months ranging between 20 h and 33 h for the AUP and 21 h and 31 h for the time it took for the upwelling to form/reach the start of the AUP.

The characteristics of upwelling events in the western (Mersrags and Roja) and eastern (Skulte) coasts had both similarities and differences (only upwelling events from June to August were used). The mean AUP and evolvement time of the upwellings were similar between these three locations, with AUP ranging between 21 h and 24 h and upwelling evolved between 24 h and 30 h in all locations. The mean RP in Mersrags (28 h) was shorter if compared to that in Roja and Skulte where the mean RP was 41 h and 44 h, respectively (Figure 3A). The whole upwelling event length was slightly longer in Skulte, the eastern coast of the GoR, where the mean value was 98 h as opposed to the western coast where it was 81 h and 88 h for Mersrags and Roja, respectively. Together with the longer upwellings on the eastern coast, the average temperature in the AUP was slightly lower (approx. 0.3°C) than on the western coast. Moreover, the mean maximum temperature drop during the upwelling was also higher on the eastern coast (10.2°C) than on the western coast—8.9°C (Mersrags) and 8.5°C (Roja). Thus, there is a tendency for the eastern coast (Figure 3B, red slope) maximum temperature drop during the upwelling events to increase with increasing total length of the event itself, which can be observed in Mersrags (blue slope) and the western coast as well but is not evident in Roja (yellow slope).

The nature, structure, and type of detected upwelling events varied greatly between different months and years. The longest event was detected in Mersrags in July 2020 (Figure 4, black line). It lasted for 328 h or 13 days and 16 h with temperatures below 12.0°C evident for more than 10 days. Another long event, which was also characterized by a rapid development and relaxation phase (Figure 4, green line), was detected in Skulte in July 2021, and it lasted for 7 days (described more in detail in Section 3.3.1). Nevertheless, most of the detected events were considerably

TABLE 2 Distribution of upwelling events by year, month, and location from coastal measurements.

Year	May			June			July			August			September			Total		
	Total	W coast	E coast	Total	W coast	E coast	Total	W coast	E coast	Total	W coast	E coast	Total	W coast	E coast	Total	W coast	E coast
2010	0	0	0	2	1	1	1	1	0	2	0	2	3	1	2	8	3	5
2011	3	2	1	7	5	2	7	6	1	1	0	1	2	2	0	20	15	5
2012	2	1	1	2	2	0	1	0	1	4	2	2	1	1	0	10	6	4
2013	3	3	0	2	2	0	1	0	1	0	0	0	2	1	1	8	6	2
2014	0	0	0	2	0	2	5	4	1	2	2	0	0	0	0	9	6	3
2015	0	0	0	2	2	0	4	2	2	2	1	1	2	1	1	10	6	4
2016	1	1	0	1	1	0	2	1	1	2	2	0	0	0	0	6	5	1
2017	1	0	1	0	0	0	1	1	0	2	1	1	1	0	1	5	2	3
2018	3	2	1	2	1	1	2	1	1	3	2	1	1	1	0	11	7	4
2019	1	0	1	3	0	3	0	0	0	1	1	0	2	2	0	7	3	4
2020	0	0	0	3	2	1	1	1	0	1	1	0	0	0	0	5	4	1
2021	0	0	0	1	0	1	4	1	3	4	2	2	2	0	2	11	3	8
2022	0	0	0	1	1	0	2	0	2	3	1	2	0	0	0	6	2	4
Total	**14**	9	5	**28**	17	11	**31**	18	13	**27**	15	12	**16**	9	7	**116**	68	48

10.3389/fmars.2023.1244643

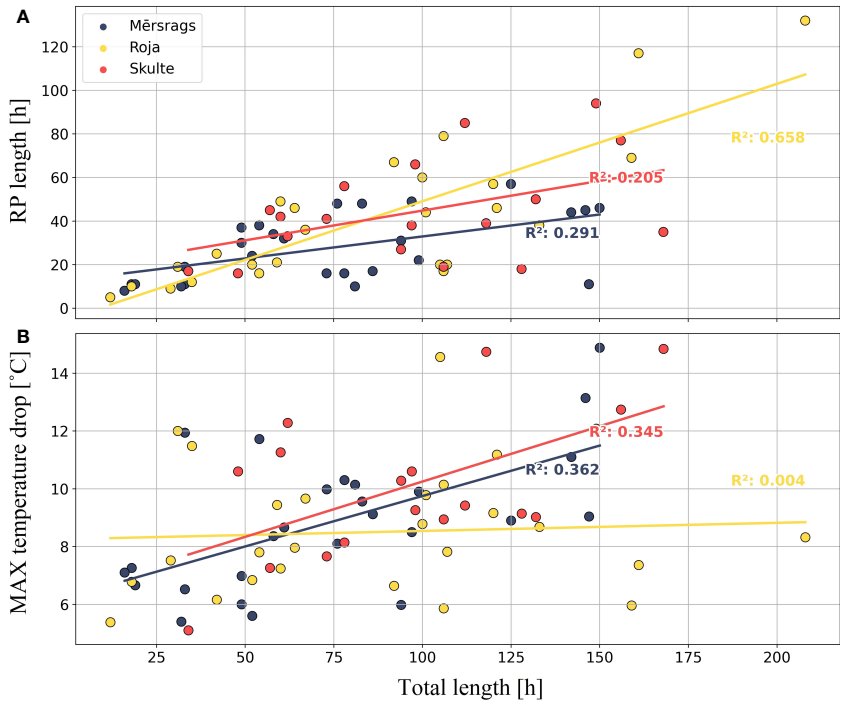

FIGURE 3
Total length and relaxation phase length **(A)** and maximum temperature drop and total length **(B)** of detected upwelling events in June–August 2010–2022 in western (Mersrags and Roja) and eastern (Skulte) coasts.

shorter but with significant temperature drops at the same time. In July 2022 (Skulte) and June 2018 (Roja), the temperatures during an upwelling dropped by more than 10.0°C, but the events lasted for only 62 h and 31 h, respectively (Figure 4, blue and brown lines). The upwelling event in Roja (June 2018) evolved and reached the minimum temperature within 19 h, which was succeeded by an immediate temperature increase or relaxation phase; thus, no AUP was defined in this case. A similar type of upwelling event was also observed in Mersrags in September 2019 (Figure 4, violet line). Altogether, 29 out of 93 events were without a defined AUP. The majority (90%) of the upwelling events evolved within 40 h, but some events were also characterized by rather long evolvement with consequent rapid RP (Figure 4, orange and red lines). During an upwelling event in July 2018 (Skulte), temperature gradually decreased from roughly 16.0°C to 7.0°C within 65 h, whereas later, temperature increased from roughly 7.0°C to 14.0°C within 19 h.

3.3 Upwelling case studies

3.3.1 July 2021 (east coast)

The upwelling event along the eastern coast on July 13–19 was described using available satellite data, coastal and SmartBuoy SST

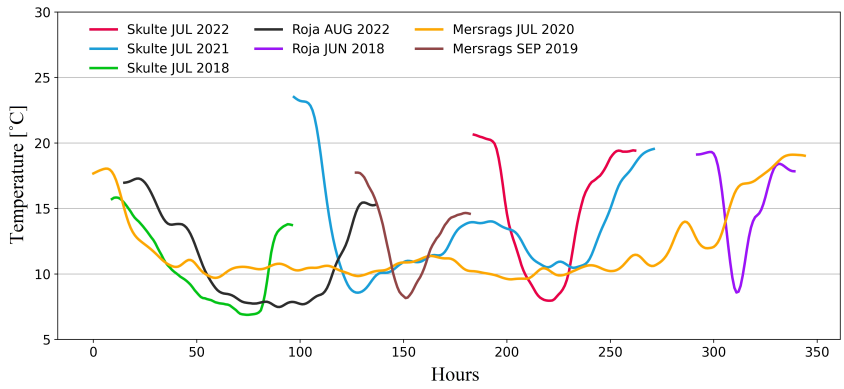

FIGURE 4
Different types and characteristics of upwelling events from coastal measurements. Lines are scattered along x-axis for pure visualization purposes.

time series, measurements from CTD survey, model data, and wind data from Skulte and ERA5 data source, whereas the upwelling event on July 22 was described using available satellite data, model data, and wind data from Skulte and ERA5a.

Available satellite data from Sentinel-3 (July 16 and 17, 2021) revealed the appearance of an upwelling event along the E coast of the GoR. Despite the fact that the two snapshots had roughly 24 h between them, a notable change in SST can be observed (Figures 5A, B).

On July 16, a lower SST signal can be seen in a narrow band between Saulkrasti and Tuja (see Figure 1), approximately 30 km along the coast. Despite the fact that the SST in this area was 6°C–7°C lower than in the open gulf (23.0°C–24.0°C), SST remained relatively high at between 17.0°C and 18.0°C, comprising an area of approximately 13 km^2 (approx. 11 km in length and 1.5 km offshore at widest place). On the contrary, July 17 was characterized by a significantly larger area with lower SST evident along the whole E coast of Latvia The area with SST below 18.0°C reached approximately 269 km^2 (approx. 70 km in length and 6 km offshore at the widest place), whereas the area with SST below 13.0°C, which could be regarded as the center of the upwelling event, reached approximately 22 km^2 (approx. 18 km in length and 2 km offshore at the widest place).

On July 22, another signal of an upwelling event was visible from the satellite data on the east coast (Figure 5C), but this time, it was not along the whole E coast. The signal was seen in the vicinity of Salacgriva and the N part of the GoR, in an area offshore of the Estonian mainland and around Kihnu Island. The area most affected by reduced SST (<16.0°C) consisted of roughly 275 km^2 near Salacgriva with temperatures as low as 14.0°C still detected 13 km offshore. In the N part, SST of roughly 13.0°C was still observed 7.5 km to the south of Kihnu Island. The total area affected by the upwelling (<16.0°C) in the N part of the GoR was roughly 655 km^2. Wind from ERA5a location (see location in Figure 1) showed N, NW winds with a speed of approximately 8 m/s on July 22.

From the SST time series of the coastal monitoring station in Skulte Port and SmartBuoy near Skulte Port, it can be seen that the first upwelling event took place between July 13 and 19 (Figure 6). On the evening of July 12, a sharp decrease in temperature was observed simultaneously in the SmartBuoy and coastal SST measurements. Within 21 h, SST in the coastal station dropped from 23.3°C to a minimum value of 8.5°C on midday of July 13. Further, the temperature was mostly below 12.0°C (except for July 15–16 when the temperature was between 12.0°C and 14.0°C), and finally, on the morning of July 18, it started to constantly increase, marking the start of the relaxation phase, which ended within 35 h when SST rose back to 19.6°C. Wind data from Skulte and ERA5 on July 12–19 showed upwelling favorable winds from N, NE, NW, and E (not shown here) with wind speeds of 1–4 m/s in Skulte and 1–6 m/s from ERA5, respectively.

The time series of SST from SmartBuoy (2.5 km offshore) revealed different dynamics in comparison to the coastal monitoring station. Despite similarities of SST decrease starting from July 12, a strong temperature variability was observed between July 13 and 15 with at least four rather distinct cycles where temperature alternately decreased and increased by approximately 5.0°C–7.0°C (Figure 6, dashed blue line). Only starting from July 16 was temperature variability less pronounced and followed the temperature curve from the coastal monitoring station with temperature at the end of the relaxation phase/end of upwelling being roughly 2.0°C higher than in the coastal monitoring station. By applying a low-pass filter, the variability of the SST from SmartBuoy considerably decreased (solid blue line).

Nevertheless, the upwelling event on July 22 was not evident in the SST time series of coastal measurements from Skulte or Skulte SmartBuoy, and temperature in the surface layer remained at approximately 21.0°C in this region. It was possible to quantitatively detect this event from the Salacgriva coastal monitoring station, which showed a minimum temperature (8.3°C) at midnight between July 21 and 22.

A targeted CTD measurement survey performed on July 13 at nine stations near Skulte port (area from port entrance to 10 km north) showed that a strong upwelling signal (8.8°C) was evident in the station closest to the port (Figure 7). However, there was an increasing temperature gradient not only offshore but along the coast to the north as well (see sections in Figures 8 and 1 for station labels). Roughly 5 km to the north along the coast the SST was 15.2°C, and another 5 km further the temperature was already 18.5°C, although it has to be mentioned that those stations were taken approximately 100–200 m further away from the coastline. This north–south SST gradient was also visible 2 km and 4 km offshore as well where SST in the northern part (in the context of the

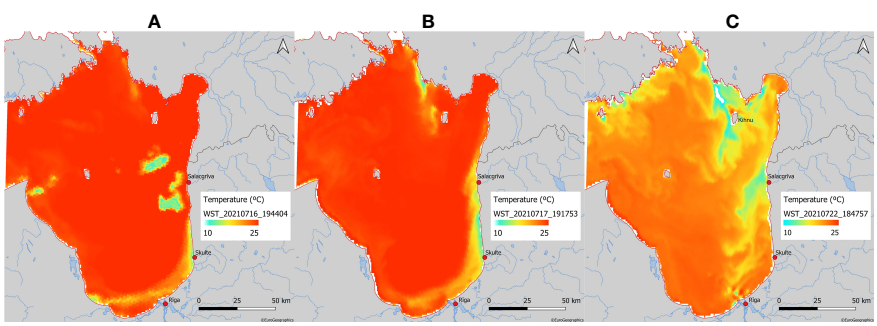

FIGURE 5
Sea surface temperature from Sentinel-3 satellite data on July 16 **(A)**, 17 **(B)**, and 22 **(C)**, 2021.

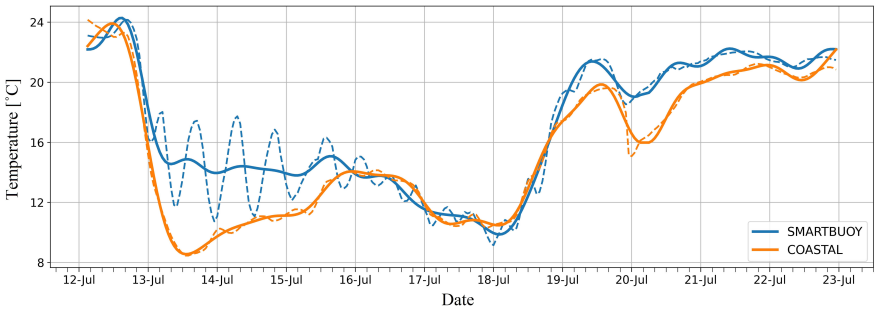

FIGURE 6
Time series of sea surface temperature from SmartBuoy and coastal monitoring station in Skulte on July 12–22, 2021. Dashed lines represent the original data, and solid lines are the fast Fourier transform low-pass filtered series with cutoff period of 16.6 h.

sampling area) was 21.6°C and 24.2°C, respectively, but in the southern part—18.8°C and 21.7°C. The closest station to the Skulte SmartBuoy measured SST as 17.8°C, whereas the closest reading to this measurement from the SmartBuoy registered 17.0°C, and it coincided with the temperature increase in one of the SmartBuoy "variability cycles" mentioned before. In addition, the coastal monitoring station registered an SST of 8.5°C as the nearest value to the recorded CTD profile (SST of 8.8°C) just outside the port entrance.

The simulated SST maps (Figure 9) coincide with the satellite observations reasonably well. The first upwelling event on July 13–19 is not as strong as in the observations; hence, the narrow strip of cold water along the eastern coast is visible only by July 17. As the upwelling develops, the simulated SST continues to decrease, and by July 18, the event is clearly visible in the spatial maps. Interestingly, the event is small, and only less than 3–4 km along the coast is affected by the model output. The second upwelling event along the eastern coast occurred only a couple of days later (July 22) with the rise of northerly winds. Compared to the first event, the area affected during the second event was much larger, and the cold-water batch (temperatures less than 16°C) exceeded more than 10 km to the west and more than 30 km in the south–north direction along the Latvian coast. In addition, the second batch of cold water was located in the west of Pärnu Bay with similar dimensions as the southern batch. Slightly decreased coastal temperatures are seen also along the Saaremaa coast (the northern boundary for the GoR), although the decrease is much smaller compared to the eastern and northeastern coasts.

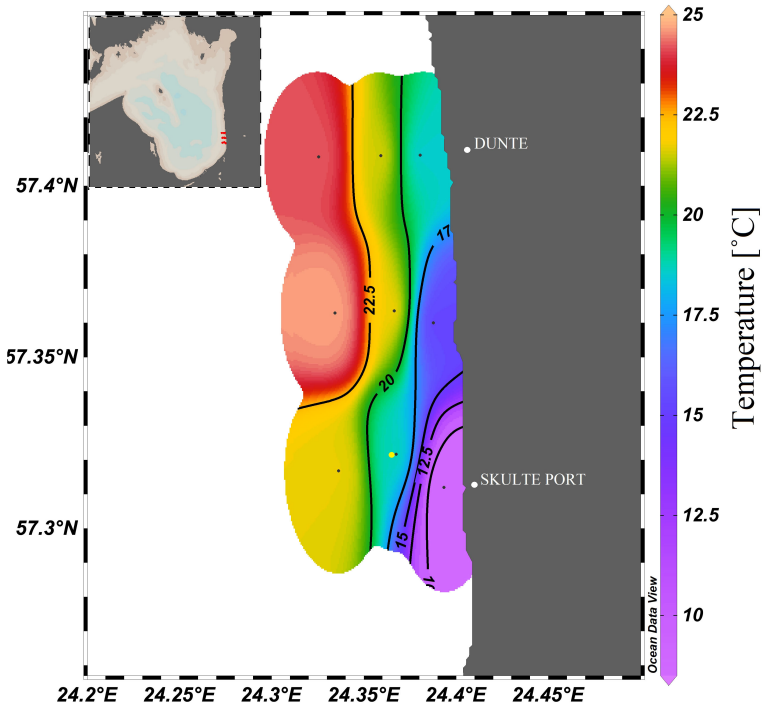

FIGURE 7
Sea surface temperature from CTD (conductivity, temperature, and depth) during the upwelling on E coast of the Gulf of Riga (GoR) on July 13, 2021. Yellow dot represents the location of Skulte SmartBuoy.

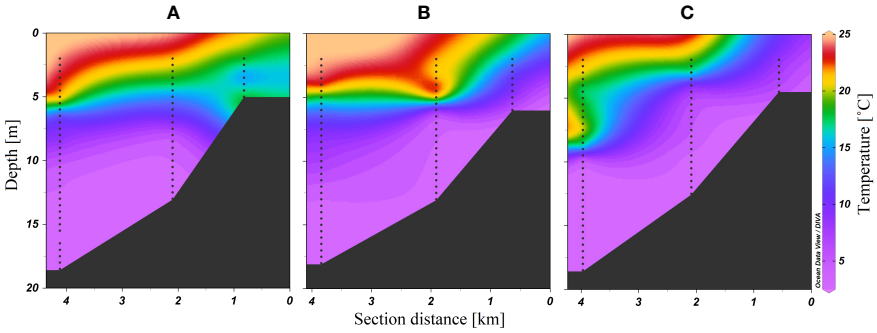

FIGURE 8
Vertical temperature distribution from CTD (conductivity, temperature, and depth) transects during the upwelling on E coast of the Gulf of Riga (GoR) on July 13, 2021. Station SK17-SK19 **(A)**, SK9-SK11 **(B)**, and SK1-SK3 **(C)**. See station labels in Figure 1.

3.3.2 August 2021 (SW coast)

This upwelling event was characterized using available measurements from the CTD survey, available satellite data, and model data.

As opposed to July 2021, on August 17, 2021, a rather local upwelling was observed along the SW coast of the GoR spanning for approx. 25 km between Ragaciems and Engure (see Figure 1) with observed SST below 10.0°C. The upwelling-affected area reached approximately 1.5–2.0 km offshore (Figure 10) with higher surface salinity (by at least 0.1 g/kg) as well.

Satellite data from this specific, local event in August were not available, but collected historical satellite maps revealed that such local upwelling events have occurred in this particular place several times before (Figure 11). In the given examples, the area affected by upwelling (defined as the area with temperature <13.0°C) ranged from approximately 24.0 to 72.0 km^2 with offshore distance ranging from 2.5 to 5.0 km at its widest point.

The simulated SST maps during different phases of upwelling along the SW part of the GoR are shown in Figure 12. On August 17 (starting phase), cold water emerged only along a narrow coastal zone on the Latvian coast, and somewhat larger upwelling is visible at the northern boundary (southern part of Saaremaa). By August 19 (active phase), the cold water had surfaced along the whole western coastline of the GoR, and also along the northern boundary, the temperatures had reduced further, and the area affected by the upwelling increased. Relaxation of the upwelling is ongoing by August 21 with some filaments of cold water extending toward the center of the basin. Interestingly, both the relaxation and duration of the upwelling were much larger along the Saaremaa coast compared to the Latvian coastline.

The vertical distributions of temperature, salinity, and density during different phases of upwelling are shown in Figure 13. During the starting phase, one can observe the tilting of the clines below the surface layer toward the coast and cold-salty-dense water surfacing at the coast. During the active phase, the tilting of the clines remained the same, and a detaching filament with a width of less than 4 km formed. During the relaxation phase, the areas affected by the upwelling have much smaller mixed layer depth—less than 10 m—compared to the open sea areas, where the mixed layer depth is close to 20 m.

4 Discussion

Based on the main upwelling regions in the Baltic Sea derived by Bychkova et al. (1988) in relation to weather conditions, the previous studies have shown that upwelling frequency (%) in the GoR is lower (e.g., Lehmann et al., 2012; Bednorz et al., 2021). Our study adds that a quantitative measure for the number of upwelling

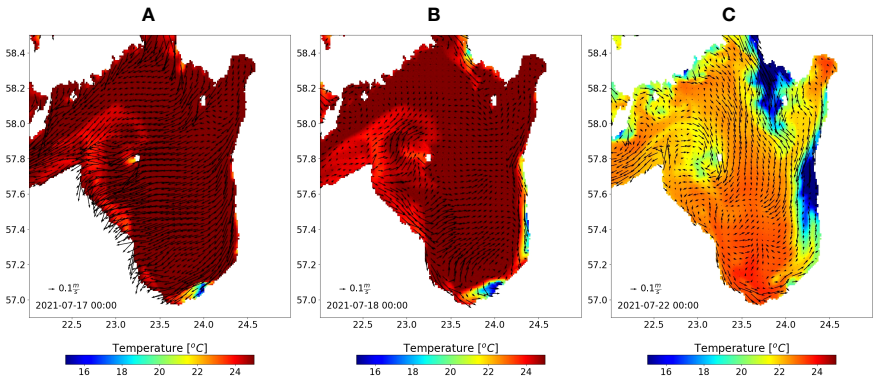

FIGURE 9
Simulated sea surface temperature from the GETM for July 17 **(A)**, 18 **(B)**, and 22 **(C)**. Arrows indicate the surface currents in the Gulf of Riga (GoR).

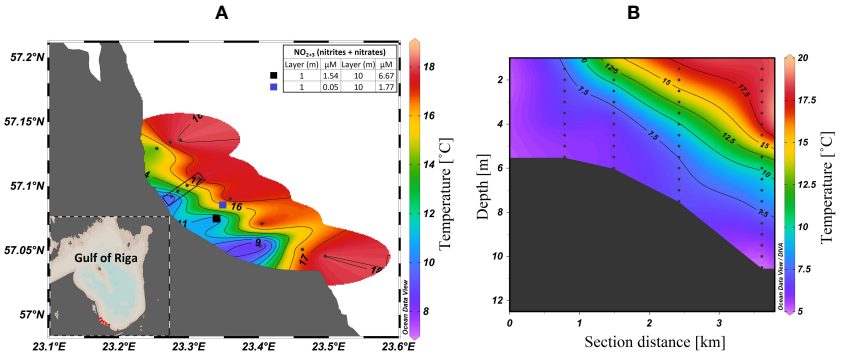

FIGURE 10
Sea surface temperature **(A)** and vertical distribution **(B)** of temperature within CTD (conductivity, temperature, and depth) section (marked as black rectangle) from CTD measurement survey during the upwelling on SW coast of the Gulf of Riga (GoR) on August 17, 2021. Black/blue squares represent the water samples taken inside/outside of the upwelling-affected area.

events in the GoR in 2010–2022 is 9 events/per year on average. Previous results obtained *via* satellite data (e.g., Bednorz et al., 2021) and model data (e.g., Myrberg and Andrejev, 2003) suggest that upwellings are more frequent on the W coast of the GoR rather than the E coast, which is in accordance with our acquired results based on coastal measurements. Even if we consider the previously mentioned no measurement data from Skulte and Roja and apply the correction based on the average number of events/per year, the

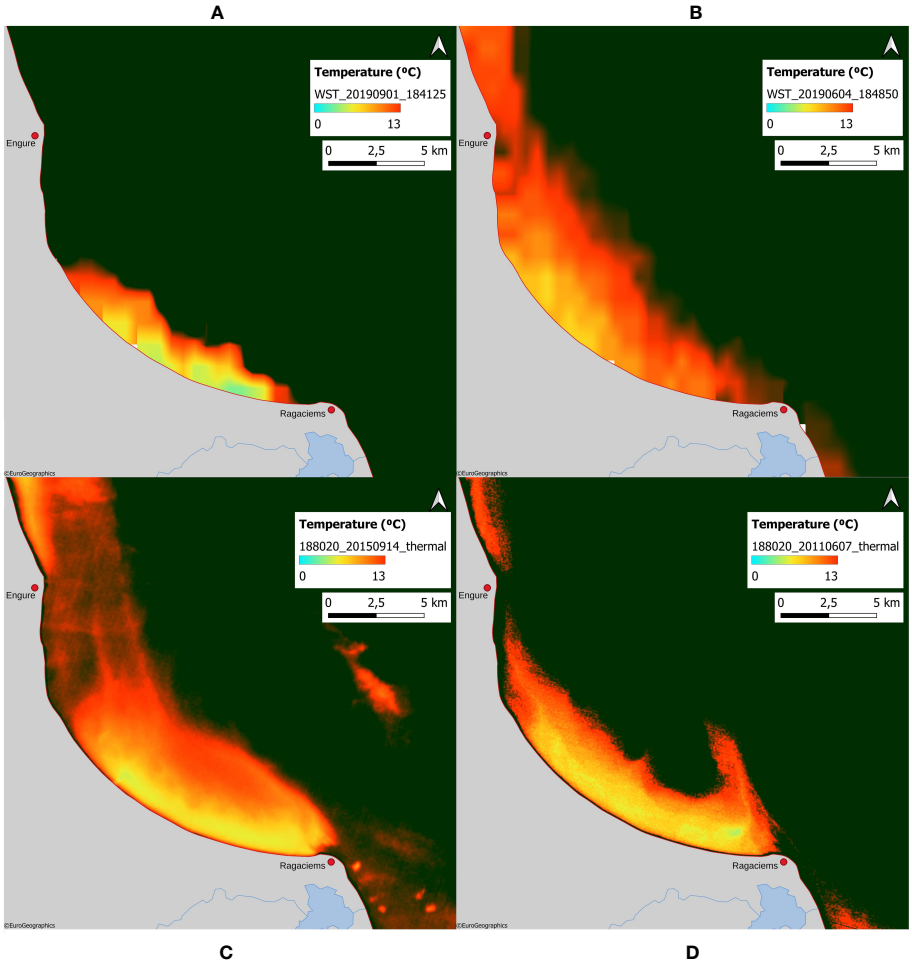

FIGURE 11
Sea surface temperature from Sentinel-3 **(A, B)** and Landsat 8 **(C, D)** satellite data on September 1, 2019 **(A)**, June 4, 2019 **(B)**, September 14, 2015 **(C)**, and June 7, 2011 **(D)**.

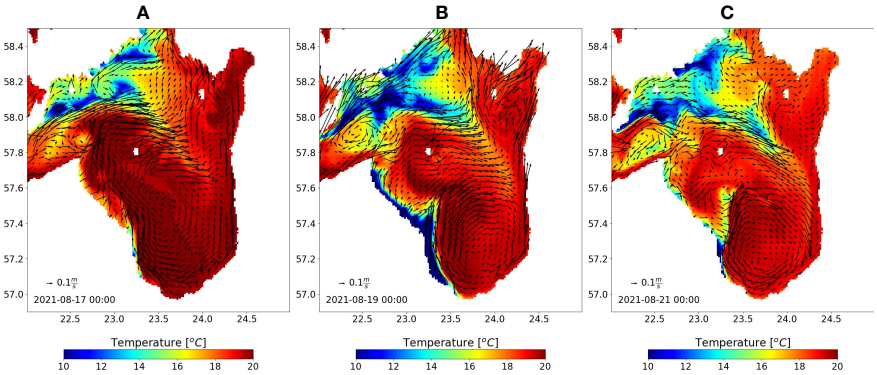

FIGURE 12
Simulated sea surface temperature (SST) during different phases of upwelling along the western part of the Gulf of Riga (GoR) together with the surface currents (black arrows) for August 17 **(A)**, 19 **(B)**, and 21 **(C)**, 2021.

total amount of upwelling events in the W coast would yield 71 events as opposed to 55 events in the E coast, with a ratio of 56%:44% in 2010–2022.

It is noteworthy to mention that detected upwelling events along the W coast differed between Mersrags and Roja despite the fact that these locations are only roughly 30 km apart. While in 20 cases upwelling events overlapped between Mersrags and Roja, 32 and 17 events, respectively, were unique in each location. The respective coastal morphology can provide a possible explanation—Mersrags is located in the coastal section whose direction is very close to S–N, whereas Roja is located in the coastal section whose direction is closer to SE–NW (see Figure 1). As an example, upwelling was evident in Roja but absent in Mersrags when the SE winds were blowing. The winds from Mersrags coastal station (results not shown here) revealed more frequent winds from the S direction than SE in 2010–2022, thus providing a plausible explanation of more frequent upwelling events detected in Mersrags than Roja. In conclusion, the W coast of the GoR has a more complex structure than the E coast, and we suggest that together with the prevailing winds in the region (SW, W, see also Supplementary Material, Figure S02), coastal structure and its orientation itself are also reasons why upwelling events are more frequently observed in the W coast than the E coast. In general, Lehmann et al. (2012) concluded the same governing principles on a bigger scale when describing the whole BS region—they showed that upwelling events occurred most frequently along the Swedish east coast and the Finnish coast of the Gulf of Finland (GoF), and upwelling frequencies were related to prevailing wind conditions and the orientation of the coastline with respect to the wind direction. An earlier study by Soomere and Keevallik (2001) of prevailing winds in the Baltic Proper supports this. Furthermore, Uiboupin and Laanemets (2015) concluded that upwellings are more extensive on the N coast than on the S coast of the GoF, which is according to the prevailing wind regime as well. Spatial wind analysis over the GoR in 2010–2022 revealed that directional change is relatively small—the dominant wind direction is SW, which tends to shift to more westerly during the summer time (see Supplementary Material, Figure S01). Thus, it complements the obtained results with more upwelling events on the W coast than the E coast.

On a monthly basis, fewer upwelling events in May can be explained by seasonal variations of temperature in the GoR (e.g.,

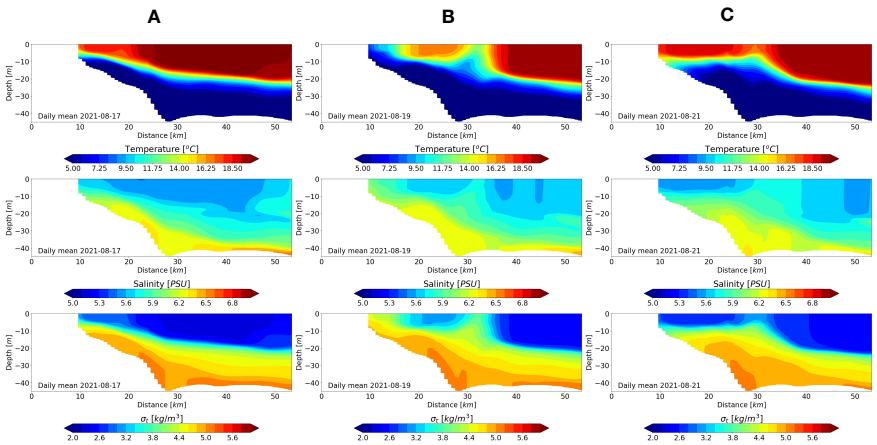

FIGURE 13
Vertical distributions of temperature, salinity and density from longitudinal transect 22.77-23.66 E and 57.45 N during different phases of upwelling along the western coast of GoR (GoR) for August 17 **(A)**, 19 **(B)**, and 21 **(C)**, 2021.

Raudsepp, 2001) when the temperature starts to gradually increase from spring, but the upper mixed layer is still shallow and not so warm; thus, only partially stratified conditions prevail (e.g., Skudra and Lips, 2017). During summer when water masses are well-stratified, the frequency of detected upwelling events in the GoR increased, which is in accordance with other studies from different areas of the Baltic Sea (e.g., Lehmann et al., 2012). In September, detected upwelling events were again scarcer if compared to summer months, which is mostly related to the gradual decrease of temperatures starting from the surface layers. Similar dynamics were described by Dabuleviciene et al. (2018) in a study of the overall number of upwelling events from the water temperature measurements at the Klaipeda monitoring station in the SE Baltic Sea from April to September 2000–2015.

Usually, coastal upwelling is divided into two phases—the active phase when upwelling favorable winds are blowing and cold water reaches the surface layers, and the relaxation phase when winds are reduced but strong temperature gradients in the sea exist. During the second phase, it is common that due to the baroclinic instability in the coastal upwelling jet filaments, squirts and eddies are formed (e.g., Zhurbas et al., 2008; Laanemets et al., 2011; Väli et al., 2017). The present study defined the Start/End, AUP (active upwelling phase), MIN (minimum temperature during upwelling), and RP (relaxation phase) points of each upwelling event based on coastal *in-situ* measurements. This approach allowed also us to judge how fast the upwelling evolves and for how long each of the phases lasts, something which has not been performed in the GoR and, to our knowledge, not published in the BS region as well.

The general warming of water masses and consistency with the annual cycle of air–sea heat exchange explains also the whole length of the upwelling events—in May and June, upwelling events were almost 20 h shorter than in July–September (e.g., Skudra and Lips, 2017). The mean RP length also gradually increased in May–September and in that sense was similar (R^2 = 0.74) to what was observed regarding the whole length of the upwelling events. We suggest that the longer an upwelling event lasts, the more the colder water masses reach the surface layers, and it takes more time for the system to return to the initial conditions during the relaxation phase. Unlike the length of the whole upwelling event and RP length, we observed that the AUP and the evolvement (how rapidly upwelling formed) length were variable between different months, which suggests that these parameters are more dependent on specific/local conditions like coastal morphology and respective wind conditions.

Summer upwelling events in the W (Mersrags, Roja) and E (Skulte) coasts had similarities regarding the mean length of AUP and evolvement length, whereas upwelling events themselves lasted longer in the E coast and were accompanied by at least 1.3°C higher maximum temperature drop than in the W coast upwellings. Higher maximum temperature drop amplifies the previously mentioned explanation, and we suggest that this is due to longer upwellings in the E coast. It is noteworthy to mention that in specific cases, Mersrags (W coast) was more comparable to Skulte (E coast) than to Roja (W coast). For example, an increase of maximum temperature drop during the upwelling events with increasing total length of the event itself was persistent in Skulte and Mersrags but was absent in Roja. Similarly, Skulte and Mersrags were more similar when looking at the RP length and total event length relation mentioned before. Thus, this demonstrates how locally different upwelling characteristics might be despite the fact that Roja and Mersrags are only roughly 30 km apart. Similarities between Mersrags and Skulte might hint that the orientation of the coastline could explain these differences between Roja and Mersrags—Roja is oriented in the SE–NW direction, whereas Mersrags and Skulte are oriented in the S–N direction. Spatial analysis of wind patterns over the GoR (see Supplementary Material, Figure S01) did not reveal substantial differences between the cells where Mersrags and Roja are located. Thus, we suggest that the orientation of the coastline is the most probable reason for the differences between Mersrags and Roja. Nevertheless, the upwelling favorable wind direction is different for each of these three stations. More detailed statistical analysis not performed within this research (e.g., multivariate analysis) would be welcome in order to address this question thoroughly. In addition, the dynamics of water mass offshore transport would be another factor, which might highlight the possible differences between both coasts during the upwelling events, although this was not explored in detail within the scope of this research.

The length of different upwelling phases indicated on presence of various types of upwelling events—from 12 to 328 h for whole upwelling length to almost all possible combinations regarding RP and evolvement length. There were upwelling events with rapid evolvement and rapid RP (with and without AUP), rapid evolvement but steady or gradual/slow RP, and, finally, with steady/slow evolvement but rapid RP. The slow evolvement of the upwelling event was the rarest case, and only in seven out of 93 events, the time it took for the upwelling to evolve exceeded 48 h (average 26 h). We suggest that such conditions would develop in case of rather slow winds (3–4 m/s) blowing for several days with upwelling favorable wind direction, which was evident, for example, in Skulte on May 23–26, 2012 (N–NE winds, 3–4 m/s), in Roja on August 3–7, 2014 (E–SE winds, 3 m/s), and in Mersrags on August 17–21, 2021 (S–SW winds, 3–4 m/s). An interesting feature was that in roughly 30% of all upwelling events, there was no defined AUP as temperature immediately increased after it reached the minimum value. Only in three cases out of 22 from Roja and Mersrags (W coast) was an event with no observed AUP also detected in other locations, but all other events without AUP are unique only for Roja/Mersrags. Further analysis of wind data from Mersrags showed that almost all of these upwelling events without AUP are coupled with distinct wind direction changes. In the case of Roja, the wind direction changed from SW to SE and back to SW after the upwelling event. Thus, SE wind direction created the most favorable conditions (parallel to the coast) for upwelling in Roja, but the event relaxed after the subsequent changes in wind direction, whereas in Mersrags, more southerly winds were evident prior to and during the evolvement of upwelling before further relaxation. We suggest that upwelling events with no AUP are mostly characteristic of a specific location or section of the coastline (example of Roja and Mersrags) and are mainly governed by the induced change of wind direction.

Coastal sea surface temperature measurements from Skulte allowed us to determine that upwelling from the case study on

the E coast of the GoR lasted from July 13 to 19, 2021. Measurements from the Skulte SmartBuoy revealed that temperature dynamics during this upwelling event were different than those observed at the coast. Based on the findings presented in this paper, it could be argued that pronounced temperature variability at the beginning of the upwelling event is caused by the lateral movement of colder water masses (in the form of filaments or squirts) from coastal areas amid regular, warm water masses in the respective SmartBuoy location at 2.5 km offshore. This type of mechanism is shown to be typical for the BS region (see references further below regarding baroclinic instability and filaments/squirts). The filtered time series with a cutoff period of 14.6 h filtered the SmartBuoy SST fluctuations only partially, whereas with a cutoff period of 16.6, the filtered time series filtered the SmartBuoy SST fluctuations thoroughly. Thus, it confirms that these fluctuations are not only related to inertial oscillations (as the period is higher) but are strongly affected by the lateral movement of water masses as well. CTD casts collected near the SmartBuoy and Skulte port entrance seem to confirm this, as temperature values obtained were similar to SmartBuoy and coastal station results. When the event became stronger (July 16), the temperature variability also decreased offshore at the location of the SmartBuoy. CTD profiling performed on July 13 suggests that upwelling was just starting to develop, as low temperatures (8.8° C) were observed only in the vicinity of Skulte port, but the 2-km offshore temperature was still rather high. More importantly, temperatures were significantly higher also 5 km and 10 km alongshore to the N from Skulte port, indicating that upwelling was not developed there yet or was evident only in a very narrow band (a few hundred meters) along the coastline. These observations suggest that there was also an alongshore gradient with the epicenter of upwelling close to Skulte port or the S along the coastline. Available satellite data on the evening of July 16 and 17 depicting the middle of the upwelling event revealed that during roughly 24 h, the affected area size increased by approximately 250 km^2 and by approximately 50 km alongshore.

On July 22, 2021, the upwelling signal was not evident from the Skulte coastal measurements, and one would assume that it should not be anticipated throughout the whole E coast of the GoR, as the coastline here is not so complex as in the W part of the gulf. Following this path, the observations at first sight may be misleading, as a rather distinct upwelling was visible from satellite data near and offshore of Salacgriva, as well as in the area around Kihnu Island, N part of the gulf. This time satellite data matched reasonably well with the model output, and, indeed, in both outputs, there was no upwelling signal in the Skulte region. Although we used the temperature data from Salacgriva coastal station only for quantitative analysis due to the station's location rather deep inside the river mouth, the upwelling signal was detected, and it confirmed the results from the model and satellite data from July 22. Considering the preceding upwelling event along the E coast on July 13–19 (which was detected from Salacgriva measurements as well), we speculated that July 22 marked the second upwelling event or even the continuation of the preceding event. That would explain why we saw lower temperatures from satellite data more offshore (part of which might be from the preceding event) of Salacgriva on July 22 if compared to July 17. In addition, on July 22, the wind speed was 7–9 m/s, approximately 3–4 m/s higher than on July 13–19, which would amplify the offshore transport of previously upwelled water. Moreover, yellowish-orange formations in the satellite data can be seen further offshore from Skulte on July 22, which resemble the possible structure of filaments, which, in turn, are a common offshore feature related to upwelling events in the Baltic Sea region (e.g., Zhurbas et al., 2008; Laanemets et al., 2011) as well as globally (Hösen et al., 2016; Zaba et al., 2021). Judging by the distance from the coast, these formations would be associated with the upwelling event on July 13–19 and would vividly demonstrate the transport of water masses (with lower temperatures than the ambient area) induced by the upwelling event.

The upwelling event on August 17, 2021, represents a more local event in the small gulf-like curve of the coastline in the SW part of the GoR. Performed CTD casts allowed to capture the whole area of this rather small upwelling event with lower chlorophyll *a* concentrations (approx. 0.5 mg/m^3) and considerably higher total nitrogen concentration (30-fold) in the surface layers than in surface layers outside of the upwelling. Unfortunately, no temperature time series from coastal measurements or satellite data were available for this place/time, but model output provided insights regarding the length of the event and the size of the potentially affected area. In addition, historical satellite data revealed that these rather local upwelling events are quite strong and typical for this location. Three historical upwelling events shown here were characterized by predominant E–SE wind direction resembling the orientation of the coastline. On June 4, 2019, the predominant wind direction was SE–S, which explains why the upwelling signal was evident further N alongshore till the Mersrags (not shown here but visible from the full domain map).

Regarding the model output, the upwelling case studies from 2021 indicate the importance of simulating the vertical thermal stratification correctly in order to capture the upwelling with the simulations correctly. Obviously, the model captured the second upwelling along the eastern coast in July and the August upwelling along the western coast well, but it did not really capture the first eastern coast upwelling very well. Most likely, the reason is the too-deep thermocline in the model; i.e., the cold water that emerged during upwelling never reached the surface, and also during the first upwelling, the wind speeds were the smallest.

Another interesting feature revealed by the case studies is the small impact of upwelling in the GoR on salinity distribution. Namely, in Väli et al. (2017), it was shown that the upwellings in the GoF can either produce strong or weak lateral density gradients in the surface layer depending on the contribution of the salinity to the density. If the upwelling had produced only temperature gradients and no or weak salinity gradient (no density gradient), then the emergence of submesoscale features was missing, and as soon as there were also density gradients, submesoscale features emerged also in the surface layers during the relaxation phase of the upwelling. The results from the simulations indicate a rather small lateral density and salinity gradients in the sea surface, meaning that the conditions for the occurrence of baroclinic instabilities (e.g., Zhurbas et al., 2006), i.e., formation of the eddies, are rather small, and this could explain rather fast upwelling relaxation in the basin.

From model results, it was possible to see filaments; nevertheless, we have to bear in mind that the GoR is a much shallower water basin if compared to the GoF and also shaped like a bowl. The number of eddies that could fit in this bowl is definitely smaller, and, therefore, we suggest that the mesoscale features occurring in the GoR are different compared to the GoF and even more in locations outside the BS where different atmospheric forcing and climate modes prevail (e.g., Mandal et al., 2021).

Climate change predictions regarding the BS region have a possible impact on the GoR as well. Although there is no direct linkage between climate change and possible changes in the upwelling dynamics, climate change research projects further air/water temperature increase, shallower mixed layer, sharper thermocline during summer, changing seasonality in river runoff, milder winters with less snow, etc. (Meier et al., 2022a; Meier et al., 2022b). Considering all the mentioned factors, we suggest that stratification will form earlier in the GoR; thus, upwelling events might occur earlier increasing the total amount observed during the warm season. Because of large internal variability, it is unclear whether there is an overall trend in mean wind speed. There has been an increase in the number of deep cyclones over central and northern Europe but no evidence of a long-term trend (Meier et al., 2022b).

The North Atlantic Oscillation (NAO) is the dominant mode of near-surface pressure variability over the North Atlantic. During the positive (negative) phase of the NAO, the Icelandic Low and Azores High pressure systems are stronger (weaker), leading to a stronger (weaker) than normal westerly flow (Hurrell, 1995). According to the review by Meier et al. (2022b) about the future climate change regarding large-scale atmospheric circulation, the NAO is very likely to continue to exhibit large natural variations similar to those observed in the past. In response to global warming, it is likely to become slightly more positive (associated with mild temperatures and increased precipitation and storminess) on average, which complements earlier studies about climate variability in the BS region (e.g., Lehmann et al., 2011). If we assume that the positive phase of the NAO will increase, we suggest the change of existing upwelling ratio between the two coasts favoring even more upwelling events on the W coast.

For future considerations, zooplankton, phytoplankton, and nutrient data, collected in and outside of the upwelling-affected area within this study (through targeted sampling surveys in 2021 and 2022, not described here in detail), will allow us to analyze the mutual relationships between upwelling and biogeochemistry and implications for ecosystem itself. Because their size upwellings are not so decisive for ecosystem productivity in the GoR as in the world's most known upwelling areas (García-Reyes et al., 2015), still, coastal areas show certain distinctions with more offshore areas of the Gulf for both phytoplankton and zooplankton communities (Jurgensone et al., 2011; Labuce et al., 2021), and the role of upwelling has never been assessed for these discrepancies. Other studies of upwellings in the GoF have highlighted the importance of phosphate transport from deeper layers to the nutrient-depleted surface during upwelling for cyanobacterial blooms (e.g., Zhurbas et al., 2008; Laanemets et al., 2009 and Laanemets et al., 2011; Väli et al., 2011). Offshore transport (Ekman transport) and/or cross-shore (using model data) transport calculations could be applied to demonstrate the dynamic processes during upwellings, especially in those events where *in-situ* or remote measurements allow the analysis of all areas affected by the upwellings. Regarding the more local upwelling events described also within this study, we can suggest that model resolution should be higher (at least 250 m) in order to obtain more detailed and relevant results. The same approach applies to the satellite data. Finally, predicted water temperature increase and seasonal changes in the river runoff due to climate change (BACC, 2015) will potentially result in a stronger and earlier stratification in the GoR region—a precondition for possibly more frequent, stronger, and earlier upwelling events, which would only increase the role and significance of this process. The latest review on oceanographic regional climate projections for the Baltic Sea until 2100 (Meier et al., 2022a) indicates an increase in the occurrence of marine heat waves in the GoR. With longer and stronger upwellings, this heat wave tendency in the GoR could be disrupted, only strengthening the need to follow upwelling events for better local and regional projections.

In conclusion, we described and characterized the upwelling events in the GoR in 2010–2022 based on historical data and performed measurements in 2021 and 2022 with emphasis on the *in-situ* data, including the SmartBuoy data series, which has not been widely used in the Baltic Sea region in relevance to the scientific research. We showed that upwellings occur more often on the W coast than the E coast, whereas on the E coast, they tend to be longer and with higher temperature drops. Wind patterns showed prevailing W–SW winds over the GoR for the study period. For the first time in the GoR studies, we parametrized and analyzed specific phases of the upwelling events from coastal measurements to ascertain the dynamic nature and different types of upwelling events, even along the same sections or parts of the coastline. This approach has been limited also in other studies regarding the Baltic Sea region, as the majority of upwelling-related studies concentrate more on remote sensing data, model data, or a combination of both. Nevertheless, through case studies, we showed that using multiple data acquisition methods or maximum available data increases the quality of analysis (as each method has its own shortcomings), especially regarding such dynamic phenomena as upwelling, which has the potential to substantially influence the local ecosystem. Thus, we suggest that this study could serve as a basis for further upwelling-related ecosystem studies in the GoR and similar water bodies.

Data availability statement

The raw data supporting the conclusions of this article will be made available by the authors, without undue reservation.

Author contributions

MS, GV, AI and MP contributed to conception and design of the study. MS organized the database. MS, GV, MP performed the data analysis. MS wrote the first draft of the manuscript. MS, GV, AI, and MP wrote sections of the manuscript. All authors contributed to manuscript revision, read, and approved the submitted version.

Funding

The author(s) declare financial support was received for the research, authorship, and/or publication of this article. This work was funded by the European Regional Development Fund, 1.1.1.2/16/l/001 Post-doctoral project No.1.1.1.2/VIAA/4/20/733. GV was supported by the Estonian Science Council (grant number PRG602). Computational resources from the HPC centers of Tallinn University of Technology and Tartu University are gratefully acknowledged.

Conflict of interest

The authors declare that the research was conducted in the absence of any commercial or financial relationships that could be construed as a potential conflict of interest.

Publisher's note

Supplementary material

The Supplementary Material for this article can be found online at: https://www.frontiersin.org/articles/10.3389/fmars.2023.1244643/full#supplementary-material

References

BACC (2015). *Second assessment of climate change for the baltic sea basin* (Geesthacht: SpringerOpen), 69–263.

Bednorz, E., Czernecki, B., Półrolniczak, M., and Tomczyk, A. M. (2018). Atmospheric forcing of upwelling along the south-eastern Baltic coast. *Baltica* 31 (1), 73–85. doi: 10.5200/baltica.2018.31.07

Bednorz, E., Półrolniczak, M., Czernecki, B., and Tomczyk, A. M. (2019). Atmospheric forcing of coastal upwelling in the southern baltic sea basin. *Atmosphere* 10 (6), 327. doi: 10.3390/atmos10060327

Bednorz, E., Półrolniczak, M., and Tomczyk, A. M. (2021). Regional circulation patterns inducing coastal upwelling in the Baltic Sea. *Theor. Appl. Climatology* 144, 905–916. doi: 10.1007/s00704-021-03539-7

Berzinsh, V. (1980). *Interannual and seasonal changes of water salinity in the Gulf of Riga. Rybokhozyaistvennye issledovaniya (Balt-NIIRKH) 15Avots*. (Riga: Avots) 3–12, in Russian.

Berzinsh, V. (1995). "Hydrology," in *Ecosystem of the gulf of riga between 1920 and 1990*, vol. 7-32 . Ed. O. Ojaveer (Tallinn: Estonian Acad. Publ.).

Burchard, H., and Bolding, K. (2002). *GETM, A general estuarine transport model: scientific documentation*. (Ispra: Joint Research Centre).

Bychkova, I., Viktorov, S., and Shumakher, D. A. (1988). A relationship between the large-scale atmospheric circulation and the origin of coastal upwelling in the Baltic Sea. *Meteorol. Gidrol* 10, 91–98.

Dabuleviciene, T., Kozlov, I., Vaiciute, D., and Dailidiene, I. (2018). Remote sensing of coastal upwelling in the south-eastern baltic sea: statistical properties and implications for the coastal environment. *Remote Sensing* 11, 1752. doi: 10.3390/rs10111752

Dabuleviciene, T., Vaiciute, D., and Kozlov, I. (2020). Chlorophyll-a variability during upwelling events in the south-eastern baltic sea and in the curonian lagoon from satellite observations. *Remote Sensing* 21, 3661. doi: 10.3390/rs12213661

Delpeche-Ellmann, N., Dabuleviciene, T., and Soomere, T. (2017). Examining Lagrangian surface transport during a coastal upwelling in the Gulf of Finland, Baltic Sea. *J. Mar. Syst.* 171, 21–30. doi: 10.1016/j.jmarsys.2016.10.007

Delpeche-Ellmann, N., and Soomere, T. (2018). Possible Presence of Shear Instabilities at Steep Slopes during an Upwelling Event in the Gulf of Finland, Baltic Sea. *J. Coast. Res.* 85, 481–485. doi: 10.2112/SI85-097.1

Ekman, V. (1905). On the influence of the earth's rotation on ocean currents. *Ark. Mat. Astron. Fys.* 2, 1–53.

Elken, J., Raudsepp, U., and Lips, U. (2003). On the estuarine transport reversal in deep layers of the Gulf of Finland. *J. Sea Res.* 49 (4), 267–274. doi: 10.1016/S1385-1101(03)00018-2

García-Reyes, M., Sydeman, W. J., Schoeman, D. S., Rykaczewski, R. R., Black, B. A., Smit, A. J., et al. (2015). Under pressure: climate change, upwelling, and eastern boundary upwelling ecosystems. *Front. Mar. Sci.* 2. doi: 10.3389/fmars.2015.00109

Gräwe, U., Holtermann, P., Klingbeil, K., and Burchard, H. (2015). Advantages of vertically adaptive coordinates in numerical models of stratified shelf seas. *Ocean Model.* 92, 56–68. doi: 10.1016/j.ocemod.2015.05.008

Gurova, E., Lehmann, A., and Ivanov, A. (2013). Upwelling dynamics in the Baltic Sea studied by a combined SAR/infrared satellite data and circulation model analysis. *Oceanologia* 55 (3), 687–707. doi: 10.5697/oc.55-3.687

Hersbach, H., Bell, B., Berrisford, P., Hirahara, S., Horányi, A., Muñoz-Sabater, J., et al. (2020). The ERA5 global reanalysis. *Q. J. R. Meteorological Soc.* 146, 1999–2049. doi: 10.1002/qj.3803

Hösen, E., Möller, J., Jochumsen, K., and Quadfasel, D. (2016). Scales and properties of cold filaments in the Benguela upwelling system off Lüderitz. *J. Geophysical Research: Oceans* 121 (3), 1896–1913. doi: 10.1002/2015JC011411

Hurrell, J. W. (1995). Decadal trends in the North Atlantic Oscillation: regional temperatures and precipitation. *Science-AAAS-Weekly Paper Edition* 269 (5224), 676–679. doi: 10.1126/science.269.5224.676

Jurgensone, I., Carstensen, J., Ikauniece, A., and Kalveka, B. (2011). Long-term changes and controlling factors of phytoplankton community in the gulf of riga (Baltic sea). *Estuaries Coasts* 34 (6), 1205–1219. doi: 10.1007/s12237-011-9402-x

Kikas, V., and Lips, U. (2016). Upwelling characteristics in the Gulf of Finland (Baltic Sea) as revealed by Ferrybox measurements in 2007–2013. *Ocean Sci.* 12 (3), 843–859. doi: 10.5194/os-12-843-2016

Klingbeil, K., Lemarié, F., Debreu, L., and Burchard, H. (2018). The numerics of hydrostatic structured-grid coastal ocean models: State of the art and future perspectives. *Ocean Model.* 125, 80–105. doi: 10.1016/j.ocemod.2018.01.007

Kowalewska-Kalkowska, H., and Kowalewski, M. (2019). Combining satellite imagery and numerical modelling to study the occurrence of warm upwellings in the southern baltic sea in winter. *Remote Sens.* 11 (24), 2982. doi: 10.3390/rs11242982

Krek, A. V., Krek, E. V., Danchenkov, A. R., Krechik, V. A., and Kapustina, M. V. (2021). The role of upwellings in the coastal ecosystem of the Southeastern Baltic Sea. *Regional Stud. Mar. Sci.* 44 (1), 101707. doi: 10.1016/j.rsma.2021.101707

Laanemets, J., Väli, G., Zhurbas, V., Elken, J., Lips, I., and Lips, U. (2011). Simulation of mesoscale structures and nutrient transport during summer upwelling events in the Gulf of Finland in 2006. *Boreal Environ. Res.* 16 (A), 15–26.

Laanemets, J., Zhurbas, V., Elken, J., and Nyman, E. (2009). Dependence of upwelling-mediated nutrient transport on wind forcing, bottom topography and stratification in the Gulf of Finland: Model experiments. *Boreal Environ. Res.* 14 (1), 213–225.

Labuce, A., Ikauniece, A., Jurgensone, I., and Aigars, J. (2021). Environmental impacts on zooplankton functional diversity in brackish semi-enclosed gulf. *Water* 13 (14), 1881. doi: 10.3390/w13141881

Lehmann, A., Getzlaff, K., and Harlaβ, J. (2011). Detailed assessment of climate variability in the Baltic Sea area for the period 1958 to 2009. *Climate Res.* 46 (2), 185–196. doi: 10.3354/cr00876

Lehmann, A., and Myrberg, K. (2008). Upwelling in the baltic sea — A review. *J. Mar. Syst.* 74 (Supplement), s3–s12. doi: 10.1016/j.jmarsys.2008.02.010

Lehmann, A., Myrberg, K., and Höflich, K. (2012). A statistical approach to coastal upwelling in the Baltic Sea based on the analysis of satellite data for 1990–2009. *Oceanologia* 54 (3), 369–393. doi: 10.5697/oc.54-3.369

Leppäranta, M., and Myrberg, K. (2009). *Physical oceanography of the baltic sea* (Chichester: Praxis Publishing Ltd). doi: 10.1007/978-3-540-79703-6

Liblik, T., Väli, G., Lips, I., Lilover, M.-J., Kikas, V., and Laanemets, J. (2020). The winter stratification phenomenon and its consequences in the Gulf of Finland, Baltic Sea. *Ocean Sci.* 16 (6), 1475–1490. doi: 10.5194/os-16-1475-2020

Liblik, T., Väli, G., Salm, K., Laanemets, J., Lilover, M.-J., and Lips, U. (2022). Quasi-steady circulation regimes in the Baltic Sea. *Ocean Sci.* 18 (3), 857–879. doi: 10.5194/os-18-857-2022

Lips, U., Lilover, M.-J., Raudsepp, U., and Talpsepp, L. (1995). "Water renewal processes and related hydrographic structures in the Gulf of Riga," in *Hydrographic studies within the Gulf of Riga project 1993-1994*. Eds. J. Elken and A. Toompuu (Tallinn: EMI Report Series), 1–34.

Lips, U., Zhurbas, V., Skudra, M., and Väli, G. (2016a). A numerical study of circulation in the Gulf of Riga, Baltic Sea. Part I: Whole-basin gyres and mean currents. *Continental Shelf Res.* 112, 1–13. doi: 10.1016/j.csr.2015.11.008

Lips, U., Zhurbas, V., Skudra, M., and Väli, G. (2016b). A numerical study of circulation in the Gulf of Riga, Baltic Sea. Part II: Mesoscale features and freshwater transport pathways. *Continental Shelf Res.* 115, 44–52. doi: 10.1016/j.csr.2015.12.018

Mandal, S., Behera, N., Gangopadhyay, A., Susanto, R. D., and Pandey, P. C. (2021). Evidence of a chlorophyll "tongue" in the Malacca Strait from satellite observations. *J. Mar. Syst.* 223, 103610. doi: 10.1016/j.jmarsys.2021.103610

Meier, H. E. M., Dieterich, C., Gröger, M., Dutheil, C., Börgel, F., Safonova, K., et al. (2022a). Oceanographic regional climate projections for the Baltic Sea until 2100. *Earth System Dynamics* 13 (1), 159–199. doi: 10.5194/esd-13-159-2022

Meier, H. E. M., Kniebusch, M., Dieterich, C., Gröger, M., and Zorita, E. (2022b). Climate change in the Baltic Sea region: a summary. *Earth System Dynamics* 13 (1), 457–593. doi: 10.5194/esd-13-457-2022

Myrberg, K., and Andrejev, O. (2003). Main upwelling regions in the Baltic Sea – a statistical analysis based on three-dimensional modelling. *Boreal Environ. Res.* 8, 97–112.

Omstedt, A., Elken, J., Lehmann, A., Leppäranta, M., Meier, H. E. M., Myrberg, K., et al. (2014). Progress in physical oceanography of the Baltic Sea during the 2003–2014 period. *Prog. In Oceanography* 128, 139–171. doi: 10.1016/j.pocean.2014.08.010

Petrov, V. S. (1979). "Water balance and water exchange between the Gulf of Riga and the Baltic Proper," in *Sbornik rabot rizhskoj gidrometeorologicheskoj observatorii*, 20–40. in Russian. (Riga: RGMO).

Raudsepp, U. (2001). Interannual and seasonal temperature and salinity variations in the gulf of riga and corresponding saline water inflow from the baltic proper. *Hydrology Res.* 32 (2), 135–160. doi: 10.2166/nh.2001.0009

Schlitzer, R. (2018). *Ocean data view*. Available at: https://odv.awi.de.

Skudra, M., and Lips, U. (2017). Characteristics and inter-annual changes in temperature, salinity and density distribution in the Gulf of Riga. *Oceanologia* 59 (1), 37–48. doi: 10.1016/j.oceano.2016.07.001

Soomere, T., and Keevallik, S. (2001). Anisotropy of moderate and strong winds in the Baltic Proper. *Proc. Estonian Acad. Sci. Eng.* 7 (1), 35–49. doi: 10.3176/eng.2001.1.04

Soosaar, E., Maljutenko, I., Raudsepp, U., and Elken, J. (2014). An investigation of anticyclonic circulation in the southern Gulf of Riga during the spring period. *Continental Shelf Res.* 78, 75–84. doi: 10.1016/j.csr.2014.02.009

Stipa, T., Tamminen, T., and Seppälä, J. (1999). On the creation and maintenance of stratification in the Gulf of Riga. *J. Mar. Syst.* 23 (1-3), 27–49. doi: 10.1016/S0924-7963(99)00049-4

Suursaar, Ü. (2020). Combined impact of summer heat waves and coastal upwelling in the Baltic Sea. *Oceanologia* 62 (4A), 511–524. doi: 10.1016/j.oceano.2020.08.003

The BACC II Author Team (2015). *Second assessment of climate change for the Baltic Sea Basin*. (Springer Cham) 501 pp. doi: 10.1007/978-3-319-16006-1

Uiboupin, R., and Laanemets, J. (2015). Upwelling parameters from bias-corrected composite satellite SST maps in the gulf of Finland (Baltic sea). *IEEE Geosci. Remote Sens. Lett.* 12 (3), 592–596. doi: 10.1109/LGRS.2014.2352397

Väli, G., Zhurbas, V., Lips, U., and Laanemets, J. (2017). Submesoscale structures related to upwelling events in the Gulf of Finland, Baltic Sea (numerical experiments). *J. Mar. Syst.* 171, 31–42. doi: 10.1016/j.jmarsys.2016.06.010

Väli, G., Zhurbas, V., Lips, U., Laanemets, J., and Elken, J. (2011). Simulation of nutrient transport from different depths during an upwelling event in the Gulf of Finland. *Oceanologia* 53 (1), 431–448. doi: 10.5697/oc.53-1-TI.431

Wu, L., Staneva, J., Breivik, Ø., Rutgersson, A., Nurser, G., Clementi, E., et al. (2019). Wave effects on coastal upwelling and water level. *Ocean Model.* 140, 101405. doi: 10.1016/j.ocemod.2019.101405

Yurkovskis, A., Wulff, F., Rahm, L., Andruzaitis, A., and Rodriguez-Medina, M. (1993). A nutrient budget of the gulf of riga; baltic sea. *Estuarine Coast. Shelf Sci.* 37 (2), 113–127. doi: 10.1006/ecss.1993.1046

Zaba, K. D., Franks, P. J. S., and Ohman, M. D. (2021). The california undercurrent as a source of upwelled waters in a coastal filament. *J. Geophysical Research: Oceans* 126 (2). doi: 10.1029/2020JC016602

Zhang, S., Wu, L., Arnqvist, J., Hallgren, C., and Rutgersson, A. (2022). Mapping coastal upwelling in the Baltic Sea from 2002 to 2020 using remote sensing data. *Int. J. Appl. Earth Observation Geoinformation* 114 (12), 103061. doi: 10.1016/j.jag.2022.103061

Zhurbas, V., Laanemets, J., and Vahtera, E. (2008). Modeling of the mesoscale structure of coupled upwelling/downwelling events and the related input of nutrients to the upper mixed layer in the Gulf of Finland, Baltic Sea. *J. Geophysical Res. Atmospheres* 113 (C5). doi: 10.1029/2007JC004280

Zhurbas, V., Oh, I. S., and Park, T. (2006). Formation and decay of a longshore baroclinic jet associated with transient coastal upwelling and downwelling: A numerical study with applications to the Baltic Sea. *J. Geophysical Res. Atmospheres* 111 (4). doi: 10.1029/2005JC003079

Zhurbas, V., Väli, G., Golenko, M., and Paka, V. (2018). Variability of bottom friction velocity along the inflow water pathway in the Baltic Sea. *J. Mar. Syst.* 184, 50–58. doi: 10.1016/j.jmarsys.2018.04.008

Frontiers in Marine Science

Explores ocean-based solutions for emerging global challenges

The third most-cited marine and freshwater biology journal, advancing our understanding of marine systems and addressing global challenges including overfishing, pollution, and climate change.

Discover the latest Research Topics

See more →

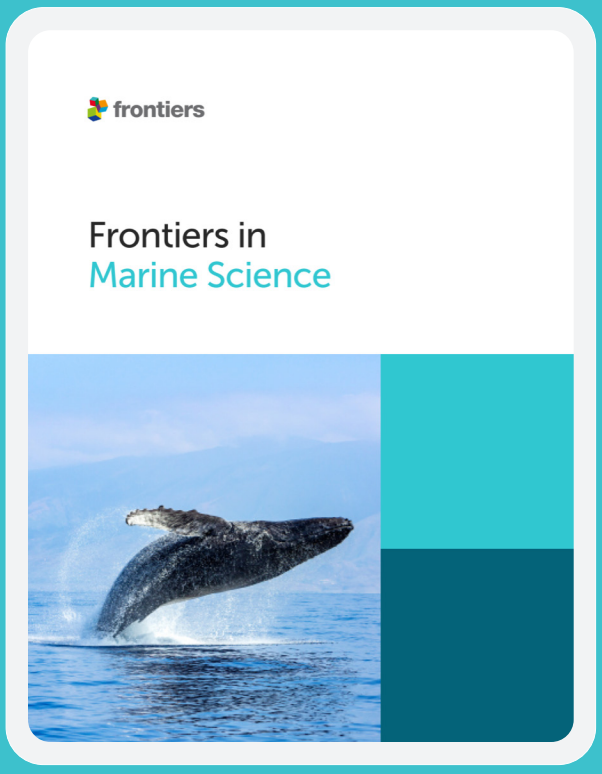

Frontiers

Avenue du Tribunal-Fédéral 34
1005 Lausanne, Switzerland
frontiersin.org

Contact us

+41 (0)21 510 17 00
frontiersin.org/about/contact